Directed synthesis and characterization of zeolite nanoparticles

A Dissertation
SUBMITTED TO THE FACULTY OF
UNIVERSITY OF MINNESOTA
BY

Xueyi Zhang

IN PARTIAL FULFILLMENT OF THE REQUIREMENTS
FOR THE DEGREE OF
DOCTOR OF PHILOSOPHY

Prof. Michael Tsapatsis, Adviser

October 2013

Acknowledgements

First of all, I would like to extend my sincere thanks and gratitude to my adviser, Prof. Michael Tsapatsis. Over the last five years, it is my greatest honor working under his directions while being impressed by his dedication and perseverance, his broad view of the entire chemical engineering field and penetrating observations of experimental details that later turned out to be crucial, his thoughtfulness on my future career plans and wisdom to prioritize my steps to carry out the plans while developing my capabilities at the same time. None of my progress over my Ph.D. career would have been made without his guidance. I would also like to thank the Tsapatsis group members and alumni, Prof. Wei Fan, Dr. Sandeep Kumar, Dr. Pyung-Soo Lee, Dr. Kumar Varoon Agrawal, Prof. Dongxia Liu, Dr. Chun-Yi Sung, Dr. Elizabeth E. Mallon, Dr. Bahman Elyassi, Dr. Nafiseh Rajabbeigi, Dr. Christopher M. Lew, Prof. Won Cheol Yoo, and many others, for their help during my time in the lab. It was them who kindly and patiently showed me for the first time every single experimental and computational technique I use every day. In my future academic career, the pursuit for academic scholarship in the Tsapatsis group will always be with me.

I would like to thank my preliminary and final exam committee members, Profs. K. Andre Mkhoyan, Alon V. McCormick, R. Lee Penn, and David J. Norris. Not only have they provided precious comments and suggestions to my research proposal and dissertation, helpful discussions with them throughout all these years have also been a very crucial part of my research.

I would also like to thank the past and current staff members in the University of Minnesota Characterization Facility, Drs. Bob Hafner, Ozan Ugurlu, Wei Zhang, Maria Torija, Wei Fan, Nick Seaton, Chris Frethem, and Fang Zhou, for their help on the materials characterization part of my research.

I acknowledge Dr. David A. Lesch of UOP LLC for his helpful advices and support on the template-free synthesis of faujasite nanoparticles.

I also acknowledge the University of Minnesota Graduate School for a Doctoral Dissertation Fellowship.

Finally, and most importantly, special thanks go to my family for their continuous and unconditional support throughout my graduate career.

Abstract

Zeolites are a class of materials with ordered micropores (smaller than 2 nm), that can be used for gas separation, catalysis, and adsorption. Structurally, zeolites are composed of SiO_4 tetrahedra sharing corners in an ordered manner. The numerous arrangements of these SiO_4 tetrahedra give zeolites micropores in the forms of channels and cages. Although the applications of each zeolite depends on the spatial arrangements and the sizes of these micropores, size and morphology of zeolite particles are equally important. By preparing zeolite nanoparticles, diffusion paths of zeolite particles can be shortened, total surface area of zeolite particles can be increased, which are beneficial to reducing energy consumption in gas separation, reducing deactivation in catalytic reactions, and increasing adsorption capacities.

This dissertation introduces various methods to prepare zeolite nanoparticles. Zeolite nanoparticles prepared with the help of mesoporous carbon templates (hard template) are firstly introduced where the shape and size of zeolite particles are imprinted from the templates. In addition to hard templates, the use of bifunctional surfactant (soft templates) to prepare ultra-small zeolite nanoparticles and lamellar zeolite membrane is also introduced. With only one structure-directing agent that is less intuitive than hard or soft templates, the preparation of hierarchical lamellar zeolite with 2 nm lamellae, the self-pillard pentasil (SPP) zeolite, is introduced, where the intrinsic growth patterns of the crystal played an important role. Finally, template-free synthesis of zeolite nanoparticles, where zeolite formation is totally driven by the intrinsic growth patterns, is introduced. In addition to the preparation methods, a series of computational methods to determine and study the structures of zeolite nanoparticles are also introduced.

Table of Contents

List of Figures

Chapter 1 Introduction

Separation and catalytic reaction are two major themes of chemical engineering. In either application, the direct manipulation of molecules is the ultimate goal. Recognition of molecules can be achieved conveniently in molecular cavities that resemble the shape, size or a certain property of the molecule. There are many porous materials with cavities of molecular size. Among them, zeolite is an aluminosilicate material with ordered micropores (molecular cavities smaller than 2 nm, which is similar to the size of industrial molecules)[1]. Comparing to other porous materials, such as enzymes and metal-organic frameworks (MOFs), the major advantage of zeolites is their thermal and mechanical stability.

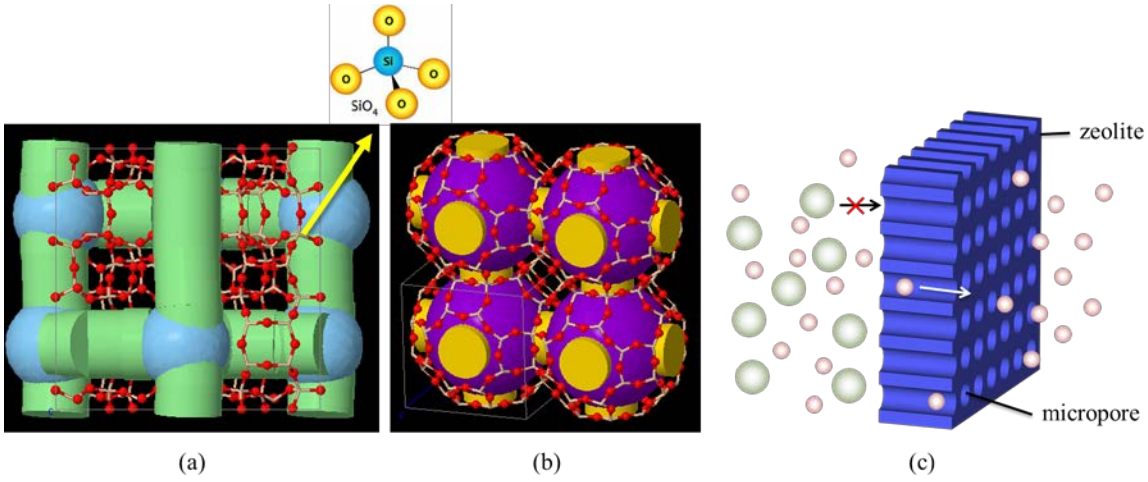

Figure 1-1 Micropores in zeolites in the form of (a) channels (in framework type MFI) and (b) cages (in framework type LTA). The micropores are formed by SiO_4 tetradehra (highlighted in (a)) sharing corners. Due to the special size of the micropores in zeolites (smaller than 2 nm), zeolites can be used to selectively sieve industrial molecules according to their size and shape (c).

As a material composed of SiO_4 tetrahedra sharing corners, the three-dimensionally ordered micropores of zeolite are in the forms of channels and cages (Fig. 1-1 (a) and (b), respectively, channels and cages generated by ZEOMICS[2]). These

micropores can selectively admit or reject molecules (molecular sieving effect, as in Fig. 1-1(c)), rendering zeolites good materials for high-resolution separation[3-4]. If catalytic centers are incorporated into the wall of the micropores, with molecular sieving effect, selective catalytic conversion can be achieved in the zeolites[5]. However, important as it is, the architecture of the micropore system in the zeolite, or pore topology, is not the only factor that matters. Morphology and size of the zeolite particles are equally important[6]. For example, zeolite membranes prepared with ultra-small zeolite seeds have higher flux, and thus requires less energy consumption during operation[7][4]; due to very short diffusion path, ultra-small zeolite nanoparticles used as catalysts have little deactivation problems and are good for fast and selective reactions[6, 8]; while very large zeolite particles have excellent shape selectivity in catalytic reactions due to the larger diffusion path for reactants and products[9]. Thus, precisely controlling the morphology and size of zeolite particles has been a very important part of zeolite synthesis.

In this dissertation, various templated and template-free syntheses of zeolite nanoparticles are introduced. In many cases, the properties of zeolite nanoparticles are very different from bulk phase materials. Correctly understanding the structure of the zeolite nanoparticles is crucial to synthesis and characterization of zeolite nanoparticles. Thus, this dissertation firstly introduces the development of a series of computational methods to determine and study the structure of zeolite nanoparticles (*Chapter 2*). Following the computational methods, as an intuitive method to prepare nanoparticles, zeolite nanoparticles imprinted from hard templates (mesoporous carbon) is introduced (*Chapter 3*). In addition to hard templates, soft templates, i.e., surfactants specifically

designed to direct zeolite nanostructure formation, is also a method to prepare zeolite nanoparticles. If the soft template has an extended structure, it could direct the formation of the pore topology as well as the shape of the entire particle. With this concept, zeolite-organic nanoassembly is introduced in *Chapter 4*, where the preparation of individual zeolite nanoparticles smaller than 10 nm is proposed and attempted. (A general introduction to zeolite synthesis is also included in *Chapter 4*.) As another example of utilizing soft templates, lamellar zeolite membrane preparation using bifunctional surfactant template is explored in this dissertation (*Chapter 5*). In the above three methods, intuitive templates are used to prepare zeolite particles with desired morphology. However, in order to form zeolite nanoparticles, the template does not need to be intuitive. In *Chapter 6*, with only one structure-directing agent (SDA), the preparation of hierarchical lamellar zeolite with 2 nm lamellae is introduced, where the formation of the nanostructure is partly driven by the intrinsic growth pattern of the crystal. In this case, one template can be used to direct the formation of both the pore topology and the mesoscale architecture. In *Chapter 7*, the preparation of faujasite nanoparticles without any template is introduced. The use of templates sheds lights on the design of zeolite nanostructures, however, the templates have to be removed to open the micropores for most applications. Thus, for industrial zeolite preparation, template-free methods are preferred due to the low cost. Although the results in Chapter 7 are still preliminary, following this path, if the intrinsic growth patterns of zeolite or any crystal is fully unleashed and controlled by template-free method, a new era of industrial nanoparticle synthesis will be at its dawn.

Chapter 2 Computational methods for studying the structures of zeolite nanoparticles[1]

2.1 Introduction

High aspect ratio zeolite single crystals with thickness in the nanometer range (zeolite nanosheets with thickness smaller than 10 nm) are desirable for applications including building blocks for heterogeneous catalysts [10-12], and the fabrication of thin molecular sieve films and nanocomposites for energy efficient separations [13]. They could also be of fundamental importance as they would allow probing mechanical, transport and catalytic properties of microporous networks at the nanoscale.

MWW- and MFI-nanosheets were prepared using exfoliation methods[14] starting from their corresponding layered precursors ITQ-1 [10] and multilamellar silicalite-1 [12], respectively (Fig. 2-1). These nanosheets were used for the fabrication of membranes for gas separation. To investigate the difference between these unit-cell-thick nanosheets and bulk phase materials, a series of modeling and simulation methods, including surface structure optimization with Car-Parrinello molecular dynamics (CPMD), powder X-ray diffraction pattern (XRD) simulation, and electron micrograph and electron diffraction patterns simulation, were developed and applied to these nanosheets. These methods were also used to prove the successful preparation of these nanosheets.

[1] Some of the results presented in this chapter is published in: K. Varoon, X. Zhang, B. Elyassi, D. D. Brewer, M. Gettel, S. Kumar, J. A. Lee, S. Maheshwari, A. Mittal, C. Y. Sung, M. Cococcioni, L. F. Francis, A. V. McCormick, K. A. Mkhoyan, M. Tsapatsis, Science 2011, 333, 72. Contents from the above publication are reprinted with permission from AAAS.

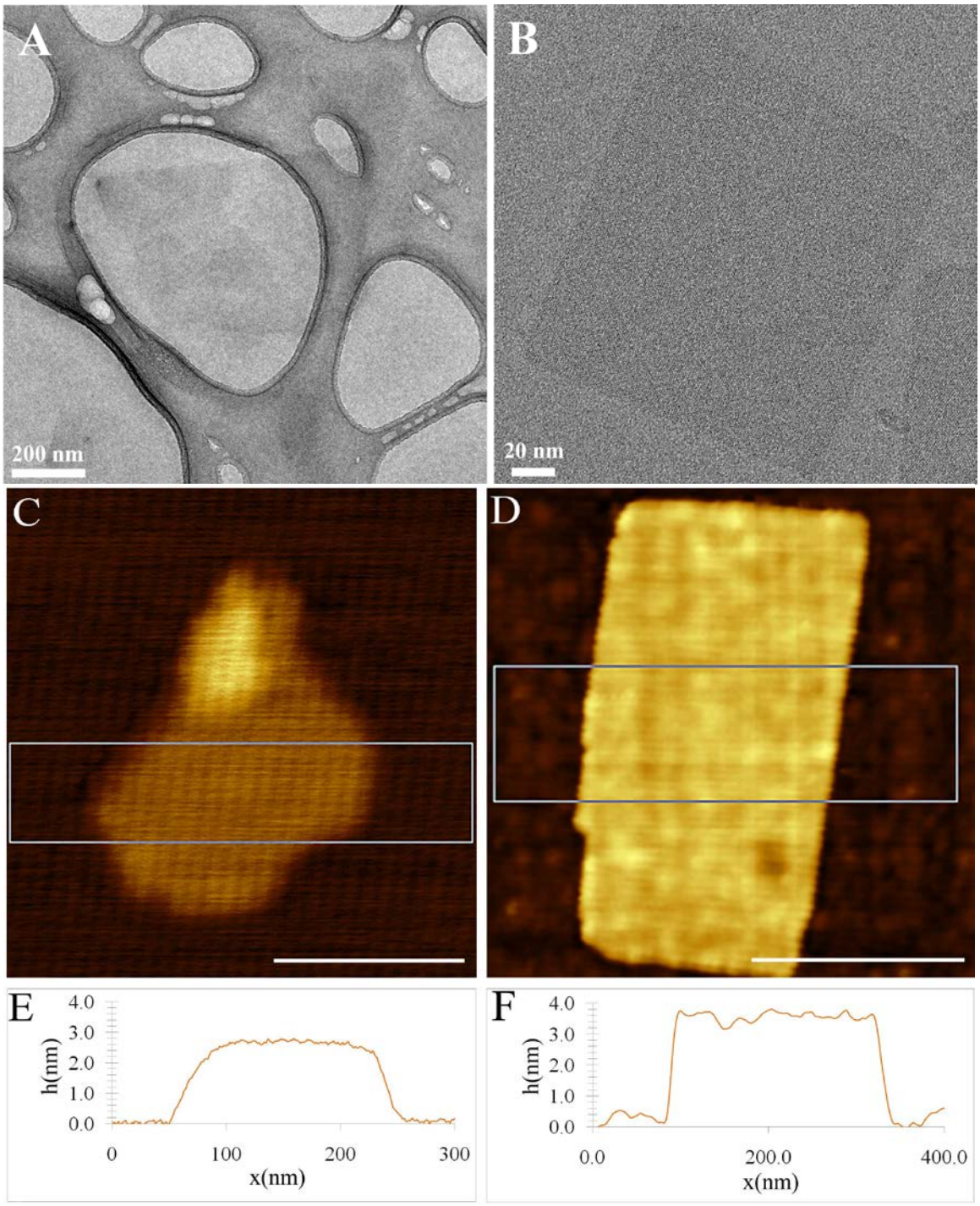

Figure 2-1 TEM images of single MWW and MFI nanosheets are shown in (A) and (B), respectively. AFM (tapping mode) topographical images of MWW and MFI nanosheets are shown in (C) and (D), respectively. The average step-height (h) data of the area highlighted in (C) and (D) are plotted in (E) (MWW nanosheet) and (F) (MFI nanosheet). The height data are calibrated using steps formed on freshly cleaved mica. Scale bars in (C) and (D), 200 nm.

2.2 Car-Parrinello Molecular Dynamics simulation of zeolite nanosheets

Background

It is not uncommon for nanoparticles to have significantly different properties from bulk materials, although they have the same crystal structure[15]. Some of these differences are due to the increased fraction of particle surface in nanoparticles. In zeolite particles with ultra-small size, such as nanosheets with thickness smaller than 5 nm, the fraction of surface atoms can be much higher than bulk phase zeolite particles. Being an interface, the structure of the nanoparticle surface can also be different. In some metal oxides, less long-range order is observed on the surface due to the partial bonding environment comparing to the bulk[16], while the (0001) surface of quartz is not very subject to rearrangement[17]. However, little is known about zeolite nanosheets. It is important to find out the surface structure of these ultra-thin nanosheets as a step to interpret any possible differences the ultra-small size brings about.

Molecular dynamics (MD) and density functional theory (DFT) are common methods to optimize atomic structures. MD is a classical method implemented by step integration of Newton's equations[18]. Although suitable for molecules, MD is not designed for covalent network or metallic materials. DFT gives better accuracy than MD by taking the configuration of electrons into account [19-20], however, the computational resources required to carry out DFT optimization of a 3-D covalent network is enormous. Car-Parrinello molecular dynamics (CPMD) is a method to combine the concepts of MD and DFT. By using reasonable assumptions for covalent networks, such as ground state electronic properties, classical mechanics assumption and Born-Oppenheimer approximation, CPMD comes with accuracy similar to DFT for optimizing covalent

systems, without demanding so much computational resources[21]. Thus, dumped-dynamics simulation by CPMD was performed on the zeolite nanosheets to reveal the surface structures of the ultra-thin nanosheets.

Structure construction

Structural models of the nanosheets are built according to the experimental observations from microscopy.

The definition of MWW unit cell and atomic coordinates used to generate the ITQ-1 nanosheet structure were from Camblor et al. [22] The structure of ITQ-1 nanosheets was proposed as one unit cell-thick (Fig. 2-2A), as by Corma et al. [23]. A thin fragment of the nanosheet highlighted with purple in Fig. 2-2A was used to represent the part of the nanosheet that will undergo structural change upon optimization. The dangling bonds on both exterior and interior sides of the fragment were terminated with hydroxyl groups (with terminal O-H bond length initially set to 98 pm, and Si-O-H bond angle set to its corresponding Si-O-Si bond angle in the original unit cell), resulting in 63 atoms in the cluster. The terminal hydroxyl groups on the interior side were kept fixed, and the other atoms were allowed to relax. Periodic boundary conditions were applied in three dimensions: the cluster is bonded with adjacent unit cells perpendicular to c direction, but is separated with a vacuum layer along the c direction (the thickness of the vacuum layer is chosen as 21.6 Å, 5 times the thickness of the cluster). In the structural optimization, the lattice parameters were kept constant, and the convergence criteria for ionic position optimization were chosen as 10^{-4} a.u. for total energy, and 10^{-6} a.u. for electron kinetic energy, typical values for covalent systems.

The definition of MFI unit cell and atomic coordinates are from van Koningsveld et al. [24]. The structure of the silicalite-1 nanosheets was chosen as three (010) pentasil layers along the b direction (1.5 unit cell thick, as in Fig. 2-1B and C). For structure optimization, one (010) pentasil layer at the surface was chosen as a cluster. Similar to MWW cluster, the dangling bonds on both exterior and interior sides were terminated with hydroxyl groups with terminal O-H bond lengths and Si-O-H bond angles treated in the same manner, resulting in a cluster with 168 atoms. The interior terminal hydroxyl groups were kept fixed, and the other atoms were allowed to relax. Periodic boundary conditions were applied in three dimensions, where the pentasil layer clusters were separated with a vacuum layer of thickness 59.6 Å, 5 times the thickness of the cluster. In the structural optimization, the lattice parameters were kept constant, and the convergence criteria for ionic position optimization were chosen as 10^{-4} a.u. for total energy, and 1.5×10^{-5} a.u. for electron kinetic energy.

Alternatively, a structure that is 1 unit cell thick (contains one complete and two incomplete (010) pentasil layers) was also chosen for comparison (Fig. 2-2D and E). The structure optimization was performed similarly to the 1.5 unit cell thick structure, except that the incomplete pentasil layer was chosen as the cluster for structure optimization, which results in a cluster with 108 atoms. Periodic boundary conditions were applied in three dimensions, where the clusters were separated with a vacuum layer of thickness 29.8 Å, 5 times the thickness of the cluster. In the structural optimization, the lattice parameters were kept constant, and the convergence criteria for ionic position

optimization were chosen as 10^{-4} a.u. for total energy, and 10^{-6} a.u. for electron kinetic energy.

Computation details

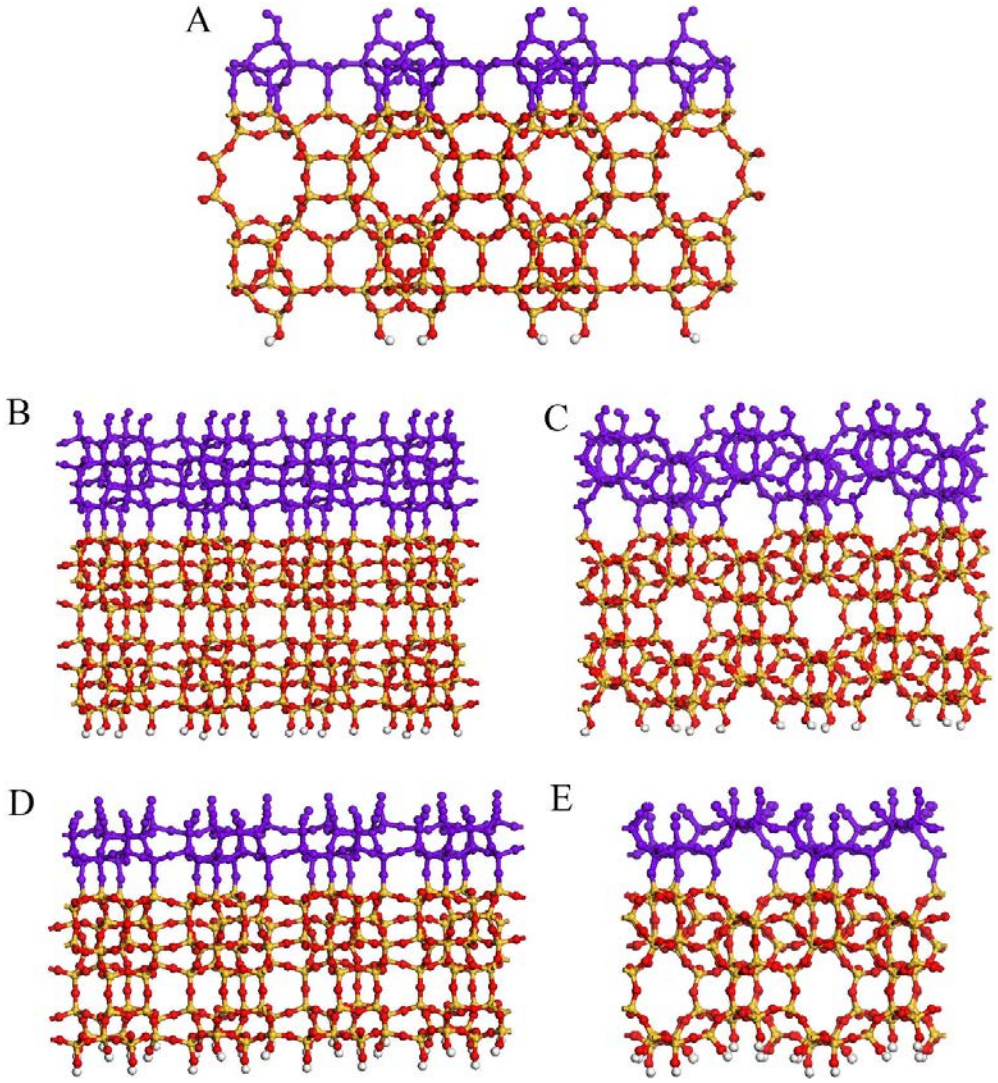

Figure 2-2 Side-views of relaxed structures of the MWW- and MFI-nanosheets obtained by structure optimization of nanosheets with Car-Parrinello molecular dynamics. (A) 1 unit cell thick MWW-nanosheet with relaxed surface structure viewed along a-axis; 1.5 unit cell thick silicalite-1 nanosheet with relaxed surface structure, viewed along c-axis (B), and a-axis (C); 1 unit cell thick silicalite-1 nanosheet with relaxed surface structure, viewed along c-axis (D), and a-axis (E). The cluster of atoms that were allowed to relax is shown in purple. The rest of the Si, O, and H atoms are colored in yellow, red and white, respectively.

These zeolite nanosheet structures were optimized using damped-dynamics simulation by the Car-Parrinello molecular dynamics (CPMD) code in the Quantum ESPRESSO package [25]. All periodic calculations were performed using the Perdew-Burke-Ernzerhof (PBE) generalized gradient approximation (GGA) [26] of the exchange-correlation functional. To describe the interaction of valence electrons with ionic cores, we employed ultrasoft pseudopotentials. The calculation required kinetic energy cutoffs, of 40 Ry and 320 Ry for wave functions and charge density, respectively. The Brillouin zone sampling was restricted to the Γ-point.

Results and discussion

The optimized surface structures were adopted into the initial structures to generate nanosheets of various thicknesses. The resulting structures are shown in Fig. 2-2. The thicknesses of these structures were calculated as the distance between the outermost hydrogen atoms on top and at the bottom of the nanosheets. The calculated thicknesses were compared with experimental observations from atomic force microscopy (AFM, Fig. 2-1E and F), and the results are shown in the following Table 2-1.

Table 2-1 Comparison of simulated and experimental thicknesses of MFI and MWW nanosheets

		Before optimization	After optimization	Experimental
MFI	1 unit cell	1.99 nm	2.39 nm	3.4±0.3 nm
	1.5 unit cell	3.21 nm	3.21 nm	
MWW (1 unit cell)		2.49 nm	2.63 nm	2.6±0.3 nm

Before and after the optimization of the structures, the positions of each atom in the layer were also recorded. The displacement of each atom is shown in the following

figures (Fig. 2-3). According to the figures, the displacement of all atoms in the structures before and after the optimization were smaller than 1 Å. Powder X-ray diffraction patterns were also simulated from the structures before and after the optimization (Fig. 2-4, the method for the XRD pattern simulation is introduced in section 2.3), with which we can also tell that the displacement of the atoms have limited effect on the structure. If the optimization of the two MFI structures are compared, the displacement from the structure with incomplete pentasil chains (2 pentasil layers, model in Figs. 2-2D and E, displacements in Fig. 2-3B) is larger than that with complete pentasil chains (3 pentasil layers, model in Figs. 2-2B and C, displacements in Fig. 2-3C), possibly due to the partial bonding environment in the incomplete pentasil layers. For the MFI nanosheets, the simulated thickness of the 1.5 unit cell structure (3 pentasil layers) agreed with the experimental measurements. The model of the one-unit-cell MWW nanosheets also agreed with the experiments.

These results preliminarily confirmed the thicknesses of the nanosheets. The models with optimized surface structures are further used in the following sections for the simulation of powder X-ray diffraction patterns and electron diffraction patterns.

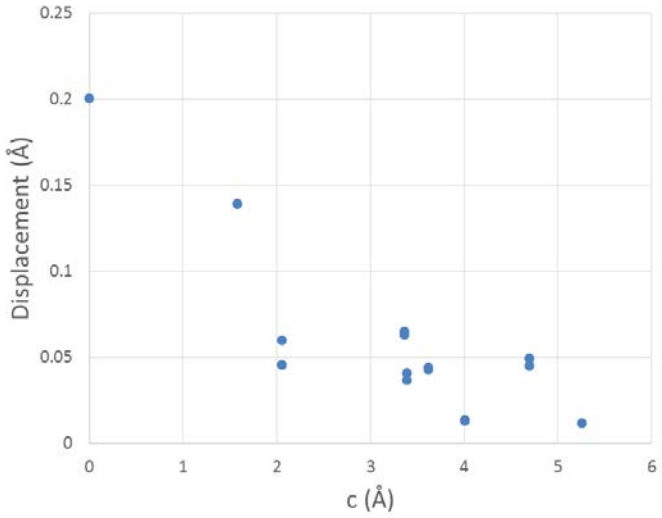
0.25
0.2
0.15
0.1
0.05
0
Displacement (Å)
0
1
2
3
4
5
6
c (Å)

(a)

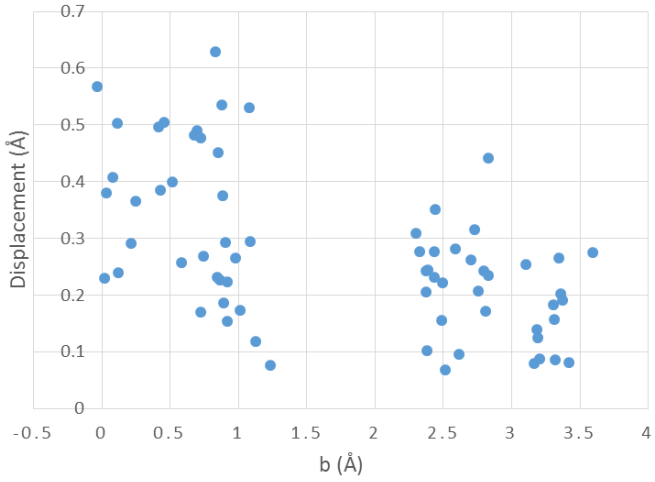
0.7
0.6
0.5
0.4
0.3
0.2
0.1
0
Displacement (Å)
-0.5
0
0.5
1
1.5
2
2.5
3
3.5
4
b (Å)

(b)

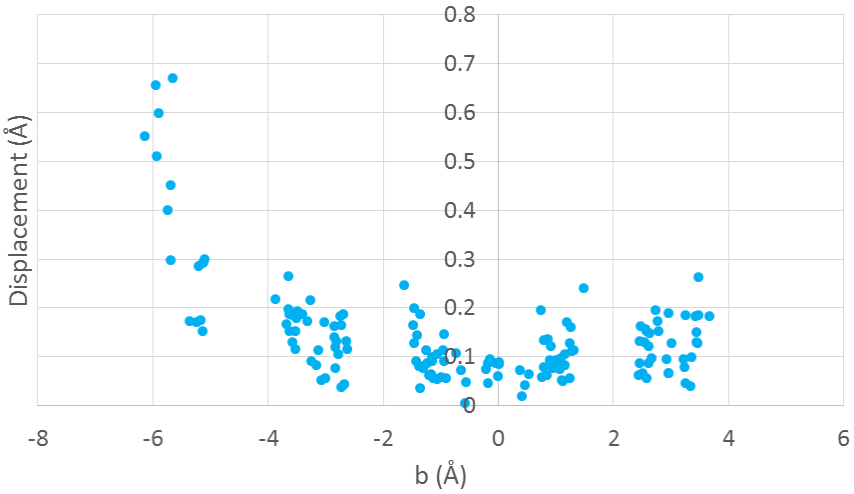

(c)

Figure 2-3 Displacement of atoms before and after the optimization of the (a) 1 unit cell MWW, (b) 1 unit cell MFI, and (c) 1.5 unit cells MFI nanosheet structures. The left side of the horizontal axes correspond to the exterior side of the structure (interface), while the right side represents the interior side of the structure (bulk).

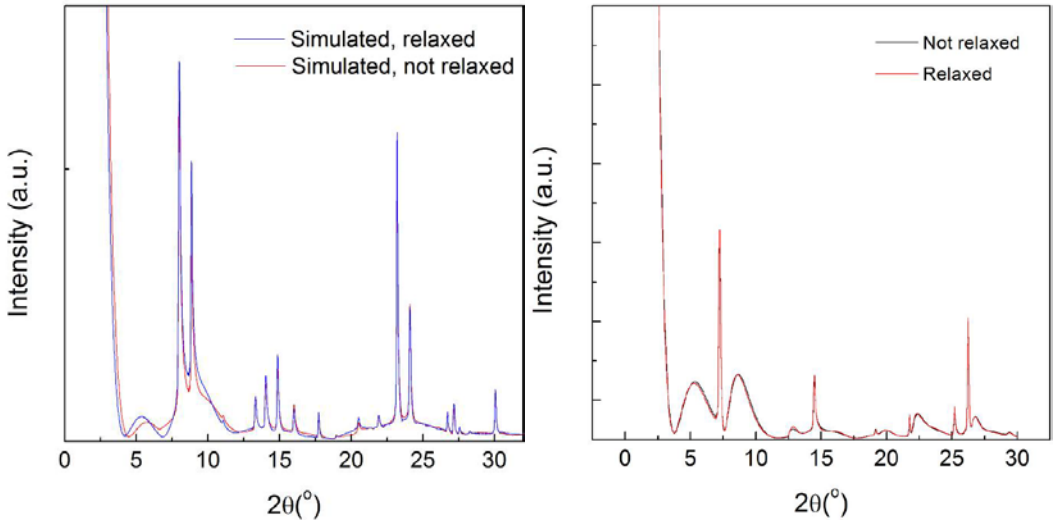

(a) (b)

Figure 2-4 Simulated XRD patterns of the nanosheets ((a) 1 unit cell MFI and (b) 1 unit cell MWW) before and after surface structure optimization.

2.3 Simulation of powder X-ray diffraction patterns of zeolite nanoparticles

Background

Powder X-ray diffraction (XRD) is a technique to study the structure of crystalline materials and detect any ordered structures in a material[27-28]. For a bulk crystal, from the locations of the peaks in an XRD pattern, the distances between atoms, and furthermore, the positions of all atoms in one unit cell, can be determined. However, the XRD patterns from nanoparticles usually have broader peaks due to the finite size along certain dimensions. When the particle size reaches the dimensions of a unit cell, some peaks may disappear due to lack of long range order along the diffracting planes, while extra peaks that contain information of size and shape of the particles may appear. In this extreme case, the very limited information from the patterns brings challenges to directly indexing the patterns. Thus, if unit-cell-size particles are prepared, comparing the experimental patterns with simulated patterns, rather than directly indexing the XRD patterns, is a more suitable approach to study the structure of the particles.

XRD patterns of bulk phase crystals can be simulated solely from atomic positions in one unit cell, where the size and morphology of the particles are not taken into consideration, since the particle is considered as an infinite crystal. In some cases, peak broadening can be added artificially (to each of the 3 dimensions) considering particle size and instrumental parameters.[29] However, for particles with arbitrary shapes, the XRD patterns would be more accurate and realistic if the simulation could be done from a model with defined shape and finite size. SKIP (small crystal interference program) is one method following this concept, where a simulated X-ray passed through

the nanoparticle and the simulated *powder* X-ray diffraction pattern is calculated with powder power theorem.[30]

In this section, SKIP is applied to zeolite nanoparticles and ultra-thin nanosheets. With results from microscopy, the simulated XRD patterns are used to determine the structures, especially thicknesses, of the nanosheets.

Structure construction and computation methods

XRD patterns were simulated using powder power theorem [30] implemented with UDSKIP[31]. In the simulation, MWW nanosheets were modeled as 50×50×*n* (*n*=1, 2, and 3) unit cells with relaxed surface structure obtained in section 2.2, and MFI nanosheets were modeled as 50×*n*×50 (*n*=1, 1.5, 2.5, and 3.5) unit cells with relaxed surface structure obtained in section 2.2. Simulations for wide-angle X-ray diffraction were carried out with step size $\Delta(2\theta)=0.01^{o}$ (Cu Kα_1 radiation, λ=1.5418 Å).

Results and discussion

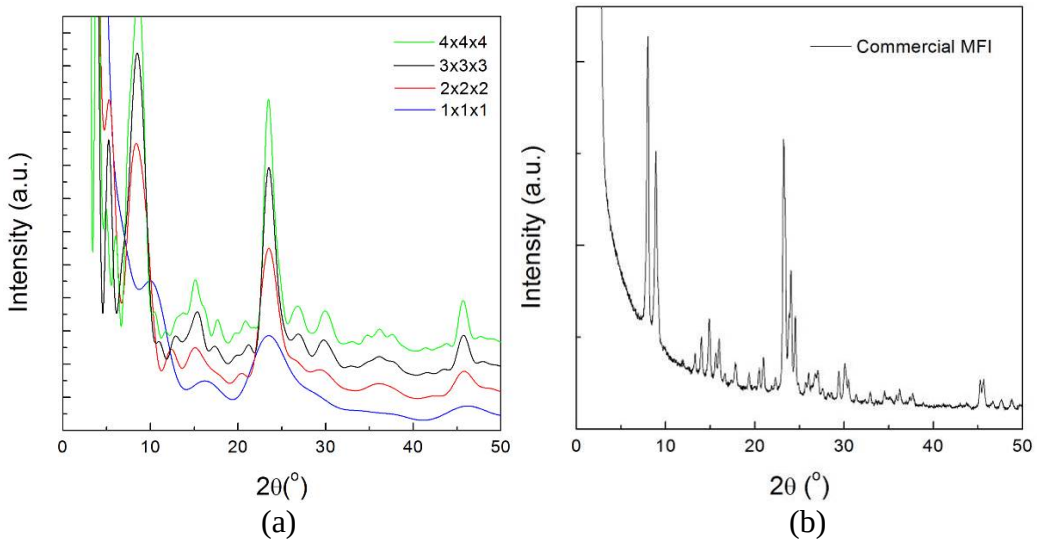

Figure 2-5 Simulated XRD pattern of MFI nanoparticles of unit cell size (a: 1x1x1, 2x2x2, 3x3x3, and 4x4x4 unit cells) compared with experimental XRD pattern of commercial MFI (b).

First, following Kragten et al.[31], XRD patterns of ultra-small MFI nanoparticles were simulated and compared with that of commercial MFI. MFI nanoparticle models of sizes 1x1x1, 2x2x2, 3x3x3, and 4x4x4 unit cell(s) were constructed using atomic coordinated from van Koningsveld et al.[24] If the XRD pattern from the 4x4x4 particle is compared with the XRD pattern of commercial MFI (Fig. 2-5(b)), although some of the peaks can still be recognized, the small sizes of the MFI nanoparticle models result in broader peaks than that of bulk phases. When the particle size is further reduced, such as the 1x1x1 particle that is of unit cell size, the patterns can no longer be indexed by comparing with bulk phase XRD patterns. While some peaks become broader, some new peaks that have information of the particle size and shape emerge (around 16^{o}).

The experimental patterns from the MWW and MFI nanosheets show very broad peaks (Fig. 2-6 (a) and (b), respectively), which is consistent with their ultra-small thicknesses. While the peaks from the experimental pattern of MFI nanosheets can be compared with that of bulk phase MFI and indexed, some broad peaks of the MWW nanosheets, such as those around 5^{o} and 9^{o}, are absent from XRD patterns of bulk phase MWW. In order to explain these patterns, simulation of various nanosheets structures (1 unit cell MWW, 2 unit cell MWW, and 3 unit cell MWW in Fig. 2-6(a), 1 unit cell MFI, 1.5 unit cells MFI, 2.5 unit cells MFI, and 3.5 unit cells MFI in Fig. 2-6(b)) were performed and compared with experimental patterns.

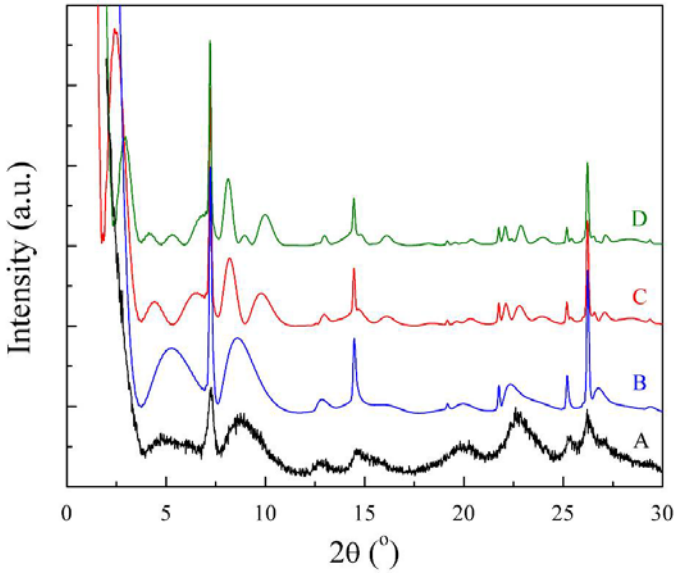

(a)

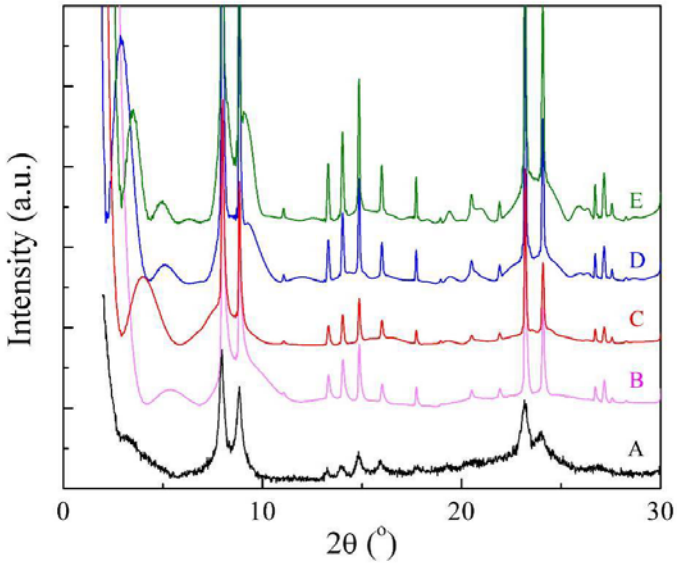

(b)

Figure 2-6 Comparison between experimental and simulated powder X-ray diffraction patterns of the nanosheets, where bottom trace is the experimental pattern, and top traces are simulated patterns. (a) Comparison for the MWW-nanosheet; trace (A) is the experimental powder XRD pattern, and traces (B), (C) and (D) are the simulated patterns for 1, 2 and 3 unit cell thick MWW-nanosheets, respectively. The comparison indicates that the simulated pattern of 1 unit cell thick nanosheets agrees with the experimental pattern. (b) Comparison for the MFI-nanosheets; trace (A) is the experimental powder XRD pattern, and traces (B), (C), (D) and (E) are the simulated patterns for 1, 1.5, 2.5 and 3.5 unit cell thick MFI-nanosheets, respectively. The comparison indicates that the simulated pattern of 1.5 unit cell thick nanosheets agrees with the experimental pattern. Both (a) and (b) indicate that the peaks at low angles are sensitive to nanosheets thickness.

For MWW nanosheets, at high angles, all the simulated patterns are similar, because high angles contain information of the long range order of the atoms in the crystal structure. The simulated patterns at high angles also agree well with the experimental pattern. This indicates that the crystallinity of the nanosheets is preserved after the exfoliation process. The major difference between these patterns lies in the low-angle patterns, where the 1 unit cell pattern shows one peak at approximately 2.5-7^{o}, the 2 unit cells pattern shows 2 peaks, and the 3 unit cells pattern shows 3 peaks. In this region, the patterns contain information about the shape and size of the particle. By comparing the simulated patterns with experimental patterns, the 1 unit cell pattern agrees the best with the experimental pattern. Considering results from microscopy, the thickness of the MWW nanosheets should be 1 unit cell.

Similarly, for MFI nanosheets (Fig. 2-6 (b)), at high angles, the simulated patterns are similar to each other, and they all agree with the experimental pattern. This indicates the crystal structure was preserved after exfoliation. Comparing the low angle regions of the simulated patterns and the experimental pattern, it is obvious that the 1.5 unit cells model agrees well with the experimental pattern, especially the minimum at 6^{o}. Therefore, the thickness of the MFI nanosheets should be 1.5 unit cells.

2.4 Simulation of electron micrographs and electron diffraction patterns of zeolite nanosheets

Background

X-ray diffraction is an effective method to collectively determine the crystalline structure and, in some cases, the size and shape of the particles, if they are uniform particles. Meanwhile, microscopy is a complimentary method to study the properties of individual

particles. Since no dispersible zeolite nanosheets has been prepared before, the difference of micrographs and electron diffraction patterns between bulk phase zeolites and zeolite nanosheets are still unknown. In order to study this difference, simulation was done to different models of zeolite nanosheets, and compared with experimental results.

Ideally, simulation of electron micrographs and diffraction patterns could be done by calculating the wave functions of electrons after they pass through the sample. However, although with maximum accuracy, this method is computationally intense, due to the manipulation of wave functions through all the atoms in a sample. By converting a thick sample (whose size is usually on the order of 100 nm) into thin slices (thickness on the order of 0.1 nm) along the direction of electron propagation, and calculate the wave functions sequentially through each slice taking advantage of reasonable simplifications, much less computational resources will be needed. This method, the Multislice method developed by Kirkland [33, 35], will be applied to the MWW and MFI zeolite nanosheets in this section.

Structure construction and computation details

Simulation of electron diffraction (ED) patterns and TEM images was performed using Multislice method [32-34] with the code developed by Kirkland [35].

For simulation, an orthorhombic MWW unit cell is reconstructed from the hexagonal MWW unit cell: $a_o = \sqrt{3}\,a_h$, $b_o = a_h$, $c_o = c_h$, where a_o, b_o, and c_o are the lattice parameters for the orthorhombic MWW unit cell, and a_h and c_h are the lattice parameters for the hexagonal MWW unit cell. The position of all the atoms are obtained from optimization done in section 2.2. The nanosheet size is chosen as 24.6 nm (a_o) x 24.2 nm

(b_o) with desired thicknesses. A vacuum layer was placed around the crystal to extend the crystal to a supercell with 34.4 nm x 34.4 nm, and periodic boundary conditions were applied in two dimensions (perpendicular to beam) to the super cell. A grid of 11700 × 11700 pixels was used in these simulations. In order to generate the projected atomic potentials, the crystal was automatically sliced along the c direction to 1 Å slices with *autoslic* module provided with the code.

For MFI, the nanosheet size is chosen as a=10.8 nm and c=13.4 nm with desired thicknesses. A vacuum layer was placed around the crystal to extend the crystal to a supercell with a=c=18.8 nm, and periodic boundary conditions were applied in two dimensions (perpendicular to beam). The position of all the atoms are obtained from optimization done in section 2.2. A grid of 6724 × 6724 pixels was used in these simulations. In order to generate the projected atomic potentials, the crystal was automatically sliced along the b direction to 1 Å slices with *autoslic* module provided with the code.

Acceleration voltage (300 kV) and spherical aberration coefficient (C_s=1.2 mm) were used as microscope parameters for simulation of electron diffraction patterns. The temperature of the simulation was set to 300 K, where thermal vibration was introduced in the simulation by randomly displacing the atoms according to their Debye-Waller factors [36].

The simulated MWW and MFI electron diffraction patterns were convolved with a normalized Gaussian function with a FWHM of 0.003 $Å^{-1}$ and 0.01 $Å^{-1}$, respectively, as

an approximate approach to account for the convergence of the electron beams at actual operating conditions.

Results and discussion

The experimental electron micrographs and diffraction patterns are shown in Fig. 2-7. From Fig. 2-7 (a) and (b), we can tell that the particles are mostly smaller than 300 nm. Fig. 2-7 (c) and (d) are high-resolution images of the MWW and MFI nanosheets, from which electron diffraction patterns were obtained (Fig. 2-7 (e) and (g), respectively). Simulation of electron diffraction patterns were obtained from the optimized models built in section 2.2. The simulated patterns, as shown in Fig. 2-7 (f) and (h), agree well with the experimental patterns. This confirmed that the particles after exfoliation are with good crystallinity.

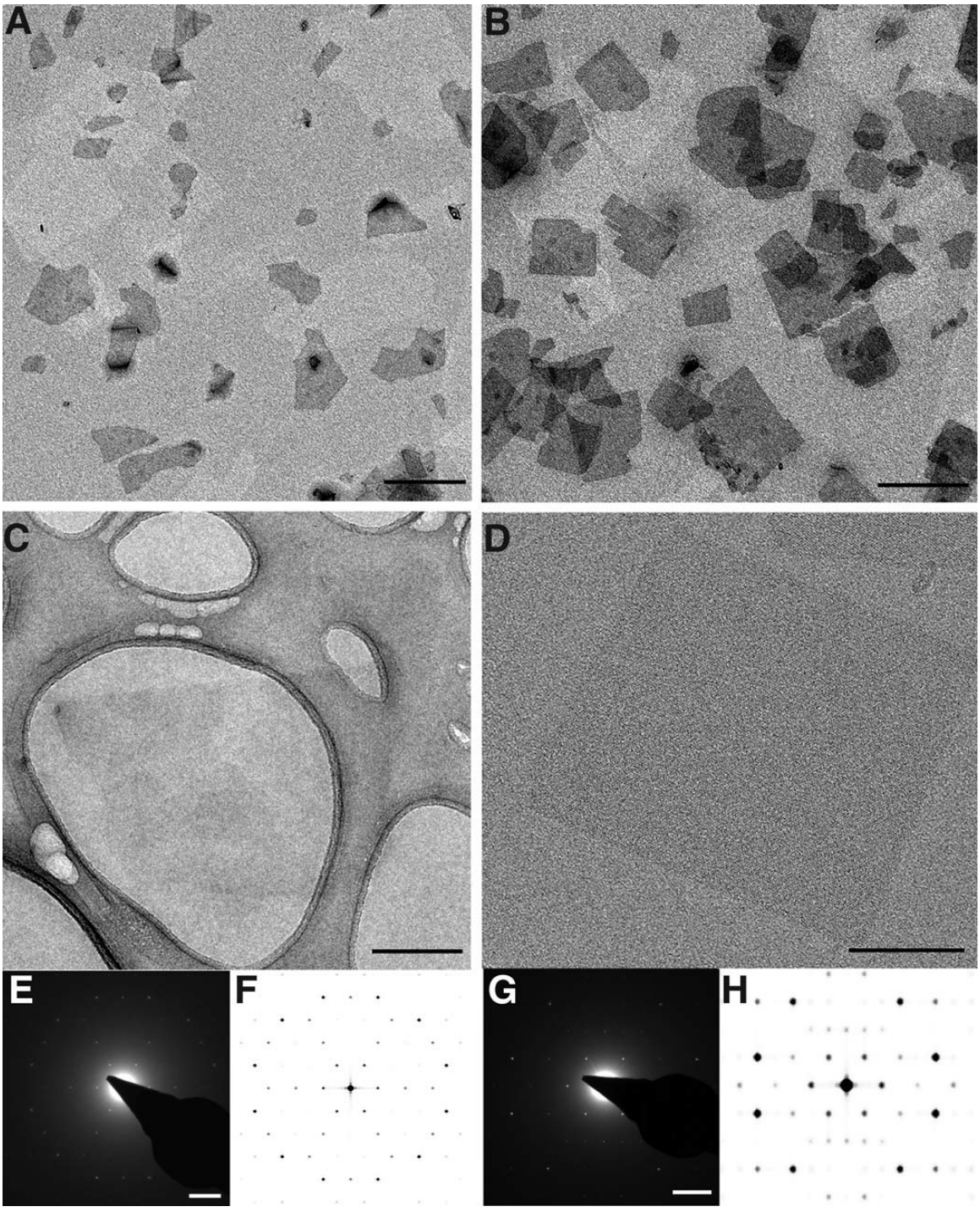

Figure 2-7 Low-magnification TEM images of c-oriented MWW (A) and b-oriented MFI nanosheets (B). TEM images of single MWW and MFI nanosheets are shown in (C) and (D), respectively. (E) and(G) are the corresponding ED patterns of the same particles shown in (C) and (D), respectively. Simulations of the ED patterns of proposed structures of nanosheets down the c axis (MWW) and b axis (MFI) are shown in (F) and (H), respectively. Scale bars in (A) to (C), 200 nm; in (D), 50 nm; in (E) and (G), 1 nm.

In addition to crystallinity, thickness determination of the nanosheets from TEM was also attempted. As a first step, models of zeolite nanosheets with different thicknesses were built, and electron diffraction patterns were simulated from each of them with beam perpendicular to the lamellae. The intensities of the diffraction spots were measured, and normalized to the brightest spots of each pattern ((501) from MWW, and (310) from MFI). For each material with different thicknesses, the intensities of all the spots in the diffraction patterns of models were plotted in one graph for comparison. In Fig. 2-8, the intensities of the diffraction spots from MFI nanosheets (1, 2, 3, 4, and 5 unit cells thick) are plotted. From the plot, although the intensity of some spots (such as {100}, {110}, {300}, and {330}) depends on the thickness, the intensities do not show significant different when the thickness of nanosheets are increased. The same is observed in the study of MWW nanosheets (Fig. 2-9), where the dependence is even less obvious.

In the electron diffraction patterns of ultra-thin lamellar materials, when the sample is tilted and the intensity of one specific diffraction spot is tracked, the intensity can show different trends that depend on the thickness. This phenomenon was observed in graphene, a lamellar material that are composed of single layers of carbon-carbon covalent network[37]. For graphene sheets with different thicknesses, the intensities reach zero at very different tilting angles. Inspired by this, electron diffraction patterns of zeolite nanosheets were also simulated with tilted samples, in order to investigate whether tilting can be an approach to determine the thicknesses of the zeolite nanosheets.

The simulated patterns of MFI nanosheets are shown in Fig. 2-10 (a)-(f).

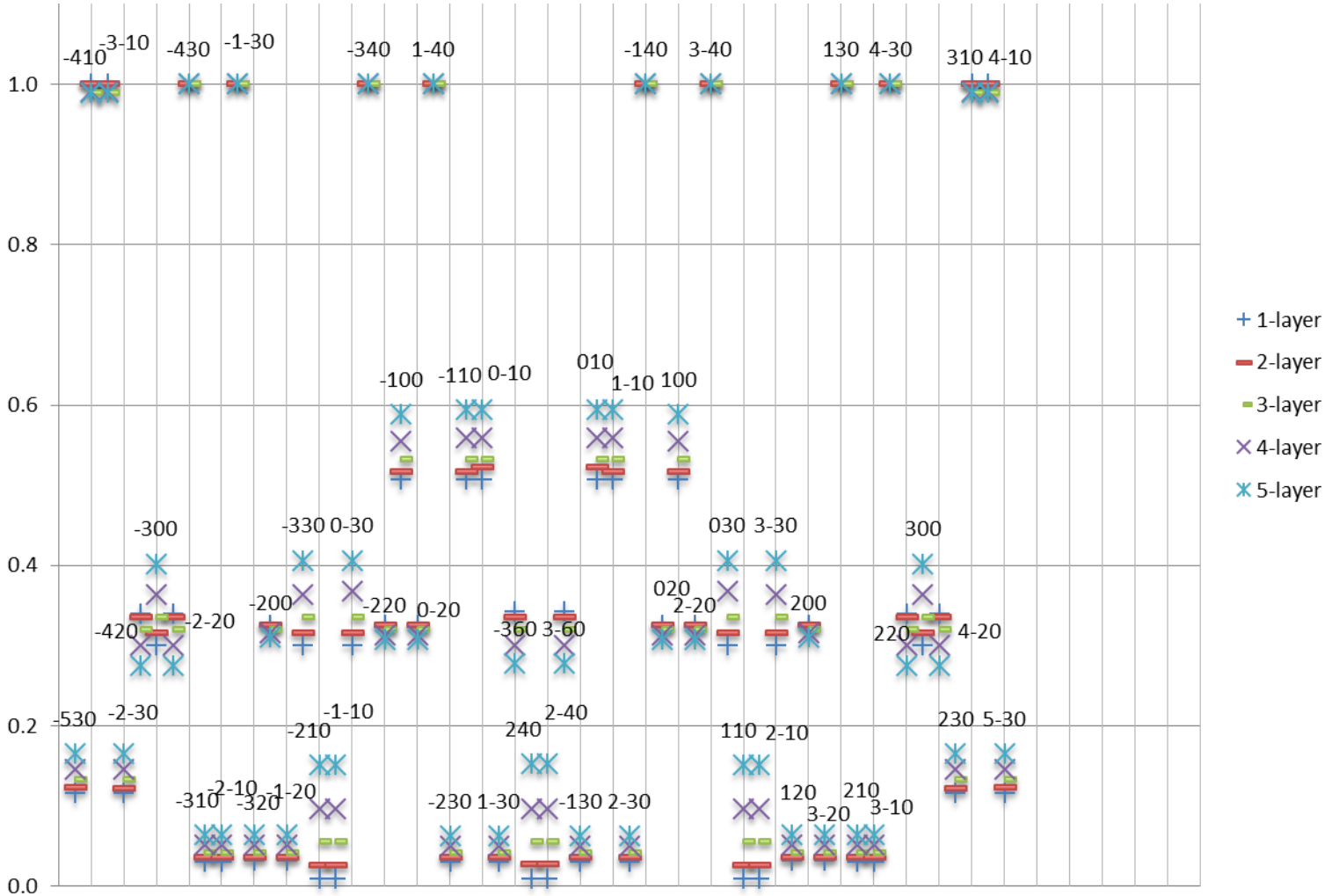

Figure 2-8 Relative intensity of each diffraction spot in the simulated diffraction pattern of MFI nanosheets with thicknesses of 1, 2, 3, 4 and 5 unit cells. The intensities are normalized with respect to the intensity from (310) spot.

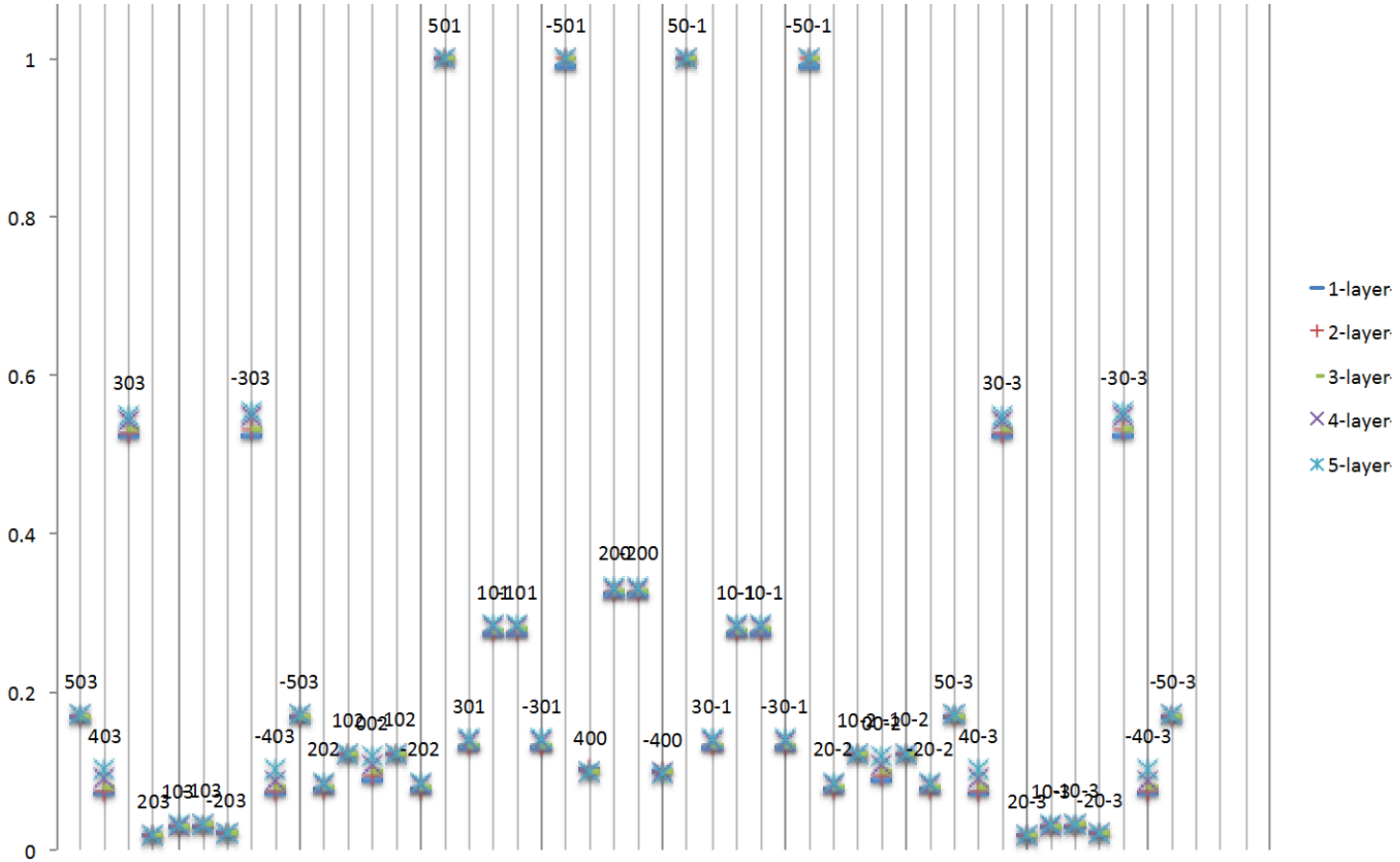

Figure 2-9 Relative intensity of each diffraction spot in the simulated diffraction pattern of MFI nanosheets with thicknesses of 1, 2, 3, 4 and 5 unit cells. The intensities are normalized with respect to the intensity from (501) spot.

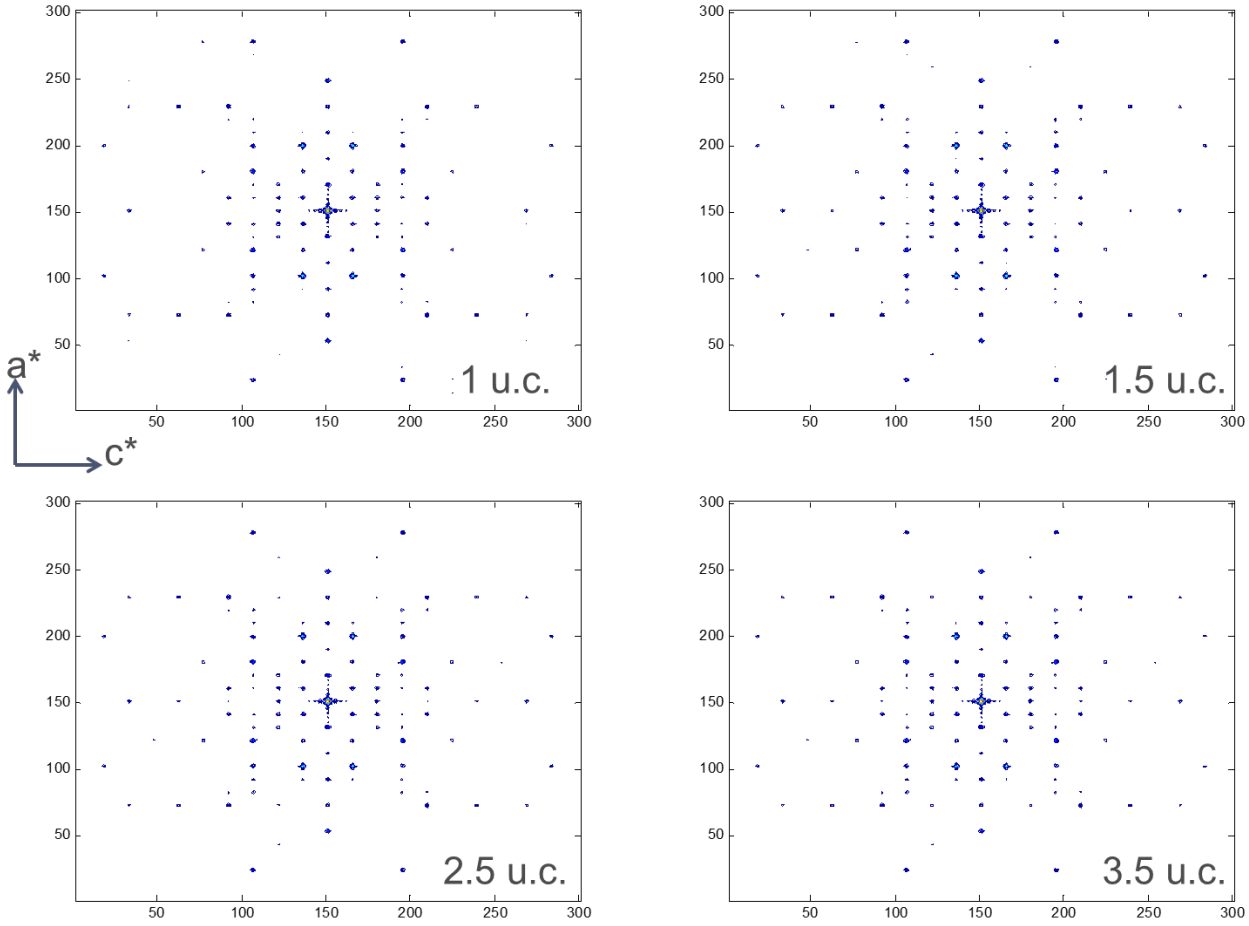

(a) 0 degree

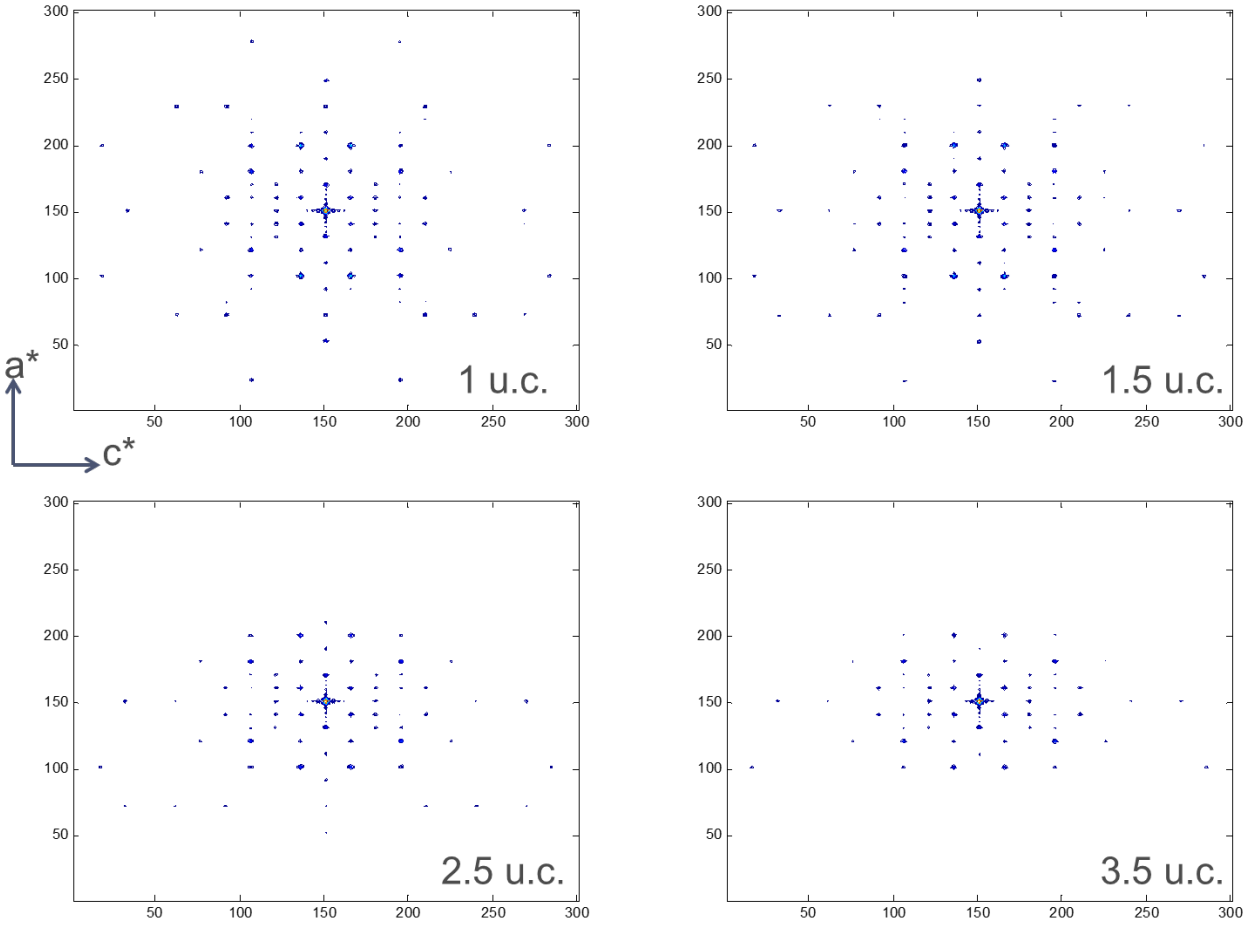

(b) 2 degrees

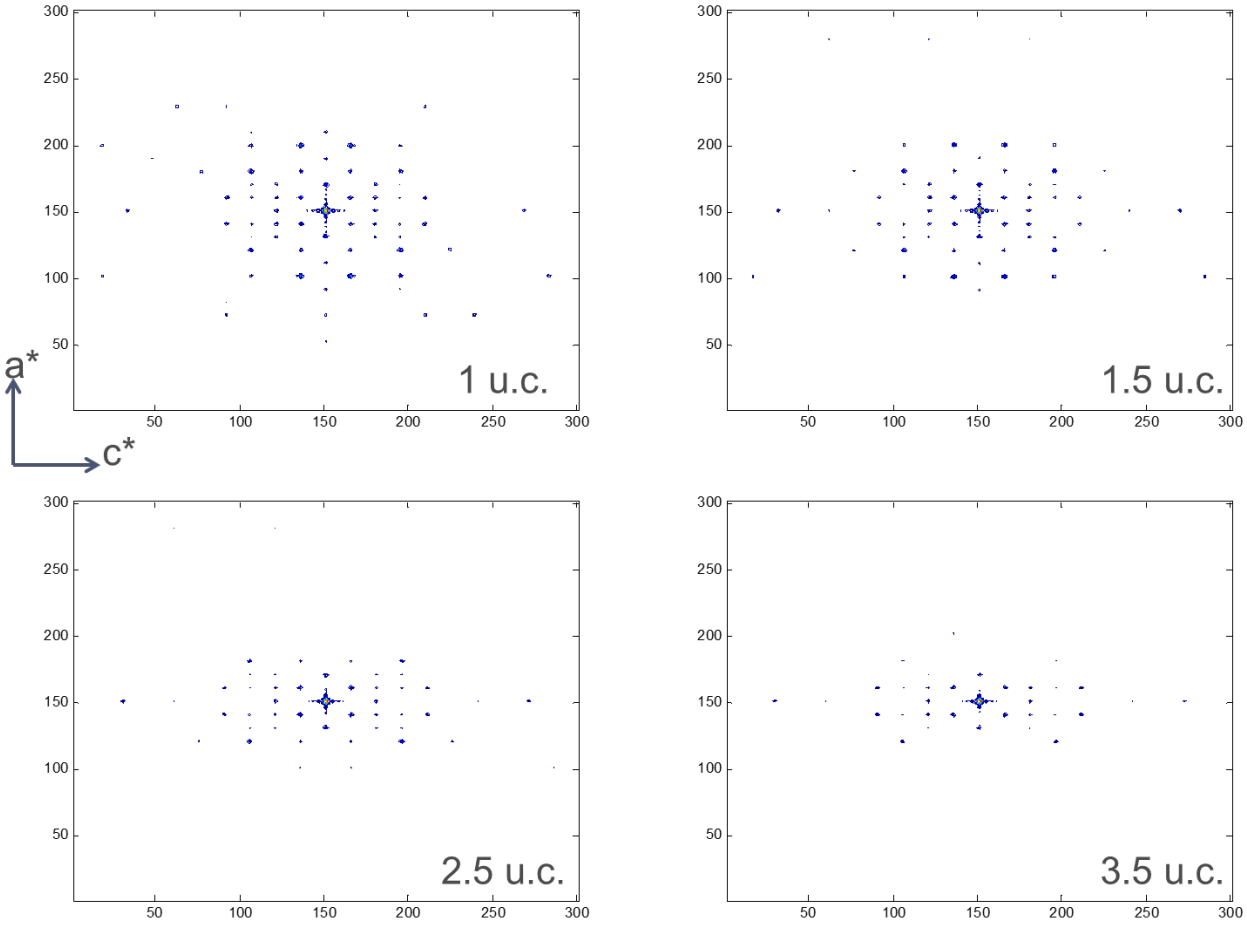

(c) 4 degrees

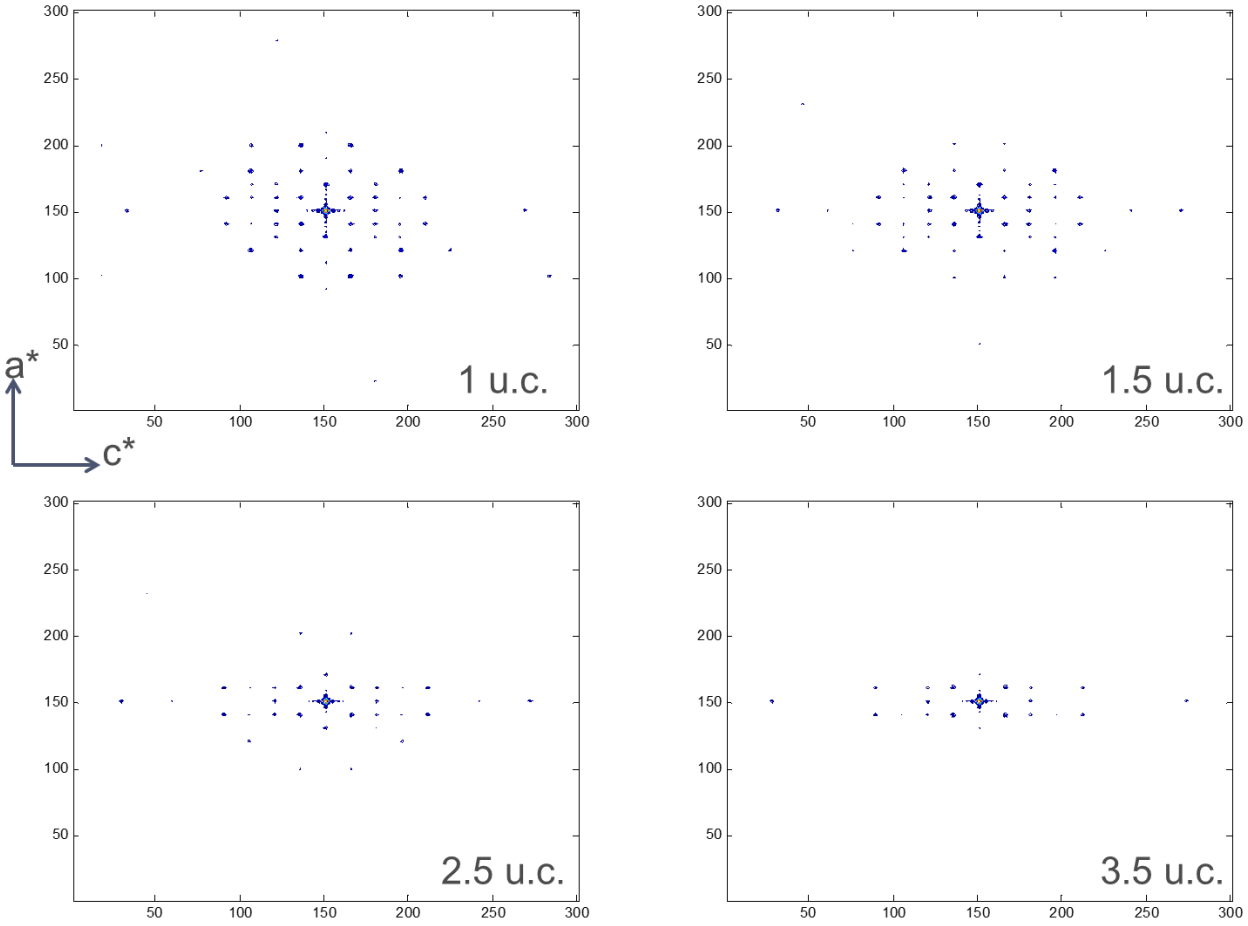

(d) 6 degrees

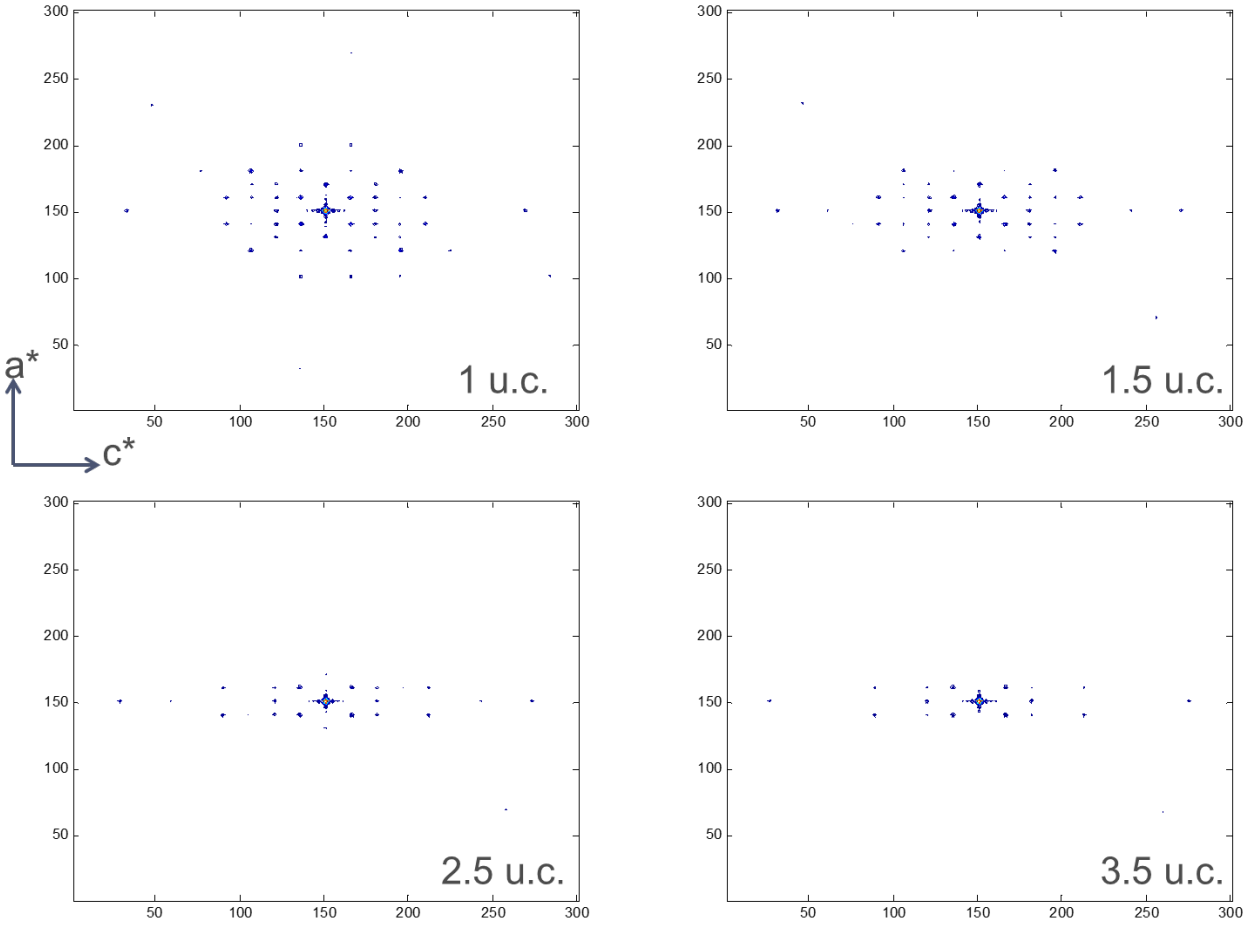

(e) 8 degrees

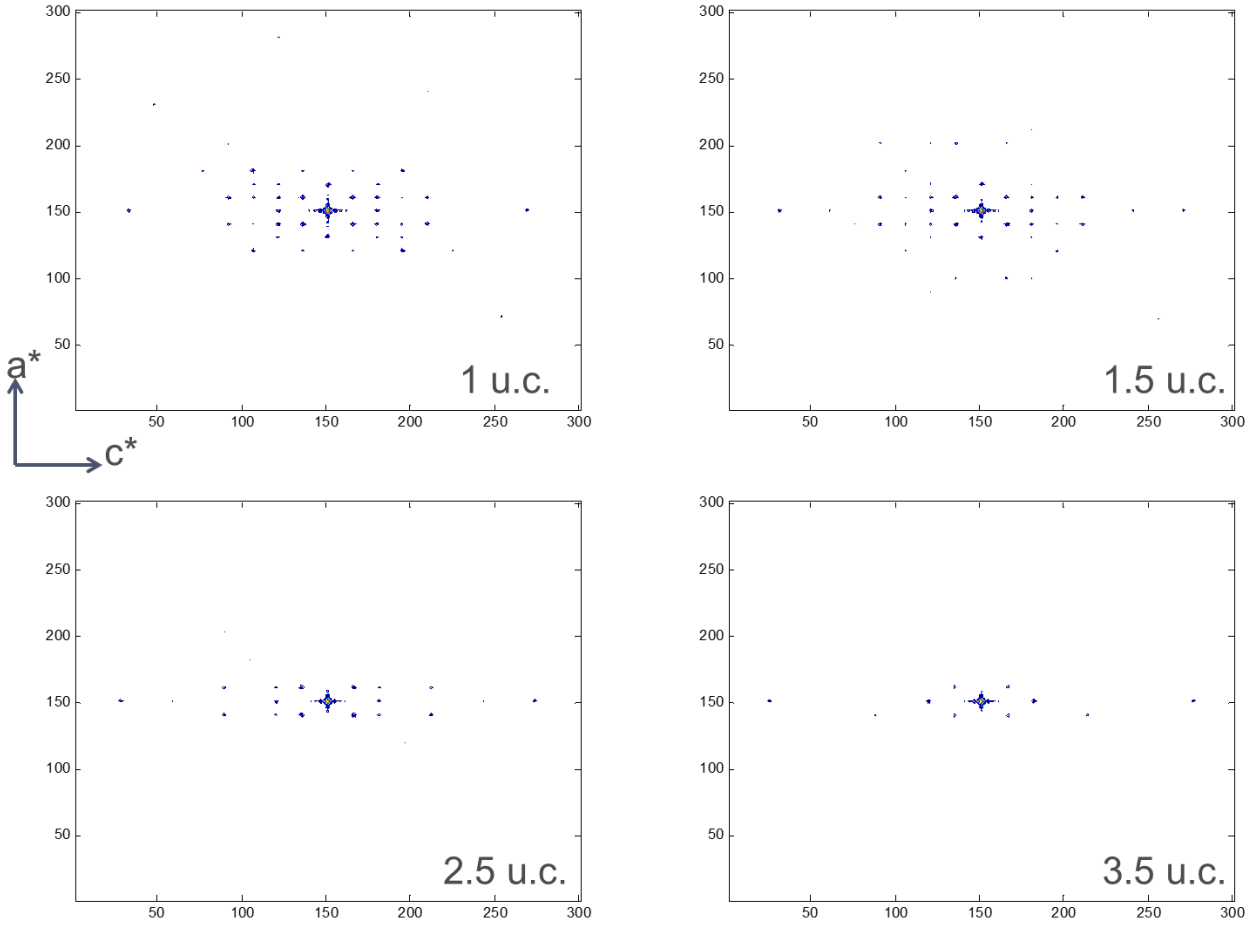

(f) 10 degrees

Figure 2-10 Simulated electron diffraction patterns of MFI nanosheets with different tilting angles (thicknesses in number of unit cells are shown in each pattern): (a) 0 degree; (b) 2 degrees; (c) 4 degrees; (d) 6 degrees; (e) 8 degrees; (f) 10 degrees.

At each tilting angle, electron diffraction patterns are simulated for structures with thicknesses of 1, 1.5, 2.5, and 3.5 unit cells. In Fig. 2-10 (a), the four patterns cannot be distinguished from each other, since the intensities of the spots are very close to each other, which is consistent to the observation from Fig. 2-8. However, as the nanosheets are tilted, the difference between the four patterns becomes increasingly obvious. For example, at high tilting angles, the spots at higher scattering angles has lower intensity for thicker samples (Fig. 2-10(f)). This method is a promising method for thickness determination of the individual zeolite nanosheets. However, accompanying experimental studies should also be done in the future to validate if this method is practical.

2.5 Conclusions

MFI and MWW zeolite nanosheets are building units for state-of-the-art zeolite thin films for gas separation. In this study, the structures of exfoliated MFI and MWW zeolite nanosheets were determined and studied using a combination of experimental and simulation methods. Based on characterization results from atomic force microscopy and transmission electron microscopy, the structures and thicknesses of the exfoliated zeolite nanosheets were proposed. After optimization with Car-Parrinello molecular dynamics, X-ray diffraction patterns and electron diffraction patterns are simulated from these structures. The agreement between experimental and simulated characterization data suggested that the 1 unit cell MWW and the 1.5 unit cells MFI models should represent the actual structures of the exfoliated zeolite nanosheets.

The methods used in this study can be extended to determining structures of other zeolite nanostructures or nanoparticles in general.

Chapter 3 Uniform zeolite nanoparticles from disassembly[2]

3.1 Introduction

Oriented MFI membranes and thin films are widely used for gas separation, especially for xylenes[38-39] and butanes[40]. The structure-performance relationships of zeolite membrane and thin films requires that the particles should be small in dimension (smaller than 50 nm) in order to reduce coating defects[41-43]. Dispersible and uniform zeolite nanoparticles smaller than 50 nm are not easy to prepare via nucleation-growth approach. However, disassembly can be a promising alternative to prepare zeolite nanoparticles. The recently reported three-dimensionally ordered mesoporous (3DOm) silicalite-1 is a novel type of hierarchical zeolite[44]. A 3DOm silicalite-1 particle is a single crystal containing uniform spherical domains (tunable from below 10 nm to 40 nm[44]) in a cubic close-packed (ccp) arrangement and interconnected with their respective 12 nearest neighbors. It has both the micropores of MFI framework zeolite (with sizes similar to many industrially important molecules[1]) and ordered mesopores corresponding to the tetrahedral and octahedral interstitial spaces of the cubic close-packed domains. Considering the tunable domain size below 40 nm, the open structure, and symmetrically ordered domains, disassembly of 3DOm domains can be a promising method to produce zeolite nanoparticles with uniform but tunable sizes. Inspired by previous studies, where dissolution methods were applied to ZSM-5 and silicalite-1 to produce mesopores on particle surfaces[45-47], a dialysis method that controls the

[2] Some of the results presented in this chapter is published in: P.-S. Lee, X. Zhang, J. A. Stoeger, A. Malek, W. Fan, S. Kumar, W. C. Yoo, S. Al Hashimi, R. L. Penn, A. Stein, M. Tsapatsis, J. Am. Chem. Soc. 2011, 133, 493.

dissolution pH range was applied to 3DOm silicalite-1 particles. This controlled dissolution method successfully produced dispersible silicalite-1 nanoparticles below 40 nm with either intact morphology or “fractured egg-shell” morphology, which further extended the size limit and morphological variety of zeolite nanoparticles.

Secondary growth (seeded growth) of zeolite is an important procedure in oriented zeolite membrane fabrication[3]. Zeolite seeds coated on a substrate can form a continuous and oriented film upon secondary growth at desired conditions[38][48]. Different aspects of secondary growth behaviors of silicalite-1 have been studied using scanning electron microscopy (SEM)[49], X-ray diffraction (XRD)[49], scanning force microscopy[49], fluorescence confocal optical microscopy[50] and dynamical light scattering (DLS)[51]. An aggregative growth model of silicalite-1 secondary growth has also been proposed[51]. However, atomic resolution study is still in need for more fundamental understandings of this important process. Kumar *et al* studied nucleation and growth of silicalite-1 from clear sol using cryogenic transmission electron microscopy (cryo-TEM) with structural resolution[52]. Similarly, in this work, secondary growth of silicalite-1 disassembled from 3DOm-i silicalite-1 was studied using cryo-TEM, which is the first time this process is observed with structural resolution.

3.2 Experimental methods

Preparation of 3DOm-i silicalite-1

The preparation of 3DOm-i silicalite-1 was prepared according to Fan et al.[44] In brief, silica nanoparticle sols were synthesized by hydrolysis of tetraethyl orthosilicate (TEOS, 98%, Aldrich) with aqueous solutions of basic amino acid lysine (Sigma-Aldrich) as

described in previous reports.[44, 53][54] Steam-assisted crystallization (SAC) was used for the confined synthesis of 3DOm-I silicalite-1 in the 3DOm carbon template.[44, 55] The synthesis sol was a 9:0.15:50:390:180 $TPA_2O/Na_2O/SiO_2$/water/ethanol mixture for all samples. The SAC was conducted at three different temperature-time combinations: 85 °C for 5 days, 135 °C for 3 days, and 180 °C for 2 days.

Disassembly of 3DOm-i silicalite-1 by dissolution

Dissolution of 3DOm-i silicalite-1 was performed in a dialysis tube (Spectra/Por 3, Spectrum Laboratories Inc.), which allowed separation of silicalite-1 crystals from dissolved silicate and other ions. A polypropylene beaker was filled with 1 L of deionized water (Millipore Elix, 10 MΩ cm). A tetrapropylammonium hydroxide solution (TPAOH, 1.0 M in water, Sigma-Aldrich) or L-lysine (Sigma-Aldrich) was added to the beaker to achieve the desired initial pH value for dissolution; 75.0 mg of 3DOm-i silicalite-1 powder was transferred to a centrifuge tube containing 8 mL of the same solution as in the beaker, to which sonication for approximately 5 min was applied to ensure the crystals were separated from each other before dissolution. The mixture was then transferred to a rinsed dialysis tube, which was then sealed and placed in the beaker. The solution in the beaker was stirred slowly, allowing the dialysis tube to rotate. The pH of the solution in the beaker was monitored regularly. The solution outside the dialysis tube was changed regularly to a fresh one with the desired initial pH, to keep the pH within the desired range and remove silicate species produced by dissolution. After the dissolution had been conducted for the desired time, the solution outside the dialysis tube

was changed to deionized water, to remove the silicate species. After 1 day, the sol inside the dialysis tube was collected and dried at 70 and 135 °C.

Secondary growth of silicalite-1 nanoparticles

The silicalite-1 seeds used to study secondary growth were 40 nm spherical elements isolated from 3DOm-i silicalite-1 crystals using the sonication procedure described above. After isolation, the seeds were suspended in water at a concentration of 1 mg of silicalite-1/mL. The suspension was visually stable with no precipitation at room temperature for a period of at least 3 months. The growth sols used for this study were prepared as described by Davis *et al.*[56] with the following compositions: 5:9:8100:20 SiO_2/TPAOH/H_2O/EtOH (denoted as C1), 10:9:8100:40SiO_2/TPAOH/H_2O/EtOH (denoted as C2), and 20:9:8100:80 SiO_2/TPAOH/H_2O/EtOH (denoted as C3). The 1 mg/mL seed suspension was mixed with an appropriate volume of growth sol to yield suspensions that were 0.2 mg of silicalite-1/mL with compositions consistent with C1, C2, or C3. The suspension was sealed in a centrifuge tube with Teflon tape to prevent evaporation of the solvent and was heated in a convection oven at 70 °C. After a certain time, the centrifuge tube was removed and plunged into an ice bath (0 °C). A cryo-TEM sample was prepared from the suspension immediately afterward. Cryo-TEM sample preparation was conducted in an FEI Vitrobot Mark III vitrification robot.[57] A droplet of the suspension was placed onto a carbon/Formvar-coated copper grid (Ted Pella Inc.) in the climate chamber of the Vitrobot system, where the temperature was kept at 25 °C and the relative humidity was kept at 100%. The specimen was transferred under liquid nitrogen to a Gatan 626 DH cryo-transfer specimen holder.

Characterization

Scanning electron microscopy (SEM) images were collected on Hitachi S-900 and Hitach S-4700 instruments after the samples were coated with 1 nm of Pt. The samples for conventional (non-cryogenic) TEM was prepared by applying a few droplets of the suspension onto a copper grid coated with holey carbon and carbon thin film (Ted Pella Inc.). The grid was then allowed to air-dry. Imaging was performed on an FEI Tecnai G2 F30 transmission electron microscope operating at 300 kV. Cryo-TEM imaging was performed at -117^{o}C on an FEI Tecnai G2 F30 transmission electron microscope operating at 300 kV. All TEM images were captured using a CCD camera. Small-angle X-ray diffraction (SAXD) measurements were taken on a homemade pinhole SAXD line with a sample-to-detector distance of 100 cm using Cu Kα radiation. N_2 adsorption and desorption isotherms were measured at 77 K on a Quantachrome Autosorb-1 system. Conventional t-plot methods were used for extracting micropore properties. X-ray diffraction (XRD) patterns were acquired using a PANalytical X-Pert PRO MPD X-ray diffractometer equipped with a Co source and a Bruker AXS D5005 diffractometer with a Cu source.

3.3 Results and discussion

Preparation of isolated uniform nanoparticles

In this study, two types of 3DOm silicalite-1 particles with 40 nm and 25 nm domains were used. Fig. 3-1 (a) and (b) are the SEM and TEM images of 3DOm particles with 40 nm domains, which show the ordered uniform domains and ordered mesopores. Fig. 3-1 (c) is the electron diffraction pattern from the particle shown in Fig. 3-1 (b), which

indicates that the particle is a single crystal. Two dissolution pH ranges (11.0~12.0 and 9.0~10.0) were investigated in this study, which was experimentally achieved by a dialysis method: a semi-permeable dialysis tube containing a aqueous suspension of 3DOm silicalite-1 particles was placed in a reservoir of tetrapropylammonium hydroxide (TPAOH) or L-lysine solution, whose pH values were kept within 11.0~12.0 or 9.0~10.0, respectively, as the desired dissolution pH ranges. The systems were kept at room temperature. In this system, ions were free to transport through the dialysis tube, while the transport of silicalite-1 particles was blocked by the semi-permeable dialysis tube. The solution in the reservoir was changed to a fresh one regularly in order to remove the dissolved species and maintain the desired pH range. The product inside the dialysis tubes was collected after desired time.

Depending on the pH ranges within which dissolution was performed, two types of silicalite-1 nanoparticles were formed: intact silicalite-1 nanoparticles were formed within dissolution pH range 9.0~10.0 (Fig. 3-1 (d) (e)), and silicalite-1 nanoparticles with observable mesopores were formed where the dissolution pH range was 11.0~12.0 (Fig. 3-1 (f) (g)). As shown in the SAXS patterns (Fig. 3-1 (i)), the domains have lost their ordered arrangements after dissolution under both dissolution pH ranges, which means that disassembly was achieved. XRD (Fig. 3-1 (h)) as well as high-resolution TEM (Fig. 3-1 (e) (f)) confirmed that the crystallinity was preserved after dissolution under both conditions.

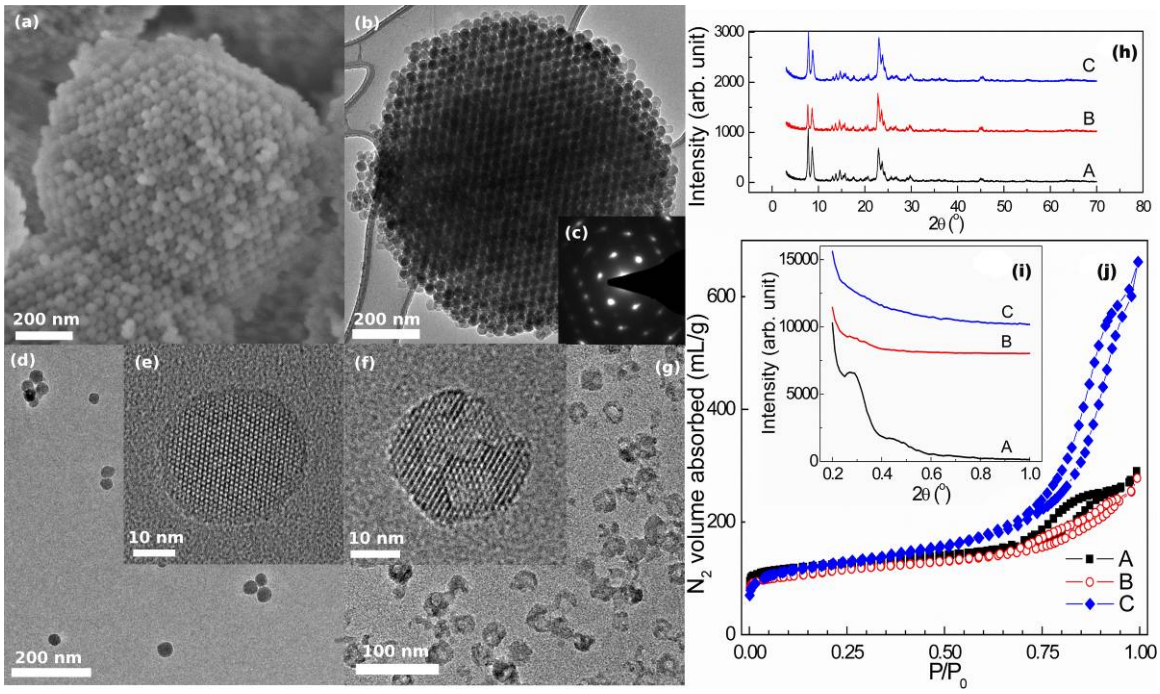

Figure 3-1 (a) SEM and (b) TEM micrographs of a 3DOm silicalite-1 particle with 40 nm domains; (c) the electron diffraction pattern (along [010] zone axis) from the particle shown in (b); (d) (e) isolated 40 nm 3DOm domains formed with dissolution pH: 9.0~10.0 after 7 days; (f) (g) isolated 40 nm 3DOm domains formed with dissolution pH: 11.0~12.0 after 7 days; (h) (i) (j) X-ray diffraction patterns, small-angle X-ray scattering pattern, and N_2 adsorption isotherm of 3DOm silicalite-1 before and after dissolution, where A: as-synthesized, B: after dissolution with pH: 9.0~10.0 for 7 days, and C: after dissolution with pH: 11.0~12.0 for 7 days.

N_2 adsorption and desorption was also performed on samples with 40 nm domains before and after dissolution (Fig. 3-1 (j) shows the isotherms). After dissolution, the specific micropore volume of the particles slightly decreased for both dissolution pH ranges (from 0.129 mL/g to 0.089 mL/g and 0.089 mL/g, after dissolution with pH: 9.0~10.0 and pH: 11.0~12.0 for 7 days, respectively), probably due to the larger specific surface area of small particles[58] and loss of micopores on new mesopore surfaces[59], as observed in previous studies. As seen in the isotherm (Fig. 3-1 (j)), dissolution with pH between 9.0 and 10.0 (B) led to a less uniform mesopore size distribution than 3DOm particles (A), which might result from the random packing of the isolated domains.

Dissolution with pH between 11.0~12.0 (C) resulted in greatly increased total pore volume, which was probably due to the new mesopores on the particles surfaces.

The results presented above can be qualitatively understood by investigating the structure and dissolution behavior of 3DOm zeolite crystals. A 3DOm silicalite-1 particle, which is a single crystal although with mesopores, belongs to MFI framework and its lattice can be described using an (microscale) orthorhombic crystal system. Similarly, the cubic close-packed domains in the particle can also be described using a mesoscale cubic crystal system, where each 3DOm domain sits on a lattice point[60]. However, no evidence has shown that these two hierarchical sets of lattices have specific relative orientation. As a result of the anisotropy of a crystal, dissolution behaviors of silicalite-1 in base are also anisotropic, as observed by Iwasaki and Sano[61]. In a 3DOm silicalite-1 particle, dissolution behavior along different directions of the microscale lattice can also be different. The mesoscale lattice intersecting the microscale lattice will allow more crystal planes to be exposed to dissolution. However, different relative orientation of these two lattices will let the more soluble planes to be exposed to different directions in the mesoscale lattice. Thus, one can expect the randomness of the positions of new mesopores in a mesoscale lattice, as well as the resulting particle morphologies. Fig. 3-2 describes the observed dissolution process, from which it is obvious that the position of the new mesopores is an important factor determining the nanoparticle morphology. If the more soluble planes are at the connections, dissolution will lead to mesopores at connections, which will also isolate the domains (Fig. 3-2 (b) and (d)). If the more soluble planes are far from the connections, dissolution will happen on the

surface of the domains, but isolation cannot be achieved in this manner: this behavior is responsible for the formation of interconnected domain groups that were also observed in the product (Fig. 3-2 (a) and (c)). Within dissolution range 11.0~12.0, a combined effect of the above two cases will lead to isolated nanoparticles with core-shell morphology (Fig. 3-2 (d)). As a summary, due to this random dissolution behavior, upon dissolution, the 3DOm particle will break into single domains and groups of interconnected domains, with loss of connection between adjacent domains. Apart from this random dissolution behavior, the groups of domains can be uniformly dissolved and have reduced size (Fig. 3-2 (a) and (c)).

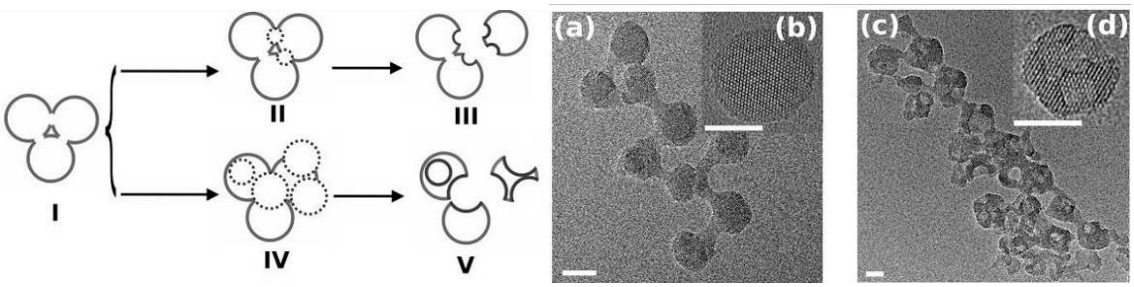

Figure 3-2 A schematic description of the dissolution process. When treated with base, new mesopores will be formed on 3DOm silicalite-1 particles (I). (II) and (III) illustrated the process under where dissolution pH is between 9.0 and 10.0; (IV) and (V) corresponds to dissolution pH range 11.0~12.0. (a), and (b) show the resulting particles with dissolution pH: 9.0~10.0 as described in (III); (c) and (d) show the resulting particles with dissolution pH: 11.0~12.0, as described in (V). (scale bar: 20 nm)

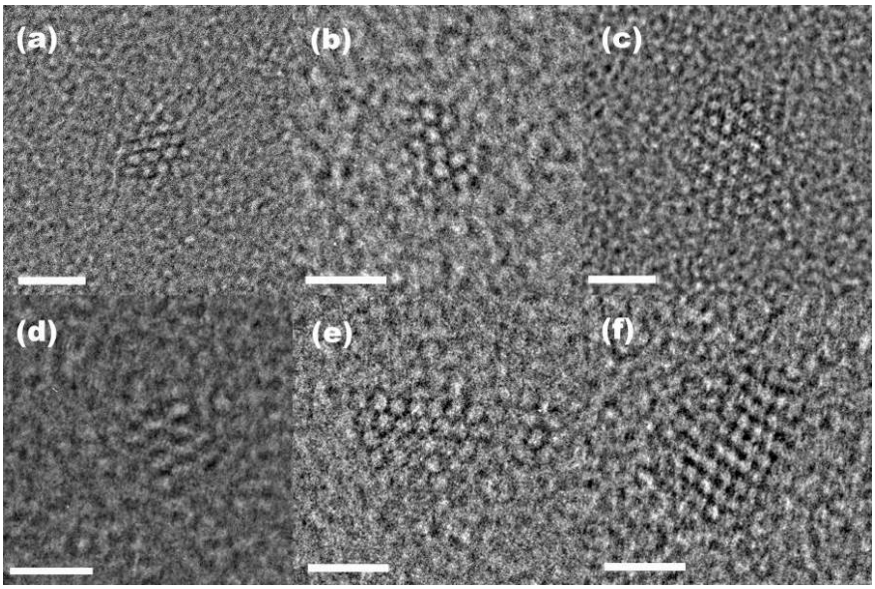

Figure 3-3 Silicalite-1 nanoparticles with at least one dimension smaller than 10 nm observed in the process of dissolution. (all scale bars=5 nm)

The same controlled dissolution method was also performed on 3DOm silicalite-1 with 25 nm domains. Silicalite-1 nanoparticles with at least one dimension smaller than 10 nm are also observed within dissolution pH range 11.0~12.0 after 21 days, as shown in Fig. 3-3 (a~f). This is evidence that zeolite nanoparticles that contains only a few unit cells exist and can be stable from structure transformation, aggregation or electron beam probing. This discovery implies that formation of zeolite with at least one dimension smaller than 10 nm by nucleation-growth approach is highly possible, if crystallization conditions are well controlled.

Cryo-TEM study of the secondary growth of MFI

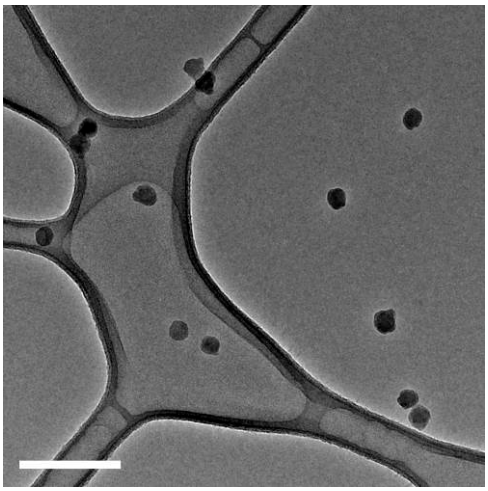

Figure 3-4 The silicalite-1 seeds used in the study of MFI secondary growth. These seeds have spherical shape, smooth surfaces and an average diameter of 40 nm. (scale bar=200nm)

The silicalite-1 seeds used in this study were spherical domains isolated from 3DOm (3-Dimensionally Ordered mesoporous) silicalite-1 particles by sonication[44], which have smooth surface and an average diameter of 40 nm. After isolation, the seeds were in a suspension with a concentration of 1 mg silicalite-1 / mL. The suspension is stable at room temperature for a period of at least 3 months. A TEM image of the seeds in the suspension is shown in Fig. 3-4.

The growth solutions used for this study were prepared as described by Davis *et al.*[56], where the compositions are as follows:

$5SiO_2$:9TPAOH:8100H_2O:20EtOH (notes as C1)

$10SiO_2$:9TPAOH:8100H_2O:40EtOH (noted as C2)

$20SiO_2$:9TPAOH:8100H_2O:80EtOH (noted as C3)

To achieve these compositions, tetrapropylammonium hydroxide solution (TPAOH, 1.0 M in water, Sigma-Aldrich) was first added to deionized water, the solution

was then stirred. Prescribed amount of tetraethyl orthosilicate (TEOS, 98%, Sigma-Aldrich) was added and the solution is stirred at room temperature for 24 hrs to allow complete hydrolysis of TEOS. The growth solution is mixed with the seed to give a suspension with seed concentration of 0.2 mg silicalite-1 /mL and desired final compositions. The suspension was sealed in a centrifugation tube with Teflon tape to prevent evaporation of the solvent, and was heated in a convection oven at 70^{o}C. After desired time, the suspension was removed and quenched into an ice bath (0^{o}C). A cryo-TEM sample was prepared from the suspension immediately afterwards.

Silicalite-1 particles showed secondary growth in C3 solution. The cryo-TEM images in Fig.3-5 show the evolution of silicalite-1 particles in C3 at 70^{o}C over a period of 36 hrs. From the images in Fig. 3-5, it can be seen that in C3 solution, silicalite-1 particles were among precursor nanoparticles with the size of approximately 5 nm[56]. After 6 hrs, the seeds showed no obvious growth, as seen in Fig.3-5 (a). However, the surfaces of the seed particles became rough, which might be attributed to a combined effect of dissolution by base (TPAOH) in the growth solution and aggregation of the precursor nanoparticles. After 12 hrs (Fig. 3-5 (b)), new parts appeared on the already rough surface of the seeds, which led to the increase of particle size. From Fig. 3-5 (b), the grown part of the particle was also crystalline as from the FFT (fast Fourier transform) of the image of the grown part, and it had the same orientation as the seed. Growth was obvious after this, as seen in Fig. 3-5 (c), (d), and (e). Throughout the growth process, the grown parts appeared crystalline, and the crystallographic orientations of the

seed and the grown parts were identical. From these images, it is apparent that during growth the particles do not maintain a defined shape.

In addition to C3 solution, the same method described above was also performed to C1 and C2 growth solutions. The SiO_2 concentration in C1 is below the silica solubility while the SiO_2 concentration in C2 is near the silica solubility, both of which have lower SiO_2 concentration than C3, whose SiO_2 concentration is above the silica solubility. Silicalite-1 particles showed dissolution if they were kept in C1 solution over a period of 36 hrs. A representative image of silicalite-1 particle in C1 is shown in Fig. 3-6 (a).

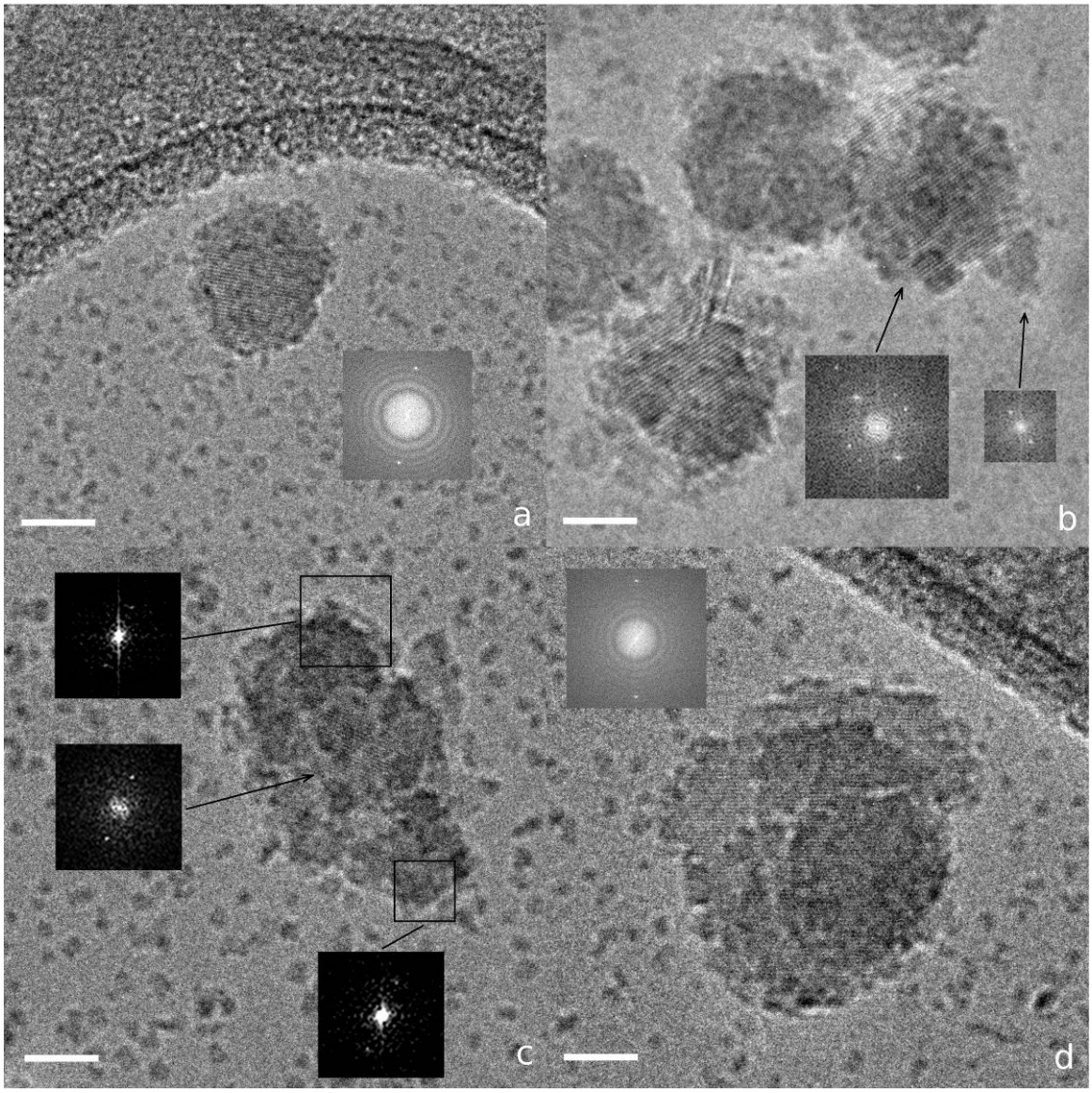

Figure 3-5 Representative cryo-TEM images of silicalite-1 particles heated at 70oC in C3 solution, the particles are among precursor nanoparticles sized approximately 5 nm: (a) after 6 hrs (the surfaces of the particles become rough, although there is no obvious growth); (b) after 12 hrs (the size of the particles increases; the two FFTs are from the seed and the grown part, they show the common set of lattice fringes ((200) or (020)) seen in both the seed and the grown part); (c) after 18 hrs (the FFTs are from different parts of the grown particle, from which a unique set of lattice fringes ((200) or (020)) can be identified throughout the particle); (d) after 24 hrs; (all scales bars correspond to 20 nm, and are of the same actual length for easier comparison)

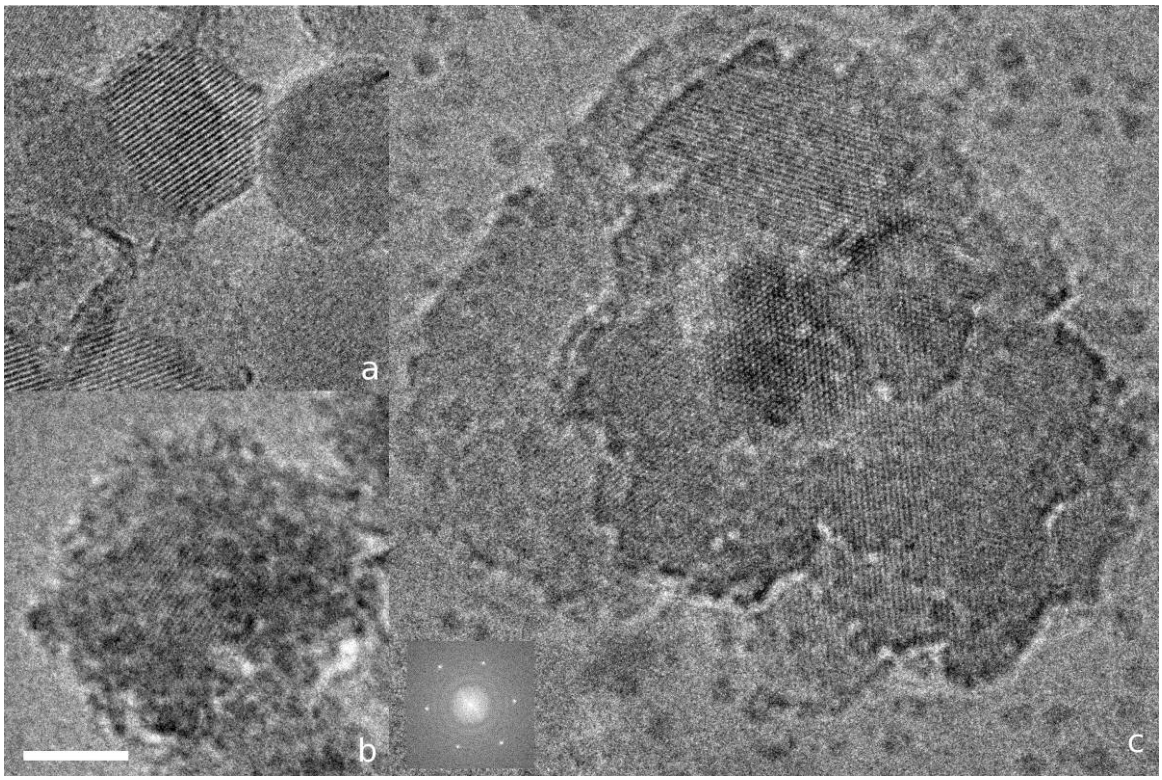

Figure 3-6 Cryo-TEM images of 40 nm silicalite-1 seeds treated at 70oC for 36 hrs: (a) in C1 solution the seeds undergo dissolution; (b) in C2 solution the seeds are surrounded by an amorphous shell; (c) in C3 solution, the seeds have increased size; the FFT from the whole image indicates that only one crystallographic orientation (along a or b direction) was observed from the image. (scale bar=20 nm for all images)

If the same silicalite-1 seeds are kept in C2 solution at 70ºC for 36 hrs, the particle size will slightly increase to approximately 60 nm (Fig. 3-6 (b)). Comparing the TEM images of grown particles in C2 and C3, the particle grown in the latter case always showed lattice fringes throughout the particles. However, the former showed a thick layer (5~15 nm) outside the particles without any fringes. Under cryo-TEM condition, defocal series from underfocus condition to overfocus condition were taken to study the crystallinity of this layer. A representative defocal series (Fig. 3-7) shows that lattice fringes do not appear near the edges. Here, we can conclude that the grown part is not

crystalline: the grown particles in C2 have a core-shell structure where the core (seed) is crystalline but the shell is amorphous.

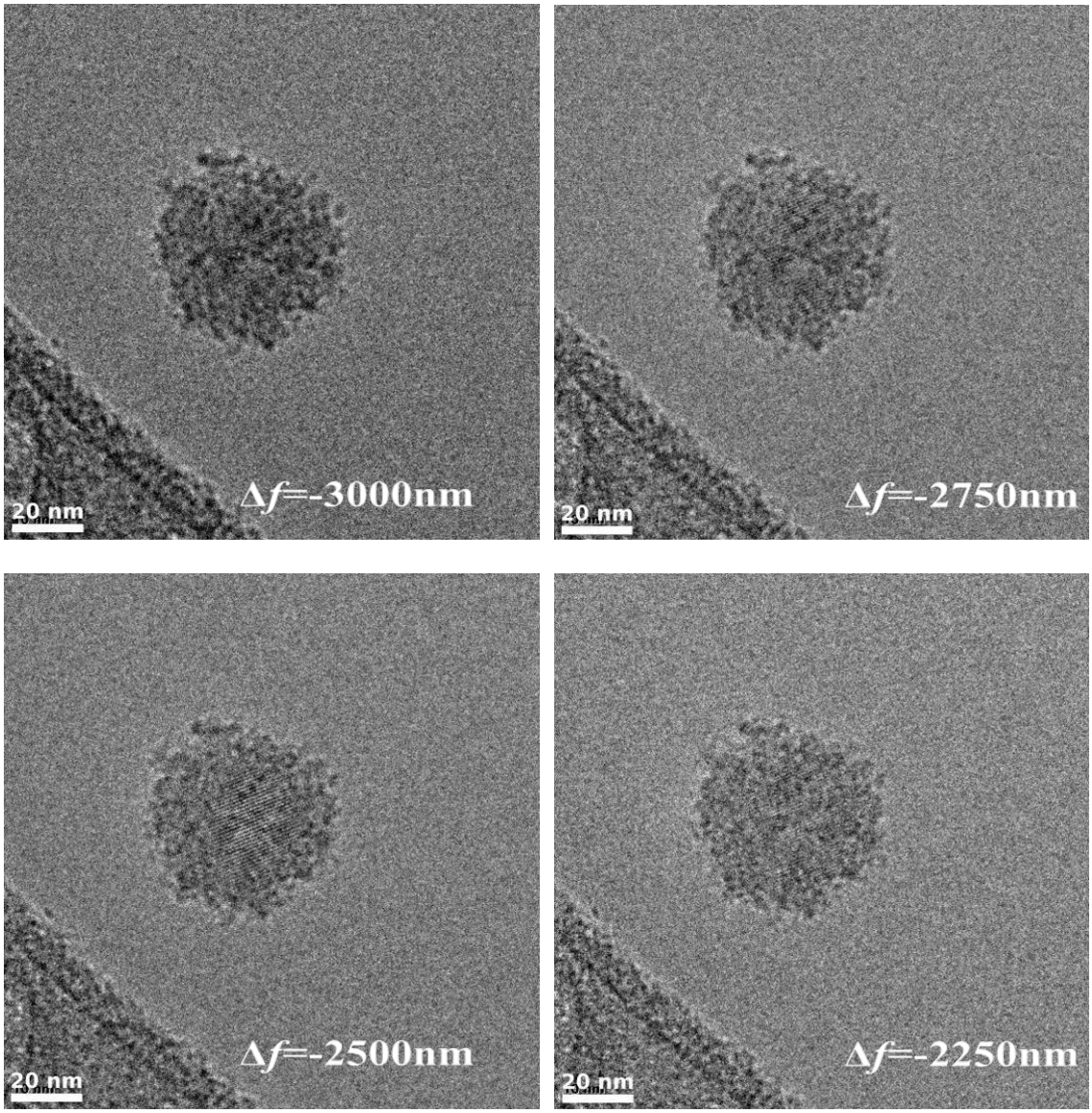

Figure 3-7 A defocal series (cryo-TEM images with defocus -3000nm~3000nm) of a 40 nm silicalite-1 seed treated at 70oC for 36 hrs in C2. Lattice fringes are not visible near the edge of the grown particle.

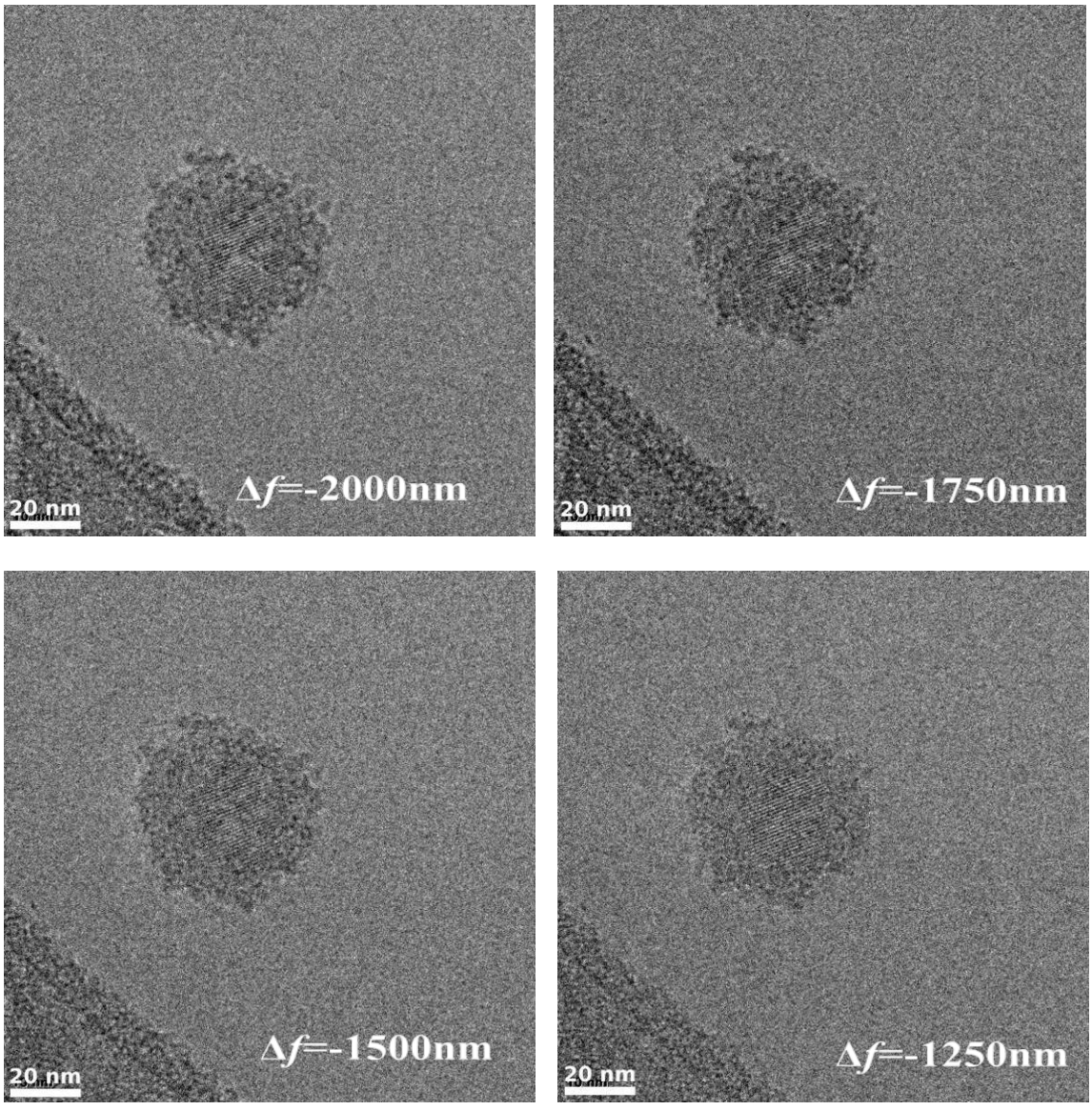

Figure 3-7 (*continued*) A defocal series (cryo-TEM images with defocus -3000nm~3000nm) of a 40 nm silicalite-1 seed treated at 70ºC for 36 hrs in C2. Lattice fringes are not visible near the edge of the grown particle.

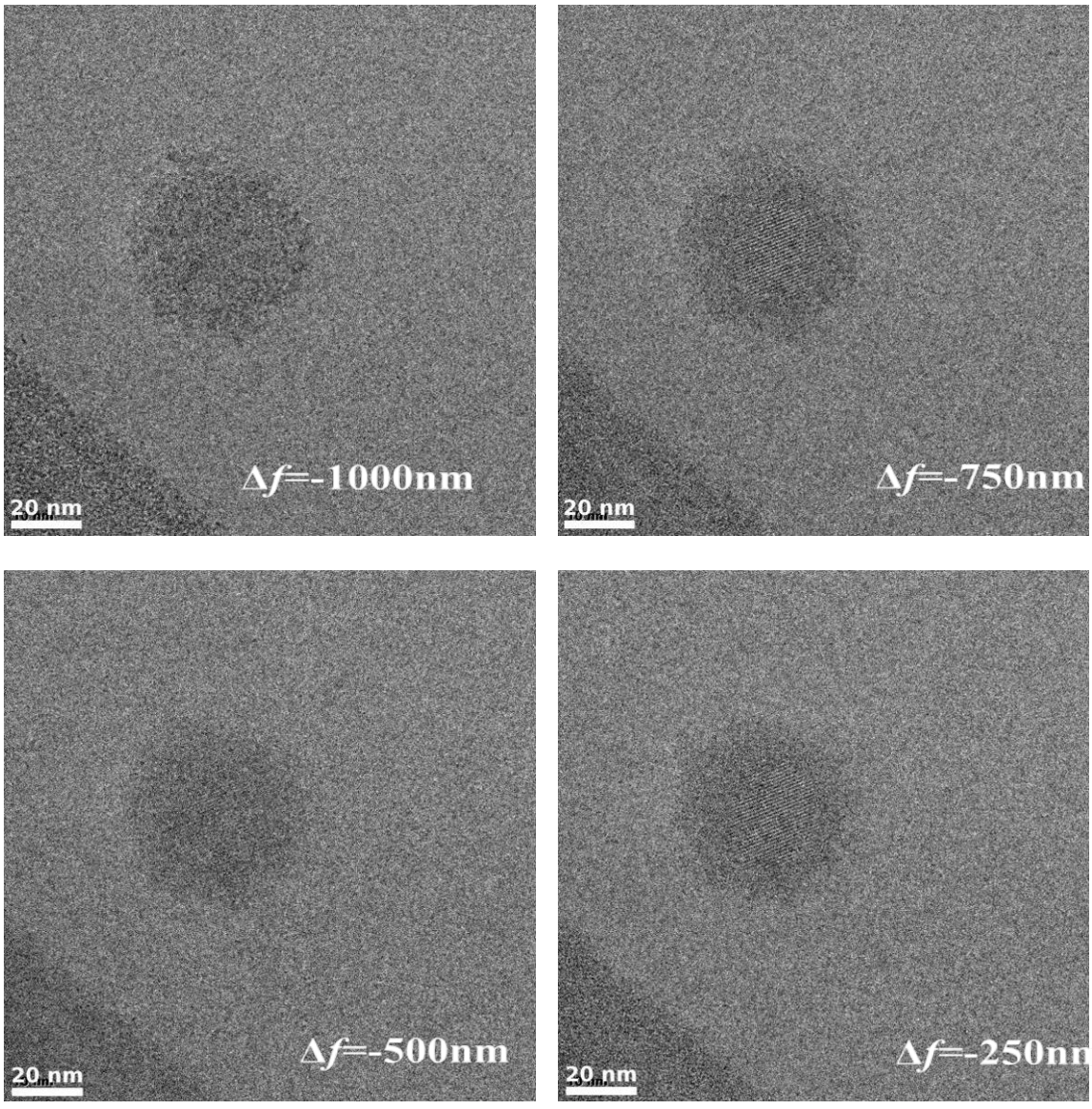

Figure 3-7 (*continued*) A defocal series (cryo-TEM images with defocus -3000nm~3000nm) of a 40 nm silicalite-1 seed treated at 70ºC for 36 hrs in C2. Lattice fringes are not visible near the edge of the grown particle.

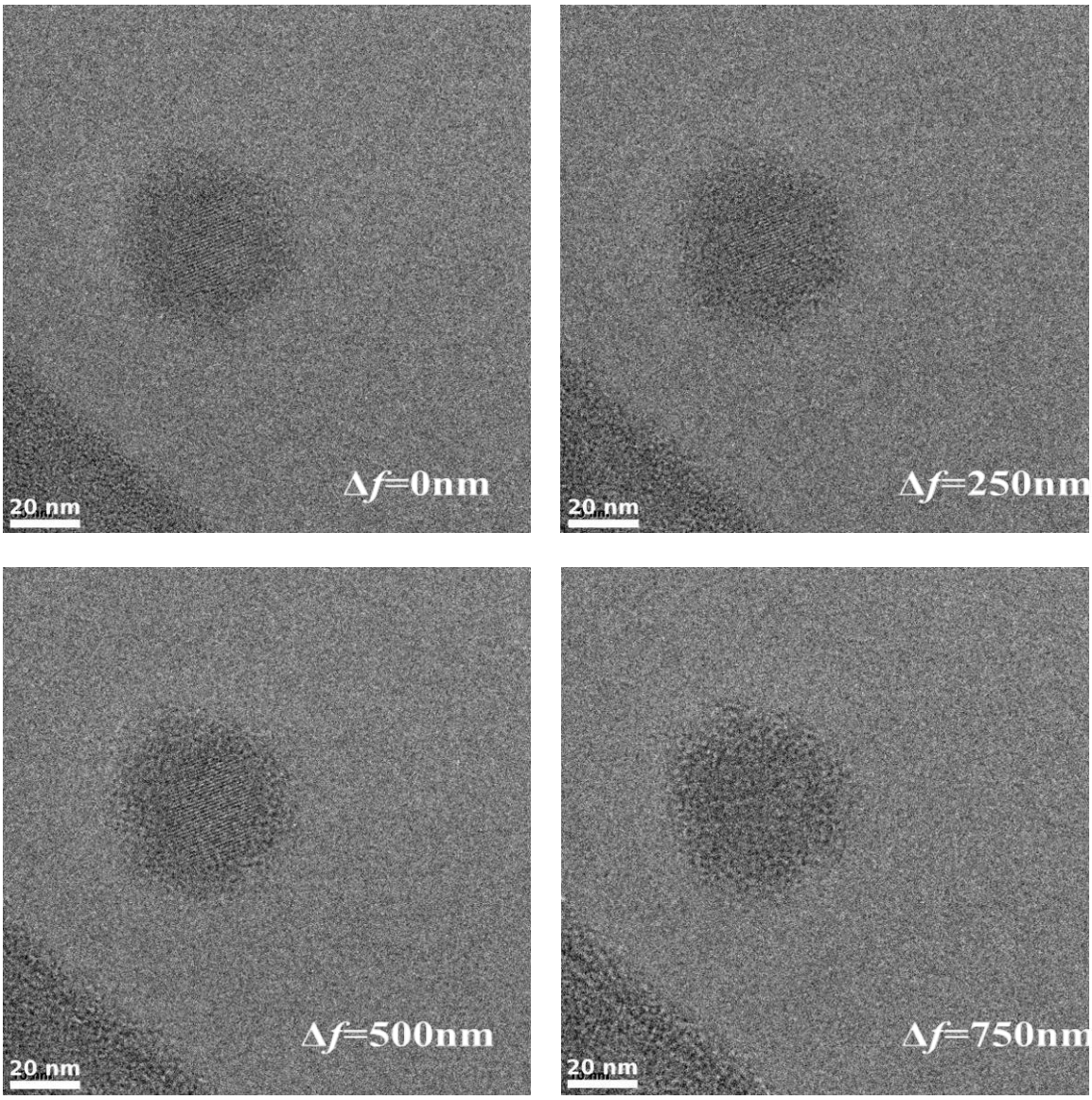

Figure 3-7 (*continued*) A defocal series (cryo-TEM images with defocus -3000nm~3000nm) of a 40 nm silicalite-1 seed treated at 70ºC for 36 hrs in C2. Lattice fringes are not visible near the edge of the grown particle.

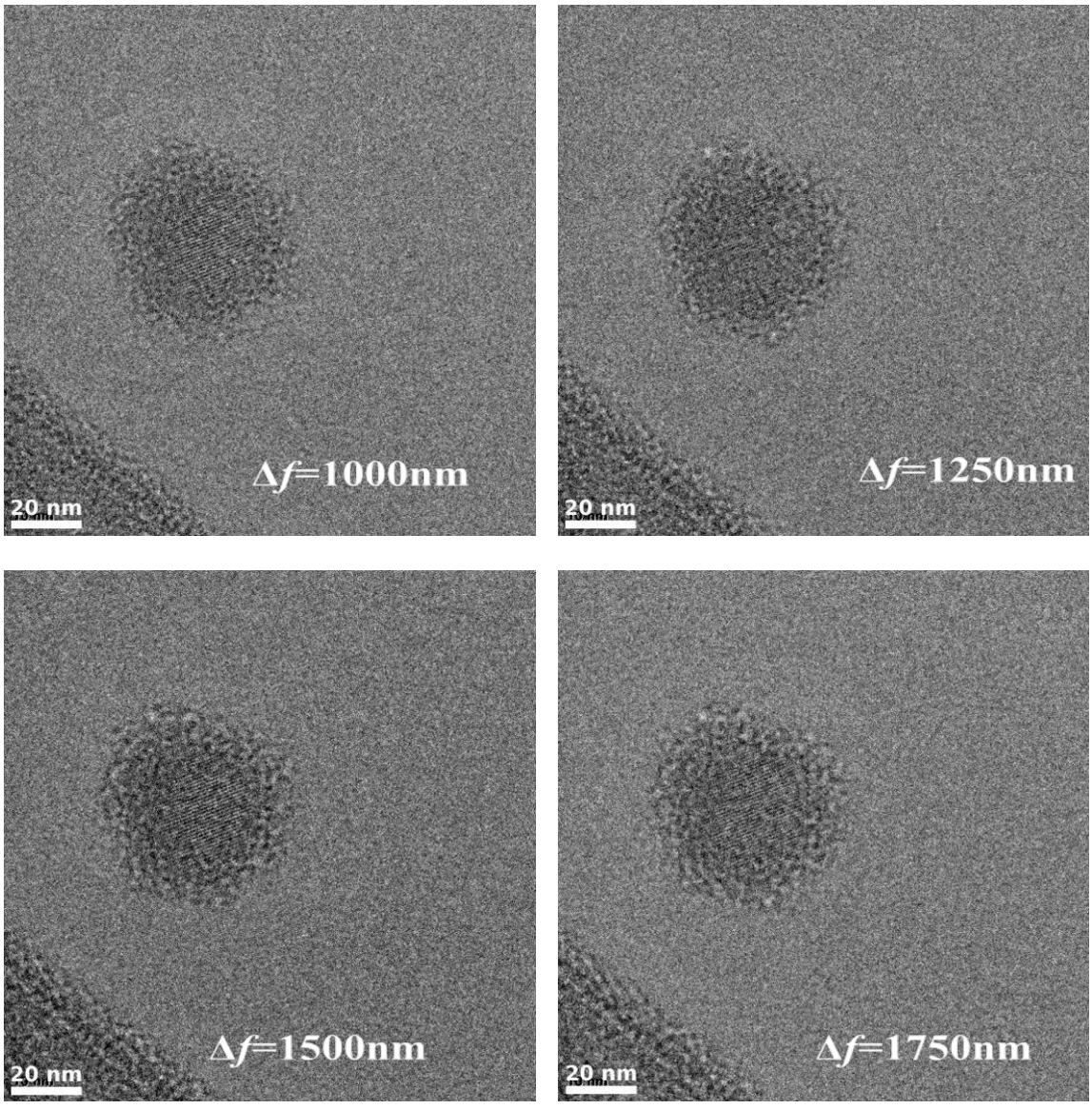

Figure 3-7 (*continued*) A defocal series (cryo-TEM images with defocus -3000nm~3000nm) of a 40 nm silicalite-1 seed treated at 70ºC for 36 hrs in C2. Lattice fringes are not visible near the edge of the grown particle.

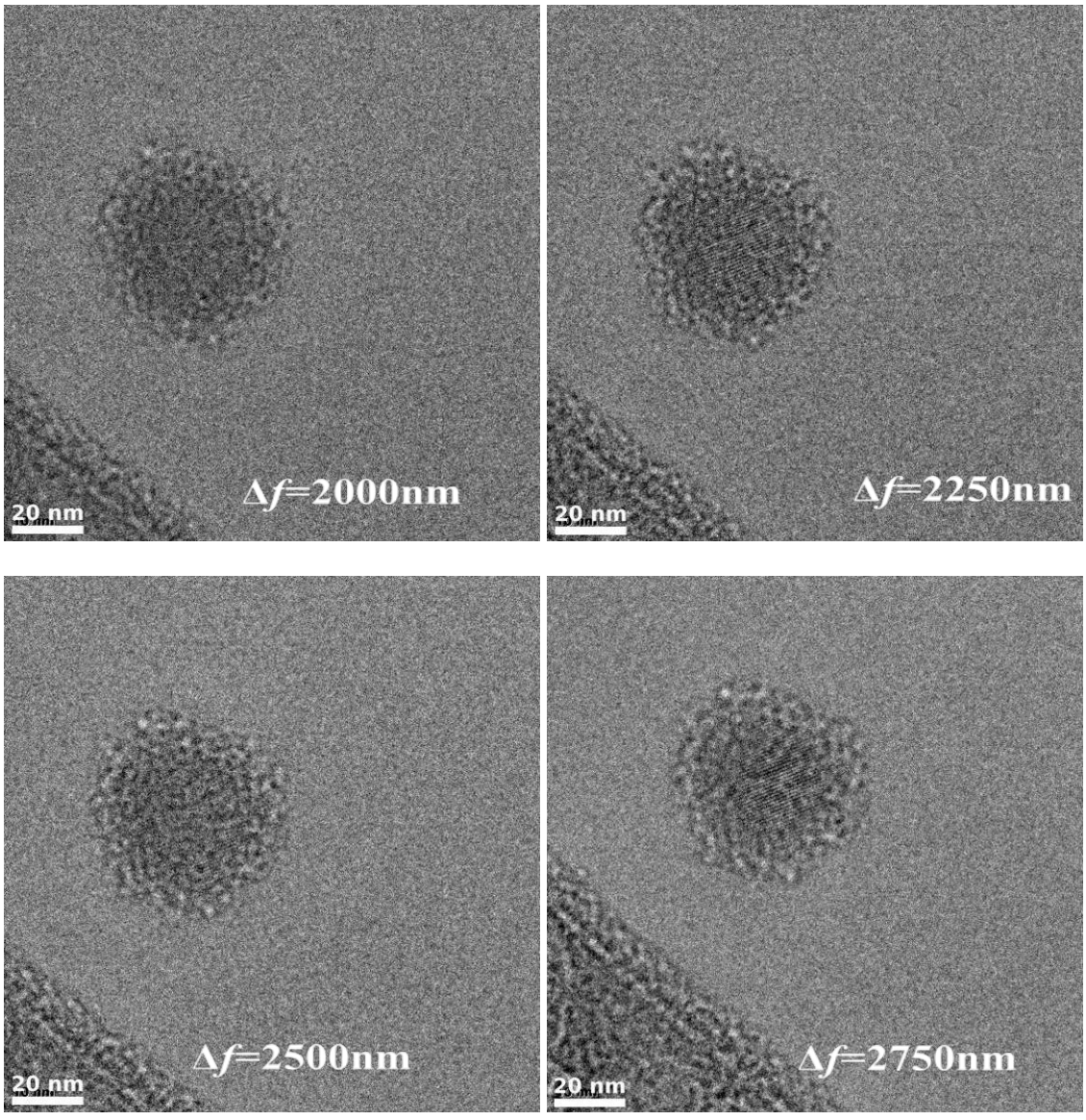

Figure 3-7 (*continued*) A defocal series (cryo-TEM images with defocus -3000nm~3000nm) of a 40 nm silicalite-1 seed treated at 70ºC for 36 hrs in C2. Lattice fringes are not visible near the edge of the grown particle.

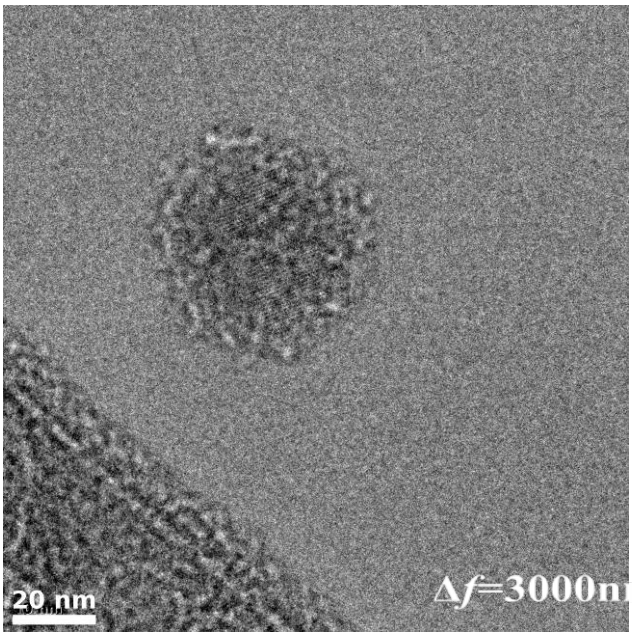

Figure 3-7 (*continued*) A defocal series (cryo-TEM images with defocus -3000nm~3000nm) of a 40 nm silicalite-1 seed treated at 70ºC for 36 hrs in C2. Lattice fringes are not visible near the edge of the grown particle.

3.4 Conclusions

Dissolution method was able to produce dispersible silicalite-1 nanoparticles with size tunable under 40 nm. However, a method with more controllable manner, especially controllable at microscopic scale, is still in need to produce nanoparticles with highly uniform morphology.

Secondary growth of silicalite-1 in different growth solutions are studied using cryo-TEM with structural resolution. In C3, secondary growth is observed, however, at early stages, the grown particles do not show defined shape. In growth solutions with different SiO_2 concentrations (C1 and C2), the seed particles show different behaviors.

Chapter 4 Zeolite-organic nanoassembly

4.1 Introduction

Zeolite nanoparticles can be prepared either through a nucleation-growth ("bottom-up") approach[62-63] or a disassembly ("top-down") approach[64]. By delicately controlling conditions of synthesis routes for bulk zeolite particles, zeolite nanoparticles smaller than 50 nm with different frameworks (SOD[65], FAU[66-67], MEL[68], MFI[69-73], LTA[74], LTL[75]) have been prepared using nucleation-growth approach. However, via this approach, it is still challenging to prepare dispersible, uniformly shaped zeolite nanoparticles smaller than 50 nm. By using confined growth method with hard-templates[44] or soft-template[76-78], nucleation-growth approach was able to prepare zeolite particles with nanoscale structural features. Three-dimensionally ordered mesoporous (3DOm) zeolites can be prepared with uniform spherical domains whose sizes are tunable below 40 nm[44]. Bifunctional structure-directing agents with a long alkyl chain as confining feature are able to template clusters of MFI nanosheets with thickness of 1-2 unit cells[76]. However, confined growth methods reported so far are not able to form dispersible individual zeolite nanoparticles, further cleavage of the nanoscale structural features from bulk phases is still required. In Chapter 3, zeolite nanoparticles with tunable size smaller than 40 nm was prepared by disassembly of 3DOm silicalite-1 (MFI framework) particles. However, disassembling nanoscale structural features from bulk phase is not able to produce nanoparticles in a highly controllable manner, and the potential damage to the crystal structure should also be taken into consideration. An

approach that can make dispersible and uniformly shaped zeolite nanoparticles with size smaller than 10 nm is still in need.

Designing structure-directing agents (SDA), which are responsible for aiding the formation of zeolitic structural features, is an effective approach to control zeolite structure and morphology. Zeolite MFI with coffin-shaped, leaf-shaped and lamellar morphologies are examples of morphology control of bulk MFI particles by designing SDAs[76-77, 79]. With this in mind, in addition to *structure-directing features* (that aids the formation of zeolite structure), if *morphology-confining features* (features around which silica cannot deposit), such as long alkyl chains, are also included in the same SDA structure, zeolite nanoparticles with smaller structural features and lower dimensions could be prepared.

Inspired by a recent use of azamacrocyclic amines for silica synthesis that showed the compatibility of azamacrocyclic amine structure with silica[80], we propose the idea of using alkyl azamacrocyclic ammonium cations as bifunctional SDA to synthesize MFI zeolite-organic nanoassemblies. This type of cyclic SDA has structure-directing features smaller than 10 nm that resemble zeolite structure, around which there are alkyl chains acting as morphology-confining features that will prevent its growth. Using this type of SDA, work introduced in this chapter intends to form *zeolite-organic nanoassemblies* with uniform zeolite domains smaller than 10 nm. The zeolite-organic nanoassemblies have zeolite domains supported and interconnected by organic species, and are hoped to release the domains as individual zeolite nanoparticles upon removal of the organic species. By exploration of structure and shape control possibilities, this method is

expected to create a new area of zeolite synthesis and a new class of zeolite materials whose size is below 10 nm, which will further extend the size limit of zeolite nanoparticles. Meanwhile, the successful synthesis of the proposed zeolite-organic nanoassemblies will allow us to gain more knowledge about the structure and properties of zeolite nanoparticles that contain only limited unit cells, which will not only add an important part to the existing literature of zeolite studies, but will also bring us deeper understandings of inorganic nanoparticle formation from a new and broader perspective.

4.2 The design of the SDA

For pure-silica-zeolite synthesis, besides Si source, OH^- or F^- as mineralizer, and solvent, structure-directing agents (SDA), usually organic ammonium cations that resemble the structural features of zeolites, are also added in the synthesis mixture of zeolites, in order to direct the formation of zeolite frameworks[62, 81]. SDAs play their roles by the electrostatic attraction between the positively charged quaternary nitrogen atoms and the negatively charged silicate species. This interaction will aid the silica species to form defined structure around the SDA, resembling zeolite structure, thus crystals with either ordered micropores or defined morphology will be formed, given the suitable crystallization conditions.

Intentional design of SDA structure, sometimes with the help of molecular modeling and simulation, is an approach to design zeolite framework or morphology[82]. There are examples of different SDAs bearing the same substructure leading to the same zeolite framework, although the exterior crystal morphology formed by those SDAs can be distinctly different. Take MFI framework for example, besides TPA^+ (Fig. 4-1 (a)), which

will yield coffin-shaped crystals, silicalite-1 can also be formed by dimer-TPA (Fig. 4-1(b))[79], trimer-TPA (Fig. 4-1(c))[79], or a recently reported diammonium with long alkyl chains $C_{22\text{-}6\text{-}6}^{2+}$ (Fig. 4-1(d))[76], that will give leaf-shaped silicalite-1 (by dimer-TPA and trimer-TPA), and silicalite-1 nanosheets, respectively. These SDAs (Fig. 4-1(b~d)) bear a C_6 chain between adjacent quaternary nitrogen atoms. This C_6 linkage can align along the straight channels of MFI (along the *b* direction), where the other alkyl groups on the quaternary nitrogen atoms will direct the formation of channels along *a* direction. Besides C_6 linkage, minor variation of number of carbon atoms between the two nitrogen atoms (e.g., C_5 or C_7) will not prevent the formation of MFI framework[79].

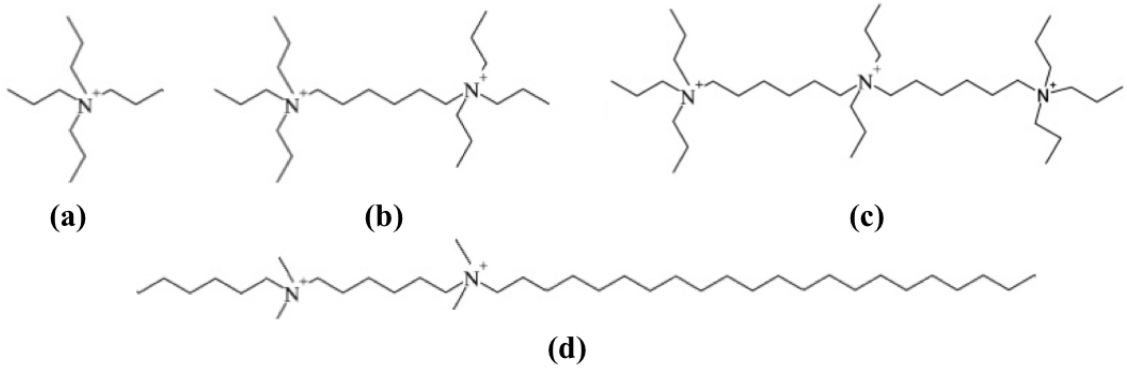

Figure 4-1 Examples of SDAs with which MFI framework can form (a) TPA^+ (b) dimer-TPA^{2+} (c) trimer-TPA^{3+} (d) $C_{22\text{-}6\text{-}6}^{2+}$

For bulk (3-D) zeolite materials, the positions of structure directing agents (SDA) in zeolite synthesis are often inside a cage or buried at the crossing of two channel systems[83-85]. This type of SDAs can be considered as zero-dimensional SDA comparing to the size of the product zeolite nanoparticles. In this way, SDAs are incorporated in zeolite framework, with which 3-D continuous zeolite structures can be formed. For example, in MFI zeolite growth, where tetrapropylammonium (TPA^+) cations are used as SDA, TPA^+ sits where the channels along *a* direction and *b* direction meet.

However, in order to form zeolite, it is not necessary for SDAs to be completely incorporated in the framework. If the complete incorporation of SDA in silica species can be prevented, confined formation of low dimensional zeolites can be achieved. The recently reported MFI nanosheet is a good example where zeolite framework is not surrounding SDA cations[76], but is confined inside the ordered SDA micelles. The reported SDA has three alkyl chains connected by two quaternary nitrogens (Scheme 1(d)). This type of SDA can be considered as one-dimensional. On one end of the SDA, there is a long C_{22} chain that acts as a morphology-confining feature, which prevent the zeolite structure from growing to the third dimension. This soft templating effect of the 1-D SDA confines zeolite growth into only two dimensions.

The above implies that if SDA can be made as a two-dimensional or three-dimensional (higher dimensional) structure with structure-confining features around it, zeolite with low dimensional structure can also be formed. However, there is no previous report of higher-dimensional SDA structure for zeolite synthesis. This chapter will focus on designing cyclic SDA attached with long alkyl chains (SDAs with higher dimensional geometry) for zeolite synthesis, hoping to form zeolite-organic nanoassemblies with uniform and releasable domains smaller than 10 nm (0-D).

Two classes of SDAs will be synthesized and investigated in the proposed work: (1) alkyl tetraazamacrocyclic ammoniums (ATA) and alkyl hexaazamacrocyclic ammoniums (AHA); (2) dimers of AHA as an example of interconnected cyclic polyammonium structures.

Alkyl tetraazamacrocyclic ammoniums (ATA) symmetrically quaternized with alkyl chains (Fig. 4-2 (S1~S4)) will be used as SDAs for the proposed zeolite-organic nanoassemblies.

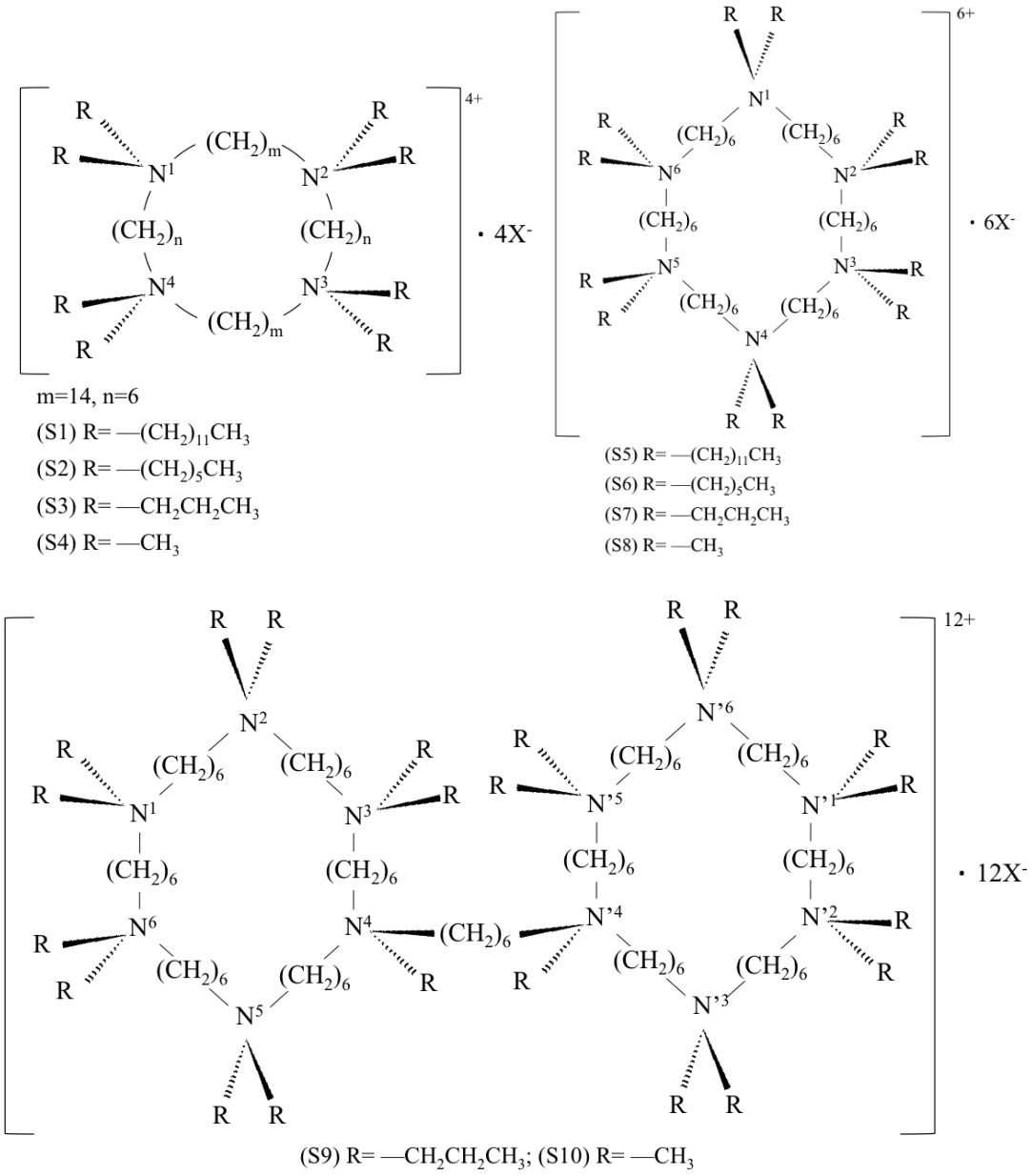

Figure 4-2 The structures of the proposed ATA (S1~S4), AHA (S5~S8), and diAHA (S9~S10) (X=Br or I, depending on the synthesis route)

In Fig. 4-2 (S1~S4), the tetraazamacrocyclic ammonium cations have C_m and C_n linkages between adjacent nitrogen atoms. For structures (S1)~(S4), *m* and *n* are chosen to be 14 and 6, respectively. This set of *m* and *n* are chosen such that the structure will match the MFI framework channel system. In this way, it is hoped that when silicate species deposits around ATA, and the structure of ATA will aid silicate species to form MFI structure.

A schematic illustration of the position of ATA in MFI framework is shown in Fig. 4-3 (a) and (b). In this case, it is hoped that the N-C_{14}-N linkage can stretch along the straight channels of the *b* direction of MFI framework, while the N-C_6-N linkage can connect adjacent straight channels. The nitrogen atoms in this SDA will be at the crossings of straight channels and zigzag channels, and the alkyl groups will be responsible for directing the formation of channels. *m* and *n* will be fine tuned according to their performance and molecular simulation studies, since previous work has shown that in some cases, minor variations in the size of the N-C-N linkage will not prevent from the formation of MFI structure[79]. Also, combinations of *m* and *n* in order to match other frameworks will be studied in the future.

(S1) is a good example of the design concept of the proposed SDA. (S1) is the extreme case where the alkyl chains will not be an effective structure-directing feature, but a possible morphology-confining feature. For (S2), the alkyl groups can direct the formation of zeolite structure, but can also act as a morphology-confining feature. These two cases are examples of larger confinement that may lead to the formation of low dimensional zeolites domains, since it is hoped that silicate species can only deposit

around the positively charges ammonium nitrogen in the ring structure, but not near the long alkyl chains. The long alkyl chains can also attract the alkyl chains of other SDA cations. As a result, the product is expected to be (ordered or disordered) aggregations of zeolite domains, or zeolite-organic nanoassemblies. The choice of the R groups for (S3) and (S4) is based on the structure of previous examples of SDAs for MFI framework. These relatively small alkyl groups will fit into the crossing of channels and direct their formation. For these two cases, isolated or aggregated zeolite domains are expected. From (S1)~(S4), where the length of R group is decreasing, we can gain some knowledge about the influence of alkyl chains on product morphology.

Alkyl hexaazamacrocyclic ammoniums (AHA) symmetrically quaternized with difference alkyl chains (Fig. 4-2 (S5~S8)) will also be used as SDAs for synthesizing zeolite-organic nanoassemblies. The structure of AHA ring structure is also designed to fit the MFI framework, such that AHA will direct the deposition of silica to form MFI structure. The AHA structure can be divided into two connected N-C_6-N-C_6-N linkages. These two linkages are expected to align along adjacent straight channels of MFI framework (along *b* direction), which are connected with the other two N-C_6-N linkages (Fig. 4-3 (c) and (d)). The structure of AHA is very similar to trimer-TPA cation that is used as a SDA for MFI framework (Fig. 4-1 (c))[79]. The alkyl groups of AHA are chosen similarly to those of ATA. They will either direct the formation of channels structures or serve as morphology-confining features. (S5)~(S8) have decreasing alkyl chain lengths, in order to study the effect of alkyl chain length on the product morphology.

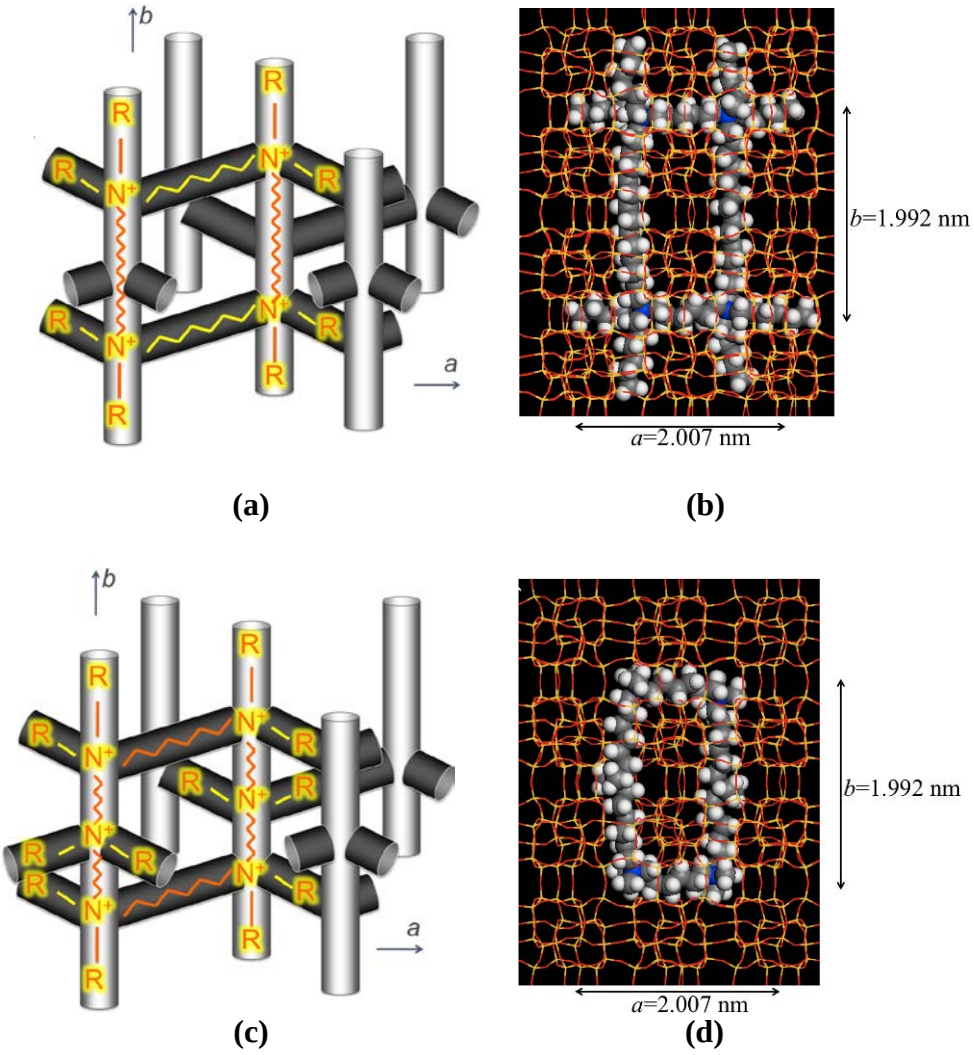

Figure 4-3 The proposed position of the SDAs in MFI framework. (a) the ATA cation sits in the channel systems of MFI framework (cylinders are channels, circles are the intersections of channels); (b) An ATA cations with R=*n*-hexyl embedded in the MFI framework, observed along *c* direction; (c) the AHA cation sits in the channel systems of MFI framework (cylinders are channels, circles are the intersections of channels); (d) An AHA cations with R=methyl embedded in the MFI framework, observed along *c* direction.

The dimers of AHA ((S9) and (S10) in Fig. 4-2) will also be synthesized and studied. Dimer AHA (diAHA) has two identical AHA connected with a N-C_6-N linkage, where the size of N-C_6-N is similar to the distance between adjacent crossings of the MFI channel systems. The expected behavior of diAHA is similar to AHA. However, the use

of dimers is hoped to effectively increase the size of the zeolite domains of the zeolite-organic nanoassemblies.

Besides (S1)~(S10), alkyl chains with other lengths, and asymmetrically quaternized SDAs may also be studied, depending on the performance of structures (S1)~(S10).

4.3 Synthesis of the SDAs[3]

ATA (in halide salt form) can be formed by quaternizing the corresponding amines. The synthesis of the 1,8,15,22-tetraazacyclooctocontane (*m*=*n*=6) as well as amines with *m*=*n*=7~10 is reported in detail by Tomohiro *et al* [86]. The route is shown in Fig. 4-4, in which four alkyl chain substructures are connected step by step. The ammonium salts can be prepare by alkylation of the amines (Fig. 4-5).

The detailed synthesis procedure is introduced below. The spectroscopic analysis of the intermediates and products are in Appendix I of this chapter.

[3] All syntheses of ATA were done by AsisChem Inc. (Watertown, MA)

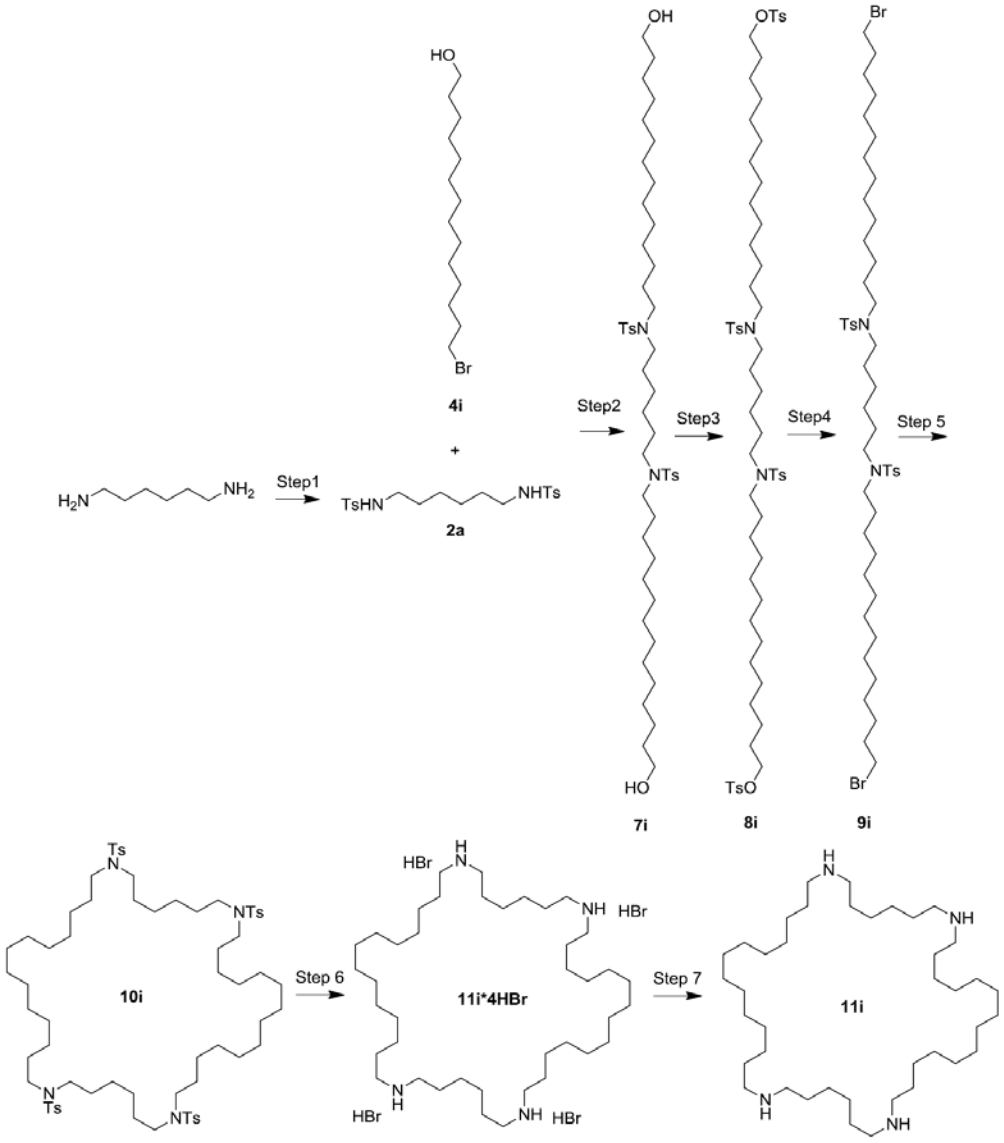

Figure 4-4 The synthesis procedure of the cyclic amine.

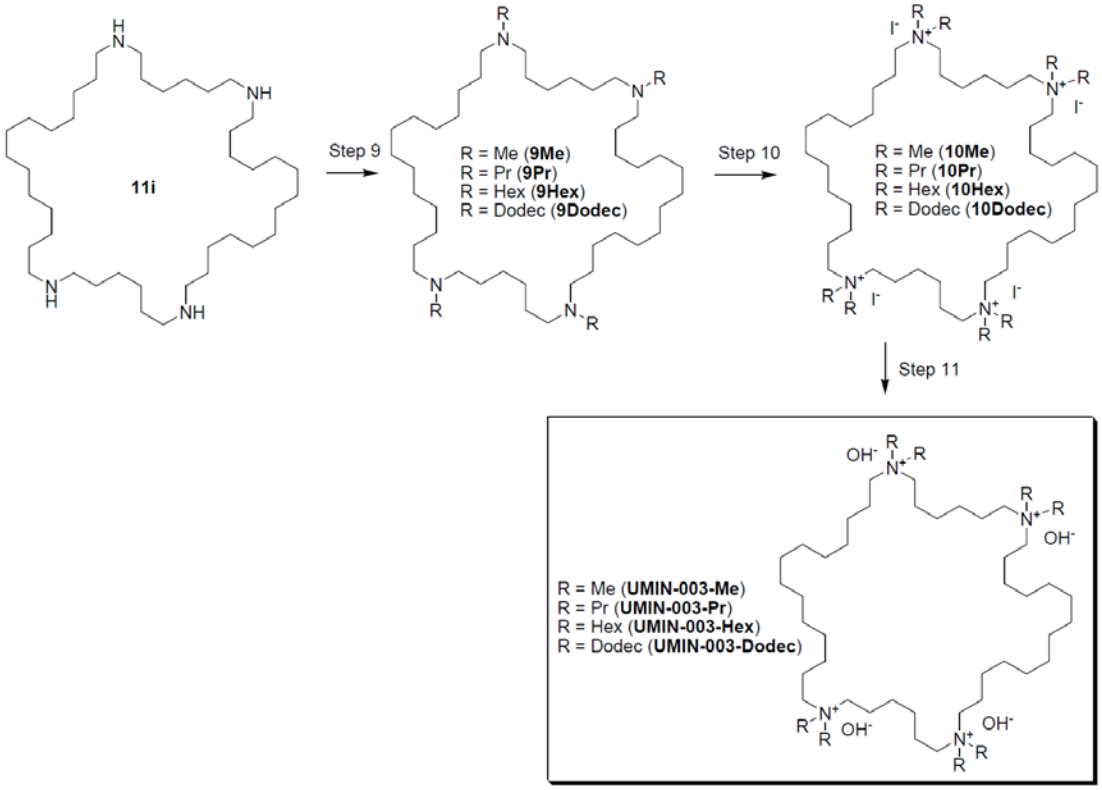

Figure 4-5 Alkylation of the cyclic amines yields cyclic quaternary ammonium hydroxides.

N,N'-(Hexane-1,6-diyl)bis(4-methylbenzenesulfonamide) (2a)

This compound was obtained using procedure from Tomohiro *et al.*[86] (Step 1 in Fig. 6-4) Yield 52% (colorless solid).

N,N'-(Hexane-1,6-diyl)*bis*(*N*-(14-hydroxytetradecyl)-4-methylbenzenesulfonamide) (7i)

To a solution of comp. **2a** (3.33 g, 7.86 mmol) in 30 ml of dry dimethylformamide (DMF) was added NaH (0.868 g, 18.08 mmol, as 50% suspension in mineral oil) in one portion with vigorous stirring under Ar atmosphere. The reaction mixture was warmed to 55°C and kept at this temperature for an hour then 14-bromotetradecan-1-ol **4i** (4.83 g, 16.5

mmol) was added (dropwise, in 20 ml of dry DMF during about 20 min). Two hours later heating mantle was removed and reaction flask cooled to room temperature. After filtration through a pad of Celite, DMF solution was concentrated *in vacuo*. To the precipitate obtained was added mixture a dichloromethane (DCM) and methanol (DCM:MeOH=100:1) (70 ml) and undissolved residue was filtered off. Then filtrate was concentrated to give 8 g of crude mixture which was chromatographed on ~140 g of silica gel (eluent DCM:MeOH 100:1) to give 3.2 g (47%) of the desired compound 7i.

_N_,_N_'-Di-_p_-toluenesulfonyl-_N_,_N_'-bis[14-(_p_-toluenesulfonyloxy)tetradecyl]-1,6-hexanediamine (8i)

To a mixture of diol 7i (2.427 g, 2.86 mmol), triethylamine (TEA) (2.2 ml, 1.58 g, 15.6 mmol) and 4-dimethylaminopyridine (DMAP) (1.9 g, 15.6 mmol) in DCM (60 ml), dry 4-Toluenesulfonyl chloride (TsCl) (2.97 g, 15.6 mmol) was added in portions. The addition was carried out at room temeprature (water bath) under Ar atmosphere. After 3 hours stirring at room temperature the reaction was stopped by addition of 3 M HCl (45 ml). Organic layer was separated, washed with brine (saturated NaCl solution, 45 ml) and dried over Na_2SO_4. Upon solvent evaporation was obtained crude product which was subjected to chromatographic purification (eluent EtOAc:Hexane 3:7 then 4:6) to give 2.2 g (66%) of product.

***N,N'*-(Hexane-1,6-diyl)bis(N-(14-bromotetradecyl)-4-methylbenzenesulfonamide) (9i)**

A mixture of **8i** (2.81 g, 2.43 mmol) and LiBr (0.84 g, 9.7 mmol**)** in dry acetone (60 ml) was refluxed for 3 hours. After the precipitate formed was filtered off, the mother liquor was concentrated. Residue obtained was dissolved in EtOAc (~50 ml), and washed with brine (~25 ml). EtOAc solution was dried over Na_2SO_4 and evaporated to give 2.01 g of colorless crystals (yield ~80%).

1,8,23,30-Tetratosyl-1,8,23,30-tetraazacyclotetratetracontane (10i)

To a solution of **2a** (0.607 g, 1.43 mmol) in dry DMF (~70 ml) in Ar atmosphere was added NaH (50% as suspension in mineral oil, 0.0864 g, 3.6 mmol) in one portion. Resulted mixture was heated to ~60°C and kept at this temperature for an hour then a solution of dibromide **9i** (1.39 g, 1.43 mmol) in 22 mL of dry DMF was added dropwise. The reaction mixture was stirred at 60°C for 5~6 hours. DMF solution was concentrated *in vacuo* to dryness, to the residue was added ~15 ml of 1M HCl and the resulted mixture was extracted with DCM (2 x 50ml), washed with brine, dried over Na_2SO_4 and concentrated to give 2.5 g of solid crude residue which was purified on chromatographic column packed with silica gel (eluent DCM:EtOAc 100:1) to give 0.374 g of colorless crystals. From mixed fractions was additionally obtained 0.245 g of the compound. Overall yield ~35% up to this step.

1,8,23,30-Tetraazacyclotetratetracontane tetrahydrobromide (11i*4HBr)

To a suspension of cyclic amide (**10i**) (0.146 g, 0.118 mmol) in 7 ml of 47% HBr was added (0.028 g, 0.295 mmol) of phenol. The reaction mixture was refluxed for 7 hours. Precipitate was filtered off and washed with EtOH in beaker (~2.5 ml) then filtered again and washed with ~ 2 ml of diethyl ether. Finally 100 mg (90%) of gray precipitate was obtained.

1,8,23,30-Tetraazacyclotetratetracontane (11i)

To a solid hydrobromide **11i*4HBr** (46.31g, 0.049 mol) was added NaOH solution (98g, 2.45 mol) in H_2O (500 ml) and 125 ml of IPA. Reaction mixture was refluxed for 2 h and cooled to room temperature and IPA was removed *in vacuo*. Resulted suspension was chilled in refrigerator (4^oC) for 3 h. Precipitate was filtered off, washed twice with H_2O and dried in oven at 60°C to give beige solid (27.01 g, 89%)

1,8,23,30-Tetrapropyl-1,8,23,30-tetraazacyclotetratetracontane (12)

To a stirred suspension of the macrocyclic tetraamine **11i** (2.73 g, 0.0044 mol) in 60 ml of DCM under Ar atmosphere propionaldehyde (2.03 g, 0.035 mol) was added in one portion at 21°C, following which sodium triacetoxyborohydride (STAB) (6.27g, 0.0295 mol) was added portionwise with cooling on ice/water bath (during 10 min) at temperature ~18-23°C. Reaction mixture was kept at room temperature for 3h and poured into saturated K_2CO_3 solution (100 ml). The resulting emulsion was filtered through glass filter and extracted with DCM (4x50 ml). DCM solution was dried over Na_2SO_4 and

concentrated. The residue obtained (about 4.5 g) was chromatographed on silica gel, eluent DCM:NH_3 (prepared by DCM extraction of conc. ammonia solution diluted to 1:1 with water) comp. **12** was obtained as pale yellow oil 1.5 g (43%).

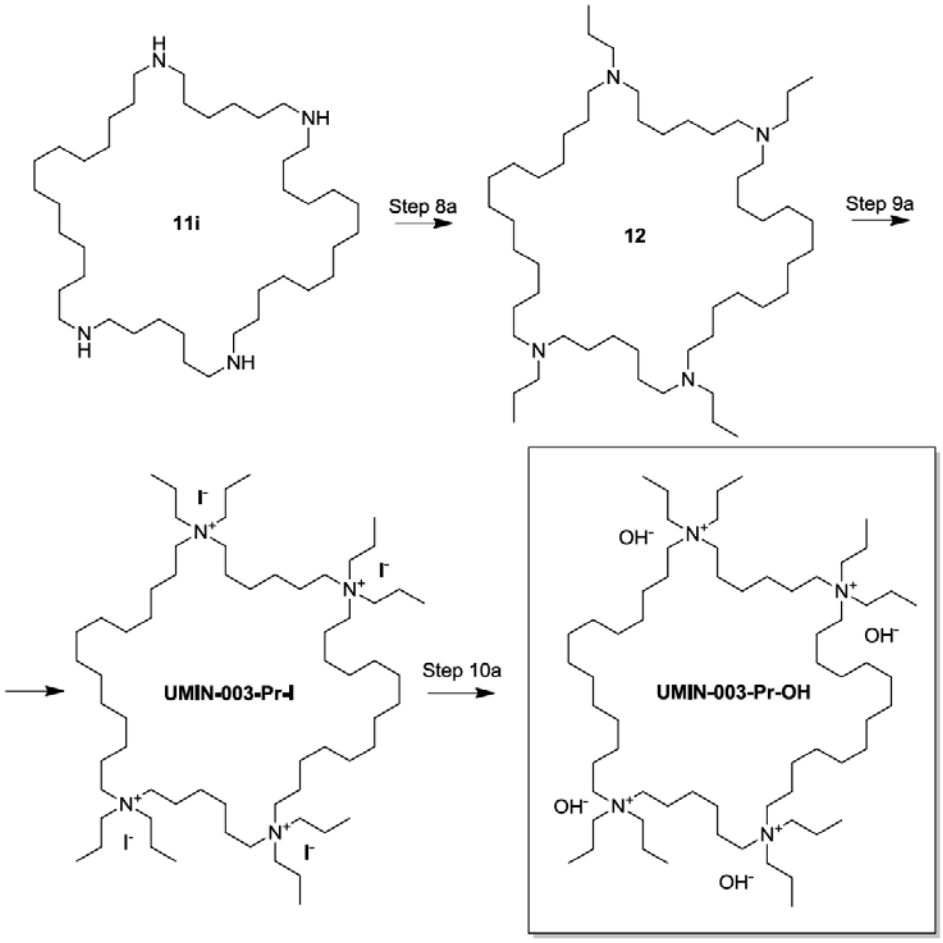

Figure 4-6 Propylation of the cyclic amine.

1,1,8,8,23,23,30,30-Octapropyl-1,8,23,30-tetraazacyclotetratetracontane-1,8,23,30-tetraium iodide (UMIN-003-Pr-I, (S3))

A reaction mixture composed of tetrapropyl compound **12** (0.691 g, 0.89 mmol), propyl iodide (6.05 g, 35.6 mmol), 1,2,2,6,6-pentamethyl piperidine (PMP) (5.52 g, 35.6 mmol), DMF (10 ml) and $CHCl_3$ (10 ml) was heated at 90-93°C with shielding from light for 5 h

under Ar atmosphere. Then reaction mixture was concentrated *in vacuo* and residue (2.9 g) was chromatographed on silica gel with DCM:MeOH (95:5) as eluent to give 0.9 g of mixture enriched with the product. It was chromatographed again, eluent DCM:MeOH (98:2 then 95:5) to give 0.17g (13%) of the target compound UMIN-003-Pr-I.

1,1,8,8,23,23,30,30-Octapropyl-1,8,23,30-tetraazacyclotetratetracontane-1,8,23,30-tetraium hydroxide: (UMIN-003-Pr-OH, (S3))

To the UMIN-003-Pr-I (iodide form) (0.246 g, 0.16 mmol) was added 150 ml of distilled water. The mixture was heated to 30°C for 2 h (until almost all starting iodide was dissolved). Amberlite IRN-78 (3.09g) was (washed with dist. water 2x65 ml) and added to the iodide solution. After stirring at ambient temperature (25°) for 3.5 h, Amberlite was filtered off, washed with 10 ml of dist. water. New portion of Amberlite (2.99 g) (washed with dist. water 2 x 40 ml prior using) was added to the solution and stirring continued over weekend. Then Amberlite was filtered, washed with distilled water (2 x 15 ml) and the aqueous solution was concentrated in vacuo (bath set to 26°C, vacuum 15 mm Hg). Evaporation was finished when volume of the solution reached 11.25 ml (0.014 M). It was kept in a refrigerator.

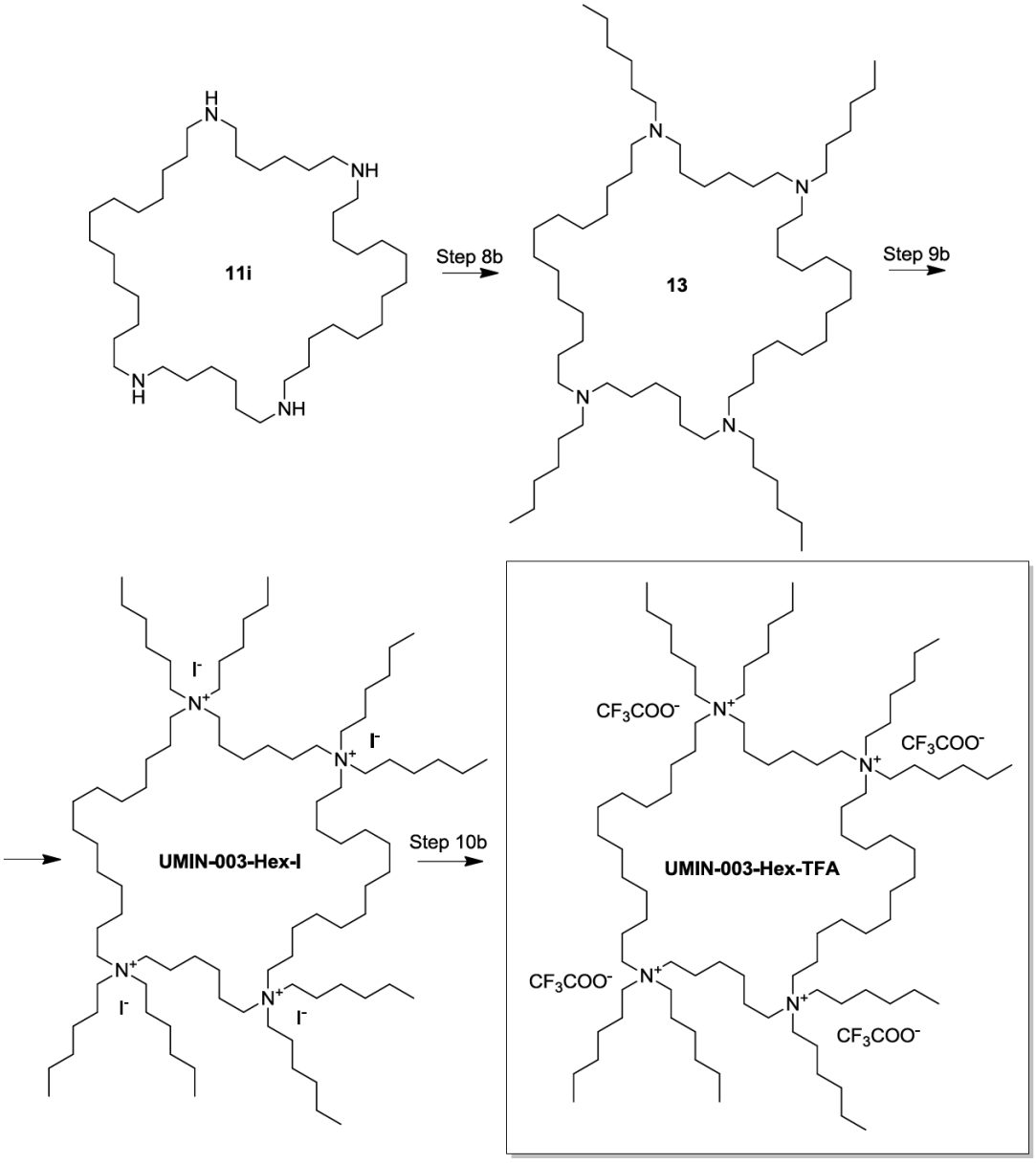

Figure 4-7 Hexylation of the cyclic amine.

1,8,23,30-Tetrahexyl-1,8,23,30-tetraazacyclotetratetracontane (13)

To a stirred suspension of the macrocyclic tetraamine **11i** (2.0 g, 0.00322 mol) in 30 ml of DCM was added hexanal (2.58 g, 0.02576 mol) in one portion at 17°C (water bath), following which, STAB (4.57 g, 0.02157 mol) was added portionwise during a period of

10 min at 18-21 °C. The reaction mixture was stirred at room temperature overnight, and then quenched by pouring into a saturated solution of K_2CO_3 (110 ml). The product was extracted with DCM (4 x 25 ml). DCM extracts were dried over Na_2SO_4 and concentrated to give 4.5 g of crude mixture as dark oil. It was chromatographed on silica gel (eluent DCM:NH_3 1:1 (prepared by DCM extraction of conc. ammonia solution diluted to 1:1 with water)) to give 1.5 g of crude product. It was subjected to second column purification to give 1.39 g of product, after third column purification (eluent DCM:NH_3+5% MeOH) 0.4 g (13%) of pure product as pale yellow oil was obtained.

1,1,8,8,23,23,30,30-Octahexyl-1,8,23,30-tetraazacyclotetratetracontane-1,8,23,30-tetraium trifluoroacetate (UMIN-003-Hex-TFA, (S2))

A reaction mixture composed of tetrahexylated macrocyclic tetraamine (0.704 g, 0.73 mmol), hexyliodide (6.26 g, 29.7 mmol), PMP (4.57 g, 29.4 mmol), DMF (6 ml) and $CHCl_3$ (6 ml) was heated at 70ºC for 12 h with shielding from light under Ar atmosphere. The reaction mixture was concentrated *in vacuo* and residue (3.5 g) was chromatographed with using mixture DCM:MeOH (eluent 99:1 then 97:3). Fractions with the product (proved by mass-spectrometry) were combined to give about 2 g of crude **UMIN-003-Hex-I** and purified by preparative HPLC (column Waters Symmetry C-18 5μm 19*50mm, flow 4 ml/min, UV detection 210 nm). Finally, 0.415 g (31%) of **UMIN-003-Hex-TFA** was obtained as a colorless oil.

The cyclic amines can be alternatively synthesized from the reduction of cyclic amides using lithium aluminum hydride ($LiAlH_4$)[87]:

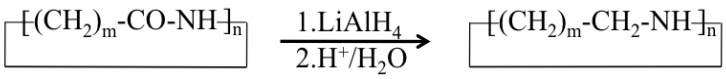

The cyclic amides can be synthesized according to Okuno *et al* [88] or Rothe *et al* [89]. For the latter the ω-amino acid monomers (or oligopeptides) can be attached sequentially one by one to form an oligoamide, a technique similar to cyclic peptide synthesis (Fig. 4-8) [89]. This can be achieved by commercial automatic peptide synthesis services. The resulted cyclic amides can be later reduced to cyclic amines using $LiAlH_4$.

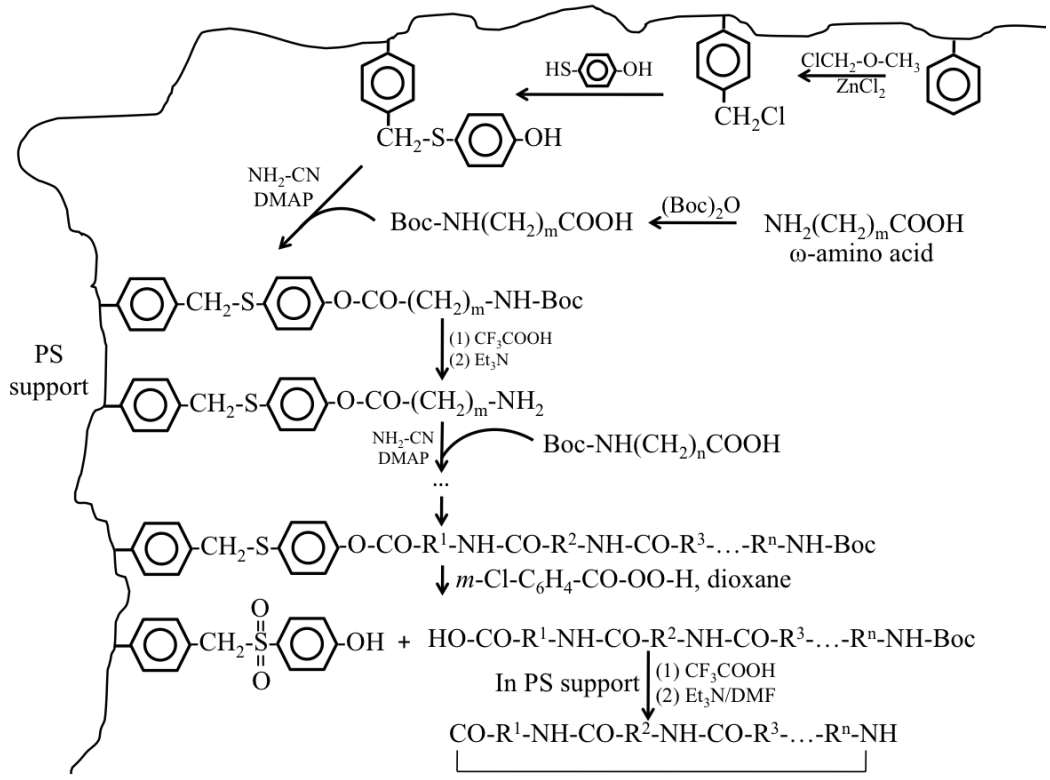

Figure 4-8 Synthesis of cyclic amides using peptide synthesis method (Adapted from Ref. [89])

For this approach, the yield of ring closure (final step) is 69%, where the attachments of each amino acid (previous steps) have nearly quantitative conversion [89]. This

approach can be used for both ATA and AHA synthesis by adjusting the number of ω-amino acids to be attached. The structure (i.e., *m* and *n*) of the final polyamide can also be tuned by using ω-amino acids with different numbers of carbons.

Dimers of AHA The dimers of AHA can be synthesized by: (1) reacting excess amount of the corresponding amines with 1,6-dibromohexane, in order to form the "bridge" connecting the two ring structure[90]; (2) alkylation of the corresponding dimers, which is introduced below.

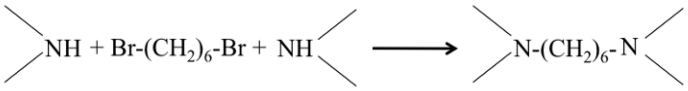

Alkylation of the amines For all the above-proposed SDAs, quaternizations are achieved by reaction between the amine and alkyl halides.

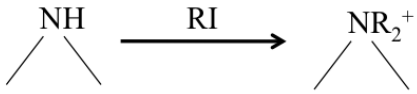

4.4 Attempts of zeolite synthesis

Typical synthesis routes for zeolites will be used: TEOS will be hydrolyzed with the help of a base (e.g., $SDA(OH)_x$) solution in water, in which SDAs (SDA^{x+}) are present. The subsequent synthesis mixture will be sealed and kept at different temperatures for desired time. Reactions with temperature above 100°C will be performed in stainless steel autoclaves that are common for zeolite synthesis. During heating, the autoclaves can be tumbled so that the mixing can be improved. Reactions with lower temperatures can be performed in conventional containers. Considering the fact that the SDAs require multi-step synthesis, which implies high cost and long

synthesis time for large amount of products, microscale Teflon reactor arrays can be used in this study as a high-throughput screening approach, such that the chemical amount, chemical cost and development time can be reduced. Previous works on new zeolite development using microscale Teflon reactor arrays [91-93] are good examples that the proposed research can follow.

A reactor array is also built for this study (see Appendix II of this chapter).

Table 4-1 briefly summarizes the desired products that the above experiments may result in. The solid phase will then be recovered by filtration or centrifugation. Calcination of the solid phase in air at 450ºC~550ºC will be one possible method to remove the organic species.

Table 4-1. A summary of desired products of the proposed research

SDA	Possible size (nm)	Possible state before removing organic species
ATA^{4+} or AHA^{6+}	3~5	(1) Soluble silica-organic composite macromolecules as a sol; (2) Zeolite-organic nanoassemblies as a suspension or precipitation
$diAHA^{12+}$	5~10	(1) Isolated nanoparticles as a sol; (2) Zeolite-organic nanoassemblies as a suspension or precipitation

Due to the small size of the proposed nanoparticles, a clear system is desired to ensure the formation of uniform particles. Inspired by previous work in the Tsapatsis group[56], dilute systems were prepared in order to achieve this goal. With SDA structure (S3) ($C_{14\text{-}6\text{-}14\text{-}6}$(*n*-Pr)$_8(OH)_4$, denoted as SDA(OH)$_4$), the following compositions were studied: *x* SiO_2: 2.25 SDA(OH)$_4$: 9500 H_2O : 4*x* EtOH, where *x*=0, 5, 10, and 20.

In these syntheses, SDA solution (0.014 mol L^{-1}, prepared by AsisChem Inc.) was first mixed with water. Then TEOS was added to the aqueous solution while stirring. The systems were kept stirring for 12 hours. Small angle X-ray scattering was performed on Anton-Parr SAXSess with quartz capillary holder.

In these systems, with x=10 and 20, precipitation was observed after 30 mins of stirring. The other two systems (x=0 and 5) remained clear after 12 hours. Small angle X-ray scattering was done on the more dilute systems with x=0 and 5. After 40 mins of exposure, the patterns are shown in Fig. 4-9.

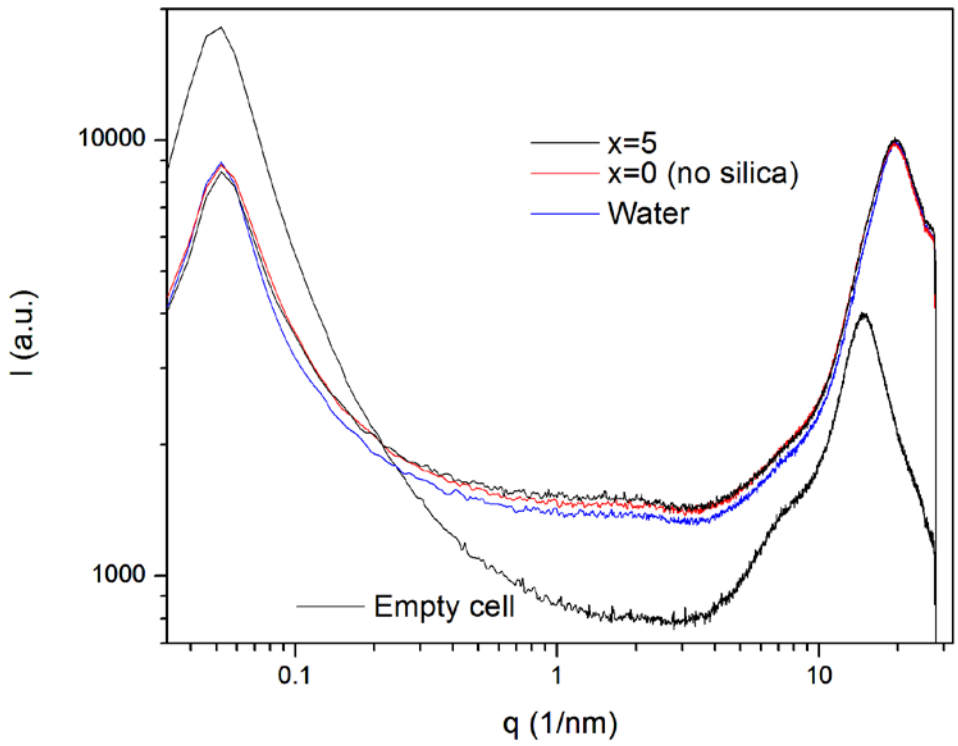

Figure 4-9 Small angle X-ray scattering patterns of the synthesis system.

From these patterns, it seems that the amount of silica in the synthesis system is too little to form nanoparticles. Therefore, in the future, larger amount of silica should be added to these dilute systems, in order to observe obvious formation of nanoparticles.

With the same SDA (S3: $C_{14\text{-}6\text{-}14\text{-}6}(n\text{-}Pr)_8(OH)_4$), in addition to dilute conditions, concentrated compositions were also studied as an attempt to produce ultra-small nanoparticles. Similar to the compositions for self-pillared pentasil zeolite synthesis[8], a composition of 40 SiO_2 : 3 $SDA(OH)_4$: 400 H_2O : 160 EtOH was chosen for the synthesis. Due to the high concentration (thus high demand) of the SDA, microscale synthesis was done in a 1 mL conical microcentrifuge tube. In this synthesis, the SDA solution was first mixed with water. TEOS (approximately 250 μL) was added slowly while stirring, to achieve the desired composition. The system was kept stirring for 24 hours.

After 1 hour of stirring, phase separation was observed in the system, where TEOS appeared on the top of the system as a separate layer. After 9 hours, the system turned to be an opaque gel. The composition studied in this case failed to produce clear system.

4.5 Future work

With the hydroxide form of the SDAs, a clear system will be the starting point for the synthesis of zeolite-organic nanoassemblies. In order to find a suitable clear system, gradual addition ("titration") of TEOS into SDA solution is one method. Similar to the work by Rimer *et al.* [94], starting from 5 SiO_2: 2.25 $SDA(OH)_4$: 9500 H_2O : 20 EtOH, more TEOS will be added to the system, until the formation of nanoparticles in a clear system is observed with SAXS. If nanoparticles are detected, the system will be heated to encourage crystallization of zeolitic species. The compositions with which nanoparticles

emerge will also be plotted to find out the solubility of silica in various conditions with the cyclic SDA in presence.

Besides basic systems with the hydroxide form of the SDAs, synthesis in neutral conditions will also be attempted, where fluoride media is occasionally used. [95-96]

Appendix I: Spectroscopic analysis of the intermediates in the SDA synthesis[4]

The NMR spectra and mass spectra of the intermediates are shown here for reference.

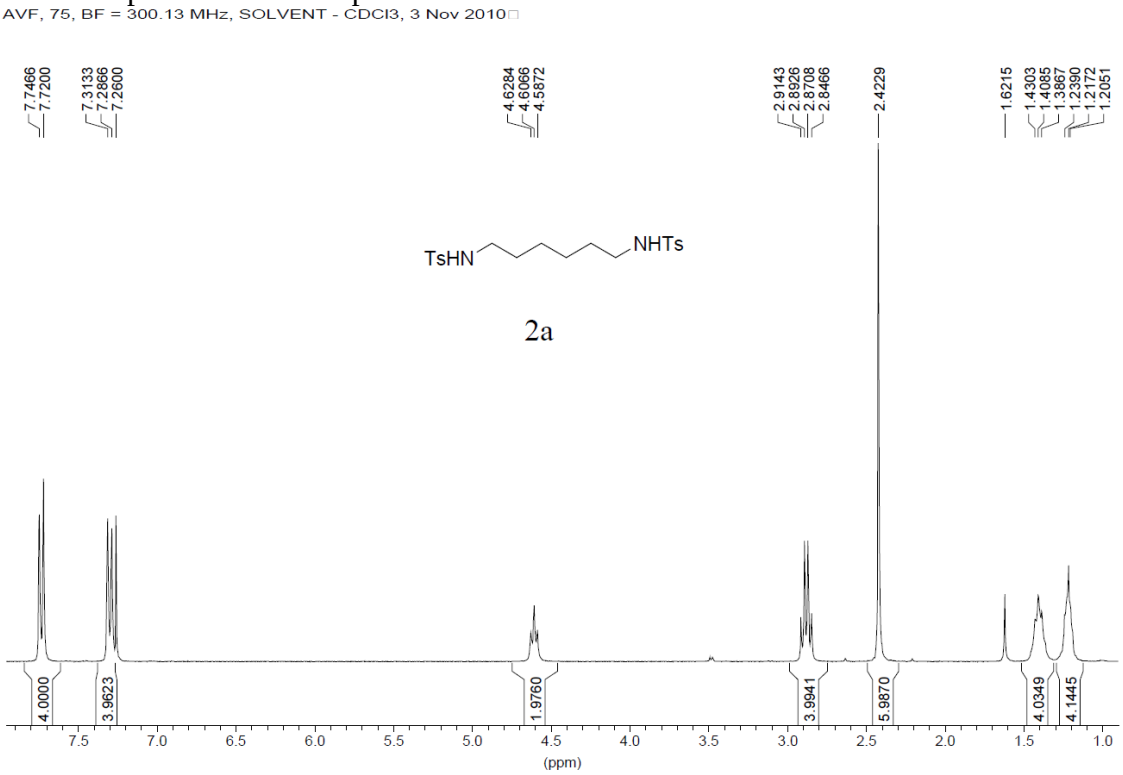

[4] All analyses were done by AsisChem Inc. (Watertown, MA)

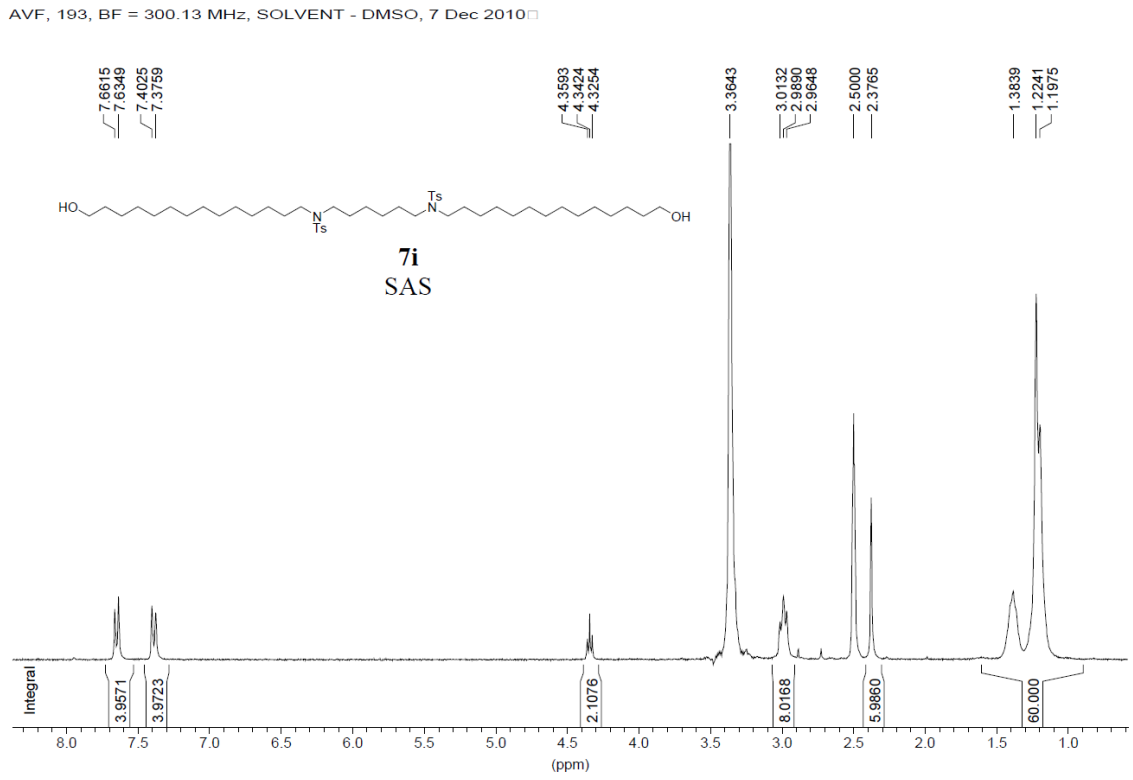
AVF, 193, BF = 300.13 MHz, SOLVENT - DMSO, 7 Dec 2010
7.6615
7.6349
7.4025
7.3759
4.3593
4.3424
4.3254
3.3643
3.0132
2.9890
2.9648
2.5000
2.3765
1.3839
1.2241
1.1975
HO
Ts
N
Ts
N
OH
7i
SAS
Integral
3.9571
3.9723
2.1076
8.0168
5.9860
60.000
8.0
7.5
7.0
6.5
6.0
5.5
5.0
4.5
4.0
3.5
3.0
2.5
2.0
1.5
1.0
(ppm)

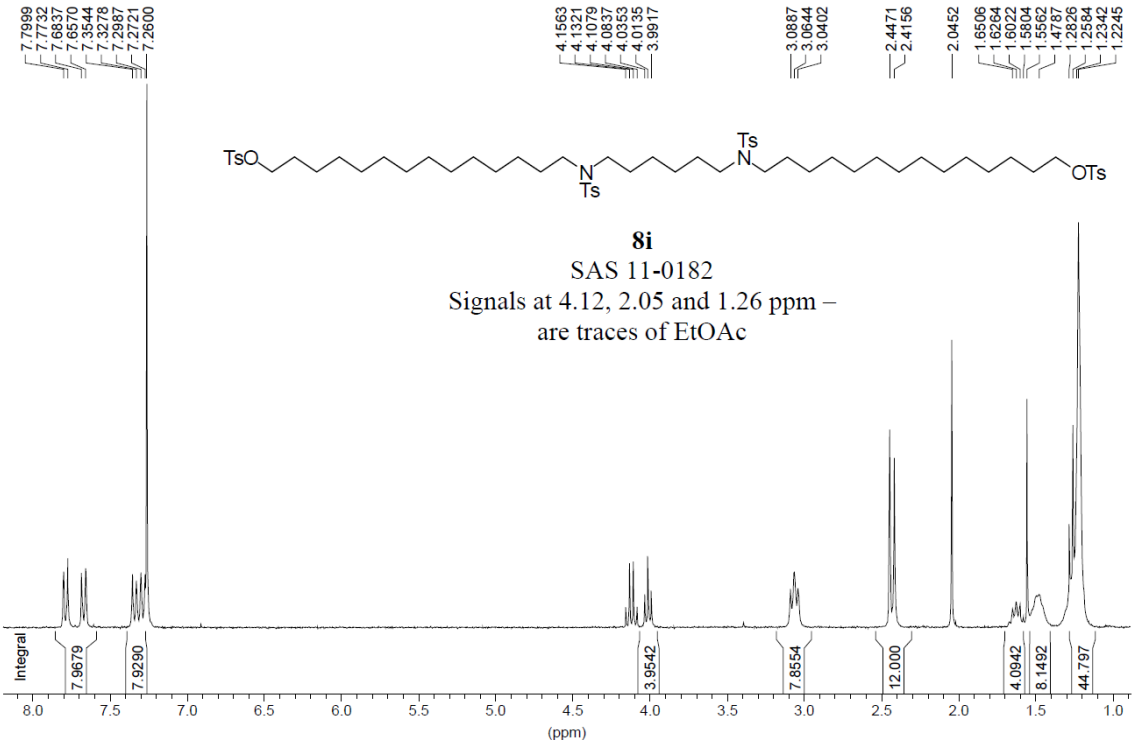
7.7999
7.7732
7.6837
7.6570
7.3544
7.3278
7.2987
7.2721
7.2600
4.1563
4.1321
4.1079
4.0837
4.0353
4.0135
3.9917
3.0887
3.0644
3.0402
2.4471
2.4156
2.0452
1.6506
1.6264
1.6022
1.5804
1.5562
1.4787
1.2826
1.2584
1.2342
1.2245
TsO
Ts
N
Ts
N
OTs
8i
SAS 11-0182
Signals at 4.12, 2.05 and 1.26 ppm –
are traces of EtOAc
Integral
7.9679
7.9290
3.9542
7.8554
12.000
4.0942
8.1492
44.797
8.0
7.5
7.0
6.5
6.0
5.5
5.0
4.5
4.0
3.5
3.0
2.5
2.0
1.5
1.0
(ppm)

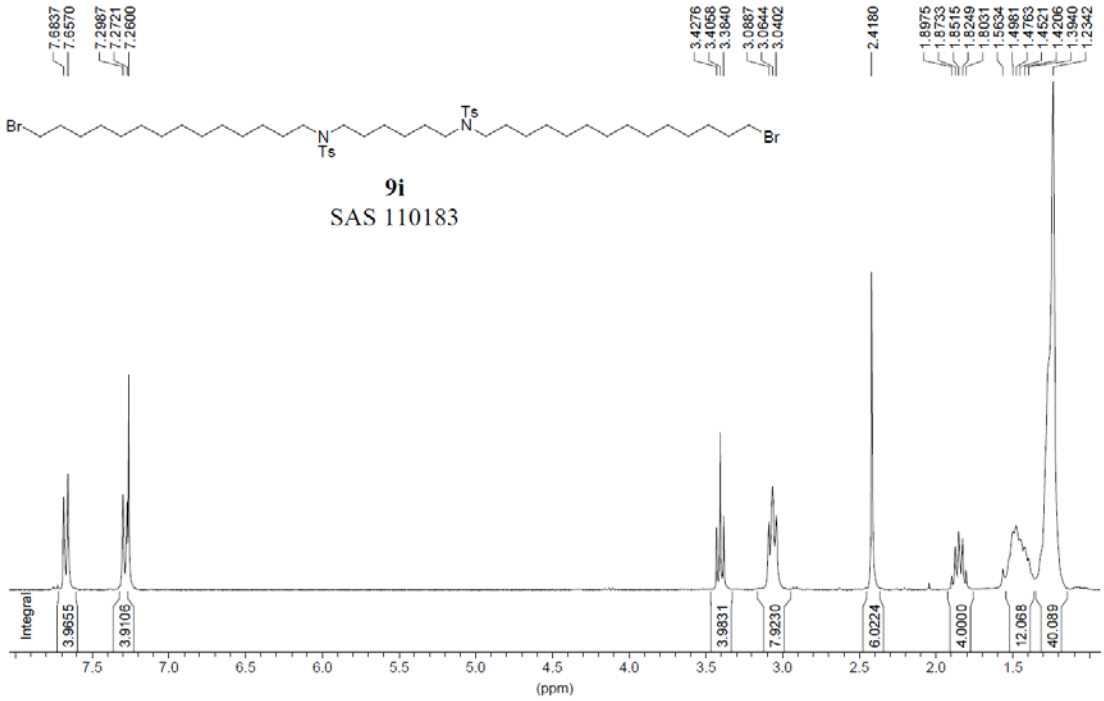

9i
SAS 110183

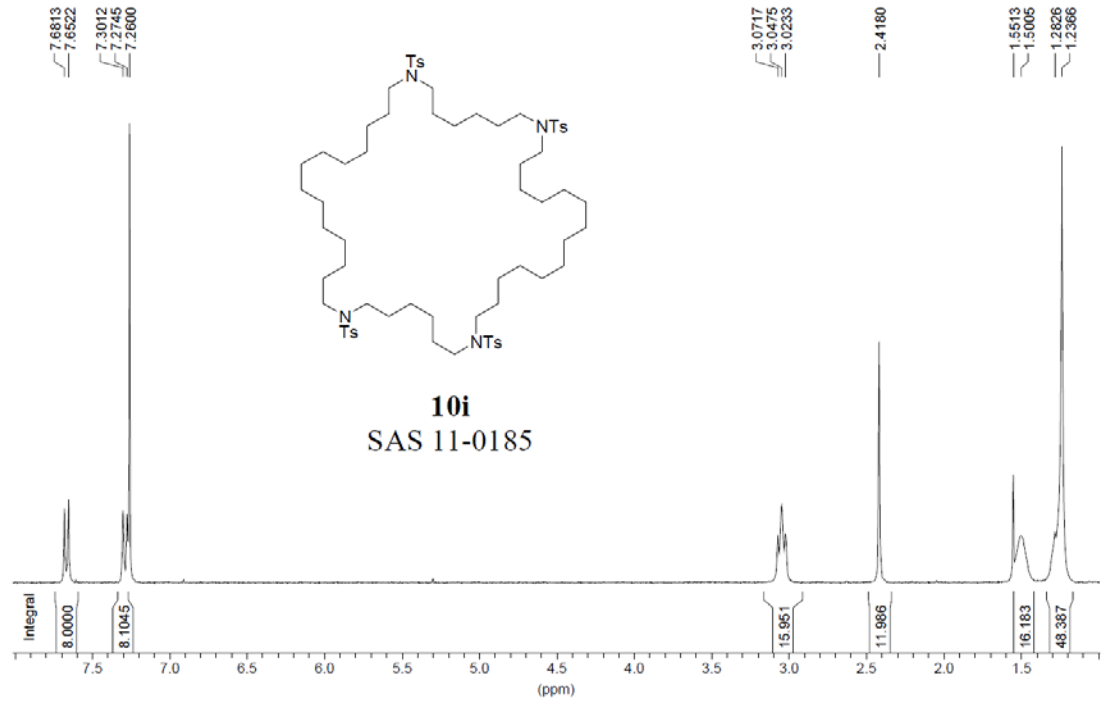

10i
SAS 11-0185

Mass spectrum of **10i**:

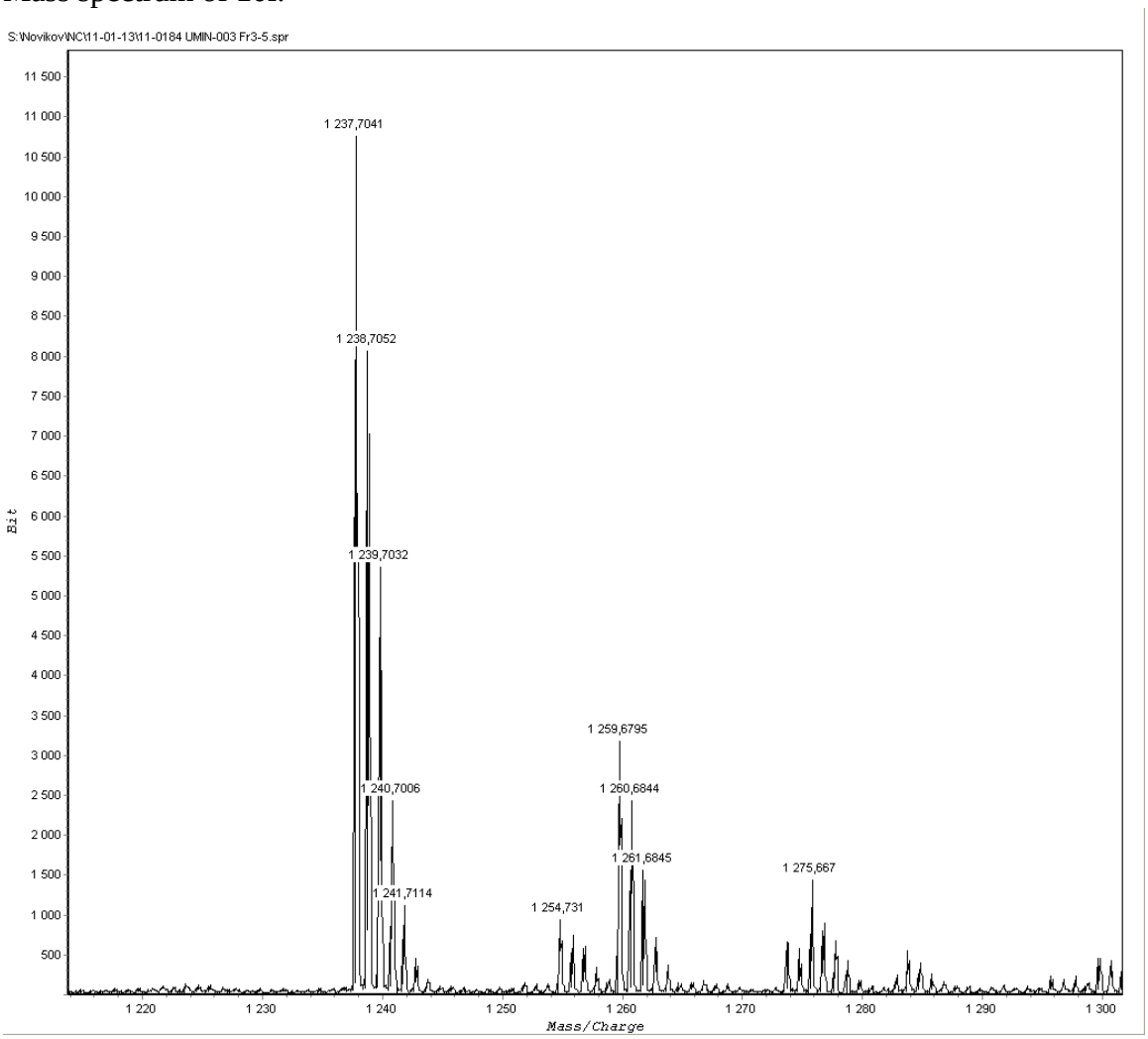

(M+H^+): Calculated – 1237.71; Found – 1237.7041
(M+NH_4^+): Calculated – 1254.74; Found – 1254.731
(M+Na^+): Calculated – 1259.69; Found – 1259.6795
(M+K^+): Calculated – 1275.67; Found – 1275.667

AVF, 296, BF = 300.13 MHz, SOLVENT - DMSO, 21 Jan 2011

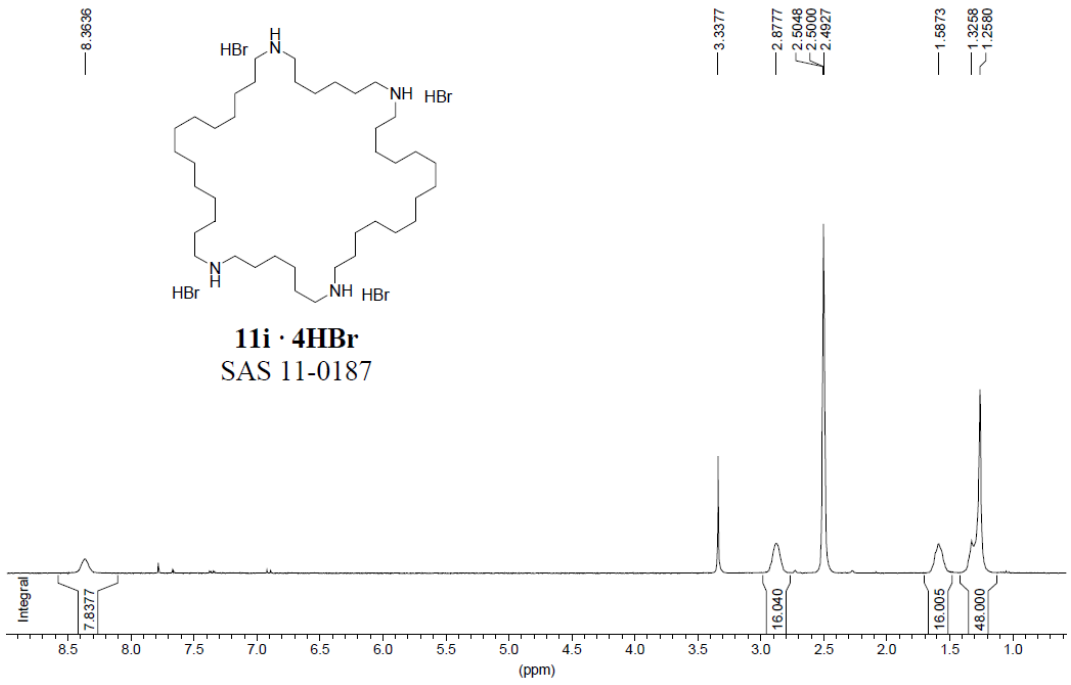

11i · 4HBr

SAS 11-0187

Mass spectrum of **11i · 4HBr:**

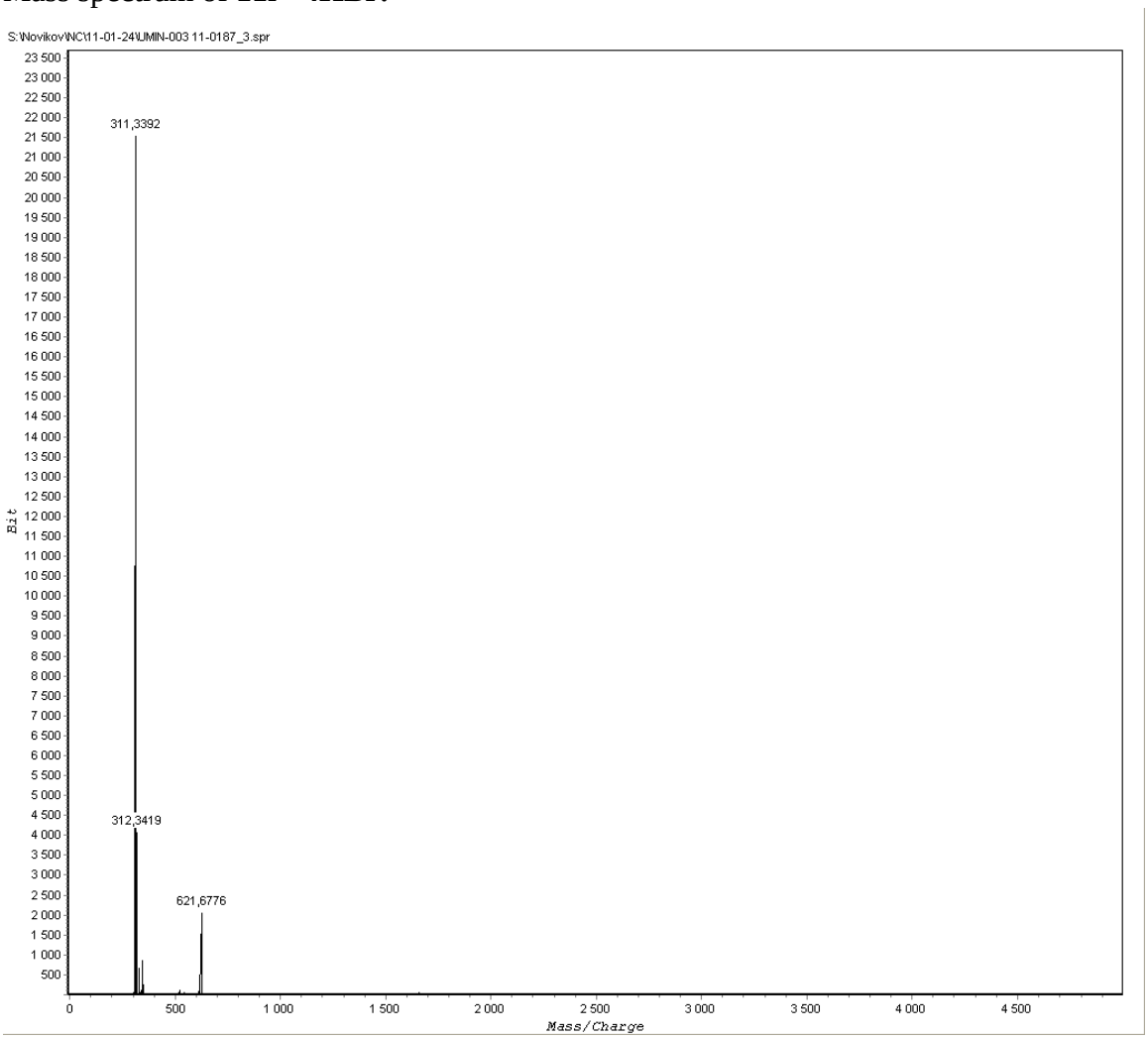

(M+H+): Calculated – 621.68; Found – 621.6776
(M+2H+): Calculated – 311.345; Found – 311.3392

AVF, 708, BF = 300.13 MHz, SOLVENT - CDCl3, 31 May 2011□

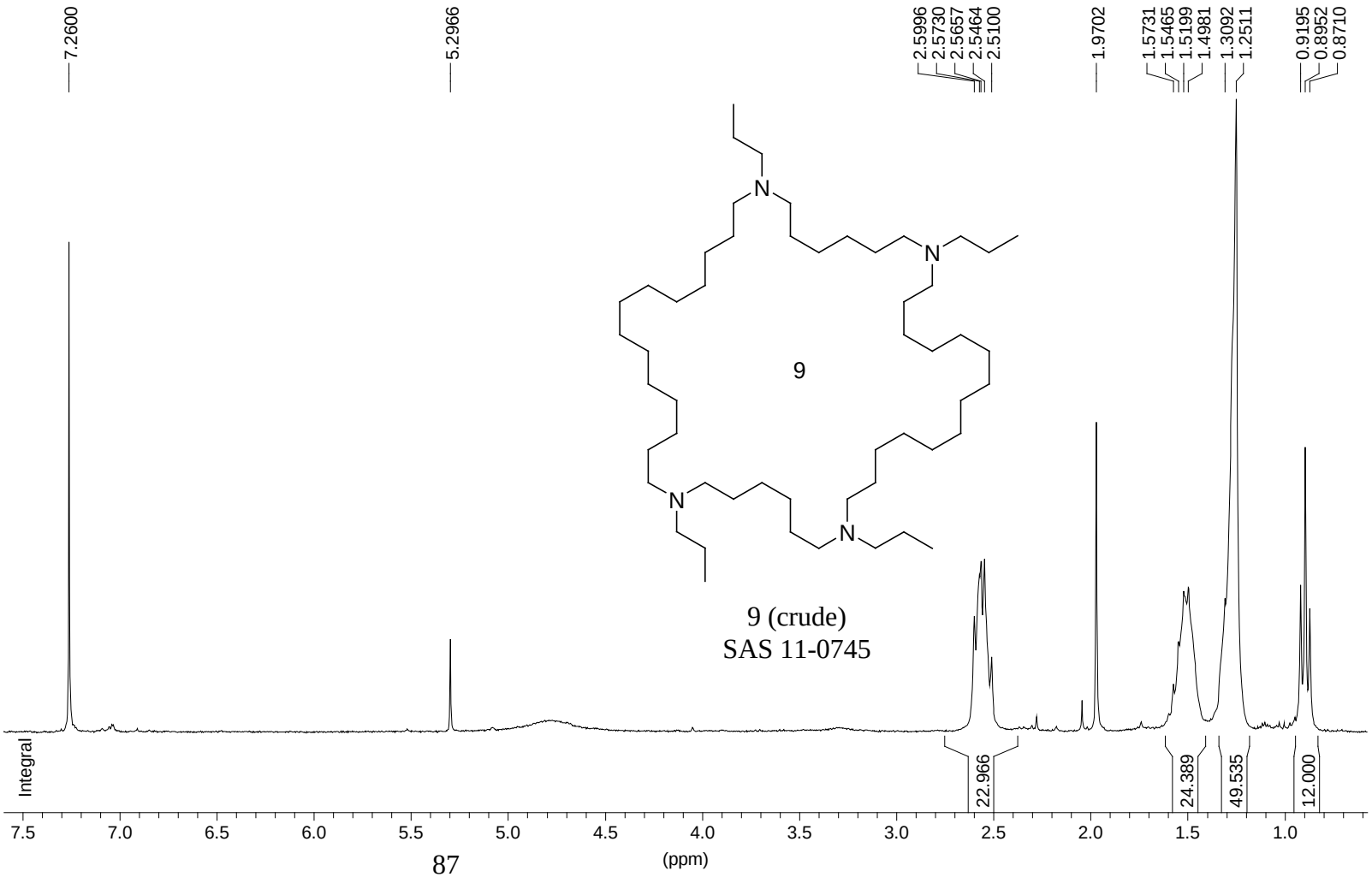

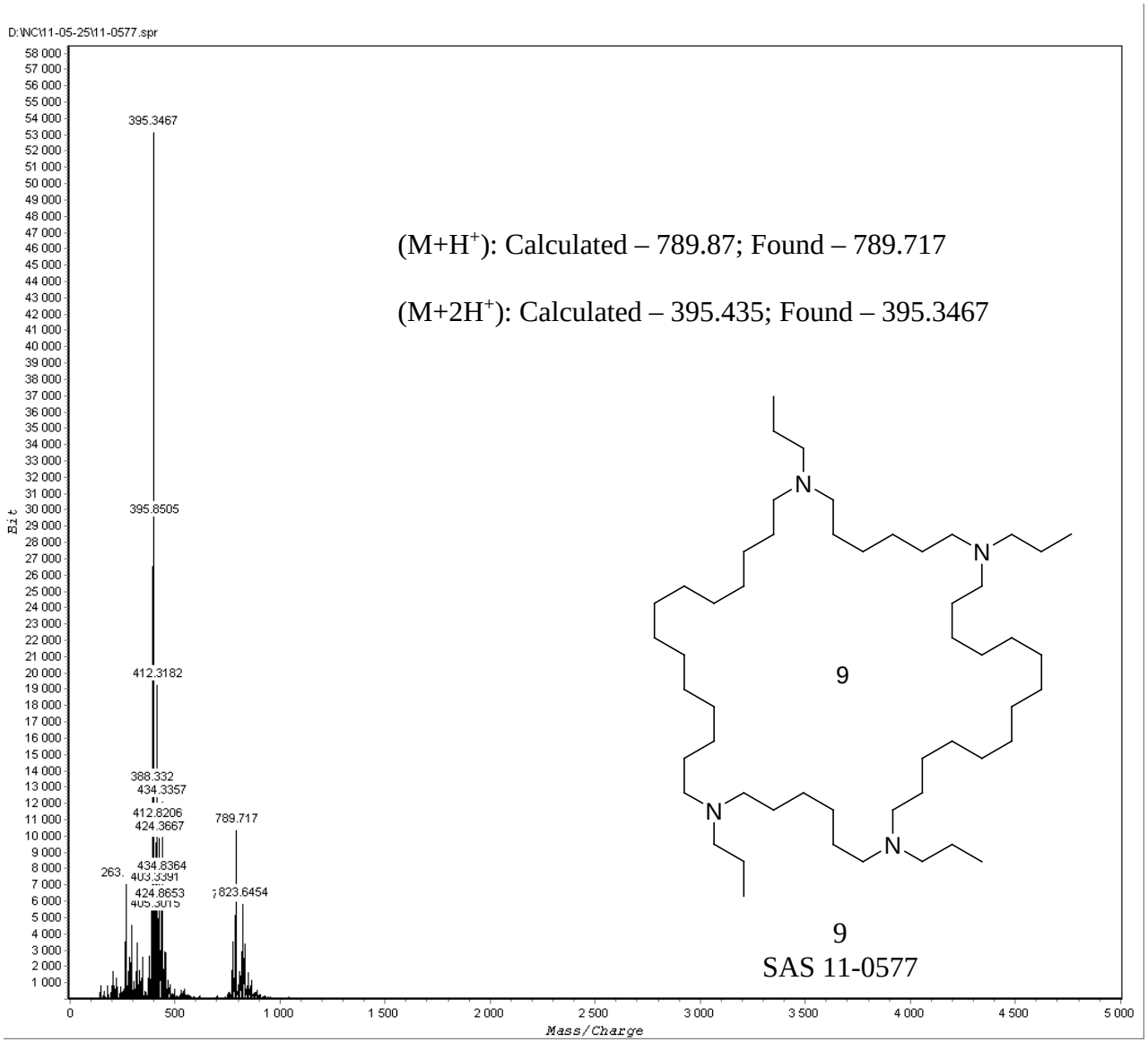
D:\NC\11-05-25\11-0577.spr
395.3467
395.8505
412.3182
388.332
434.3357
412.8206
424.3667
789.717
434.8364
263.
403.3391
424.8653
405.3015
823.6454
Abs
Mass/Charge
(M+H+): Calculated – 789.87; Found – 789.717
(M+2H+): Calculated – 395.435; Found – 395.3467
N
N
N
N
9
9
SAS 11-0577

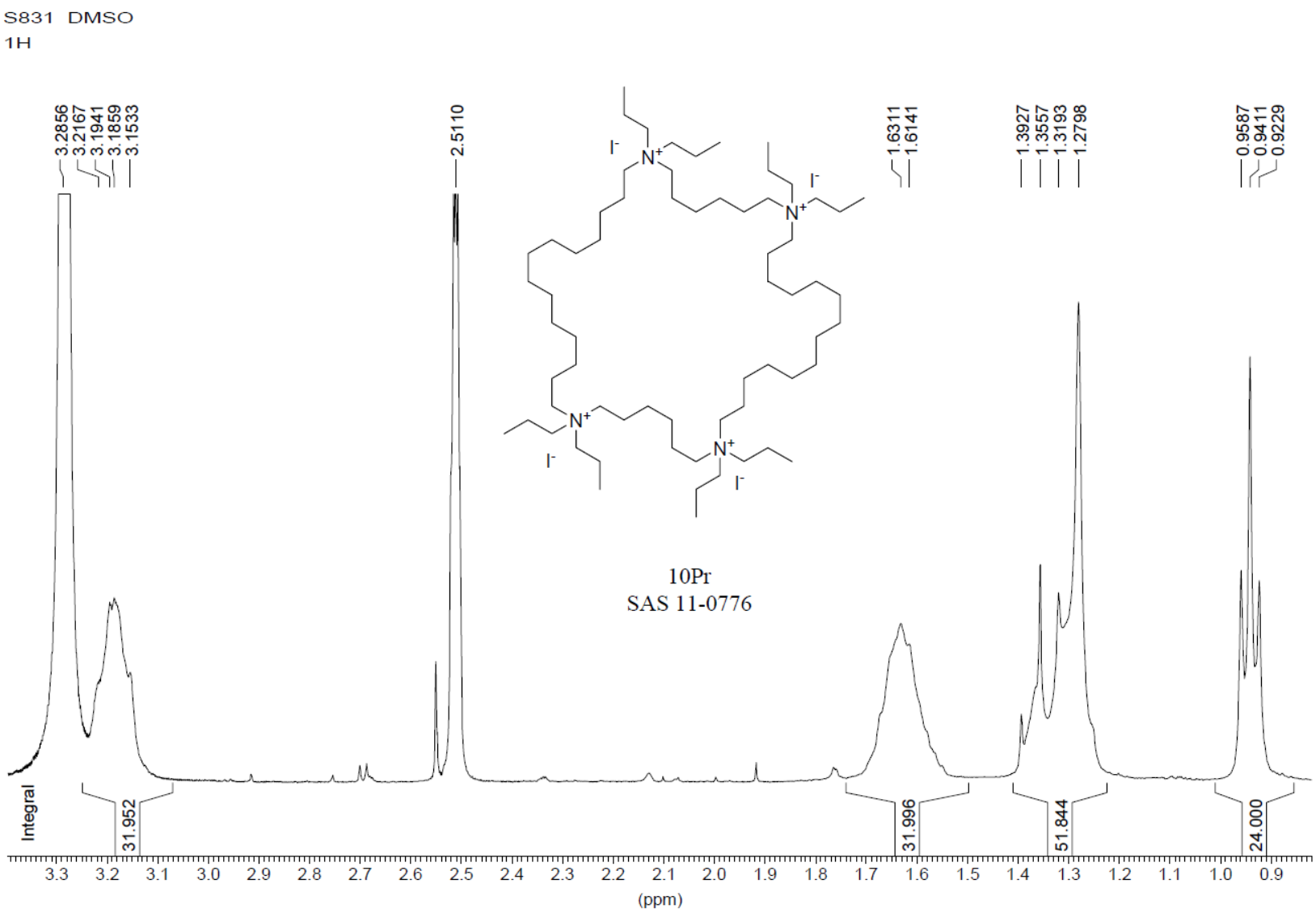
S831 DMSO
1H
3.2856
3.2167
3.1941
3.1859
3.1533
2.5110
1.6311
1.6141
1.3927
1.3557
1.3193
1.2798
0.9587
0.9411
0.9229
I-
N+
10Pr
SAS 11-0776
Integral
31.952
31.996
51.844
24.000
3.3 3.2 3.1 3.0 2.9 2.8 2.7 2.6 2.5 2.4 2.3 2.2 2.1 2.0 1.9 1.8 1.7 1.6 1.5 1.4 1.3 1.2 1.1 1.0 0.9
(ppm)

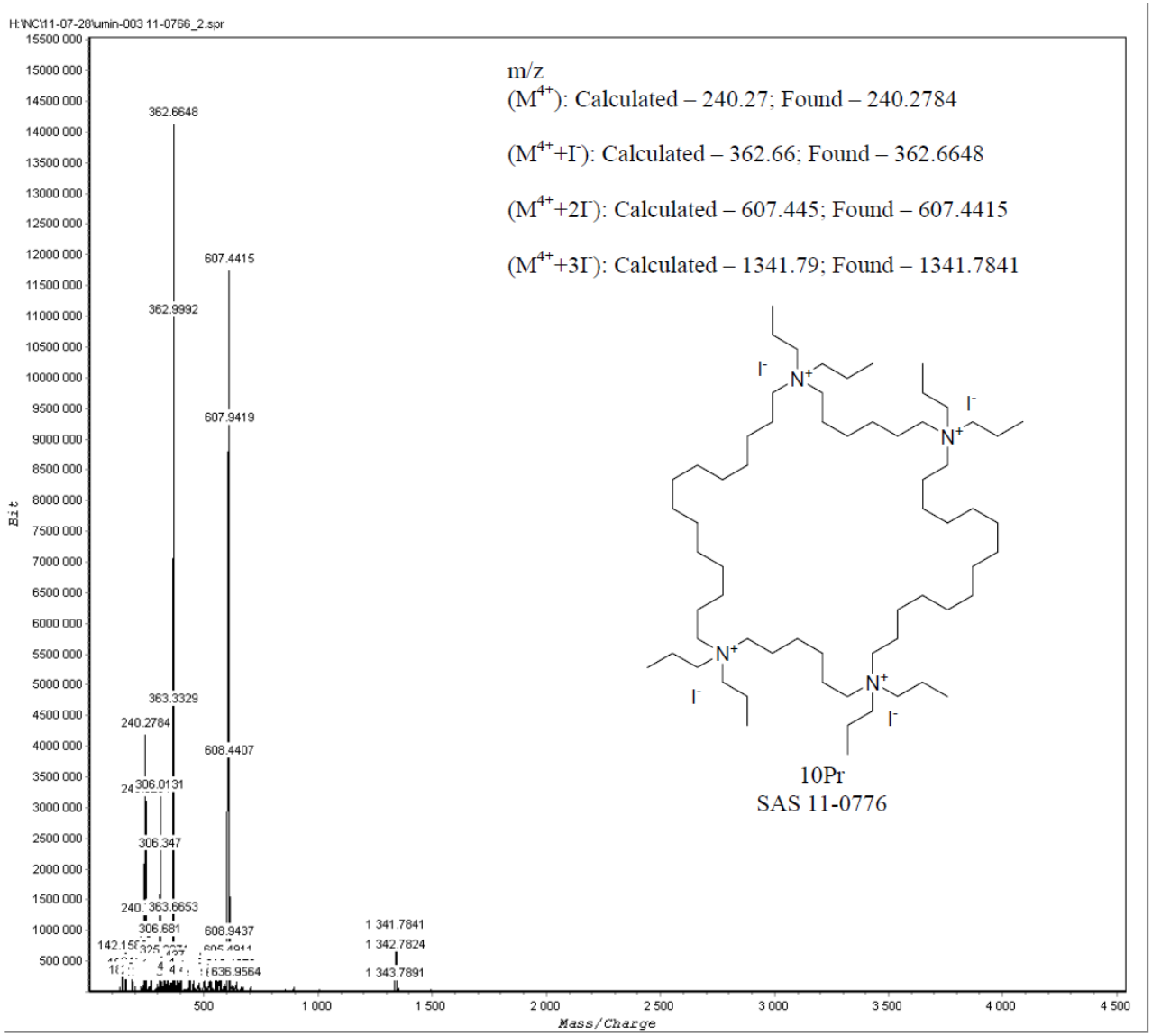
H:\NC\11-07-28\umin-003 11-0766_2.spr
m/z
(M4+): Calculated – 240.27; Found – 240.2784
(M4++I-): Calculated – 362.66; Found – 362.6648
(M4++2I-): Calculated – 607.445; Found – 607.4415
(M4++3I-): Calculated – 1341.79; Found – 1341.7841
10Pr
SAS 11-0776
Bit
Mass/Charge
362.6648
607.4415
362.9992
607.9419
363.3329
240.2784
608.4407
306.0131
306.347
363.6653
306.681
608.9437
1 341.7841
1 342.7824
1 343.7891
636.9564

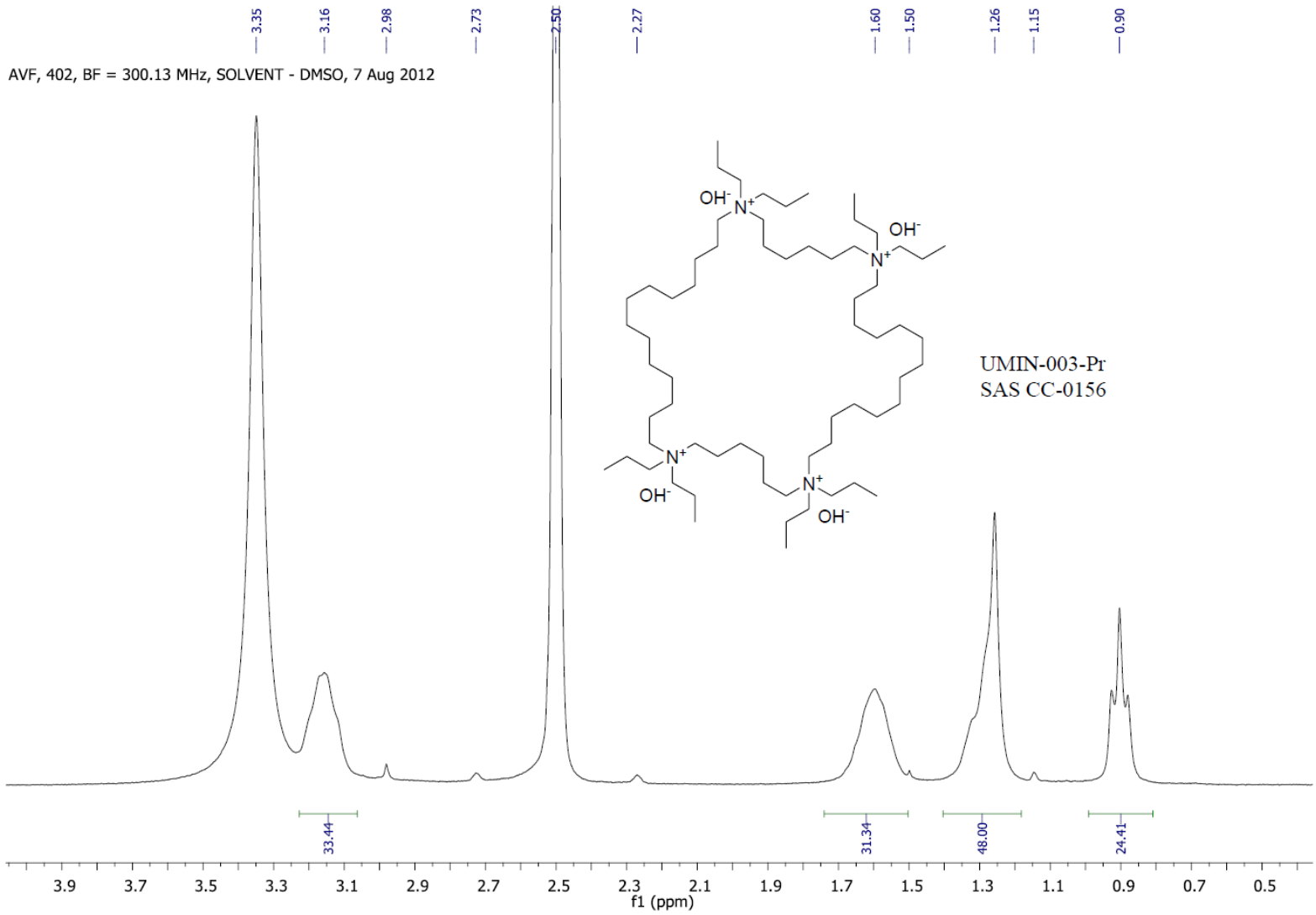
AVF, 402, BF = 300.13 MHz, SOLVENT - DMSO, 7 Aug 2012
3.35
3.16
2.98
2.73
2.50
2.27
1.60
1.50
1.26
1.15
0.90
OH-
N+
OH-
N+
N+
OH-
N+
OH-
UMIN-003-Pr
SAS CC-0156
33.44
31.34
48.00
24.41
3.9
3.7
3.5
3.3
3.1
2.9
2.7
2.5
2.3
2.1
1.9
1.7
1.5
1.3
1.1
0.9
0.7
0.5
f1 (ppm)

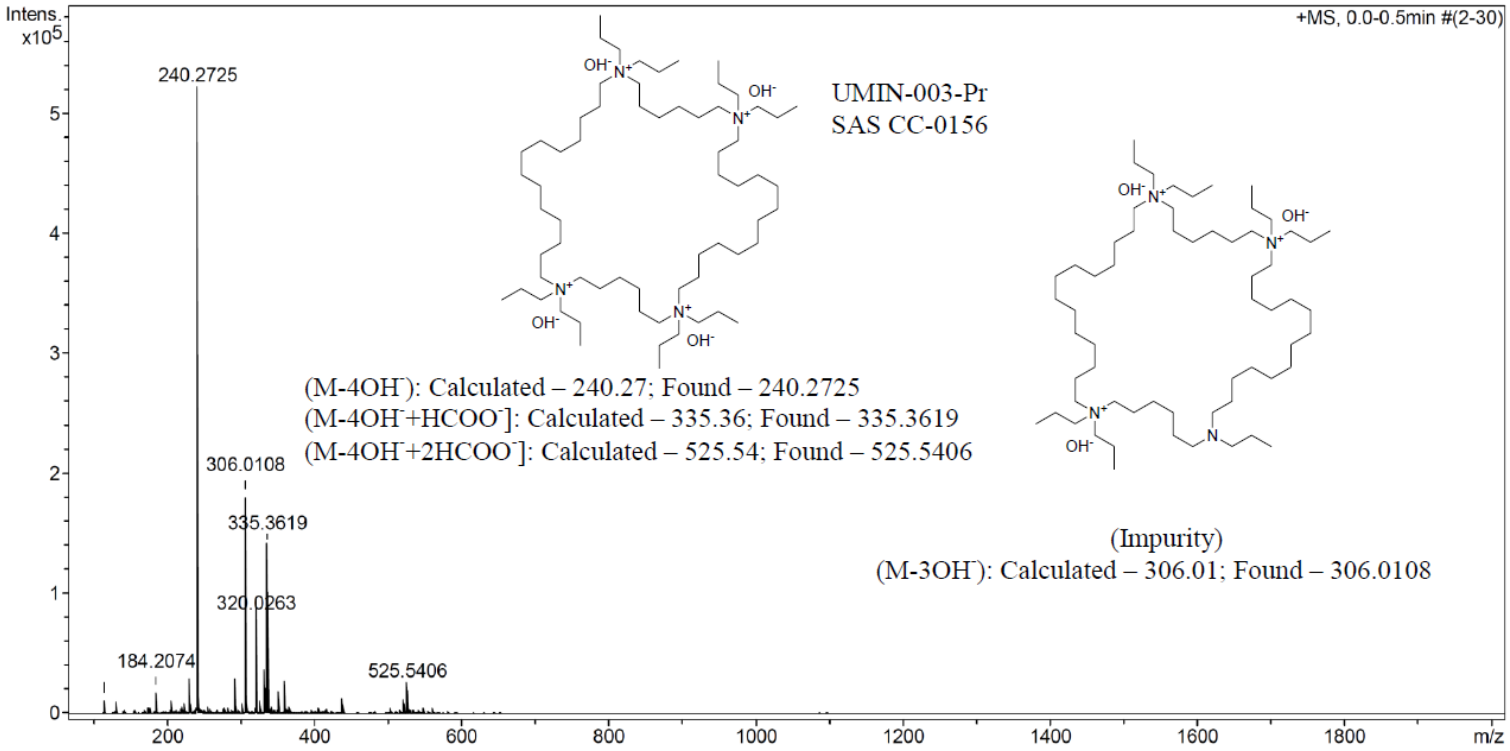
Intens.
x10^5
+MS, 0.0-0.5min #(2-30)
240.2725
306.0108
335.3619
320.0263
184.2074
525.5406
m/z
UMIN-003-Pr
SAS CC-0156
(M-4OH-): Calculated – 240.27; Found – 240.2725
(M-4OH-+HCOO-]: Calculated – 335.36; Found – 335.3619
(M-4OH-+2HCOO-]: Calculated – 525.54; Found – 525.5406
(Impurity)
(M-3OH-): Calculated – 306.01; Found – 306.0108

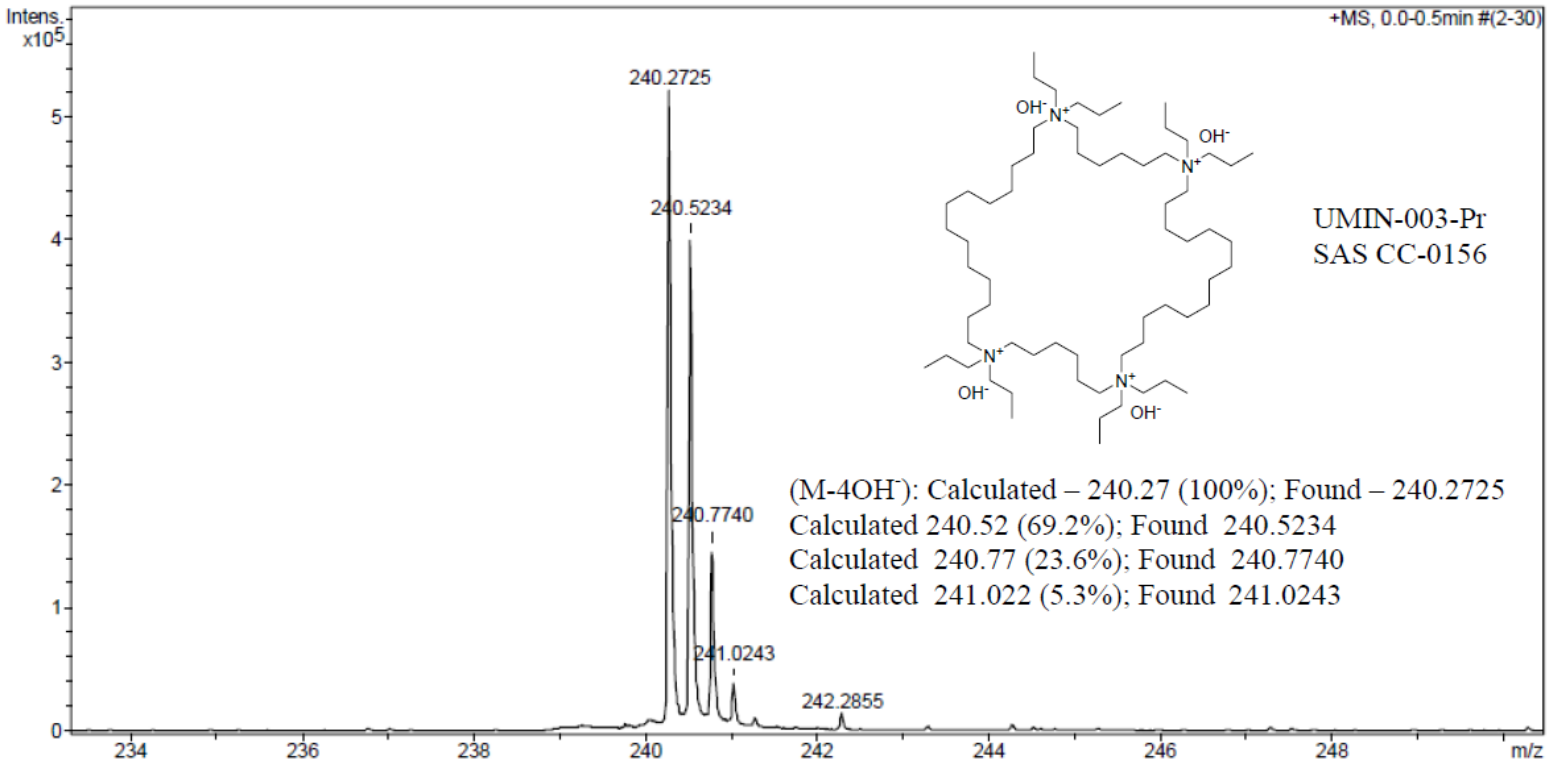
Intens.
x10^5
+MS, 0.0-0.5min #(2-30)
240.2725
240.5234
240.7740
241.0243
242.2855
UMIN-003-Pr
SAS CC-0156
(M-4OH-): Calculated – 240.27 (100%); Found – 240.2725
Calculated 240.52 (69.2%); Found 240.5234
Calculated 240.77 (23.6%); Found 240.7740
Calculated 241.022 (5.3%); Found 241.0243
m/z

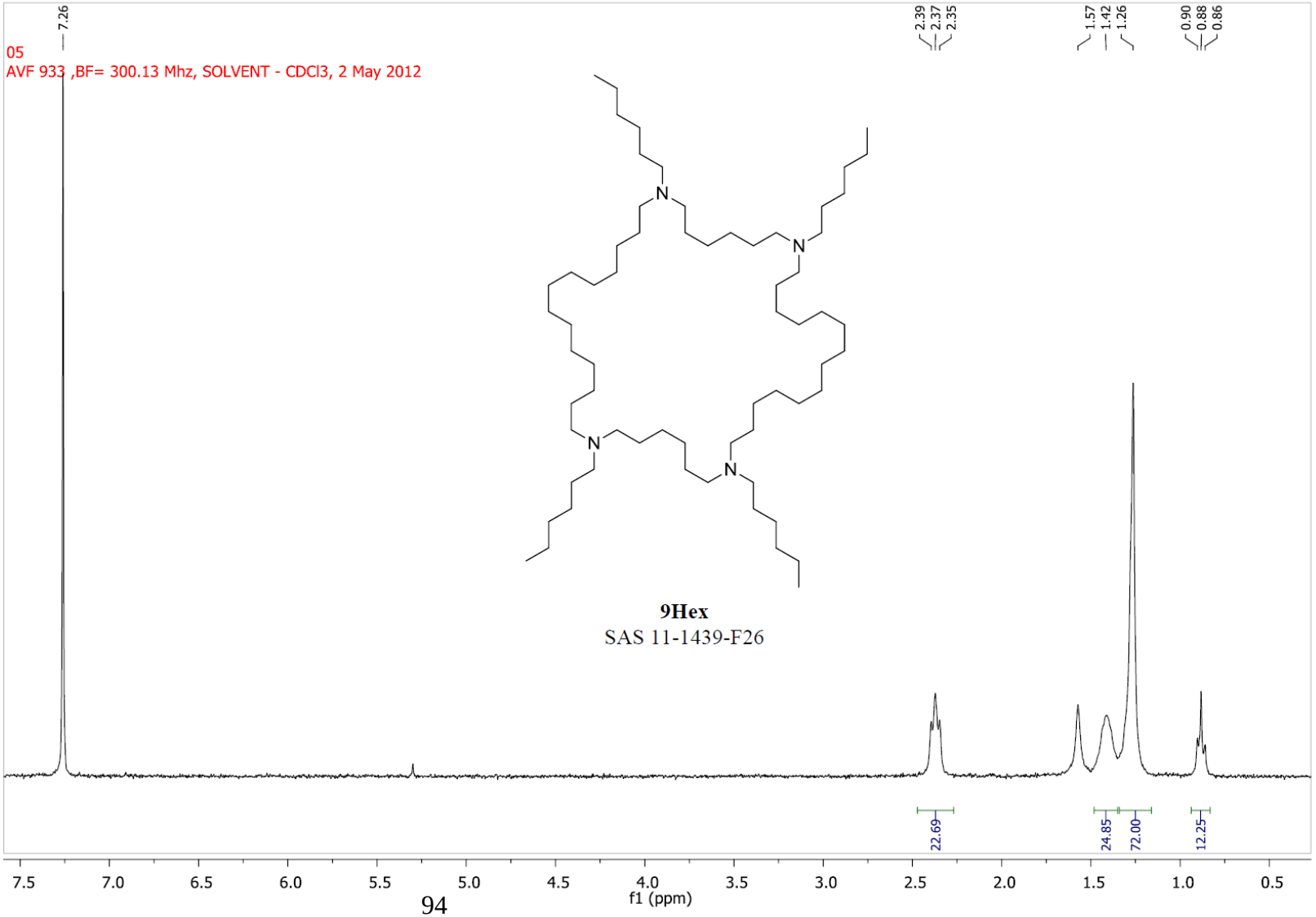
05
AVF 933 ,BF= 300.13 Mhz, SOLVENT - CDCl3, 2 May 2012
7.26
2.39
2.37
2.35
1.57
1.42
1.26
0.90
0.88
0.86
N
N
N
N
9Hex
SAS 11-1439-F26
22.69
24.85
72.00
12.25
7.5
7.0
6.5
6.0
5.5
5.0
4.5
4.0
3.5
3.0
2.5
2.0
1.5
1.0
0.5
f1 (ppm)

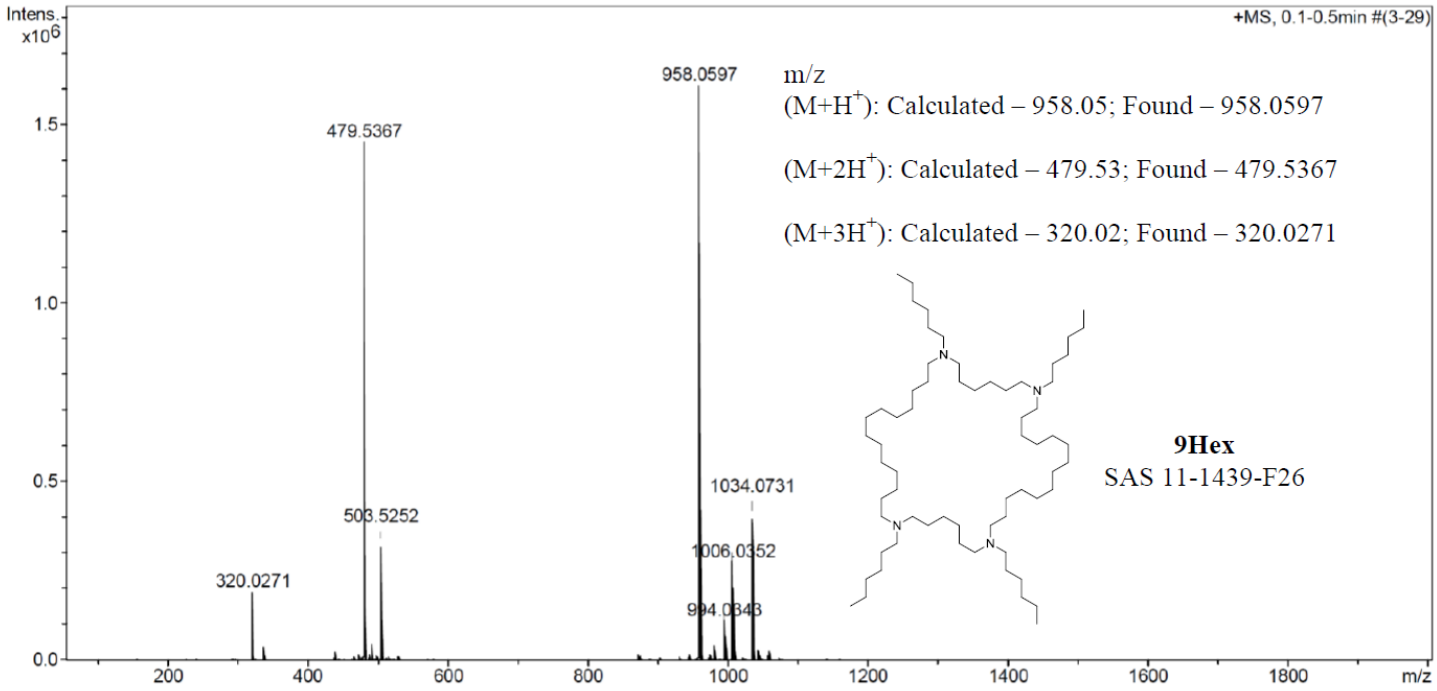
Intens.
x10^6
+MS, 0.1-0.5min #(3-29)
1.5
1.0
0.5
0.0
958.0597
479.5367
503.5252
320.0271
1034.0731
1006.0352
994.0343
200
400
600
800
1000
1200
1400
1600
1800
m/z
m/z
(M+H+): Calculated – 958.05; Found – 958.0597
(M+2H+): Calculated – 479.53; Found – 479.5367
(M+3H+): Calculated – 320.02; Found – 320.0271
N
N
N
N
9Hex
SAS 11-1439-F26

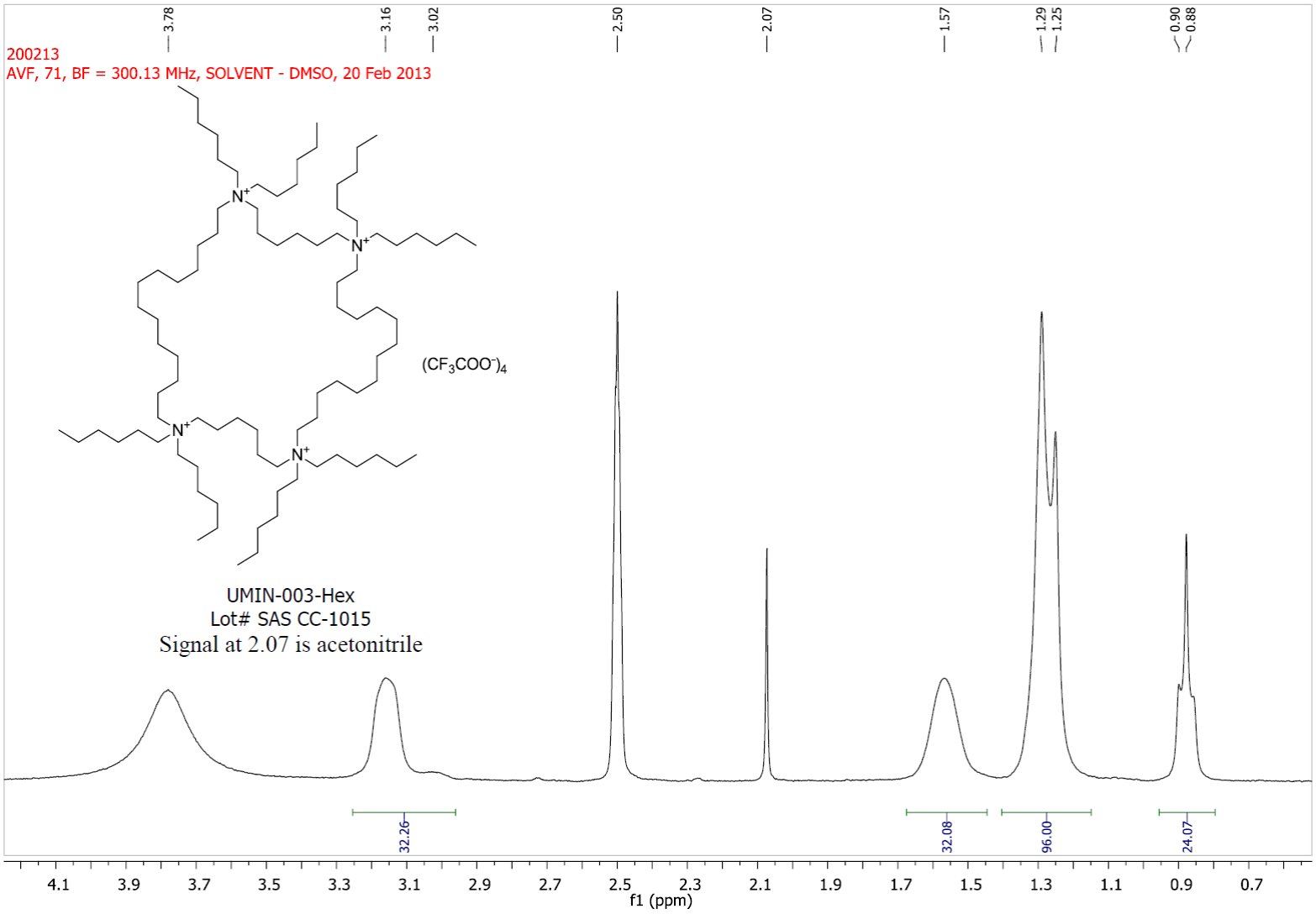
3.78
3.16
3.02
2.50
2.07
1.57
1.29
1.25
0.90
0.88
200213
AVF, 71, BF = 300.13 MHz, SOLVENT - DMSO, 20 Feb 2013
$(CF_3COO^-)_4$
UMIN-003-Hex
Lot# SAS CC-1015
Signal at 2.07 is acetonitrile
32.26
32.08
96.00
24.07
4.1
3.9
3.7
3.5
3.3
3.1
2.9
2.7
2.5
2.3
2.1
1.9
1.7
1.5
1.3
1.1
0.9
0.7
f1 (ppm)

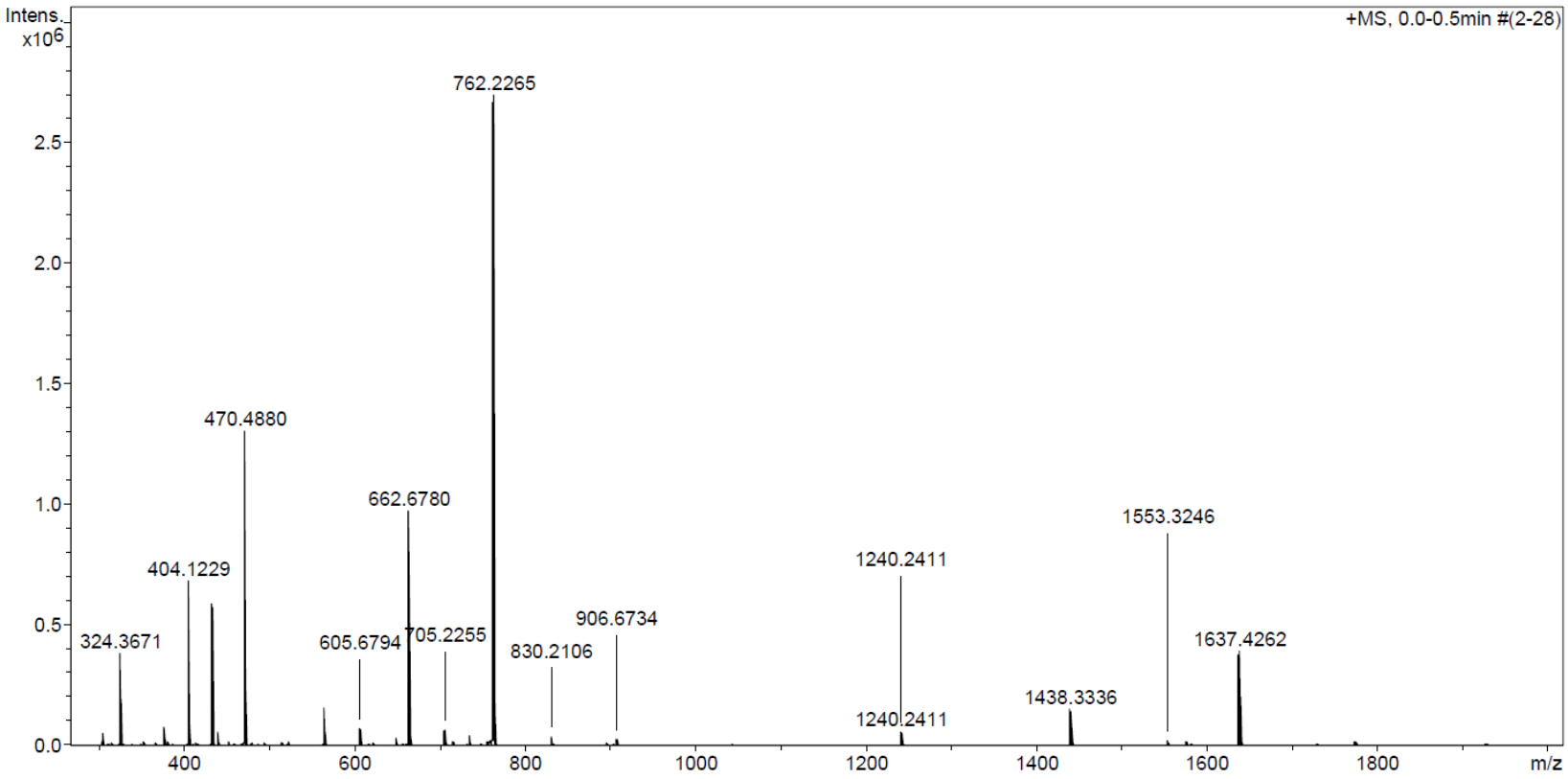
Intens.
x10^6
+MS, 0.0-0.5min #(2-28)
762.2265
470.4880
662.6780
1553.3246
404.1229
1240.2411
906.6734
324.3671
605.6794
705.2255
830.2106
1637.4262
1438.3336
1240.2411
2.5
2.0
1.5
1.0
0.5
0.0
400
600
800
1000
1200
1400
1600
1800
m/z

Appendix II: Technical drawings of the reactor array

The drawings shown here is a reactor array with 38 identical wells. However, the number of wells can vary according to the needs.

Part 1: vessel (material: PTFE, total: 38)

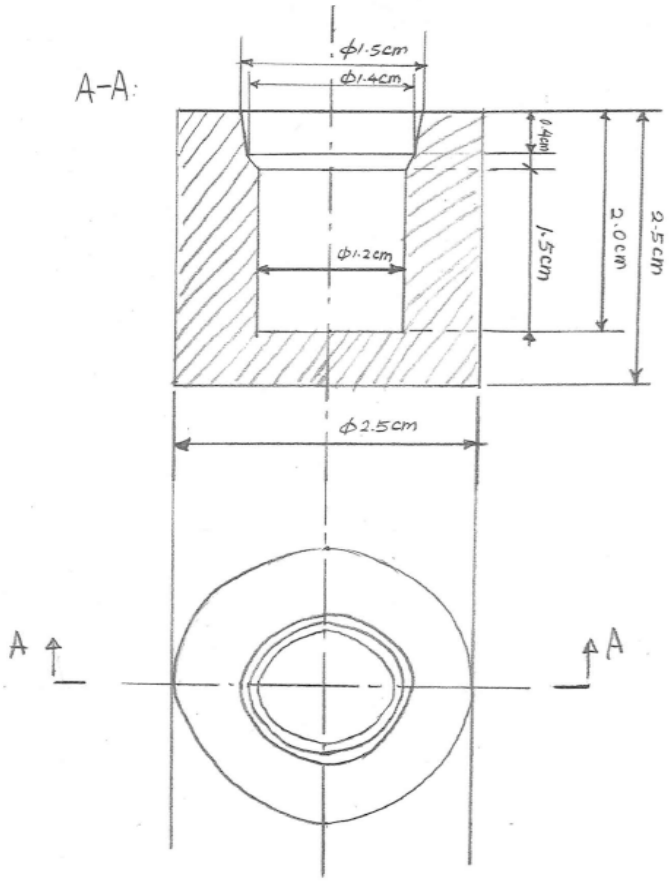

Part 2: vessel cap (material: PTFE, total: 38)

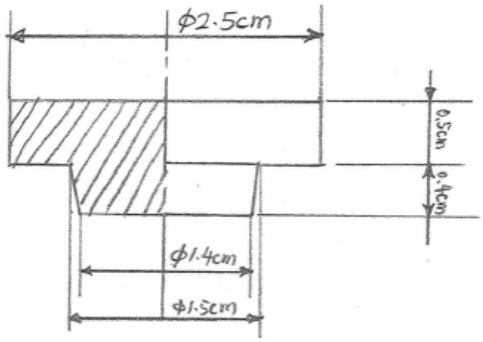

Part 3: base with 38 identical wells. (material: stainless steel, total: 1)

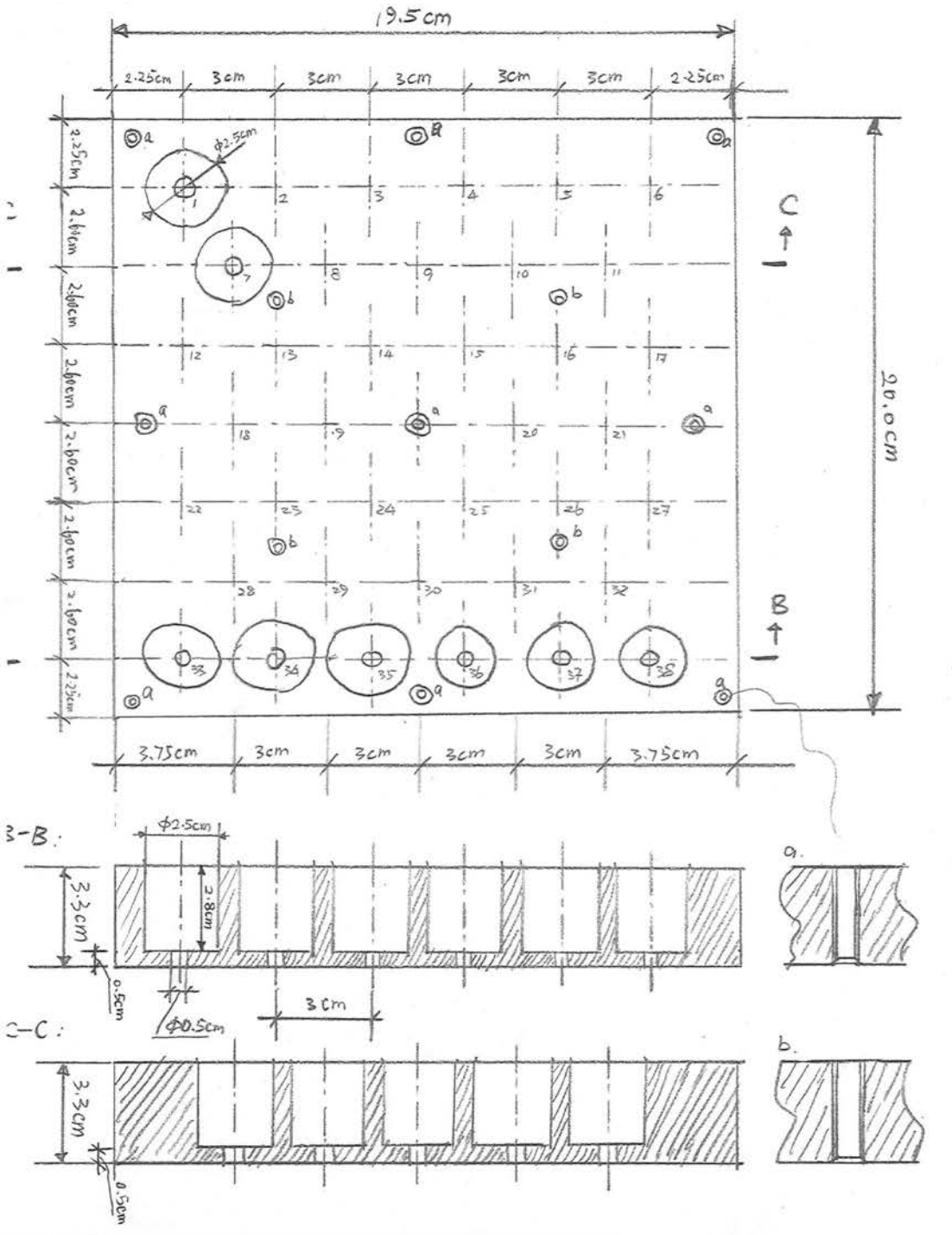

Part 4: lid (material: stainless steel, total: 1)

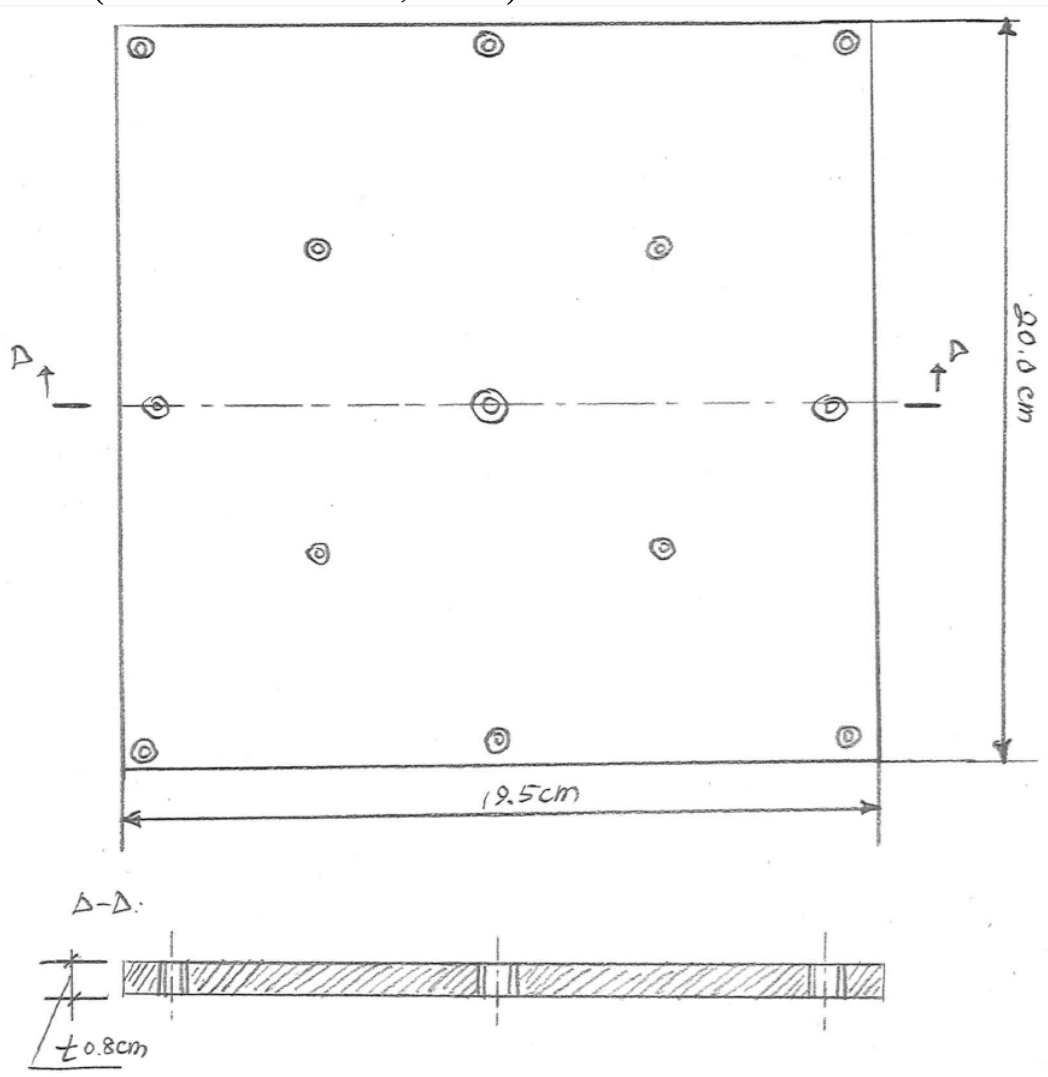

Part 5: extractor (materials: wood, PVC or LDPE, total: 1)

The extractor is used to remove all the vessels from the array. This is an optional part.

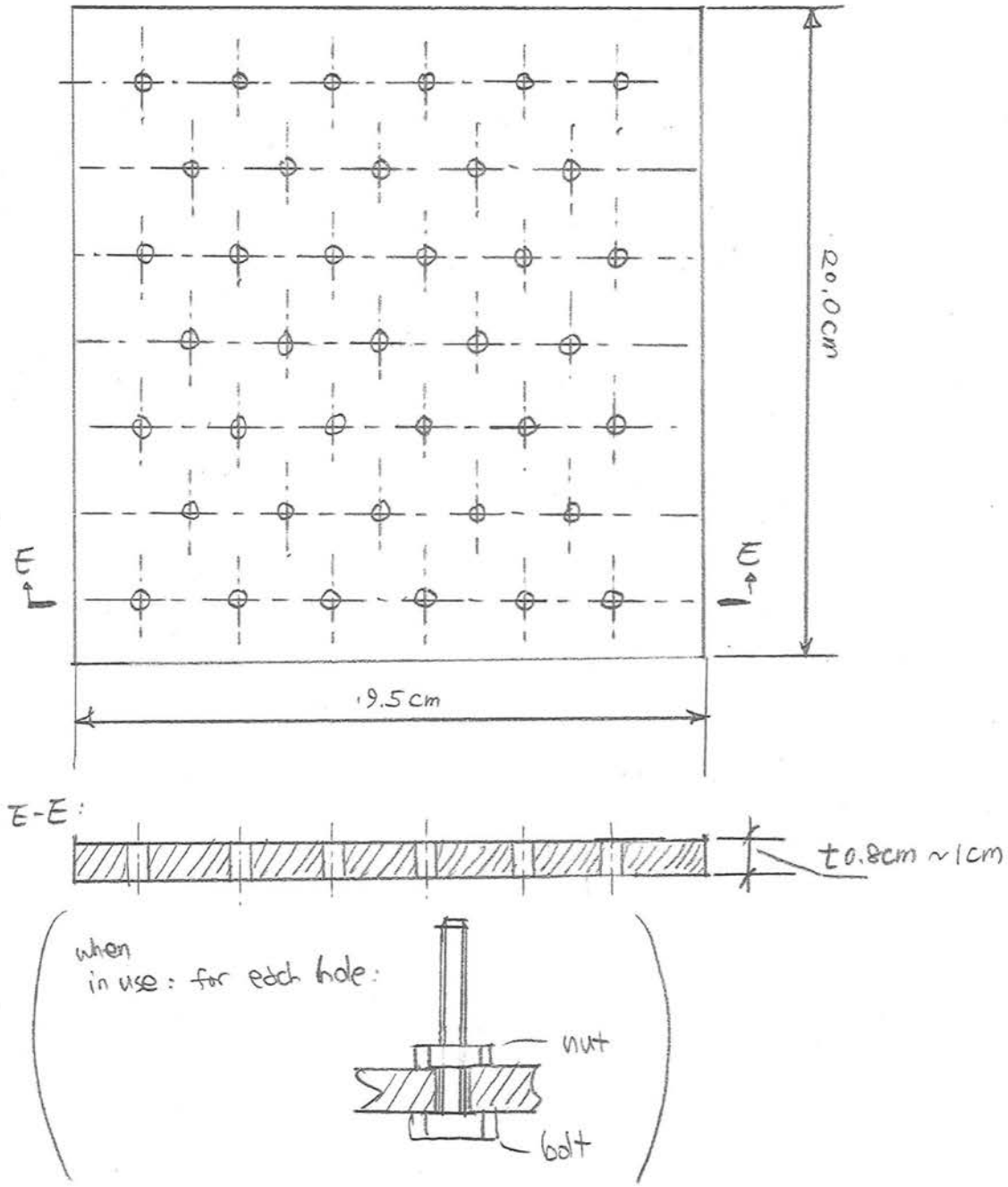

Chapter 5 Preparation of thin films of lamellar zeolite[5]

5.1 Introduction

A new lamellar zeolite with MFI layer structure and its pillared derivative were discovered recently by using a bifunctional structure-directing agent (SDA)[76, 97]. The synthetic approach used not only expands the range of available layered materials with zeolitic layers[11, 98], but also suggests a general strategy for the synthesis of zeolitic layers. Our interest in these materials stems from their potential for the formation of thin films and membranes[3, 98-99]. Synthetic approaches based on growth from relatively dilute clear sols[100] and on steam-assisted crystallization (SAC)[101] have proven beneficial for the development of film deposition process. For this reason, we decided to investigate the applicability of clear sol synthesis and SAC methods for the formation of lamellar MFI. Here, we report our initial findings on synthesis of layered silicalite-1 starting from clear sols.

In the reported synthesis[76, 97], the appearance of lamellar MFI is preceded by a hexagonal surfactant/silica mesophase which transforms to a lamellar one. Neither one exhibits detectable crystalline order in the silica domains. Here, we first show that the amorphous hexagonal to amorphous lamellar to MFI lamellar transformation can take place within distinct colloidal particles. Based on these observations we developed an SAC procedure which can be used to form intergrown coatings of lamellar MFI.

[5] Results presented in this chapter is published in: X. Y. Zhang, M. Tsapatsis, Micropor. Mesopor. Mat. 2011, 138, 239. Contents from the above publication are reprinted with permission from Elsevier.

5.2 Experimental methods

The linear bifunctional structure-directing agent ($(C_{22}H_{45}\text{-}N(CH_3)_2\text{-}C_6H_{12}\text{-}N(CH_3)_2\text{-}C_6H_{13})Br_2$, denoted as $C_{22\text{-}6\text{-}6}Br_2$) was synthesized following Choi et al. [76, 97] The as-synthesized diammonium salt $C_{22\text{-}6\text{-}6}Br_2$ was ion-exchanged over IONAC NA-38 OH^- form ion-exchange resin (J. T. Baker), resulting in an aqueous solution of $C_{22\text{-}6\text{-}6}(OH)_2$.

To prepare the clear sols, tetraethyl orthosilicate (TEOS, Aldrich) was added to an aqueous solution of $C_{22\text{-}6\text{-}6}(OH)_2$, allowing TEOS to hydrolyze for 24 hours, resulting in a molar composition 20 SiO_2 : 4.5 $C_{22\text{-}6\text{-}6}(OH)_2$: 8100 H_2O : 80 EtOH. This synthesis sol was sealed in a Teflon-lined stainless steel autoclave and heated for desired time (3 hours, 18 hours, 48 hours, 96 hours, etc.) in a pre-heated oven operating at 135^oC.

To obtain mesoporous silica particles at various stages of evolution as well as lamellar MFI, the suspension obtained from hydrothermal synthesis was washed with water by repeated centrifugation and decanting of the supernatant until a suspension with pH<8 was obtained. Centrifugation was performed with RCF=1753 for 10 min (25^oC) in Corning 50 mL conical centrifuge tubes.

For coating glass slides with mesoporous silica particles, 100 µL of the suspension before washing was spread over a 1 cm x 1 cm glass slide (which was previously rinsed in 2% hydrofluoric acid for 30 s) and dried at 70^oC.

Steam-assisted crystallization (SAC) was achieved following the work by Jacobsen and coworkers[55, 102] and Stein and coworkers[103]: A glass vial containing dried mesoporous silica particles or a mesoporous silica particle-coated glass slide was placed in a stainless steel autoclave where water was present outside the glass vial. The autoclave was heated at 135^oC for 10 days.

The samples for transmission electron microscopy (TEM) studies were prepared by applying a few droplets of the washed suspension onto a copper grid coated with holey carbon film (Ted Pella Inc.). The grid was then allowed to air-dry at room temperature. TEM imaging was performed on an FEI Tecnai G^2 F30 TEM operating at 300 kV. All TEM images were captured using a CCD camera. Scanning electron microscopy (SEM) was performed on a JEOL JSM-6700F with acceleration voltage 1 kV ~ 3 kV without coating the samples. Small-angle X-ray diffraction patterns were collected using a Bruker-AXS D5005 X-ray diffractometer (Cu Kα radiation). Wide-angle X-ray diffraction patterns were collected using a Bruker-AXS D5005 X-ray diffractometer (Cu Kα radiation) and a Bruker-AXS D8 Advance X-ray diffractometer (Cu Kα radiation).

5.3 Results and discussion

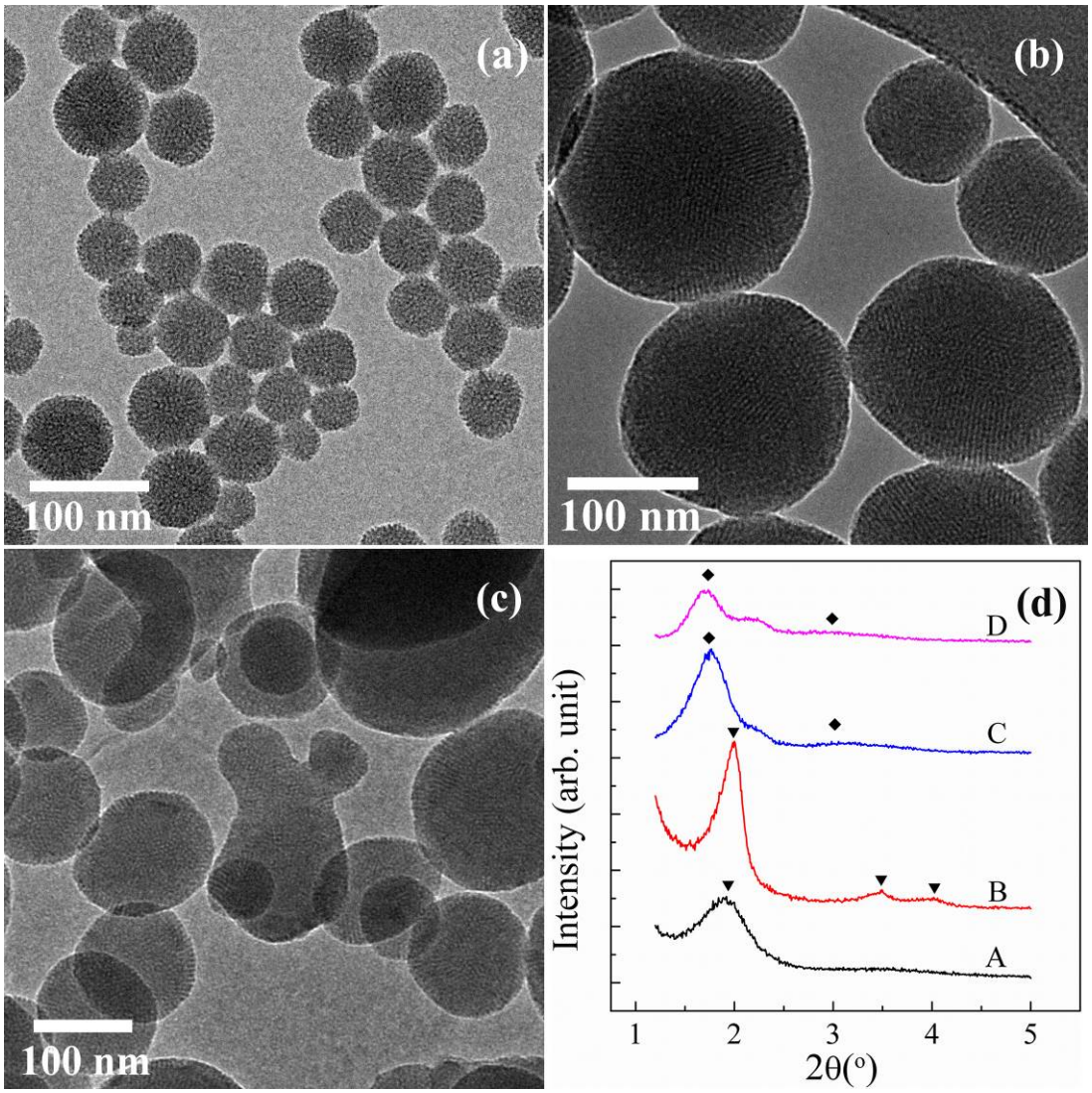

Figure 5-1 Mesoporous silica nanoparticles formed after heating a clear sol with composition 20 SiO_2 : 4.5 $C_{22\text{-}6\text{-}6}(OH)_2$: 8100 H_2O : 80 EtOH at 135°C for (a) 3 hours; (b) 18 hours; (c) 48 hours. (d) X-ray diffraction patterns of the mesoporous silica nanoparticles after heating at 135°C for A: 3 hours; B: 18 hours; C: 48 hours; D: 96 hours.

A suspension of nearly spherical particles can be obtained by heating the clear synthesis sol at 135°C for 3 hours. Their size range is 40 nm ~ 100 nm and they exhibit a disordered mesostructure as shown by TEM (Fig. 5-1(a)). Suspensions with increased

polydispersity are obtained after 18 hours (Fig. 5-1(b)) while after 48 hours mesostructured

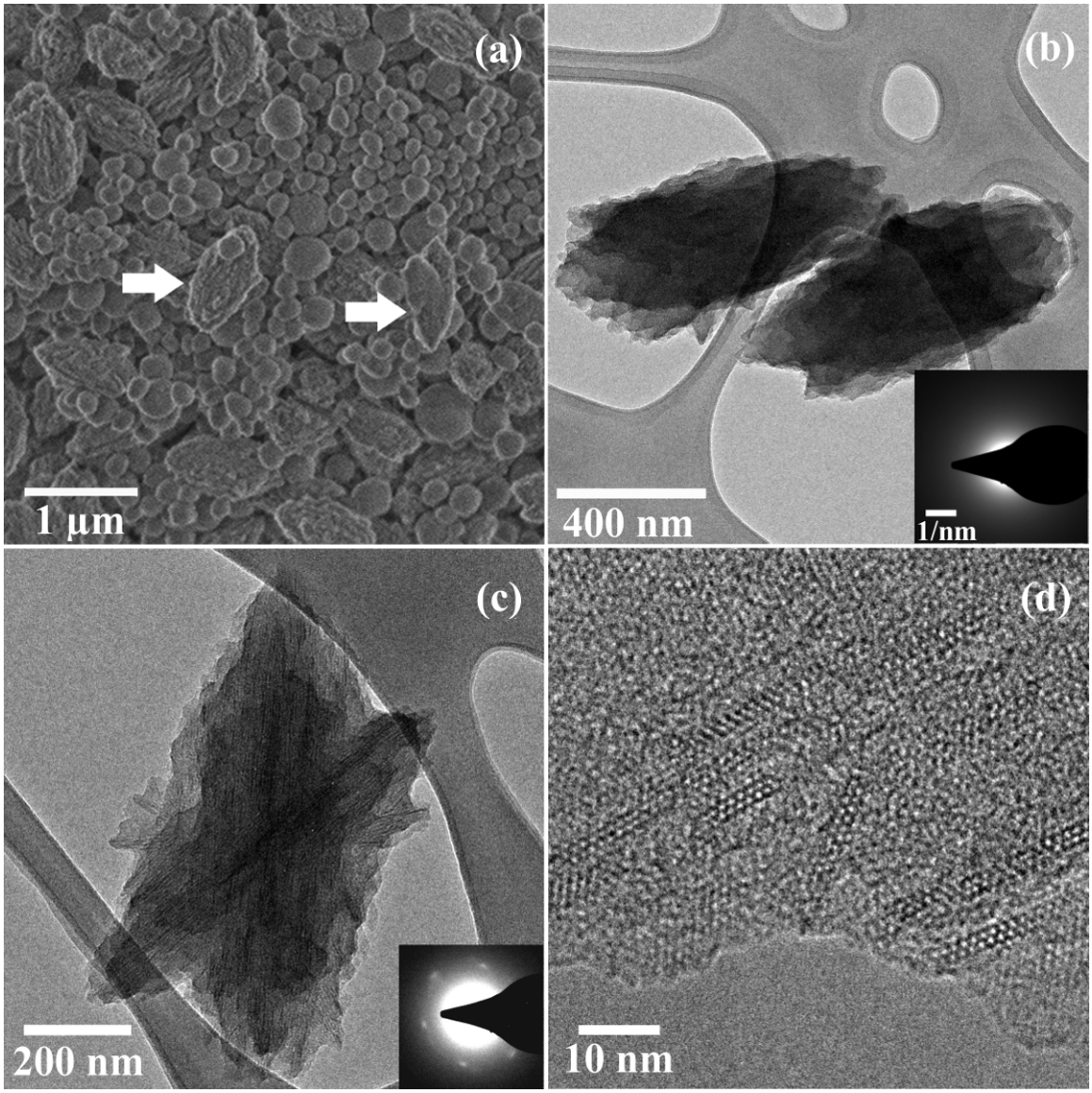

Figure 5-2 Mesoporous silica nanoparticles formed after hydrothermal synthesis at 135ºC for 96 hours. (a) an SEM image showing different types of particles in the product suspension with arrows pointing to ovaloid particles; (b) TEM image of two ovaloid particles with the morphology similar to lamellar MFI but without MFI crystal structure (inset: electron diffraction pattern from both particles that show no obvious spots from MFI); (c) TEM image of a lamellar MFI particle (inset: electron diffraction pattern from the entire particle shows that the particle has MFI structure (with a preferred orientation along [100] zone axis)); and (d) detail of a lamellar MFI particle showing the lamellae.

particles with irregular shapes but still smooth surfaces are formed (Fig. 5-1(c)) possibly by merging of the smaller spherical particles. Low-angle XRD (Fig. 5-1(d)) indicates an evolution of the mesostructure in agreement with that found in Ref. [104].

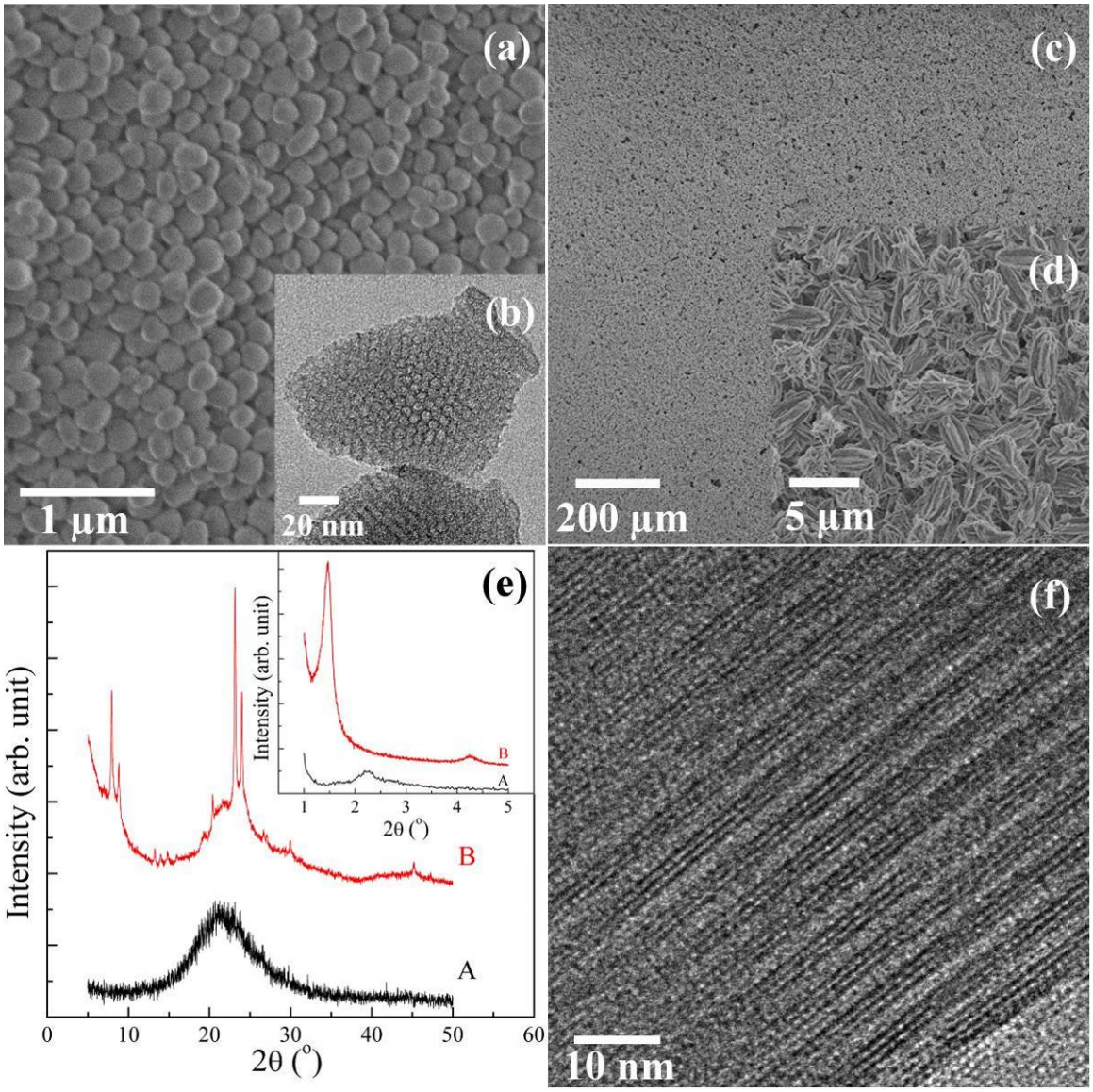

Figure 5-3(a) SEM and, (b) TEM images of mesoporous silica particles (smaller than 200 nm) separated using centrifugation after hydrothermal synthesis at 135°C for 96 hours; (c) and (d) SEM images of the film formed by steam-assisted crystallization (SAC) of the mesoporous silica particles shown in (a) and (b) spread on a glass slide showing uniform deposit consisting of crystals with layered silicalite-1 morphology; (e) X-ray diffraction patterns of the mesoporous silica nanoparticles before (trace-A) and after (trace-B) SAC; (f) TEM detail of the lamellar MFI film formed after SAC.

A hexagonal phase emerges as the synthesis sol was heated at 135^{o}C for up to 18 hours (Fig. 5-1(d), trace A and B, with characteristic peaks marked with triangles), after which, a new structure that appears to be a lamellar phase was observed (Fig. 5-1(d), trace C and D, with characteristic peaks marked with diamonds).

For up to 48 hours, no evidence for MFI layers can be found by TEM or XRD. At 96 hours, a new particle morphology emerges and coexists with the mesostructured particle. Two of these particles are marked by arrows in Fig. 5-2(a). They are larger, ovaloid-shaped, and with rough surfaces. Examination of these particles by TEM and SAED indicates that these particles can be further divided in two categories: (1) those that show no evidence of MFI structure (Fig. 5-2(b)) and (2) those for which clear evidence of MFI layers is obtained by SAED and high-resolution TEM images (Fig. 5-2(c) and (d)).

The findings described above show that starting from a clear sol, mesostructured SDA/silica particles are formed and undergo changes in size, shape and mesostructure before the appearance of MFI layers. Based on this sequence of events leading to lamellar MFI we hypothesized that the mesostructured particles could be transformed to layered MFI by the SAC method. This proved to be feasible as shown in Fig. 3. We isolated and washed by centrifugation and then dried at 70^{o}C the smaller (200 nm) particles formed after 96 hours hydrothermal synthesis at 135^{o}C. SEM and TEM images of these particles are shown in Fig. 5-3 (a) and (b) respectively. They showed an ordered mesostructure with no evidence of MFI layers. Because of their nanoscopic dimensions, the precursor particles shown in Fig. 5-3(a) and (b) can form stable suspension which can be used to

form coatings. When these coatings are treated by SAC, intergrown continuous films of MFI layers can be obtained as shown in Fig. 5-3 (c) and (d). The XRD patterns (Fig. 5-3 (e)) show that after SAC, the initially mesostructured material becomes lamellar silicalite-1 with interlayer distance of 6.1 nm exhibiting the characteristic absence of the second order reflection[97, 105]. TEM images of the film show that the film consists of uniform MFI layers with thickness of 1 unit cell along the b direction, as shown in Fig. 5-3(f).

The SAC procedure demonstrated here could be useful for the formation of membranes and catalytic coatings with hierarchical porosity.

5.4 Conclusion

In this study, we have shown that hydrothermal treatment on a clear synthesis sol was able to yield mesoporous silica nanoparticles. These mesoporous nanoparticles could be transformed to lamellar silicalite-1 by continued hydrothermal treatment, during which intermediate mesostructures appeared. Steam-assisted crystallization (SAC) on coatings of these intermediate mesostructures gave intergrown lamellar silicalite-1 films. Flexibility is the main advantage of this SAC method, since manipulation of colloidal suspensions of seed particles for different purposes is well studied and convenient. With this, the formation of lamellar MFI films can be achieved.

Chapter 6 Self-pillared pentasil zeolite[6]

6.1 Introduction

Zeolites with structural features as small as the size of a unit cell (e.g., 1-5 nm), including those with lamellar structure [11, 104, 106-107], can be used as building blocks for thin films [3-4, 68]. Additionally, hierarchical adsorbents and catalysts constructed by introducing mesopores between the zeolitic domains allow access of bulkier molecules often encountered in oil and biomass processing [6, 108]. Methods for the preparation of mesoporous zeolites involve either multifunctional structure-directing agents (SDA), and/or post-synthesis processing, such as pillaring or desilication/dealumination [6, 109-111]. We introduce crystal growth by repetitive branching of layers as a novel, simple, low-cost approach for bottom-up synthesis of hierarchical zeolites and pillared materials. Although branching by twinning, rotational intergrowths and polytypic overgrowths has been used to design nanostructures [112-113], it has not been explored for the formation of pillared zeolites. Among several candidates of epitaxially and rotationally overgrown zeolites (e.g., MFI/MEL [114], EMT/FAU [115], ETS-4/ETS-10 [116], CAN/SOD [117], MFI [118] and CHA [119]), we focus on exploring the 90° rotational intergrowths (or twins) of the MFI framework motivated by the prominence of the corresponding aluminosilicate (called ZSM-5) as a catalyst in chemical processing. By employing this approach, using a single, simple and relatively inexpensive SDA, we demonstrate the one-step synthesis of

[6] Some of the results presented in this chapter is published in: X. Zhang, D. Liu, D. Xu, S. Asahina, K. A. Cychosz, K. V. Agrawal, Y. Al Wahedi, A. Bhan, S. Al Hashimi, O. Terasaki, M. Thommes, M. Tsapatsis, Science 2012, 336, 1684. Contents from the above publication are reprinted with permission from AAAS.

a hierarchical self-pillared zeolite composed of orthogonally connected single-unit-cell lamellae (2 nm thick) resembling a house-of-cards construction [120].

6.2 Experimental procedures

Pure-silica SPP synthesis

In a typical synthesis, an aqueous solution of tetra(n-butyl)phosphonium hydroxide (TBPOH, 40% by weight, Sigma-Aldrich or TCI America) was added dropwise into tetraethyl orthosilicate (TEOS, 98%, Sigma-Aldrich) while stirring. Distilled water was then added to the mixture. The mixture was stirred for 12 h, and a clear sol with composition 1 SiO_2 : 0.3 TBPOH : 10H_2O : 4 EtOH was formed (compositions 1SiO_2 : 0.3TBPOH : (7-80)H_2O : 4EtOH, and 1SiO_2 : (0.2-0.4)TBPOH : 10H_2O : 4EtOH were also studied). The sol was sealed in a Teflon-lined stainless steel autoclave and heated for 40 h in a pre-heated oven operating at 388 K. The SPP yield with respect to the total amount of silica is ~40%. Tetra(n-butyl)ammonium hydroxide solution (TBAOH, 40% by weight, Sigma-Aldrich) can also be used instead of TBPOH.

When fumed silica was used as silica source, fumed silica (Sigma-Aldrich), an aqueous solution of tetra(n-butyl)phosphonium hydroxide (TBPOH, 40%, Sigma-Aldrich), and distilled water were mixed to give a gel with composition 1SiO_2 : 0.3TBPOH : 10H_2O. The gel was transferred to a Teflon-lined stainless steel autoclave and heated for 96 h while rotating at 30 rpm in a pre-heated oven operating at 388 K.

The product was washed with distilled water by repeated centrifugation and decanting of the supernatant, until the pH of the final supernatant is lower than 9. The final precipitate was dried at 343 K for 12 h. Some of the dried product was calcined at

823 K for 12 h in air for SEM, TEM, XRD, catalytic and gas adsorption/desorption measurements.

For some experiments, the synthesis sol was first sealed in a Teflon bottle and aged at 353 K in an oil bath with stirring for 2 d, and was then quickly transferred to a Teflon-lined stainless steel autoclave and heated to 388 K for up to 30 h.

Aluminosilicate SPP synthesis (Si/Al=253)

Tetra(n-butyl)phosphonium hydroxide solution (TBPOH, 40% by weight, Sigma-Aldrich), water, sodium hydroxide (Mallinckrodt) and aluminum sulfate octadecahydrate (Sigma-Aldrich) were mixed to form a solution, which was added dropwise into tetraethyl orthosilicate (TEOS, Sigma-Aldrich) while stirring. After stirring for 12 h, a clear sol with composition $60SiO_2 : 0.15Al_2O_3 : 0.45H_2SO_4 : 18TBPOH : 0.30NaOH : 600H_2O : 240EtOH$ was obtained. It was sealed in a Teflon-lined stainless steel autoclave and heated for 30 h in a pre-heated oven operating at 388 K. The product was washed with distilled water by repeated centrifugation and decanting of the supernatant, until the pH of the final supernatant is lower than 9. The final precipitate was dried at 343 K for 12 h, and calcined at 823 K for 12 h in air.

Aluminosilicate SPP synthesis (Si/Al=75)

Aluminum isopropoxide (Sigma-Aldrich) and tetraethyl orthosilicate (TEOS, Sigma-Aldrich) were mixed while stirring, into which tetra(n-butyl)phosphonium hydroxide solution (TBPOH, 40% by weight, Sigma-Aldrich) and then a sodium hydroxide solution (prepared with sodium hydroxide from Mallinckrodt, and distilled water) was added dropwise while stirring. After stirring for 12 h, a clear sol with

composition $60SiO_2$: $0.30Al_2O_3$: 18TBPOH : 0.75NaOH : $600H_2O$: 240EtOH was obtained. It was sealed in a Teflon-lined stainless steel autoclave and heated for 48 h in a pre-heated oven operating at 388 K. The product was washed with distilled water by repeated centrifugation and decanting of the supernatant, until the pH of the final supernatant is lower than 9. The final precipitate was dried at 343 K for 12 h, and calcined at 823 K for 12 h in air.

Other zeolite synthesis

Pillared, 3DOm-i, and 17, 1.4, and 0.2 μm conventional MFI are synthesized following reported procedures in refs. [104], [121], [9], [73], and [122], respectively.

Ion exchange to obtain the proton form

The calcined zeolite was mixed with distilled water to yield a 5% (by weight) suspension. The suspension was heated at 343 K for 12 h, and washed once with distilled water by centrifugation and decanting of the supernatant, such that the pH of the supernatant is 6-7. The precipitate was mixed with 1.0 mol L^{-1} ammonium nitrate solution to yield a 5% (by weight) suspension. The suspension was then heated at 353 K for 5 h to allow Na^+ in the framework to be exchanged with NH_4^+. The solid was recovered with centrifugation. The process was repeated three times, and the final product was washed with water, dried at 343 K and calcined in air at 823 K for 4 h.

Exfoliation

The as-synthesized zeolite powder was exfoliated by melt compounding to obtain polymer-zeolite nanocomposite, as reported by Maheshwari et al. [99]. In a typical exfoliation process, 3.84 g of polystyrene (M_n = 45,000 g mol^{-1}, Sigma-Aldrich) and 0.16 g of the zeolite powder was manually mixed and loaded in a vertical, co-rotating twin

screw extruder with a recirculation channel (DACA mini compounder). The mixture was blended sequentially at 393 K for 20 min, 443 K for 25 min, 423 K for 30 min and 473 K for 20 min under a nitrogen environment and at a screw speed of 300 rpm. The zeolite-polymer nanocomposite was then extruded out at 423 K. From this nanocomposite, thin sections with 60 nm thickness were prepared on a Leica EM UC6 Ultramicrotome with a diamond knife. The sections were then mounted on a TEM grid (400 mesh Cu, PELCO).

Zeolite thin-section preparation

Similarly to the exfoliation process, 3.84 g of polystyrene (M_n = 45,000 g mol^{-1}) and 0.16 g of zeolite powder was manually mixed and loaded in the same melt compounding set-up. The mixture was blended at 473 K for 20 min under a nitrogen environment and at a screw speed of 300 rpm and then extruded out at 423 K to form a zeolite-polymer composite. From this composite, thin sections with 60 nm thickness were prepared on a Leica EM UC6 Ultramicrotome with a diamond knife. The sections were then mounted on a TEM grid (400 mesh Cu, PELCO).

Materials characterization

The samples for transmission electron microscopy (TEM) studies were prepared by applying a few droplets of an aqueous suspension of the washed zeolite product onto a copper grid coated with ultra-thin carbon film and holey carbon film (Ted Pella Inc.). Both calcined and uncalcined samples were examined. In order to study the morphology of smaller particles obtained at early stages, the final suspension after synthesis was diluted 10 times (volume) with H_2O, and deposited on the same type of grid. The grid was then allowed to air-dry at room temperature. TEM imaging was performed on an FEI Tecnai G^2 F30 TEM operating at 300 kV. All TEM images were captured using a CCD

camera. Low-voltage scanning electron microscopy (SEM) was performed using a JEOL JSM-7800F scanning electron microscope operated at 0.3 kV (primary electron at 5.3 kV and specimen bias at 5 kV). Conventional SEM was performed on a JEOL JSM-6700F scanning microscope operated at 2 kV. X-ray diffraction (XRD) patterns were acquired using a PANalytical X'Pert PRO MPD X-ray diffractometer equipped with a Co source.

Argon (87.3 K) adsorption was performed using a commercially available automatic manometric sorption analyzer (Quantachrome Instruments AutosorbiQ MP). Prior to adsorption measurements, the samples were outgassed at 573 K for 16 h under turbomolecular pump vacuum. Full micro- and mesopore size distributions were calculated from the argon isotherms using the argon on zeolites/silica cylindrical pore adsorption branch method [123].

AFM specimen was prepared by drying a drop of the suspension on freshly cleaved muscovite mica following by calcination in air at 813 K for 6 h. Imaging was done in tapping mode in repulsive regime using a Molecular Imaging PicoPlus scanning probe microscope (since renamed Agilent 5500 AFM/SPM system). Gwiddion 2.22 software was used for image analysis and height profiling.

^{27}Al MAS NMR spectra were recorded as described in reference [108].

XRD pattern simulation

XRD patterns were simulated using powder power theorem [30] implemented with UDSKIP [31, 124]. In the simulation, atomic coordinates of zeolite MEL are from Fyfe et al. [125], and atomic coordinates of zeolite MFI are from van Koningsveld et al. [126]. All the zeolite nanosheets contain two complete pentasil layers and have their terminal Si atoms

terminated with hydroxyl groups. Simulations for wide-angle X-ray diffraction were carried out with step size $\Delta(2\theta)=0.01^{o}$ (Cu $K\alpha_1$ radiation, λ=1.5418 Å).

Dimethyl ether (DME) titration

The number of Brønsted acid sites in each zeolite sample was assessed by DME titration experiments assuming that the Brønsted acid sites participate in reactions of DME with H^+ to form surface methyl groups, $CH_3OCH_3 + 2[SiO(H)Al] = 2[SiO(CH_3)Al] + H_2O$ [127]. The experiments were carried out in a tubular packed-bed quartz reactor (10 mm inner diameter) under atmospheric pressure. The reactor temperature was held constant by a resistively heated furnace (National Electric Furnace FA120 type). Catalyst temperatures were measured using a K-type thermocouple touching the bottom of a well on the external surface of the quartz reactor. The catalyst samples (0.015-0.100 g) were supported on a coarse quartz disk inside the reactor and treated in He (0.0083 mL s^{-1}, ultrapure, Minneapolis oxygen) at 773 K (0.0167 K s^{-1}) for 3 h prior to cooling in He flow to the reaction temperature of 423 K. A mixture of DME/Ar/He (0.0083 mL s^{-1}; 24.9% DME, 25.1% Ar and 50% He; Praxair) was introduced by He during each pulse with 120 s intervals. The effluent, physisorbed DME and water formed upon dehydration reactions, was subsequently removed by He (0.0083 mL s^{-1}) for 2.5-3.5 h. A mass spectrometer (MKS Cirrus 200 Quadrupole mass spectrometer system) was used to record the titration curves of DME.

2,6-di-tert-butylpyridine (DTBP) and pyridine titration

The accessibility of Brønsted acid sites on zeolite catalysts was examined by base (DTBP and pyridine) titration during ethanol dehydration reactions. The experimental set

up and reaction conditions were the same as those described in a previous publication [108]. Typically, catalyst samples (0.015-0.100 g) diluted with acid-washed quartz particles (0.5-0.8 g, 160-630 μm, European Commission) were treated in He (0.0083 mL s^{-1}, ultrapure, Minneapolis oxygen) at 773 K (0.0167 K s^{-1}) for 3 h prior to cooling in He flow to the reaction temperature of 416 K. A liquid mixture of organic base (pyridine (Aldrich, 99.9% purity) or DTBP (Alfa, 98% purity)) with ethanol (>99.5%, Sigma-Aldrich) was prepared using 10 mL of ethanol and 10-20 μL of organic base, and was introduced using a syringe pump (Cole Parmer 74900 series). The liquid mixture was vaporized into a gas flow which contained He (0.55-9.4 mL s^{-1}) and internal standard Ar (0.0137-0.0297 mL s^{-1}, Minneapolis oxygen); transfer lines were maintained at temperatures greater than 393 K by resistive heating to prevent any condensation. The ethanol dehydration rate was measured at constant intervals as titrant was continuously added until it reached a plateau indicating that acid sites accessible to the titrant became saturated with the organic base. The loss in dehydration rate after saturation by the titrant given by the difference between the initial and the residual rates was used to calculate the number of acid sites accessed by the base titrant. The uptake of DTBP titrant by the catalyst was measured from its concentration in the effluent, recorded by gas chromatography (Agilent HP-5890 GC, Series II), using the same chromatographic protocols as for ethanol dehydration in reference [108]. The uptake of the titrant (per Brønsted acid site) was comparable to that assessed from the loss in rate of ethanol dehydration (per Brønsted acid site) [108]. The external Brønsted acid sites were defined as those accessible to the DTBP titrant.

Adsorption of benzyl alcohol in mesitylene

In a typical adsorption experiment, approximately 1 mL mesitylene (Sigma-Aldrich), 1-32 μL benzyl alcohol (Sigma-Aldrich), 20 mg zeolite, and a stir bar were added sequentially into a glass vial (Chemglass, 1.8 mL). The exact weights of mesitylene, benzyl alcohol, and zeolite were recorded. The vials were heated at 343 K in an oil bath for 18 h while stirring (750 rpm). Approximately 25 μL sample was taken from each vial while the vials were in the oil bath. The composition of the samples was analyzed using a gas chromatograph (Agilent HP-5890GC, Series II) equipped with a methylsiloxane capillary column (HP-1, 50.0 m x 320 μm x 0.52 μm) connected to a flame ionization detector.

Mesitylene alkylation and benzyl alcohol self-etherification

The reactivity of Brønsted acid sites on the self-pillared pentasil (SPP), pillared MFI, 3DOm-i MFI, commercial MFI (Zeolyst, CBV 8014) and three conventional microporous MFI zeolites with crystal sizes of 17 μm, 1.4 μm, and 0.2 μm were compared by studying the reactions (mesitylene alkylation with benzyl alcohol and benzyl alcohol self-etherification) in a mixture of mesitylene and benzyl alcohol in a batch reactor at 343 K. Reactions of the bulkier mesitylene reactant are limited to the external surface of the zeolite, as shown by the absence of mesitylene alkylation when MFI samples are selectively deactivated by DTBP. Etherification can take place both inside the micropores and at the external surface of the zeolite catalysts. By selectively poisoning the external acid sites with DTBP, the rate of etherification reactions occurring inside the zeolite micropores can be quantitatively assessed.

(a) Mesitylene alkylation (on external surface)

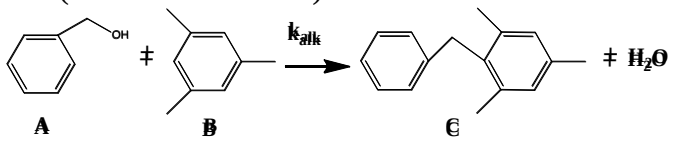

The liquid phase catalytic alkylation of mesitylene (Sigma-Aldrich, 99% purity) by benzyl alcohol (Sigma-Aldrich, 99.95% purity) to form 1,3,5-trimethyl-2-benzylbenzene was carried out in a three-necked round bottom flask (100 mL) equipped with a reflux condenser and heated in a temperature controlled oil bath (343 K) under atmospheric pressure and magnetic stirring (1" stirring bar) conditions. The reactions were carried out at 500 rpm stirring speed which was determined to be sufficient to eliminate external transport limitations (by rate measurement at different stirring speeds). No benzyl alcohol was reacted in absence of the zeolite catalyst at the reaction conditions investigated.

In a typical experiment, 15 mL of mesitylene was added to the desired amount of zeolite catalyst, which had been calcined at 823 K in flowing air (1.667 mL s^{-1}) for 4 h before the experiment. The reaction mixture was kept for 0.5 h at the required reaction temperature under stirring before 0.25 ml of benzyl alcohol was added. Reaction time was defined as the time after addition of benzyl alcohol. Liquid samples were withdrawn at regular intervals and analyzed by a gas chromatograph (Agilent HP-5890GC, Series II) equipped with a methylsiloxane capillary column (HP-1, 50.0 m x 320 μm x 0.52 μm) connected to a flame ionization detector.

(b) Benzyl alcohol self-etherification in presence of DTBP (in internal micropores)

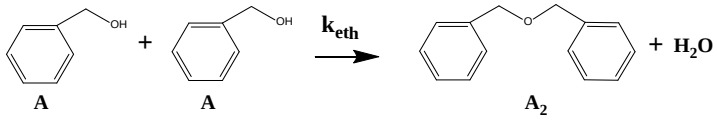

The internal etherification reaction took place under the same reaction conditions as those for alkylation reactions after the addition of DTBP. Typically, the zeolite catalyst, DTBP, and mesitylene were added to the reactor sequentially, and then the reactant was held at the reaction conditions for 2.5 h before benzyl alcohol was added. Excess amount of DTBP (5 times the total number of acid sites) and 2.5 h mixing time prior to benzyl alcohol addition ensured that DTBP completely poisoned acid sites on the external surface. Greater than 99% selectivity to etherification reactions was observed in the experiment, and this preferential selectivity can be attributed to acid sites circumscribed in the internal micropores.

5-hydroxylmethyl-2-furaldehyde (HMF) etherification

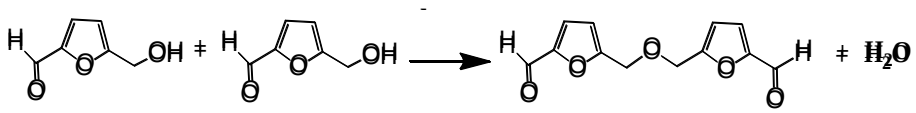

HMF etherification was carried out under the same reaction conditions as those of mesitylene alkylation and benzyl alcohol etherification reactions except that mesitylene and benzyl alcohol were replaced with benzene and HMF, respectively. Typically, the zeolite catalyst and benzene (Sigma-Aldrich, anhydrous 99.8% purity) were added to the reactor sequentially, and then the reactant mixture was held at the reaction conditions for 0.5 h before HMF (Sigma-Aldrich, >99% purity) was added.

6.3 Results and discussion

Synthesis and structure

We decided to explore tetrabutylphosphonium (TBP)- and tetrabutylammonium (TBA)-silica sols which are known to yield MFI as well as mixtures of MFI with the related structure MEL [68, 128]. Fig. 6-1A shows particles obtained after 3 h at 388 K starting from

a clear sol with composition $1SiO_2 : 0.3TBPOH : 10H_2O : 4EtOH$ [129]. Fig. 6-1B shows a high-resolution transmission electron microscopy (HRTEM) image along with the corresponding fast Fourier transform (FFT) confirming that the particles are MFI plates, thin along the b-axis. Their thickness was determined by atomic force microscopy (AFM) (Fig. 6-2) to be ~2 nm, i.e., a unit cell along the b-axis, thinner than previously reported lamellae made by exfloliation [7].

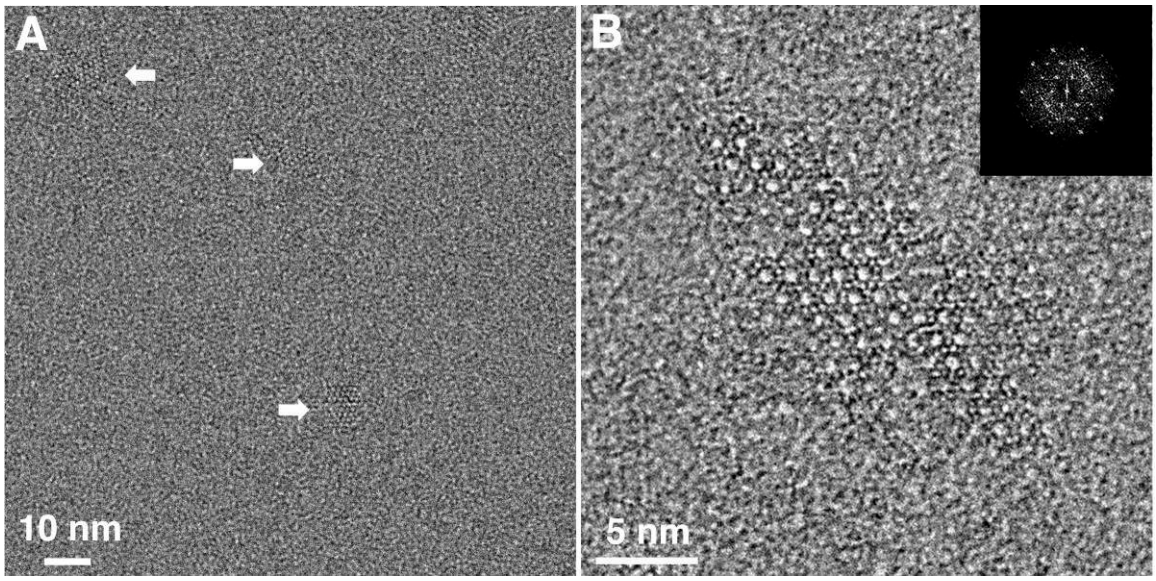

Figure 6-1 TEM image of zeolite nanoparticles obtained after 3 h (A) and high-resolution TEM image of a representative zeolite particle obtained after 7 h (B) at 388 K following aging at 353 K for 2 days. The inset in (B) is the fast Fourier transform (FFT) of the high-resolution TEM image.

With further heat treatment, the lamellae become intergrown. After 40 h at 388 K, the product contained crystalline particles with size varying from 100 - 200 nm, as shown in Fig. 6-3A. HRTEM images (Fig. 6-3B) showed that the particles consist of crystalline zeolite lamellae with a layer thickness of 2 nm. Remarkably, the zeolite lamellae are intergrown in a house-of-cards arrangement, i.e., with the lamellae arranged perpendicular to each other, to define pores between them. TEM images, taken after

calcination in air at 823 K for 12 h, do not reveal any change in the house-of-cards arrangement (Fig. 6-3C). The pores as well as the connectivity of the lamellae can also be seen by low voltage scanning electron microscopy (SEM) from calcined samples (Figs. 6-3D and E). To further probe their internal structure, the calcined particles were embedded in polystyrene, thin-sectioned and studied with TEM. Intermittent lattice fringes, as shown in Fig. 6-3F, provide evidence for pores between adjacent lamellae penetrating throughout the particles.

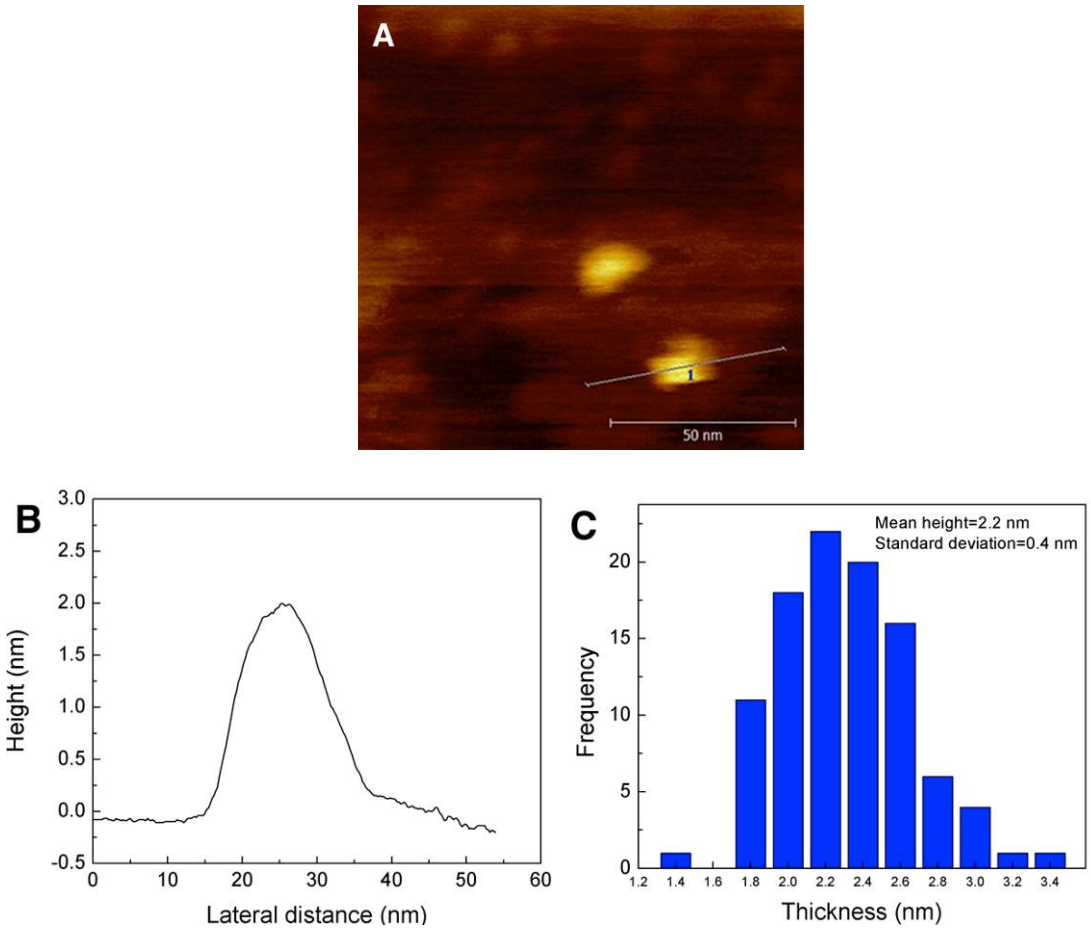

Figure 6-2 (A) AFM images of the nanoparticles formed after 7 h at 388 K following 2 d at 353 K. Thickness profile (B) was scanned on one of them (the line in (A) shows scan path). (C) A histogram of particle thickness from measuring *N*=101 particles shows that the particle thickness is 2.2±0.4 nm. The height determination was performed using nanometer-sized steps on mica as an internal standard [7].

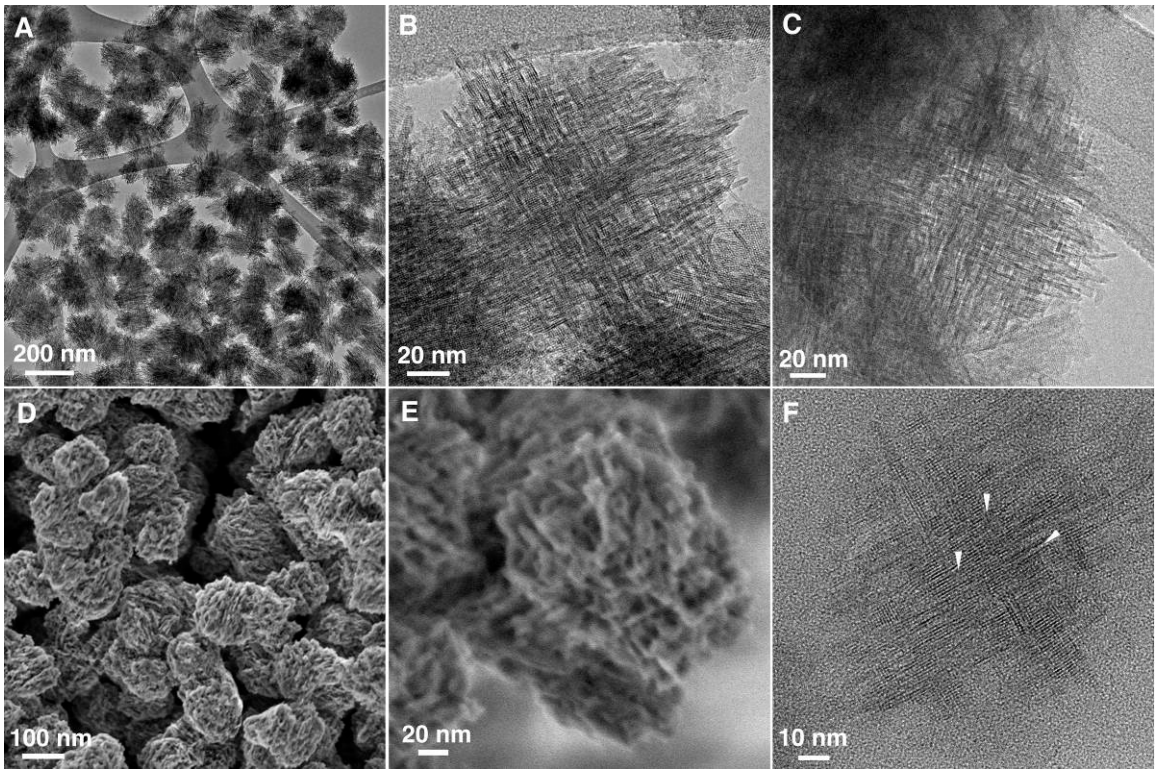

Figure 6-3 Structure and morphology of the pure-silica self-pillared pentasil (SPP) zeolite particles after 40 h hydrothermal synthesis at 388 K: (A) Low-magnification, and (B) high-magnification TEM images of the particles before calcination showing the morphology and the mesopores formed within the intersecting zeolitic lamellae; (C) TEM image of the particles after calcination, showing the retained mesoporosity; (D) and (E) Low-voltage high-resolution SEM images of the calcined particles showing the mesopores and lamellar connectivity; (F) high-resolution TEM image of a thin section of the calcined zeolite embedded in polystyrene: intermittent lattice fringes (shown with arrows) suggested that mesopores exist throughout the particle.

Further TEM imaging and FFT analysis (Fig. 6-4A) indicated that the thin dimension (~2 nm) of the lamellae is along the b-axis of MFI and that the lamellae are longer along the c-axis and shorter (~100 nm) along the a-axis.

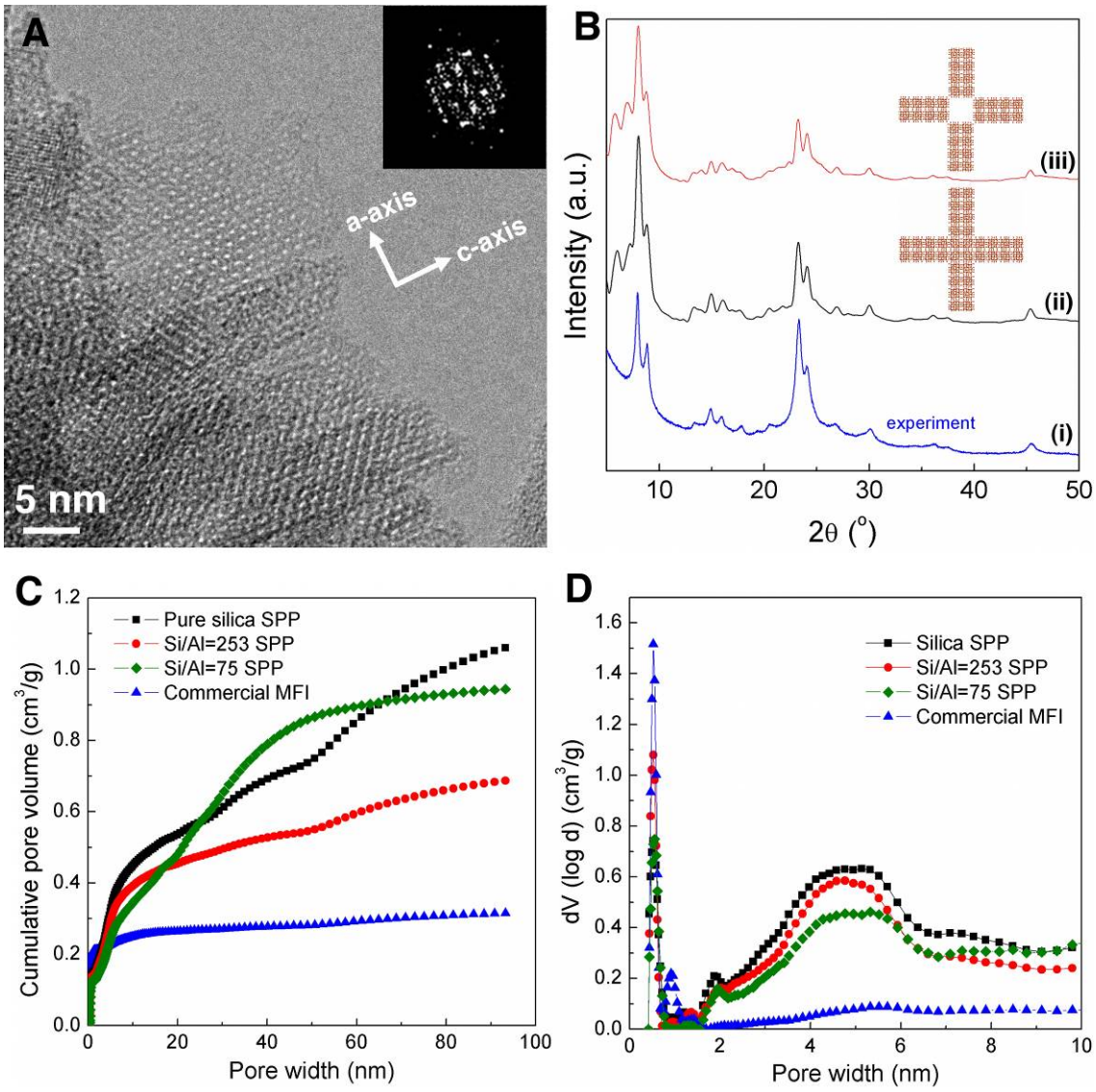

Figure 6-4 (A) A high-resolution TEM image of a self-pillared pentasil (SPP) lamella viewed across its thin dimension, the FFT from the lamella is consistent with [010]-zone axis of zeolite MFI; (B) Experimental (i) and simulated (ii, and iii) powder XRD patterns of the pure-silica SPP zeolite (insets are the intergrowth models from which the simulated XRD patterns were obtained: the model for trace (ii) is the idealized MFI/MEL model, and that for trace (iii) is the idealized model with MEL removed; the dimension of the model along the common c axis is 10 unit cells); (C) Argon (87.3 K) NLDFT cumulative pore volume plots over the entire pore width range and (D) Argon (87.3 K) NLDFT pore size distributions up to 10 nm for silica (squares), aluminosilicate SPP zeolite (circles Si/Al=253 and diamonds Si/Al=75), and commercial MFI (triangles).

Two plausible models for the local structure of the intergrown lamellae are shown in the inset of Fig. 6-4B. According to these idealized fragment models, single-unit-cell

MFI lamellae (with thickness of one unit cell along the b-axis of the MFI structure) are intergrown with their 90° twins or rotational intergrowths having a common c-axis. In one of the idealized models, we hypothesize that the twins are connected through a needle of MEL (1 unit cell along the a- and b-axes and long along the c-axis). The MEL connection runs through the entire interface of the MFI twins ensuring full connectivity.

There are 12 different ways to make the idealized connection and only one of these is shown in the inset of Fig. 6-4B. The rest are given in Fig. 6-5. A 1×1×n MEL needle has two possible structure projections along [001]. According to the representation in Ohsuna et al. [114], they are called here *A* and *B*: *A* (L_IR_I;R_IL_I) , and *B* (R_IL_I;L_IR_I) (fig. S4A).

For both MEL needles (*A* or *B*), each of the four sides of the MEL needle, (*a*, *b*, *c*, and *d*) can accommodate one MFI nanosheet (with single unit cell thickness along the b-axis of MFI). Take side *a* as an example, the two possible MFI structures that can be fully connected to it are depicted as 0 (R_IL_I; $L_{II}R_{II}$), and 1 ($R_{II}L_{II}$; L_IR_I) in Fig. 6-5A.

Therefore, for each MEL needle, there are at most 2^4=16 different ways of attaching defect-free MFI nanosheets. If we use a sequence of five symbols to denote one intergrowth model: *xabcd*, the 16 different structures can be enumerated as: *x*0000, *x*1000, *x*0100, *x*0010, *x*0001, *x*1100, *x*1010, *x*1001, *x*0110, *x*0101, *x*0011, *x*1110, *x*1101, *x*1011, *x*0111, and *x*1111, where *x* can be *A* or *B*.

The actual unique structures of intergrowth are less than 16 due to the symmetry of the MEL needle. We now use proper symmetry operations to find duplicate structures in the 16 different connections. A 2-fold rotational axis implied in the 4-fold rotoinversion

axis (element in space group $I\bar{4}m2$) along [001] shows that *xcdab* is identical as *xabcd* (*xabcd=xcdab*). Two perpendicular 2-fold rotational axes (elements in space group $I\bar{4}m2$) in (001) will further lead to *xabcd=xdcba=xbadc*. Applying these relationships (*xabcd=xcdab=xdcba=xbadc*) to the above-enumerated structures, there are only 6 unique structures for each MEL needle: *x*0000, *x*1000, *x*1100, *x*1010, *x*1110, and *x*1111. For the two possible MEL needle structures (*x=A* and *B*), there are 12 unique structures. The ones for *x=A* are shown in Figs. 6-5 B-G. Full connectivity of the MEL needle and MFI plates is achieved in these 12 structures. Of course, more structures can be generated considering defective (not fully connected) rotational intergrowths of the MFI plates.

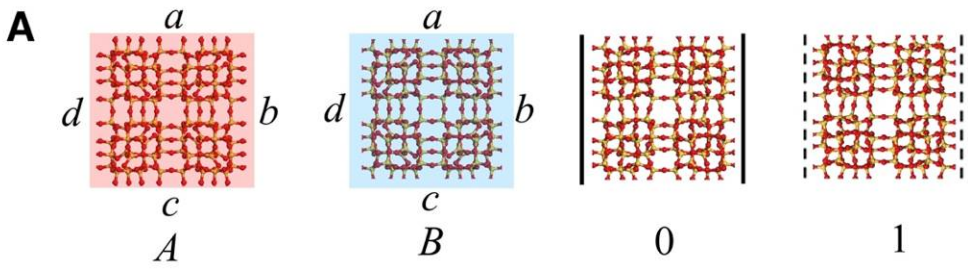

Figure 6-5 Representation of the arrangements of MEL and MFI in the idealized intergrowth structure models. (A) *A* (highlighted in red), *B* (highlighted in blue) are the two different arrangements of the MEL single-unit-cell needle along c-axis. *0* (surrounded by solid line), *1* (surrounded by dashed line) are the two different arrangements of the MFI lamellae; (B) to (G) are the 6 distinct intergrowths for MEL type *A* (the 6 intergrowths for type *B* are not shown) viewed along three directions.

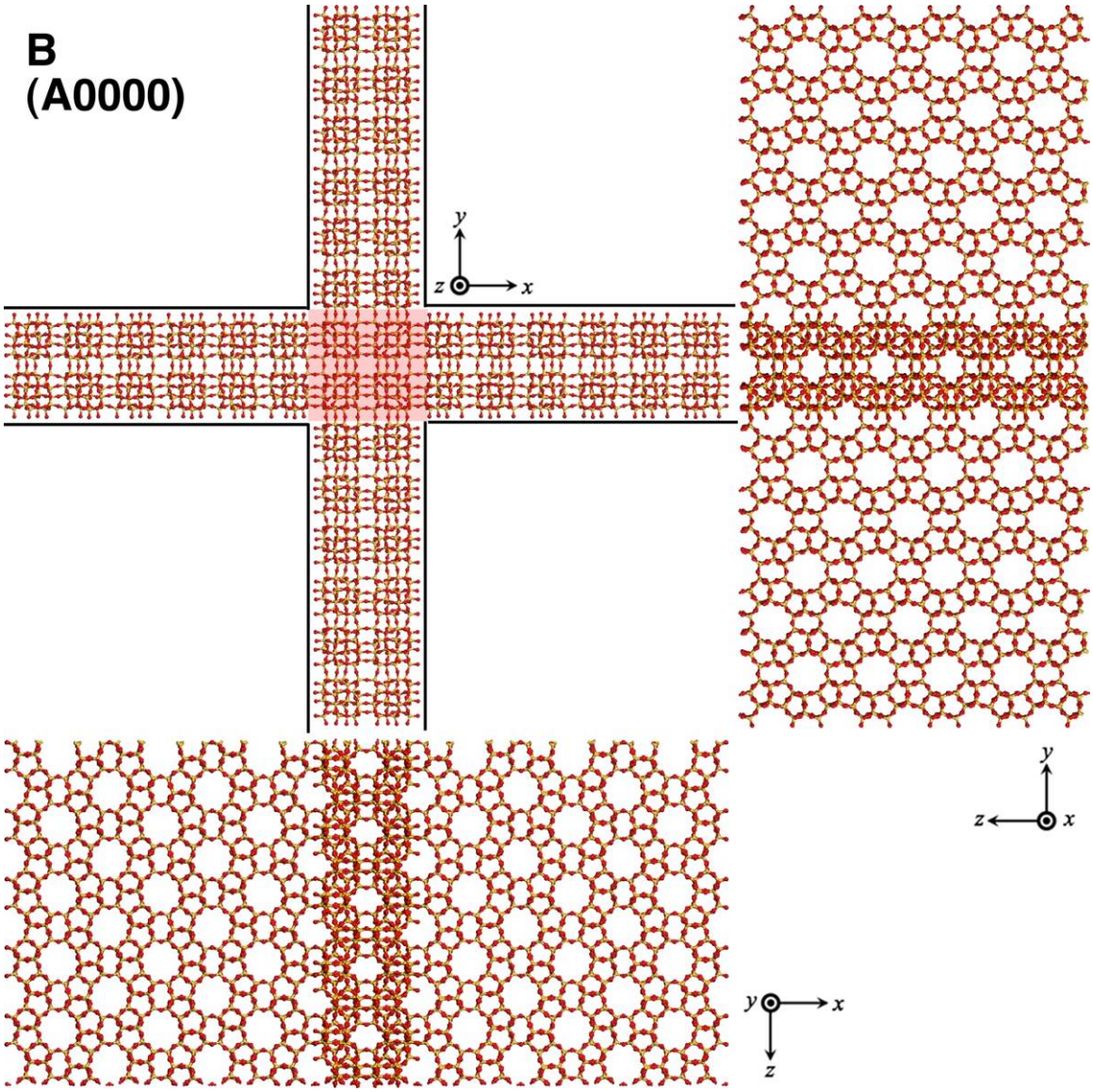

Fig. 6-5
(Cont.)

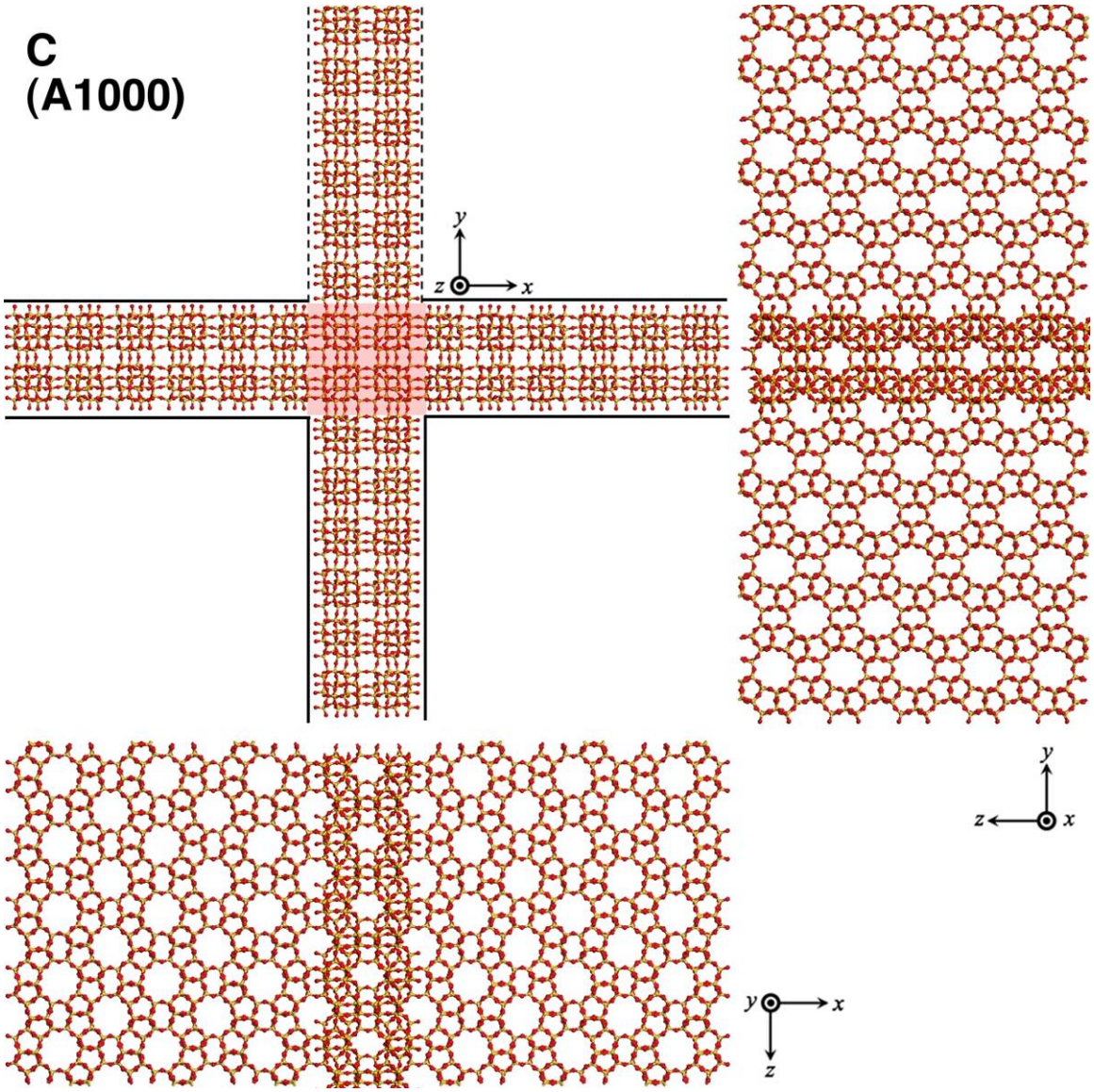

Fig. 6-5
(Cont.)

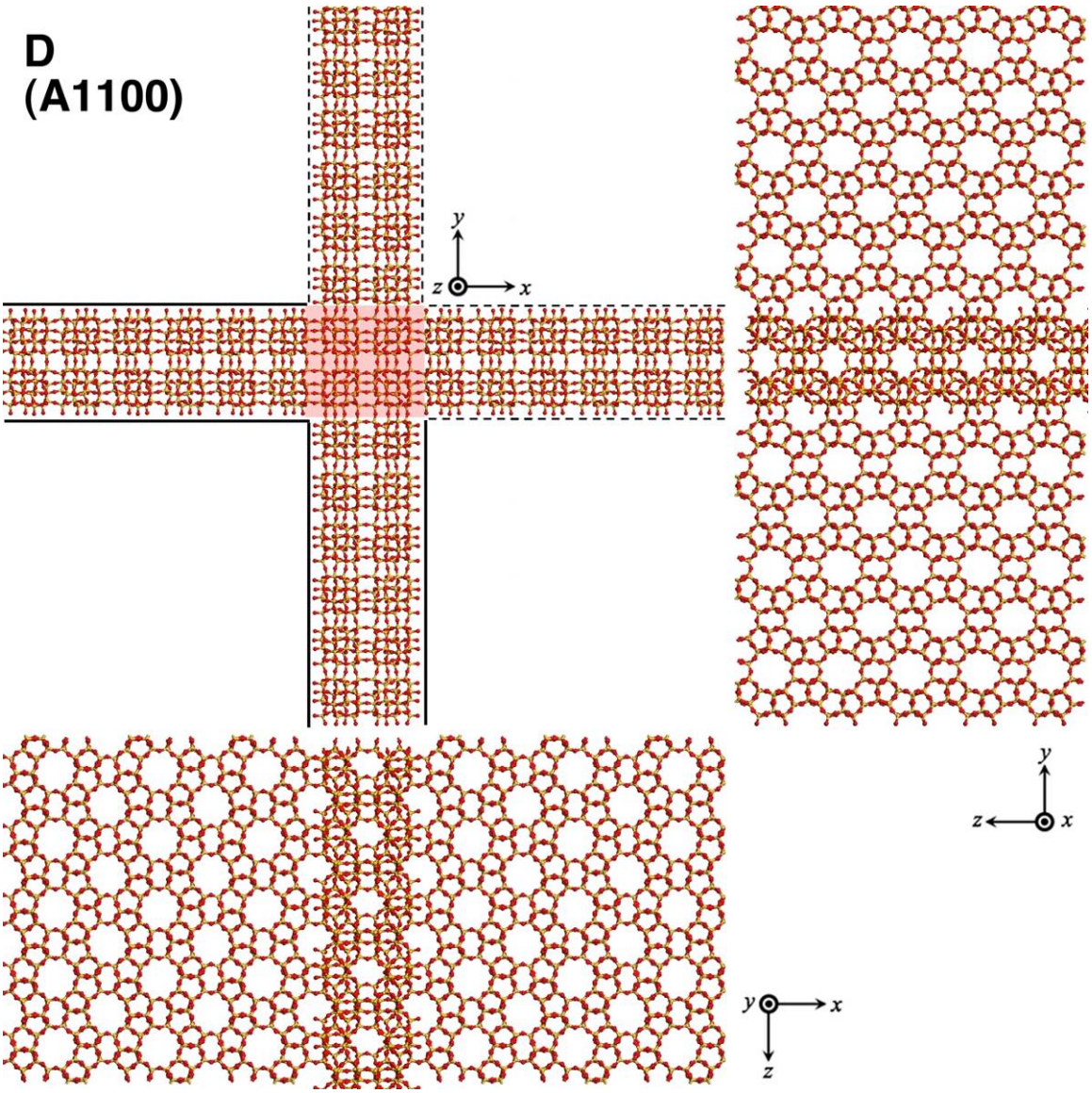

Fig. 6-5
(Cont.)

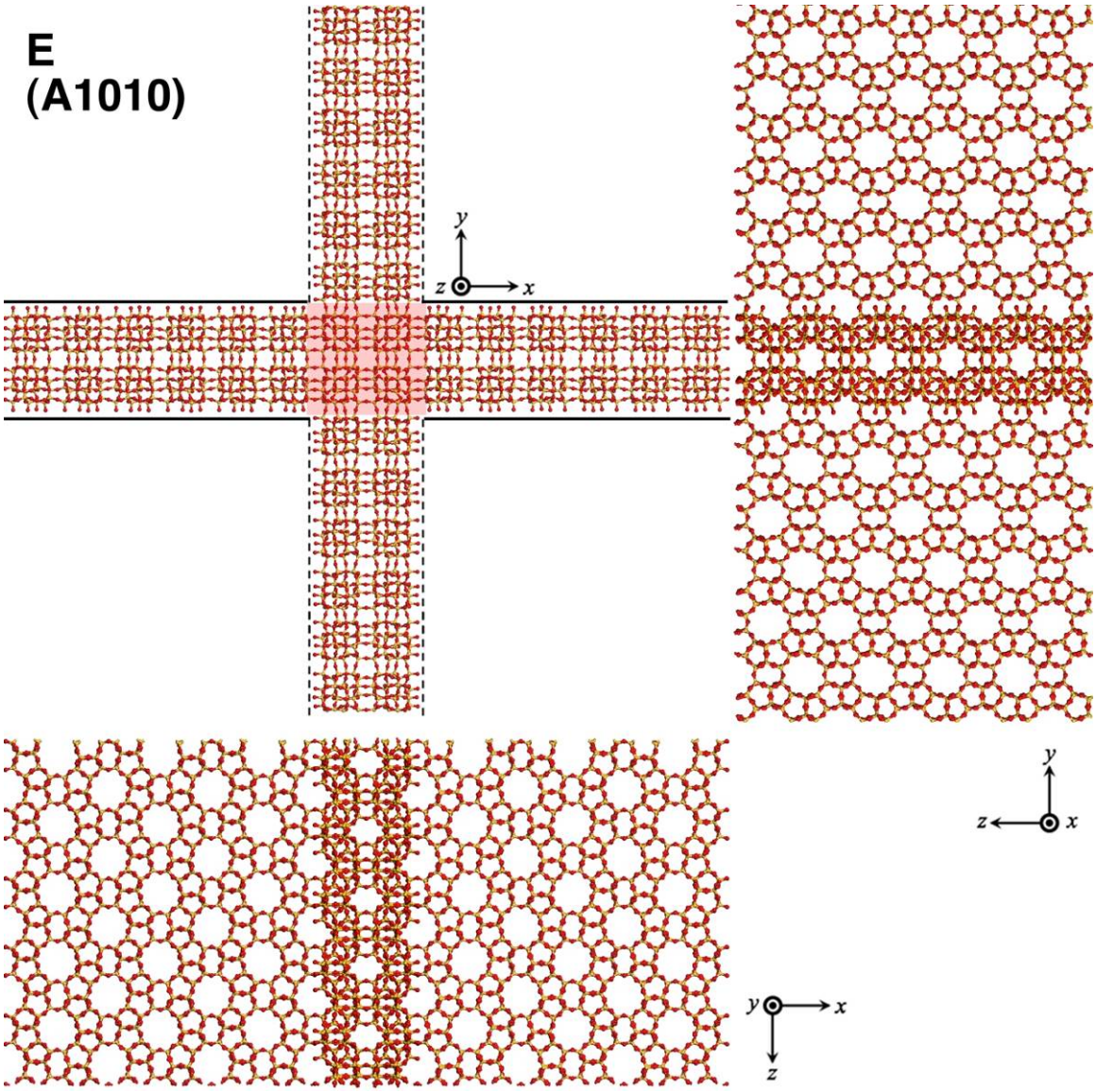

Fig. 6-5
(Cont.)

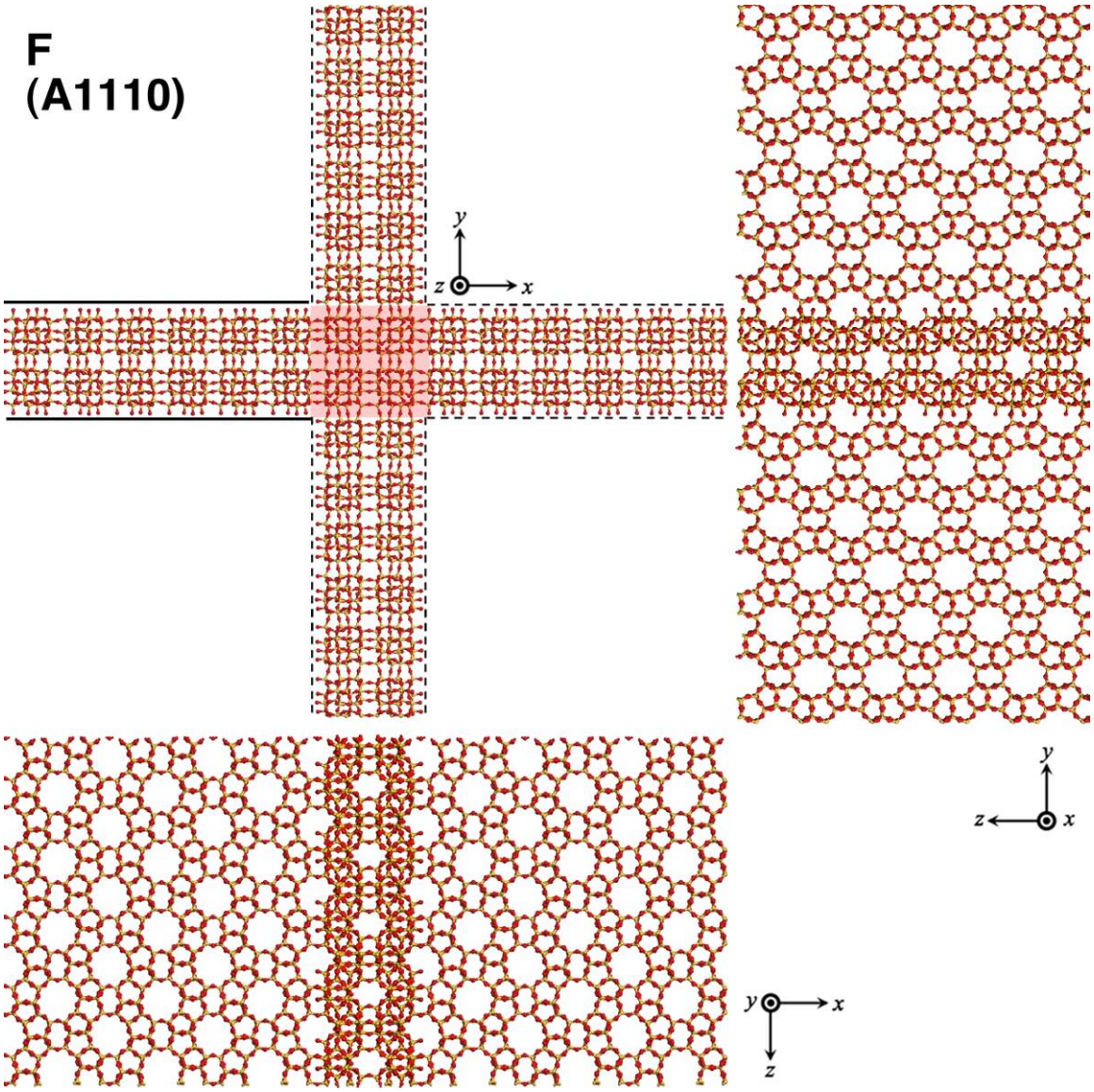

Fig. 6-5
(Cont.)

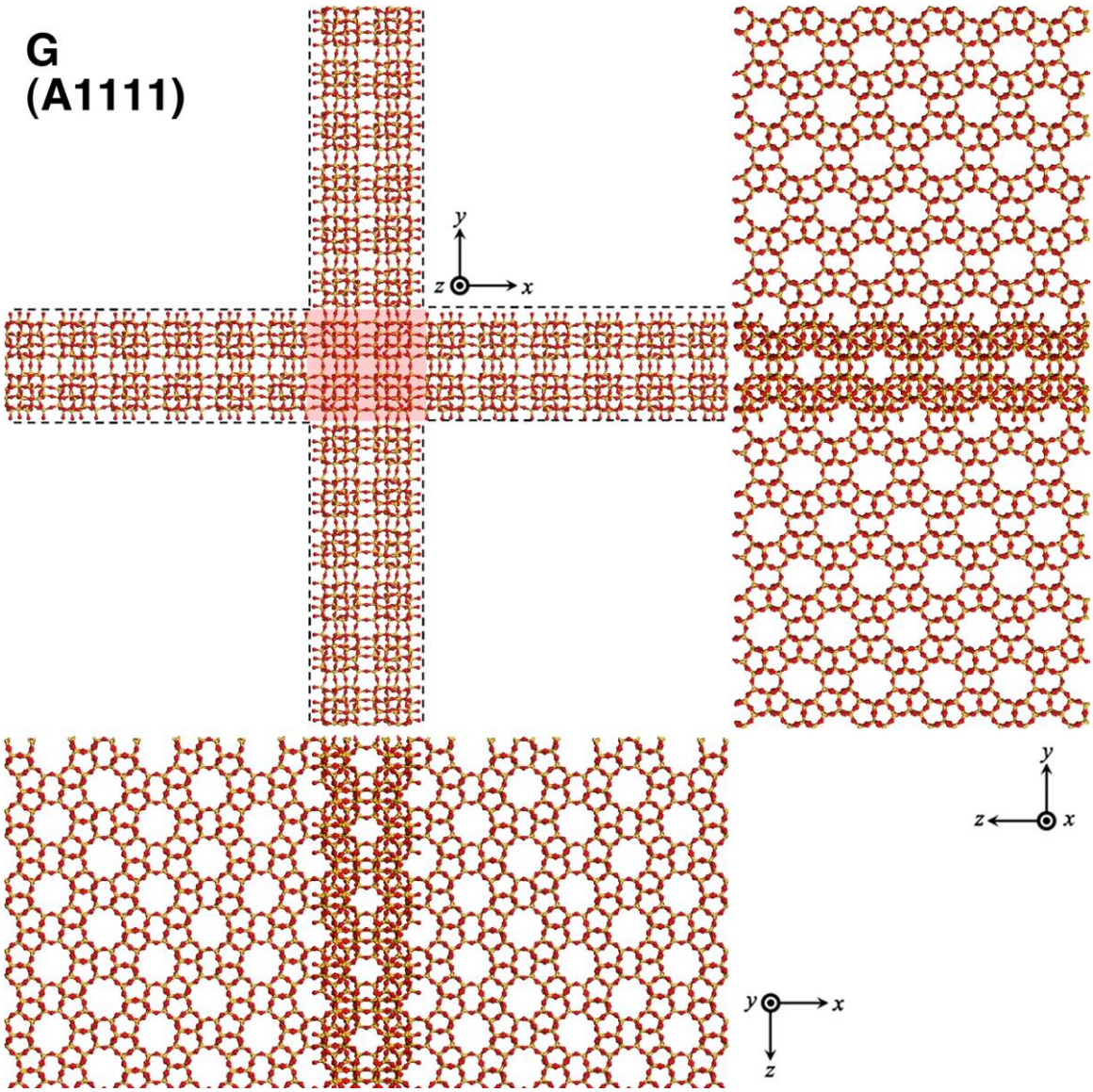

Fig. 6-5
(Cont.)

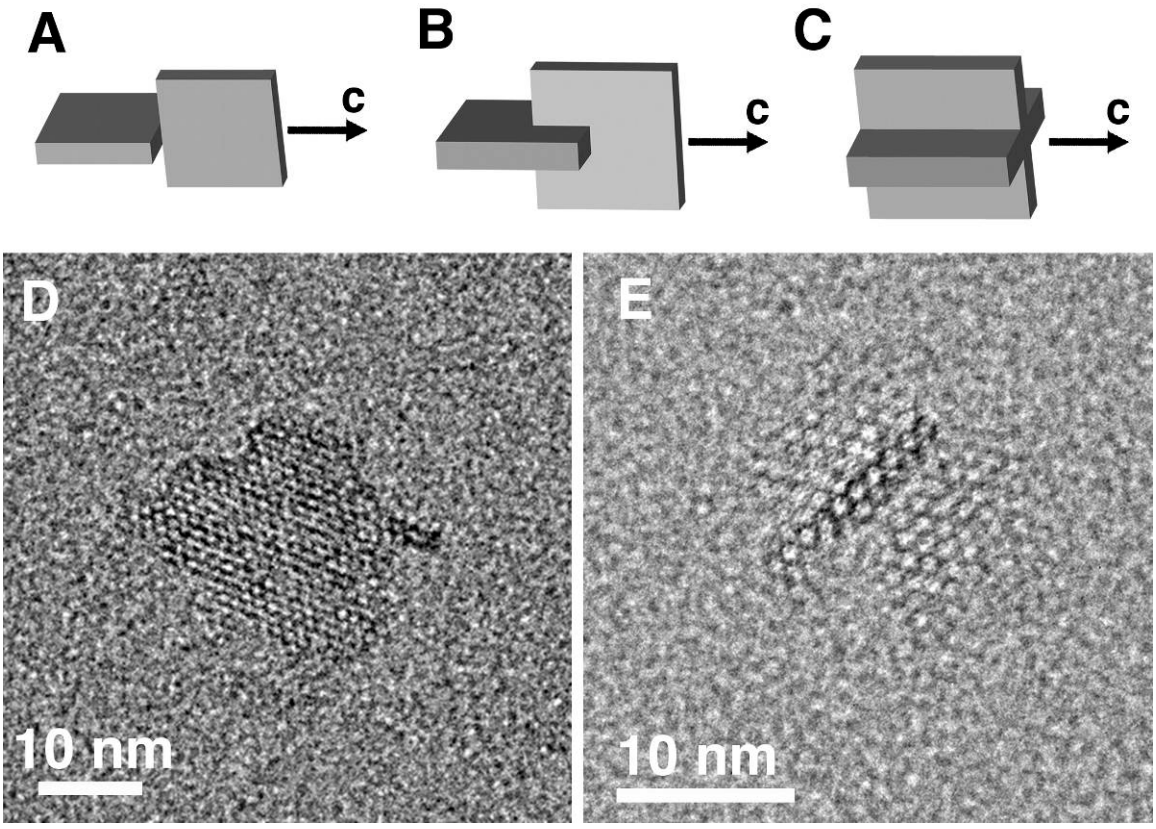

Figure 6-6 Schematic drawings of possible intergrowths of two MFI lamellae: from loose connection without overlap (A), to partial overlap (B) to full connection (C). Sampling of smaller zeolite nanoparticles showing the emergence of single unit cell needles: (D) after 30 h at 388 K following aging at 353 K for 2 d; (E) after 30 h at 388 K.

In the actual material, looser connections are possible, as depicted schematically in Fig. 6-6 A-C, with partial overlay of the MFI lamellae. An idealized fragment with no connection between the MFI lamellae is also shown as inset in Fig. 6-4B. TEM images from particles at an early stage of intergrowth (Fig. 6-6 D, E) provide evidence for the presence of single unit cell outgrowths emerging from the MFI plates. MEL/MFI intergrowths when using TBA and TBP ions have been reported before [114, 130] while twining or rotational intergrowths are well known in MFI crystals. However, they were not associated with single unit cell lamellae formation nor repetitive branching to create a

hierarchical zeolite. The tetrabutyl SDA, which is stable at crystal growth conditions, and is incorporated intact in the framework (Fig. 6-7), appears to be an important contributor to the anisotropic growth giving rise to the single-unit-cell lamellae.

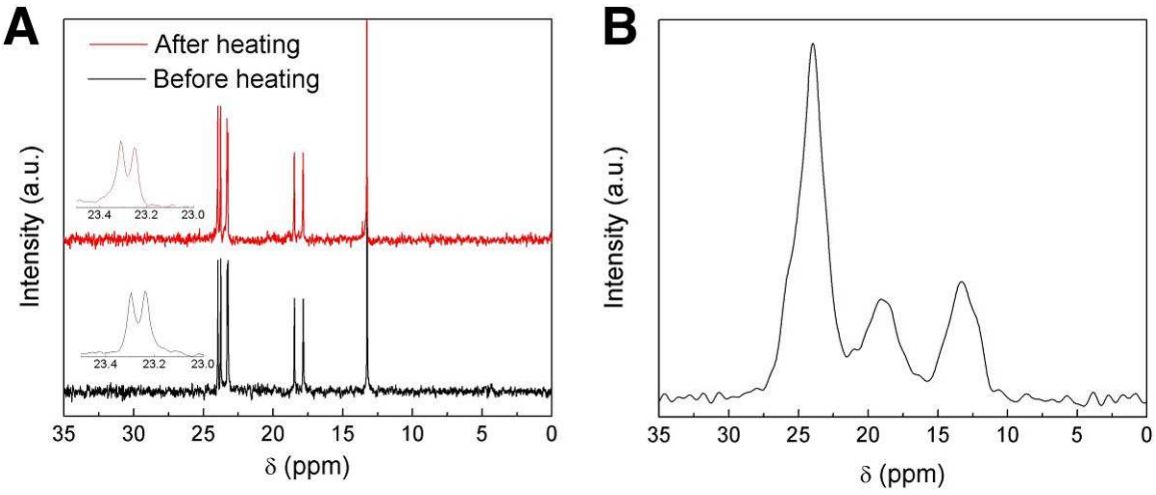

Figure 6-7 (A) ^{13}C NMR spectra of the 40% (weight) TBPOH solution before and after heating at 388K for 40 hours. The unchanged spectrum after heating shows that TBPOH solution was stable at hydrothermal synthesis conditions; (B) ^{13}C CPMAS NMR spectrum of the as-synthesized SPP zeolite is consistent with previous work [130], which shows that the tetrabutylphosphonium cations remained intact in the framework after hydrothermal synthesis.

In the range of MFI and MEL reflections, the simulated powder X-ray diffraction pattern of both fragment models, obtained using UDSKIP [129], are in good agreement with the experimental data (Fig. 6-4B). At lower angles, the simulation shows broad reflections (similar for both fragments) due to the small dimensions of the fragment model. As expected, these reflections are absent from the experimental diffraction pattern of the 100-200 nm crystals because even though they consist of numerous interconnected fragments, they preserve their crystallographic alignment (long range order) due to the ordered branching growth mechanism. Since the new material could be an MFI/MEL intergrowth, we refer to it from now on as self-pillared pentasil (SPP) zeolite although it consists mostly of MFI with MEL being present, if at all, at the branching points.

Additional synthesis and characterization (Fig. 6-8 and 6-9) show that the self-pillared zeolite can be prepared in a range of conditions that allow composition and particle size manipulation. The synthesis conditions that lead to the self-pillared zeolite were determined by systematic examination of concentrated clear sols at compositions typical for the synthesis of MFI zeolites. Based on the base-case synthesis sol composition $1SiO_2$: 0.3TBPOH : $10H_2O$: 4EtOH described above, variations in the amount of water, SiO_2:TBPOH ratio, and silica source indicate that self-pillared and highly branched zeolite crystals can be prepared in a specific but rather wide composition range. As shown in the images in Fig. 6-7 and the XRD patterns in Fig. 6-8, if SiO_2:TBPOH ratio is held at 1:0.3, a SiO_2:H_2O ratio within 1:7 and 1:20 results in single-unit-cell branched structures. Larger particles (750 nm) were produced at SiO_2:H_2O ratio of 1:20. However, an even lower SiO_2:H_2O ratio results in amorphous phase within the times tested (up to 40 h). Similarly, if SiO_2:H_2O ratio is held at 1:10, a SiO_2:TBPOH ratio within 1:0.2 and 1:0.4 also yields single unit cell self-pillared zeolite. The particle sizes and shapes appear similar within this range as the TEM images reveal only subtle textural differences like that the protruding lamellae are reduced compared to the base case ratio of 1:0.3. In addition to TEOS, fumed silica can also serve as silica source to crystallize self-pillared zeolite. Interestingly, 500 nm self-pillared crystalline particles were obtained using this silica source, larger and smoother compared to the 100-200 nm particles obtained using TEOS.

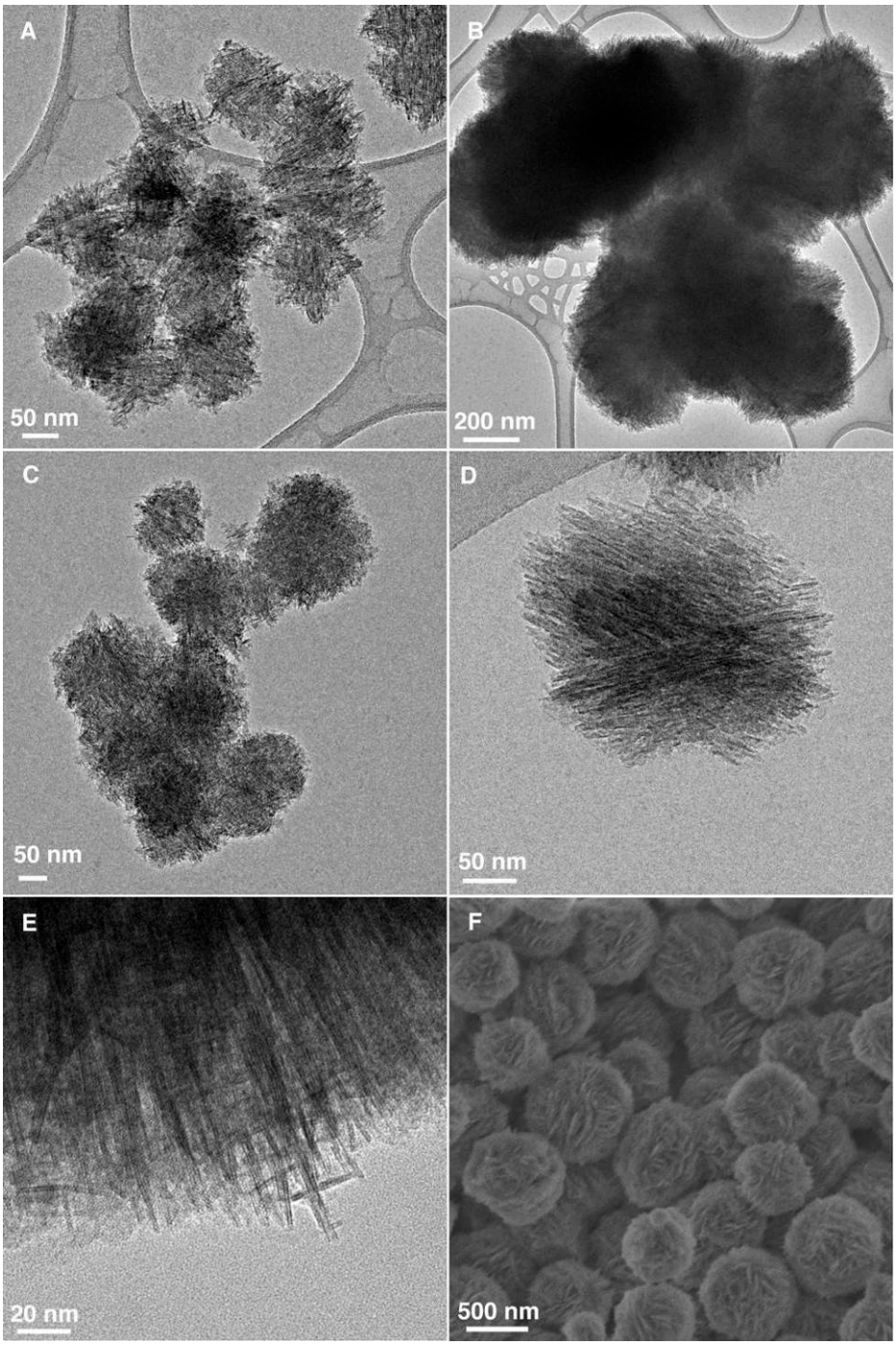

Figure 6-8 Representative electron micrographs of the products of pure-silica SPP synthesis with different compositions at 388K for 40 h: (A) $1SiO_2$: 0.3TBPOH : $7H_2O$: 4EtOH; (B) $1SiO_2$: 0.3TBPOH : $20H_2O$: 4EtOH; (C) $1SiO_2$: 0.4TBPOH : $10H_2O$: 4EtOH; (D) $1SiO_2$: 0.2TBPOH : $10H_2O$: 4EtOH; (E) and (F) $1SiO_2$: 0.3TBPOH : $10H_2O$ with fumed silica as silica source.

Lower temperatures appear to favor self-pillared morphologies, since synthesis at 408 and 448 K yield self-pillared and regular zeolite crystals, respectively (Fig. 6-10 (a)(b)). Using TBAOH instead of TBPOH results in similar morphologies. However, using TPAOH will lead the formation of conventional MFI. (Fig. 6-10 (c)(d)) Finally, we note that the omission of the aging step at 353K before hydrothermal growth at 388K does not have an effect on the final morphology. These results show that the self-pillared zeolite can be prepared in a rather broad range of synthesis conditions with flexibility to fine-tune its particle size.

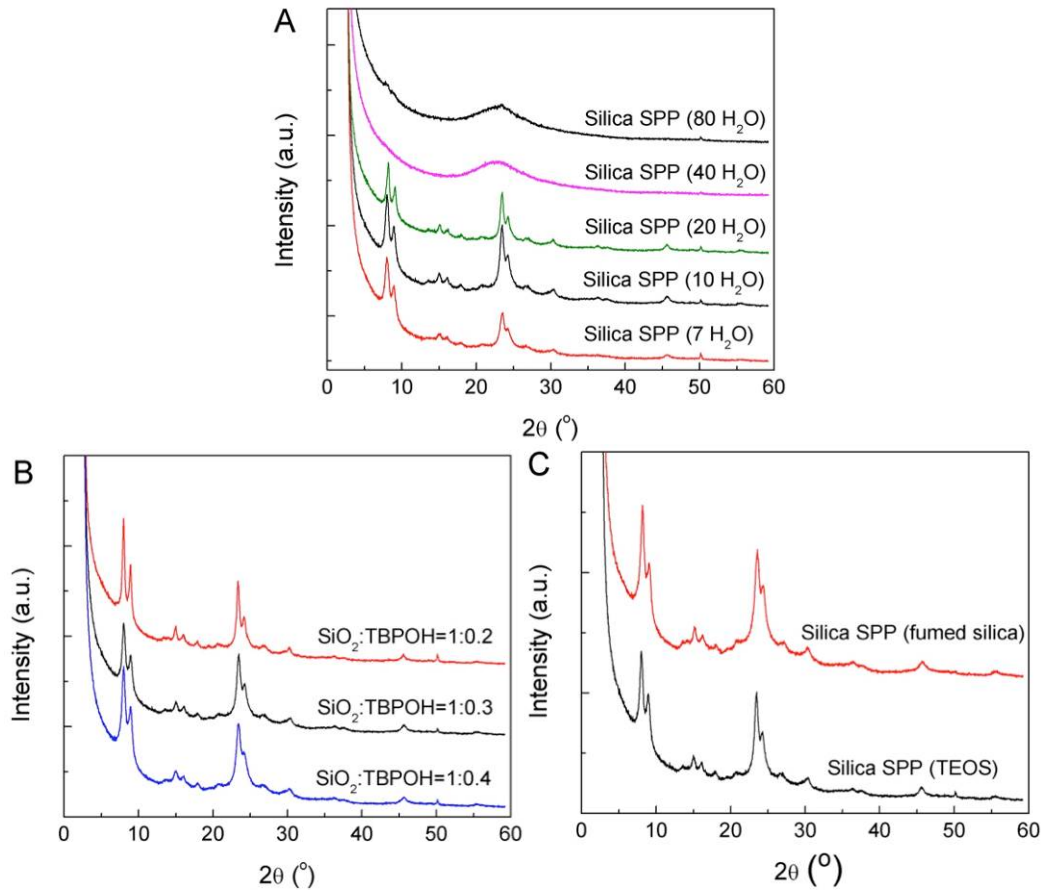

Figure 6-9 X-ray diffraction patterns of the products of SPP zeolites synthesis with different compositions: (A) $1SiO_2$: 0.3TBPOH : yH_2O : 4EtOH, where y ranges from 7 to 80; (B) $1SiO_2$: xTBPOH : $10H_2O$: 4EtOH, where x ranges from 0.2 to 0.4; (C) $1SiO_2$: 0.3TBPOH : $10H_2O$: 4EtOH (made with TEOS) and $1SiO_2$: 0.3TBPOH : $10H_2O$ (made with fumed silica).

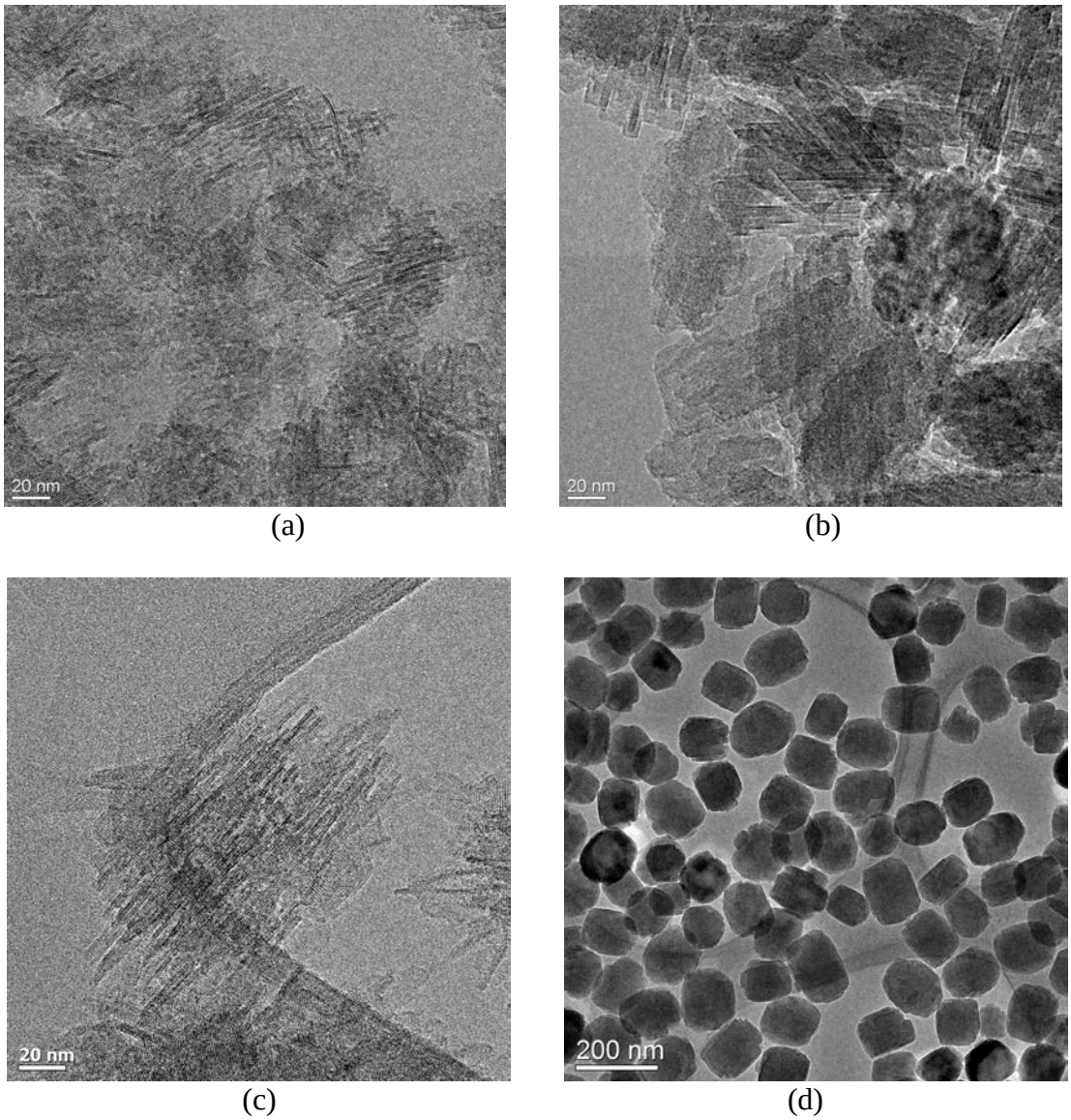

Figure 6-10 More studies on synthesis conditions. Synthesis performed at higher temperatures: (a) 408 K; (b) 448 K. The high-resolution TEM images show that the self-pillared morphology can be prepared at 408 K, but not at 448 K. Using TBAOH instead of TBPOH (c) can lead to the formation of SPP, however, TPAOH (d) will lead to the formation of conventional MFI.

Nucleation of the single-unit-cell lamellae, observed at early stage of growth, should be rationalized by explaining why anisotropic growth should be favored and why growth in the b-direction is greatly inhibited. Tetrabutyl SDAs are known to nucleate and grow MFI crystals [130]. However, unlike their tetrapropyl analogues, they are not

accommodated optimally within the MFI framework with b-axis stacking being the less favored due to the shorter distance of channel intersections along this direction. It is therefore conceivable that they will favor formation of single unit cell lamellae. Previous studies have employed mixtures of SDAs or high temperatures where SDA decomposition is likely, thus compromising TBP's ability to drive anisotropic growth. This may explain why numerous previous studies failed to identify conditions appropriate for single-unit-cell lamellae formation. ^{13}C NMR shows that the SDA is stable under reaction conditions and is incorporated intact in the SPP framework (Fig. 6-7).

A second question is how crystal growth proceeds from the 2 nm lamellae to 200 nm or larger particles with no or very minimal growth along the b-axis of the lamellae. Prolonged exposure of the nucleated lamellae to the precursor sol will eventually lead to some growth along the b-axis eliminating the single unit cell thickness. Therefore, in addition to the anisotropic growth discussed above, some type of protective mechanism must be in operation. We attribute this protective mechanism to branching and we argue that the protection of single-unit-cell lamellae by branching is two-fold (see Fig. 6-11):

(i) As soon as the rotational intergrowth emerges orthogonally to a lamella, a fast growing direction (a-axis of the newly formed branch) is established along the slow growing direction (b-axis) of the parent lamella. The new branch grows fast by consuming nutrients and depleting their availability for growing the parent lamella along the b-axis (Fig. 6-11B).

(ii) As branching takes place with high frequency (every ca. 5 nm), after a few generations of branching, a network of ~5 nm pores is created (Fig. 6-11C),

which strongly inhibits transport of the colloidal precursors present in clear sols (typically sized in the few nm range) [56].

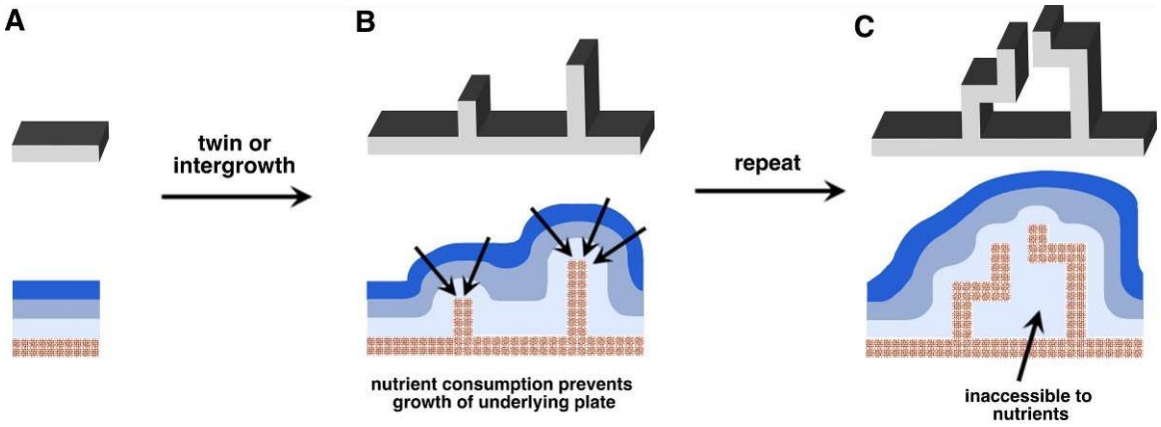

Figure 6-11 Growth model explanation of arrested growth of MFI nanosheets due to nutrient consumption by outgrowing twins (B) followed by creation of inaccessible porosity (C). The darker color away from the models indicates higher nutrient concentration.

Applications

We carried out the exfoliation procedure developed by Maheshwari et al. [99] to the as-synthesized material. As shown in Fig. 6-12, it is possible to obtain individual lamellae. The high-resolution TEM image from one isolated lamella is given in Fig. 6-12B and further confirms that the thickness of the lamellae is 2 nm. The exfoliated lamellar zeolites can be potentially used as building units for selective membranes following the recently reported procedure [7].

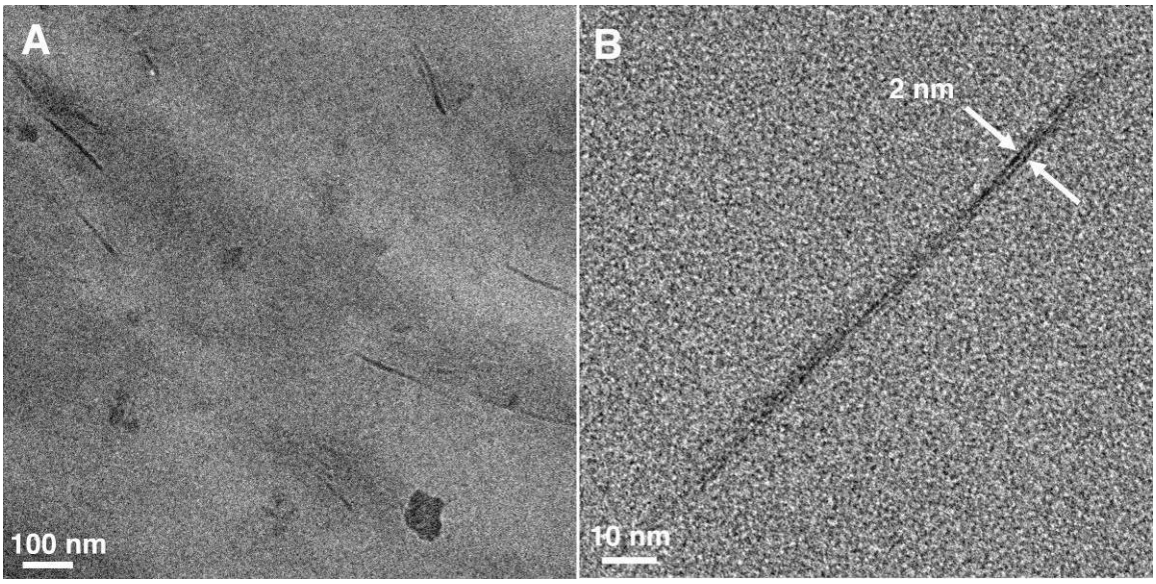

Figure 6-12 (A) TEM image of a thin section of the SPP zeolite-polystyrene composite, showing the existence of zeolite single layers after exfoliation; (B) high-resolution image of one of the exfoliated lamella with a thickness of 2 nm.

To explore the catalytic properties of SPP zeolites, Al was incorporated in the framework (Fig. 6-13) at two different levels of Si/Al: 253 and 75, which required the addition of NaOH [129]. Synthesis in the presence of sodium and aluminum did not prohibit branching and self-pillaring as clearly seen by TEM imaging (Fig. 6-13A and B). Argon adsorption isotherms at 87.3 K and pore size analysis are given in Fig. 6-14, 6-15 and 6-16. The cumulative pore volume plots calculated from NLDFT [123] over the complete pore size range are shown in Fig. 6-4C and indicate the presence of micro- and mesoporosity in the SPP samples. The pore size distributions plotted up to 10 nm (Fig. 6-4D) indicate micropores centered around 0.522 nm, typical of MFI and MEL, and a broad distribution of mesopores (from ~2-7 nm) for both the silica and aluminosilicate SPP in good agreement with the TEM and SEM images.

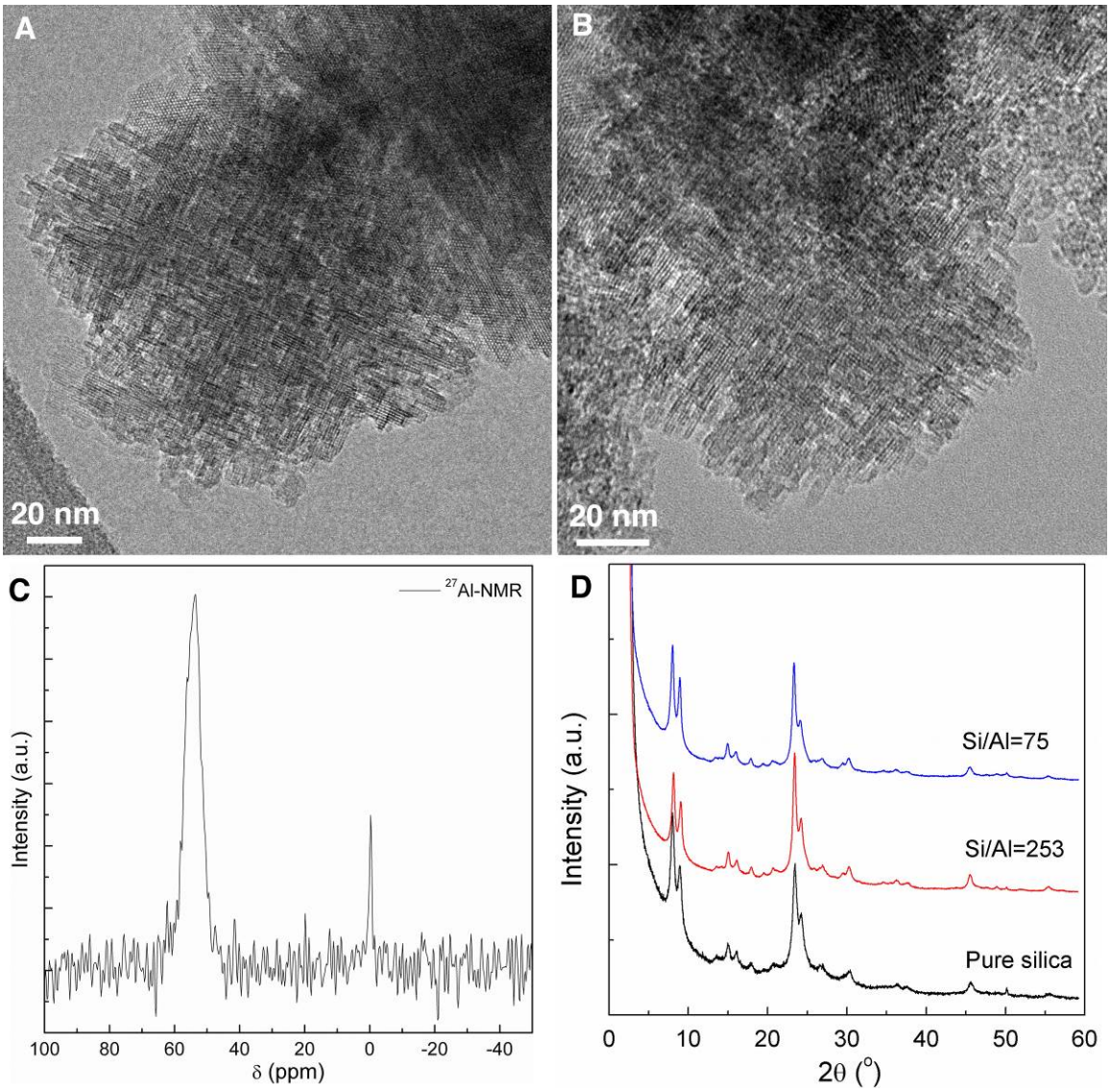

Figure 6-13 Structure and morphology of aluminosilicate SPP zeolite (converted to proton form before characterization): TEM image of the (A) Si/Al=253 and (B) Si/Al=75 SPP showing the single-unit-cell-thick zeolitic lamellae and the mesopores formed by the intersection of the lamellae; (C) ^{27}Al-NMR spectrum of the Si/Al=253 SPP showing that Al is incorporated in the SPP zeolite framework; (D) XRD patterns compared to that from the pure silica SPP zeolite.

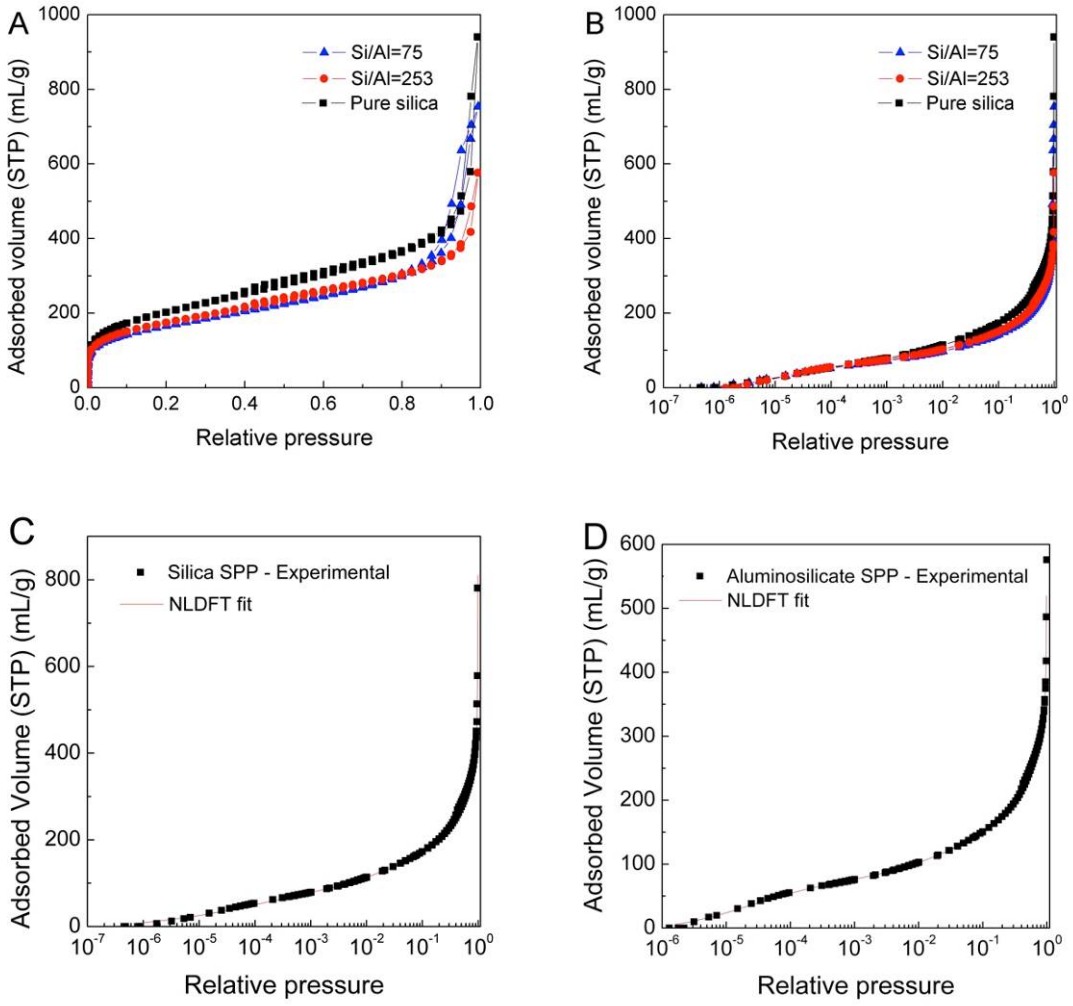

Figure 6-14 Argon (87.3 K) adsorption isotherms plotted on a (A) linear scale and (B) semi-logarithmic scale to highlight the low relative pressure region; (C) Argon (87.3 K) isotherm for the silica SPP zeolite with the NLDFT (cylindrical pore model) fit; (D) argon (87.3 K) isotherm for the aluminosilicate SPP zeolite (Si/Al=253) with the NLDFT (cylindrical pore model) fit.

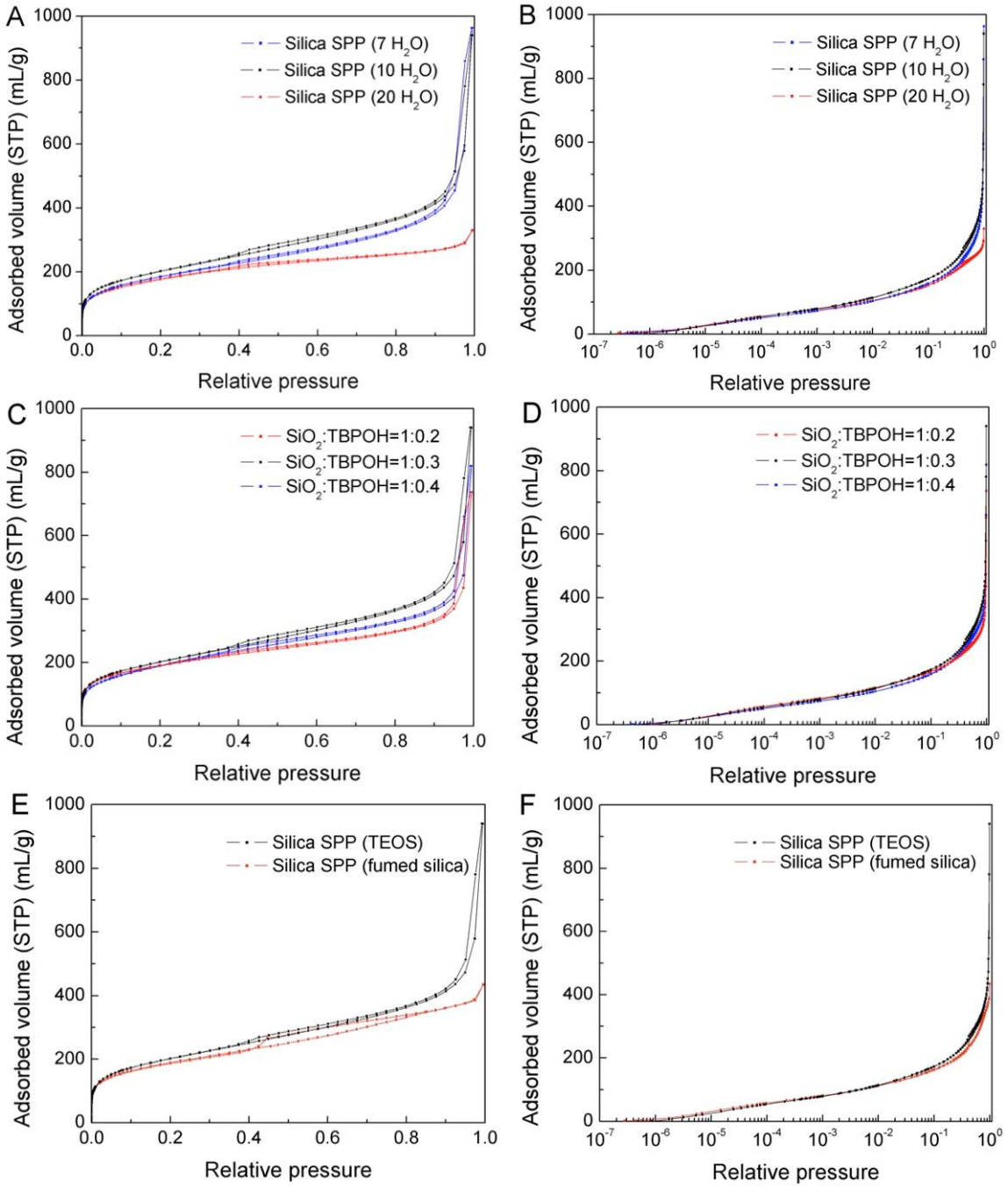

Figure 6-15 Argon (87.3 K) isotherms of the products of SPP zeolites synthesis with different compositions: (A) and (B) $1SiO_2$: 0.3TBPOH : *y*H_2O : 4EtOH, where y ranges from 7 to 20; (C) and (D) $1SiO_2$: *x*TBPOH : $10H_2O$: 4EtOH, where x ranges from 0.2 to 0.4; (E) and (F) $1SiO_2$: 0.3TBPOH : $10H_2O$: 4EtOH (made with TEOS) and $1SiO_2$: 0.3TBPOH : $10H_2O$ (made with fumed silica).

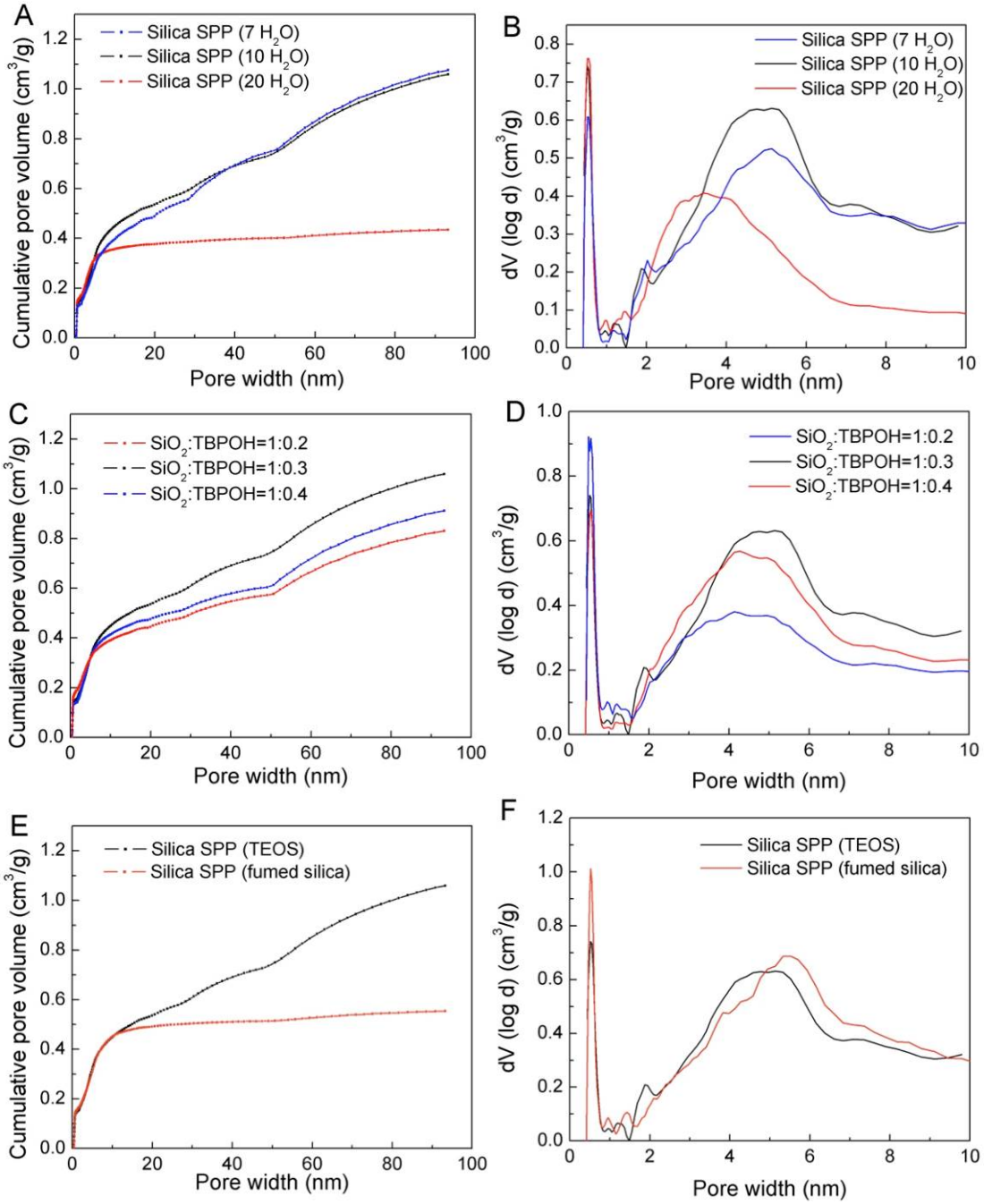

Figure 6-16 Cumulative pore volume and pore size distributions of the SPP zeolites prepared with different compositions: (A, B) $1SiO_2 : 0.3TBPOH : yH_2O : 4EtOH$, where y ranges from 7 to 20; (C, D) $1SiO_2 : xTBPOH : 10H_2O : 4EtOH$, where x ranges from 0.2 to 0.4; (E, F) $1SiO_2 : 0.3TBPOH : 10H_2O : 4EtOH$ (made with TEOS) and $1SiO_2 : 0.3TBPOH : 10H_2O$ (made with fumed silica).

The catalytic properties of SPP were compared with those of pillared MFI [104], three-dimensionally ordered mesoporous-imprinted (3DOm-i) MFI and three conventional MFI catalysts with different crystal size (17, 1.4 and 0.2 μm) [129]. The Brønsted acid site concentrations of all zeolites, including that of the aluminosilicate SPP, were determined by chemical titration methods [127] and were found to agree well with those expected from the Si/Al ratio from elemental analysis.

The fraction of acid sites present at the external surface was determined for each catalyst using a titrant molecule, 2,6-di-*tert*-butylpyridine (DTBP), that cannot enter the zeolite pores. The results were in good agreement with the values expected from the external surface areas of the corresponding catalysts [108] (Table 6-1). Specifically, 30% and 45% of the acid sites in pillared MFI and SPP, respectively, are sites that are accessible by a molecule that cannot enter the micropores, while for a micron-sized crystal this fraction is approximately 2%. As a result of the increase in number of accessible acid sites, the pseudo-first order rate constant for the liquid phase alkylation of mesitylene (a molecule that is effectively excluded from the zeolite micropores) by benzyl alcohol was found to vary by more than two orders of magnitude. However, when normalized per external acid site, the rate constant was found to be nearly invariant across all samples tested (Fig. 6-17A) showing that the reactivity of external acid sites is similar among all samples tested, despite the different morphologies and synthesis conditions.

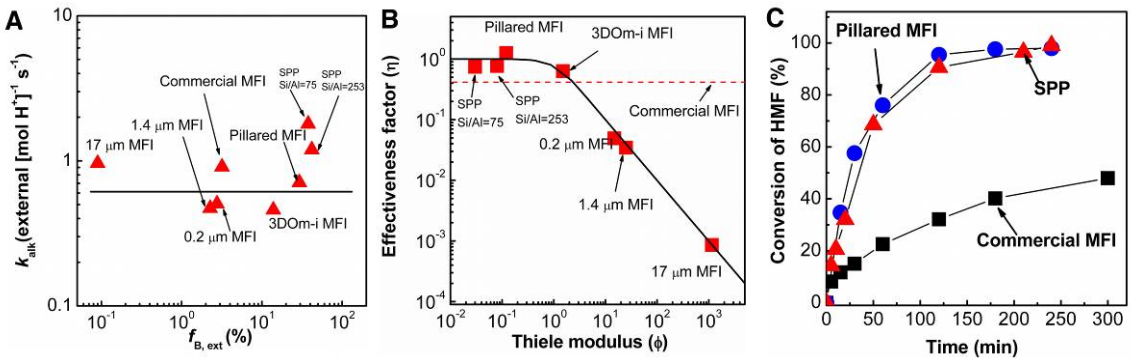

Figure 6-17 Comparison of catalytic performance of SPP zeolite with pillared, 3DOm-i, commercial and conventional (0.2, 1.4 and 17 μm) MFI. (A) Pseudo-first order rate constant per external Brønsted acid site for mesitylene alkylation by benzyl alcohol; (B) Effectiveness factor vs. Thiele modulus plot (solid line) and experimental data. The effectiveness factor of commercial MFI is indicated by the dashed line because the particle size of the commercial zeolite as determined by SEM is broad (0.1 to 1 μm) and therefore, its Thiele modulus cannot be determined. (C) HMF to OBMF conversion vs. time plot for pillared MFI (circles), SPP zeolite (triangles) and commercial MFI (squares).

MFI lamellae are unique among the other available aluminosilicate zeolite lamellae because they have pores that run across the lamella thickness [104]. The nanometer-scale diffusion lengths of pillared MFI and SPP allow for fast transport even for molecules with small micropore diffusivity. In this respect, pillared MFI and SPP are valuable model materials to assess quantitatively diffusion limitations and intrinsic kinetics. The self-etherification of benzyl alcohol in the presence of DTBP (used in order to deactivate the external sites) was considered as an example. The plot of the effectiveness factor vs. the Thiele modulus shows excellent agreement with the experimental data [129, 131]. It can be concluded, that Brønsted acid sites in the micropores of SPP and pillared MFI have similar reactivity with those in conventional and nanocrystalline MFI and that the observed differences in apparent reaction rates can be fully accounted for by diffusion limitations. A comparison of effectiveness factors with that of a commercially available ZSM-5 catalyst (indicated by the dashed line in Fig. 6-17B) reveals that 3DOm-i, pillared MFI and SPP catalysts exhibit higher apparent

reaction rates. Improved behavior of pillared MFI and SPP was also established in other reactions. For example, etherification of 5-hydroxymethyl-2-furaldehyde (HMF) to 5,5'-oxy(bismethylene)-2-furaldehyde (OBMF) proceeds to completion, unlike commercial ZSM-5 which suffers from deactivation (Fig. 6-17C). Since OBMF is a desirable biobased intermediate [132], this finding underscores the potential of single unit cell layers in applications beyond petrochemical processing.

6.4 Conclusions

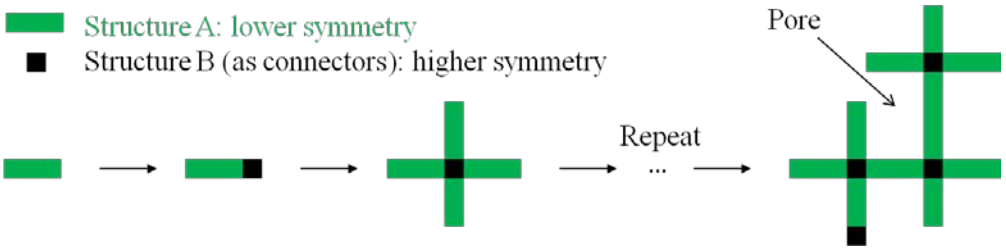

Figure 6-18 Generating high surface area and porosity by repetitive branching. In an environment where structure A (with lower symmetry) and structure B (with higher symmetry) can be formed epitaxially, their intergrowth will form materials with high surface area and porosity.

Branching of zeolite nanometer-sized lamellae through repetitive twinning or other intergrowth process is a new low-cost approach toward hierarchical materials with interconnected micro and mesopores. It is in principle applicable to all zeolite structures that can (i) be grown anisotropically as thin layers and (ii) can support branching at certain acute angles. As shown in Fig. 6-18. In an environment that encourages the epitaxial intergrowth of two structures with different levels of symmetry, the higher-symmetry structure acts as a connector to connect the lower-symmetry structures to create branching. After this process is repeated, a hierarchical zeolite is formed where the

mesopore dimensions are determined by the frequency of branching. Although the work described here features the intergrowth of MFI and MEL to generate a self-pillared pentasil (SPP) hierarchical zeolite, the approach could be generalized.

Chapter 7 Template-free synthesis of faujasite nanoparticles

7.1 Introduction

As shown in the previous chapters, the synthesis of high-silica zeolites (Si/Al>5) usually requires structure-directing agents (SDA) that can direct the formation of the micropore structure of zeolites. The formation of aluminosilicate zeolite, on the other hand, can occur without SDA (i.e., template-free synthesis).[62] In fact, the first synthesis attempts in zeolite synthesis history were carried out without organic templates (such as the first synthetic zeolite, mordenite by Barrer in 1948[133]), until the incorporation of organic SDA (tetramethylammonium) in zeolite synthesis by Barrer and Denny in 1961 for the first time[85]. Involving organic SDA in the system brings robustness in the synthesis, where in many case pure phase material with uniform particle size and morphology can be formed. (such as SOD[65], FAU[66-67], MEL[68], MFI[69-73], LTA[74], and LTL[75] already introduced in Chapter 4) However, in zeolite synthesis, like any templates, SDA is a sacrificing agent, since it has to be removed by calcination or other methods before the pores systems of zeolite can be opened and utilized. Despite of the sacrificing nature of SDA, the synthesis of SDA is usually challenging, which brings in even more additional cost. Economically speaking, template-free synthesis is desired for the industrial preparation of zeolites. However, the control of the synthesis condition for template free systems is challenging in some cases: a minor variation in the composition or other conditions can lead to the formation of a different phase.[93]

FAU is one of the most important zeolites in industry, especially in catalytic cracking (FAU as zeolite Y is used).[134] As proved in Chapter 6, zeolite nanoparticles with ultra-small sizes eliminates deactivation problems and diffusion limitation, which could improve the conversion and selectivity of some catalytic reactions. The template-free approach to prepare FAU has been widely studied, especially in industry. However, there has been no report about the preparation of uniform FAU nanoparticles without organic SDA. The goal of this study is to find a template-free system can produce pure and uniform isolated FAU nanoparticles, and study the formation mechanisms in order to gain control over the crystallization process.

In this chapter, starting from US Patent 3,808,326[135], various synthesis conditions were explored, the formation of faujasite (FAU, EMT or FAU/EMT intergrowth) nanoparticles was achieved with several systems. Some of the systems are optically clear after mixing silicon and aluminum sources (no large aggregates), which brings about convenience to study the formation process using small angle X-ray scattering and cryo-TEM. A clear system that can lead to crystallization of faujasite at room temperature under static conditions was also found. Small angle X-ray scattering and cryo-TEM was also attempted to study the formation process of the nanoparticles.

7.2 Experimental methods

Use sodium silicate solution as silica source

Sodium hydroxide (Mallinckrodt) was dissolved in deionized water, into which sodium silicate solution (Sigma-Aldrich, ~26.5% SiO_2, ~10.6% Na_2O) was added. This clear solution was cooled down in an ice bath (0^oC) for 1 hour. Anhydrous sodium

aluminate (MP Biomedicals) was dissolved in deionized water to obtain a clear solution, and was cooled down in an ice bath (0^{o}C) for 1 hour. The total amount of deionized water added into the Si and Al sources were of fractions of ϕ and 1-ϕ, respectively. In the ice bath, under vigorous stirring, the sodium aluminate solution was added to the sodium silicate solution by a syringe, to achieve the desired composition. In some cases, LUDOX HS-40 (Sigma-Aldrich) was added to the system as a second SiO_2 source, maintaining the same synthesis mixture composition, where the fractions of SiO_2 in sodium silicate solution and LUDOX HS-40 were ψ and 1-ψ, respectively.

The mixture was stirred for 1 hour in an ice bath (0^{o}C). This solution was then aged at room temperature (20^{o}C) for 16 hours, followed by heating at various temperatures with stirring.

Use LUDOX AS-40 as silica source

Sodium hydroxide solid (Mallinckrodt) was dissolved in deionized water, and LUDOX AS-40 colloidal silica (Sigma-Aldrich, 40% SiO_2) was added to the sodium hydroxide solution. The mixture was heated at 90^{o}C for 1 hour, and a transparent gel was obtained. The gel was cooled down in an ice bath (0^{o}C). Anhydrous sodium aluminate (MP Biomedicals) was dissolved in deionized water to obtain a clear solution, and was cooled down in an ice bath (0^{o}C) for 1 hour. In the ice bath, the sodium aluminate solution was added to the silica gel. Precipitation was observed in the sodium aluminate solution. The mixture was stirred for 1 hour in the ice bath, and a transparent solution was

obtained. This solution was then aged at room temperature (20^{o}C) for 16 hours, followed by heating at 85^{o}C for 6 hours with stirring.

Use TEOS as silica source

Sodium hydroxide (Mallinckrodt) was dissolved in deionized water, and TEOS (Sigma-Aldrich) was added to the sodium hydroxide solution. The hydrolysis was carried out at room temperature for 6 hours or 90^{o}C for 1 hour. After the hydrolysis, an immiscible ethanol layer appeared on top of a white gel. The ethanol layer was removed with a pipette and blotted dry. The gel was cooled down in an ice bath (0^{o}C). Anhydrous sodium aluminate (MP Biomedicals) was dissolved in deionized water to obtain a clear solution, and was cooled down in an ice bath (0^{o}C) for 1 hour. In the ice bath, the sodium aluminate solution was added to the silicate gel. Precipitation was observed in the sodium aluminate solution. The mixture was stirred for 1 hour in the ice bath, and a transparent solution was obtained. This solution was then aged at room temperature (20^{o}C) for 16 hours, followed by heating at 85^{o}C for 6 hours with stirring.

Use fumed silica as silica source

Sodium hydroxide (Mallinckrodt) was dissolved in deionized water, and fumed silica (Carb-O-Sil, Sigma-Aldrich) was added to the sodium hydroxide solution. The mixture was heated at 90^{o}C for 1 hour, and a clear solution was obtained. The solution was cooled down in an ice bath (0^{o}C). Anhydrous sodium aluminate (MP Biomedicals) was dissolved in deionized water to obtain a clear solution, and was cooled down in an ice

bath (0^{o}C) for 1 hour. In the ice bath, the sodium aluminate solution was added to the silicate mixture. Precipitation was observed in the sodium aluminate solution. The mixture was stirred for 1 hour in the ice bath, and a transparent solution was obtained. This solution was then aged at room temperature (20^{o}C) for 16 hours, followed by heating at 85^{o}C for 6 hours with stirring.

Characterization

X-ray diffraction was performed on a Siemens Bruker-AXS D5005 diffractometer (Cu Kα radiation). Scanning electron microscopy (SEM) was done on a JEOL JSM-6500 operating at 3.0 kV. The samples were not coated. TEM was done on a FEI Tecnai G^2 F30 TEM equipped with a Schottky field-emission gun operating at 300 kV.

The small-angle X-ray scattering experiments were done on an Anton Parr SAXSess with Cu Kα radiation. For each scattering experiment, approximately 100 μL sample was used to fill a quartz capillary holder, and exposed under X-ray for 35 minutes. The scattering patterns were recorded on image plates, and scanned into the computer.

A cryo-TEM sample was prepared from the suspension at different time. Cryo-TEM sample preparation was conducted in an FEI Vitrobot Mark III vitrification robot. A droplet of the suspension was placed onto a carbon/Formvar-coated copper grid (Ted Pella Inc.) in the climate chamber of the Vitrobot system, where the temperature was kept at 25 °C and the relative humidity was kept at 100%. The specimen was transferred under liquid nitrogen to a Gatan 626 DH cryo-transfer specimen holder, with which imaging was done at -117 ^{o}C.

7.3 Study of synthesis conditions

Composition

In these experiments, composition was chosen as a parameter to study the phase and morphology of the products, where a clear system that can lead to the formation of nanocrystalline zeolite is desired. Sodium silicate solution was used as the silica source. A tertiary phase diagram was introduced in the design of these experiments, similar to Akporiaye *et al.*[93] (where TMAOH is used as SDA). Each phase diagram corresponds to compositions with fixed water molar composition. The phase diagram used in the following syntheses was based on 92.51% (mol/mol) water.

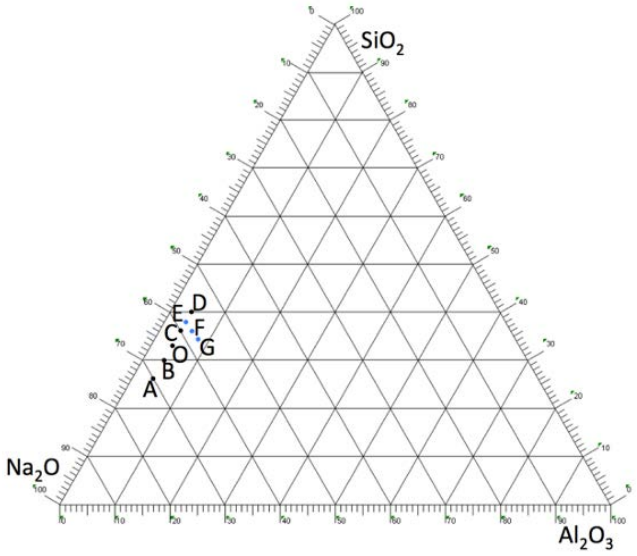

Figure 7-1 A tertiary phase diagram for the template-fres synthesis of aluminosilicate zeolites.

Four compositions were studied firstly in this set of experiments: (A) 70:4:26:1236 (Na_2O:Al_2O_3:SiO_2:H_2O); (B) 66:4:30:1236; (C) 60:4:36:1236; (D) 56:4:40:1236.

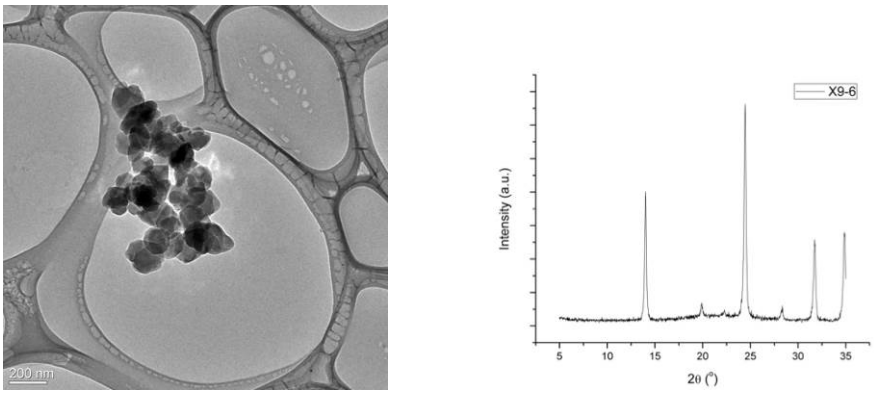

(a) (b)

Figure 7-2 Representative TEM image (a) and powder X-ray diffraction pattern (b) of the products from system (A) 70 Na_2O : 4 Al_2O_3 : 26 SiO_2 : 1236 H_2O.

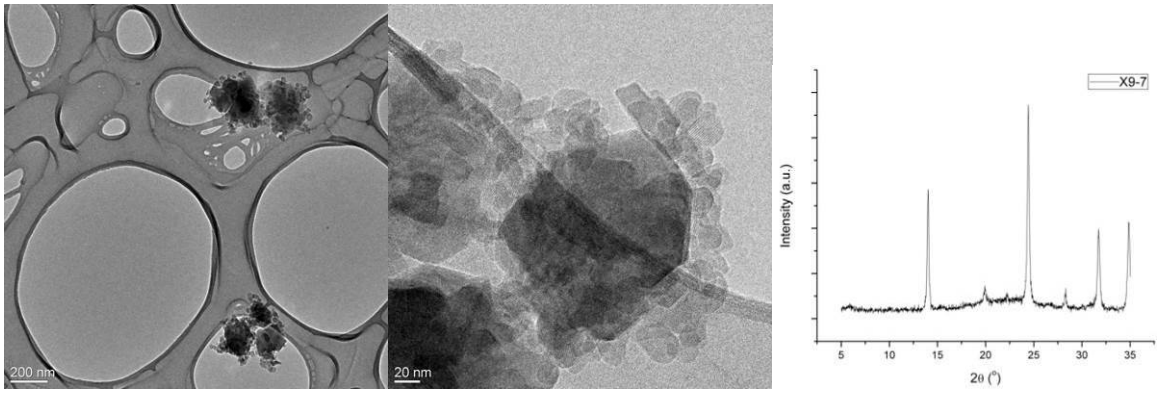

(a) (b) (c)

Figure 7-3 Representative TEM image (a, b) and powder X-ray diffraction pattern (c) of the products from system (B) 66 Na_2O : 4 Al_2O_3 : 30 SiO_2 : 1236 H_2O.

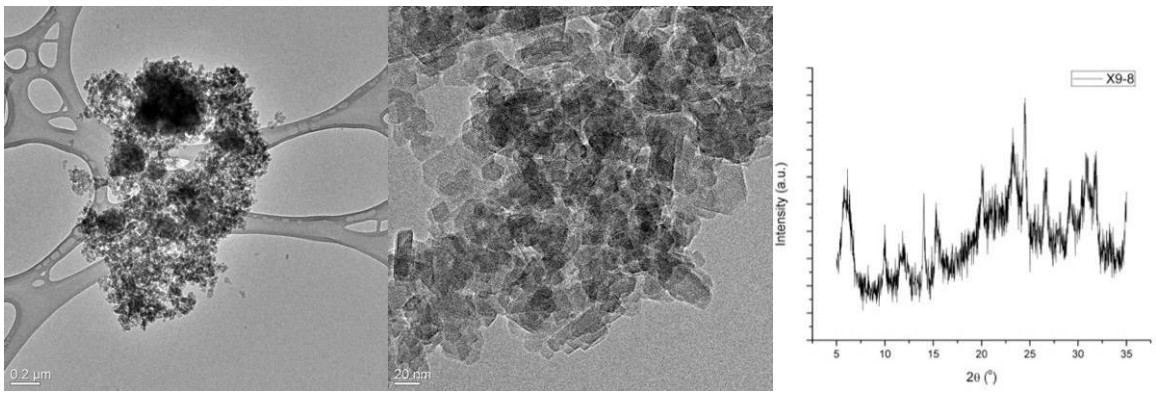

(a) (b) (c)

Figure 7-4 Representative TEM image (a, b) and powder X-ray diffraction pattern (c) of the products from system (C) 60 Na_2O : 4 Al_2O_3 : 36 SiO_2 : 1236 H_2O.

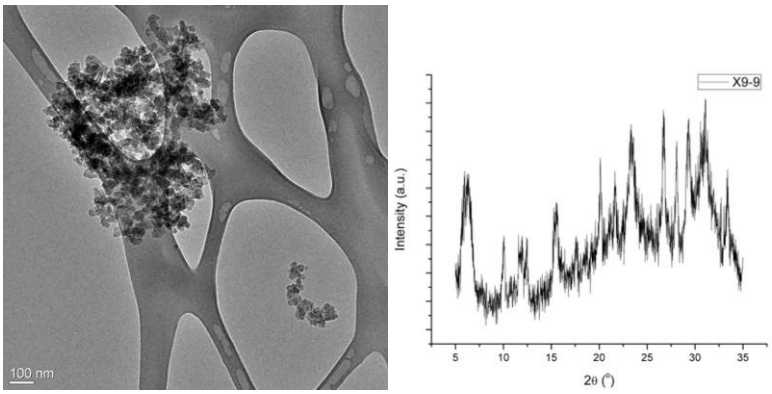

(a) (b)

Figure 7-5 Representative TEM image (a) and powder X-ray diffraction pattern (b) of the products from system (D) 56 Na_2O : 4 Al_2O_3 : 40 SiO_2 : 1236 H_2O.

(A), (B), (C) and (D) all turned into white suspensions right after mixing silicon and aluminum sources. After heating at 85^oC for 6 hours, different crystal phases were observed in them: (A) contains SOD nanoparticles (where SOD is a common dense phase formed in template-free synthesis) (Fig. 7-2); (B) contains a mixture of SOD (major product) and faujasite nanoparticles, as confirmed from TEM and XRD (Fig. 7-3); (C) contains a mixture of faujasite (major product) and SOD nanoparticles (Fig. 7-4); while only faujasite were observed in (D). The crystallite sizes of faujasite in (C) and (D) were found to be 28 nm and 22 nm, respectively, using Scherrer equation from the broadening of the (331) peaks in the XRD patterns. In this case, under the same conditions, less silica will favor the formation of SOD.

Three more experiments with minor variations in compositions were studied to find out how the product phase depends on the composition. Systems (E) 58:4:38:1236, (F) 58:6:36:1236, and (G) 58:8:34:1236 were heated at 85^oC for 6 hours (the same condition as A-D).

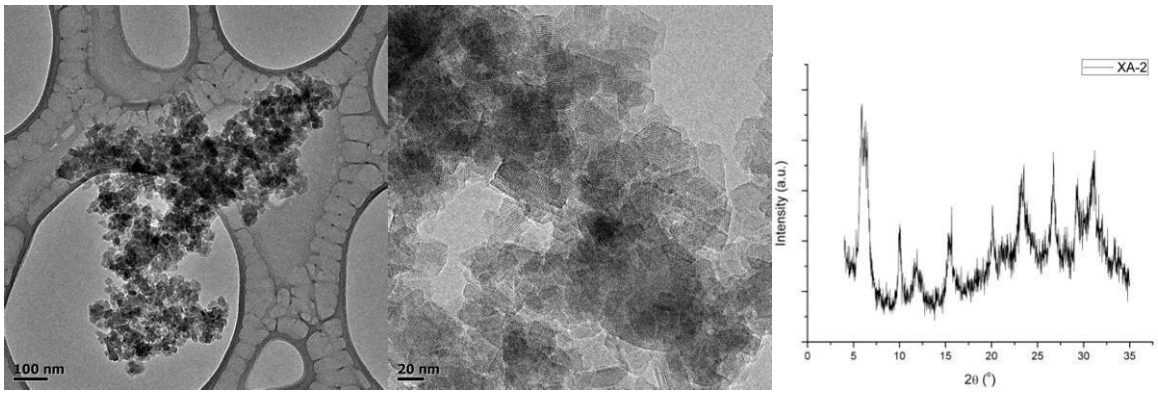

(a) (b) (c)

Figure 7-6 Representative TEM image (a, b) and powder X-ray diffraction pattern (c) of the products from system (E) 58 Na_2O : 4 Al_2O_3 : 38 SiO_2 : 1236 H_2O.

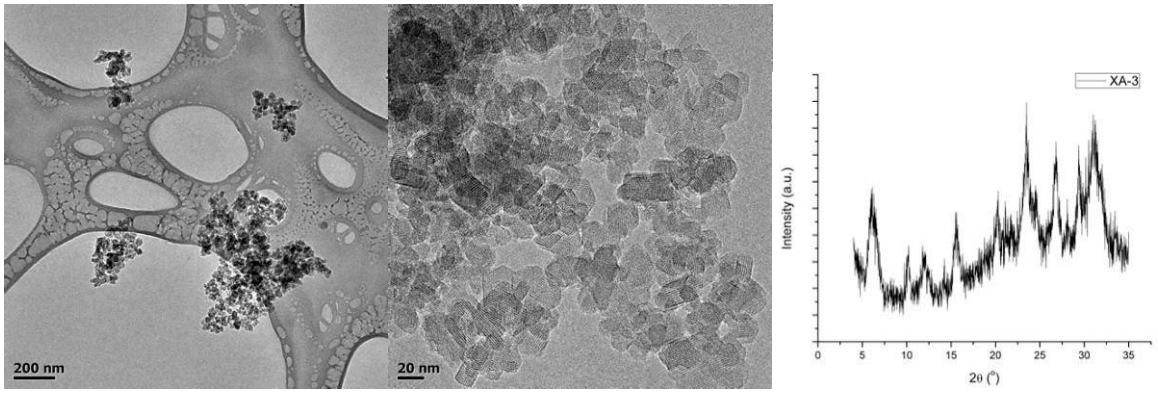

(a) (b) (c)

Figure 7-7 Representative TEM image (a, b) and powder X-ray diffraction pattern (c) of the products from system (F) 58 Na_2O : 6 Al_2O_3 : 36 SiO_2 : 1236 H_2O.

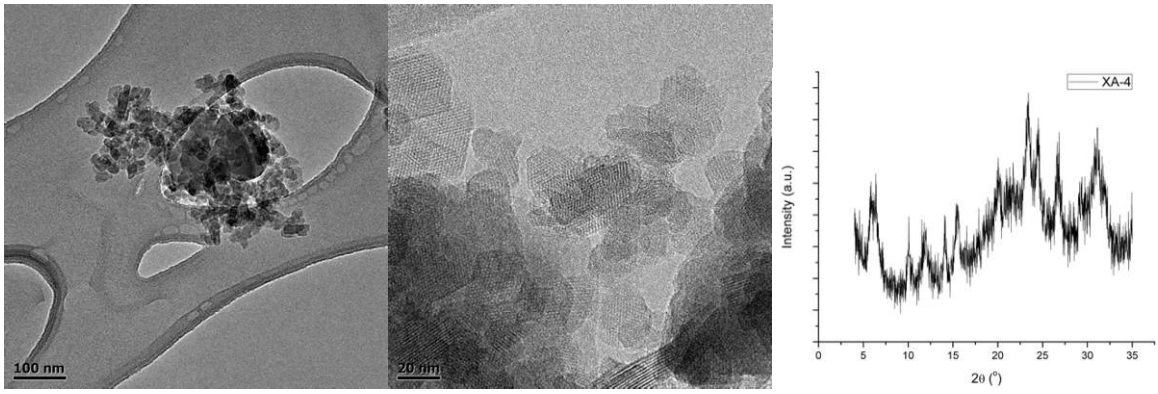

(a) (b) (c)

Figure 7-8 Representative TEM image (a, b) and powder X-ray diffraction pattern (c) of the products from system (G) 58 Na_2O : 8 Al_2O_3 : 34 SiO_2 : 1236 H_2O.

After heating, nanoparticles were observed in all 3 above compositions. (E) and (F) gave faujasite nanoparticles with crystallite sizes of approximately 23 nm and 18 nm, respectively. (G) gave a mixture of faujasite and SOD nanoparticles, where the crystallite size of faujasite is approximately 27 nm. Although the crystallite sizes from these systems are small, these systems are still not clear systems after mixing silicon and aluminum sources.

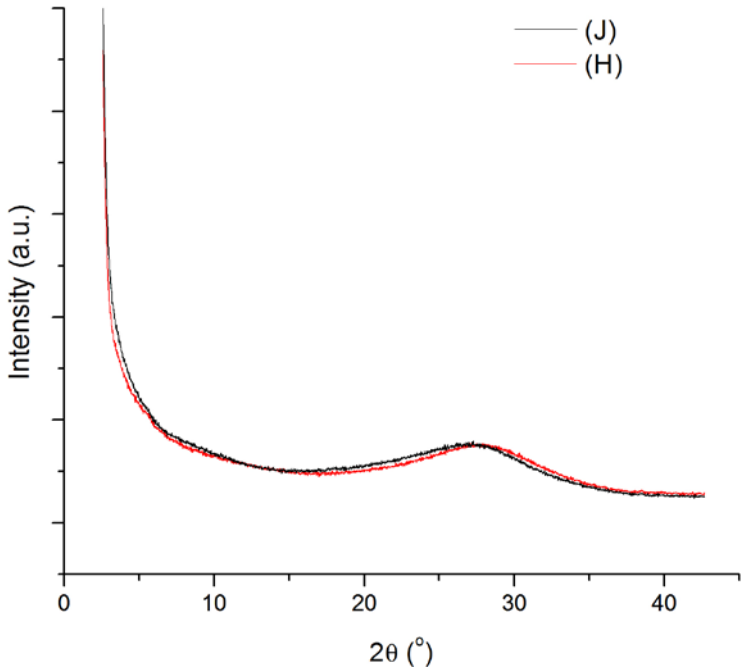

Figure 7-9 XRD patterns of (H) 54 Na_2O : 4 Al_2O_3 : 42 SiO_2 : 9500 H_2O and (J) 15 Na_2O : 4 Al_2O_3 : 31 SiO_2 : 9500 H_2O after heating. (No crystallization was observed in (I)).

In all the above compositions, intergrowth of FAU and EMT was observed in the faujasites nanoparticles (discussed in detail in the next section). More compositions were studied, as an attempt to form higher fraction of FAU or pure FAU, as well as to form clear systems for nanoparticle synthesis. Dilute conditions are chosen as an attempt to prepare a clear system for more convenient cryo-TEM studies: (H) 54:4:42:9500

(Na_2O:Al_2O_3:SiO_2:H_2O); (I) 4.5:2:20:9500; and (J) 15:4:31:9500. The systems were aged at room temperature for 16 hours, and heated at 70°C for 6 hours. The XRD patterns from the systems are shown in Fig. 7-9. However, system (I) was still a clear system after room-temperature aging and heating (thus, no XRD pattern was shown). Thus, these very dilute systems were not able to produce crystalline material.

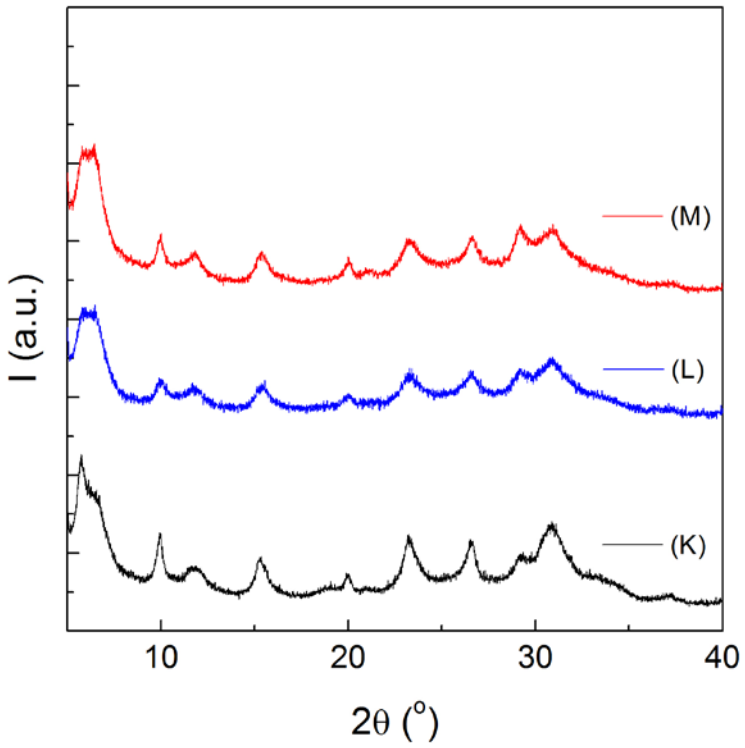

Figure 7-10 XRD patterns of systems (K) 54 Na_2O : 4 Al_2O_3 : 42 SiO_2 : 750 H_2O, (L) 54 Na_2O : 4 Al_2O_3 : 42 SiO_2 : 977 H_2O, and (M) 54 Na_2O : 4 Al_2O_3 : 42 SiO_2 : 1236 H_2O after heating at 50°C for 9 hours.

Based on the compositions (A)~(G), a series of compositions that lead to clear systems after mixing silicon and aluminum sources were found. With less Na and more Si, three compositions (K) 54 Na_2O : 4 Al_2O_3 : 42 SiO_2 : 750 H_2O, (L) 54 Na_2O : 4 Al_2O_3 : 42 SiO_2 : 977 H_2O, and (M) 54 Na_2O : 4 Al_2O_3 : 42 SiO_2 : 1236 H_2O with different amounts of water were studied. They were able to lead to the formation of

nanocrystalline faujasites, after heating at 50°C for 9 hours (XRD patterns shown in Fig. 7-10).

Mixing conditions

Based on composition: (L) 54 Na_2O : 4 Al_2O_3 : 42 SiO_2 : 977 H_2O (where 9 h heating was done at 50°C), more process parameters were explored for better mixing and the convenience to study the early stages of crystal formation.

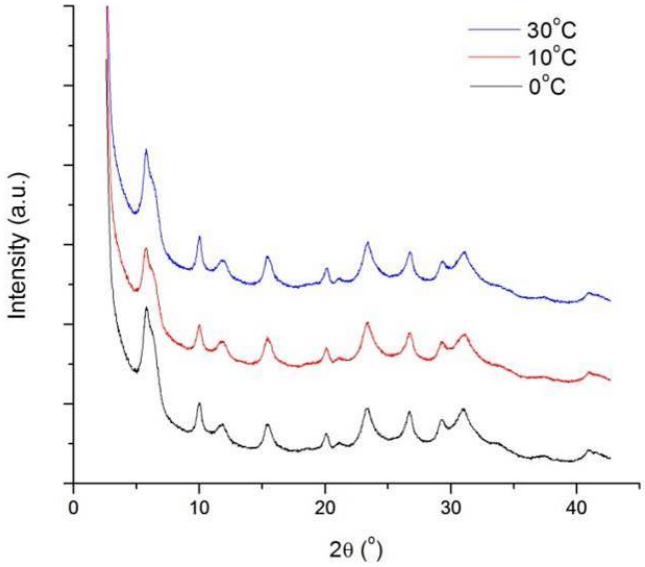

Figure 7-11 XRD patterns of the particles with Si and Al sources mixed at different temperatures.

Mixing the Si and Al sources to give a clear and homogeneous system is desired for the formation of ultra-small nanoparticles, as well as the study of the systems using X-ray scattering and cryo-TEM. For composition (L), a viscous gel was formed after mixing Si and Al sources in ice bath, which prevents the system from mixing well without vigerous stirring. As an effort to decrease the viscosity of the system, mixing was carried out at 0°C, 10°C, and 30°C. The XRD patterns from the products of all three syntheses are identical, as shown below in Fig. 7-10. However, only mixing at 0°C gives a clear

system, mixing at higher temperatures gives precipitation in the system after mixing, although the viscocity is lower. 0°C will be chosen for future studies.

In a typical synthesis procedure, the amount of water to be added was divided to two parts: (1) water to be added to the sodium silicate solution (with a fraction of ϕ); and (2) water to be added to sodium aluminate (with a fraction of 1-ϕ). Different values of ϕ were studied (0.35, 0.45, 0.55, and 0.65). By increasing the fraction of water to be added into the sodium silicate solution (ϕ=0.65), the system becomes less viscous during mixing at 0°C. ϕ=0.65 is chosen for future synthesis.

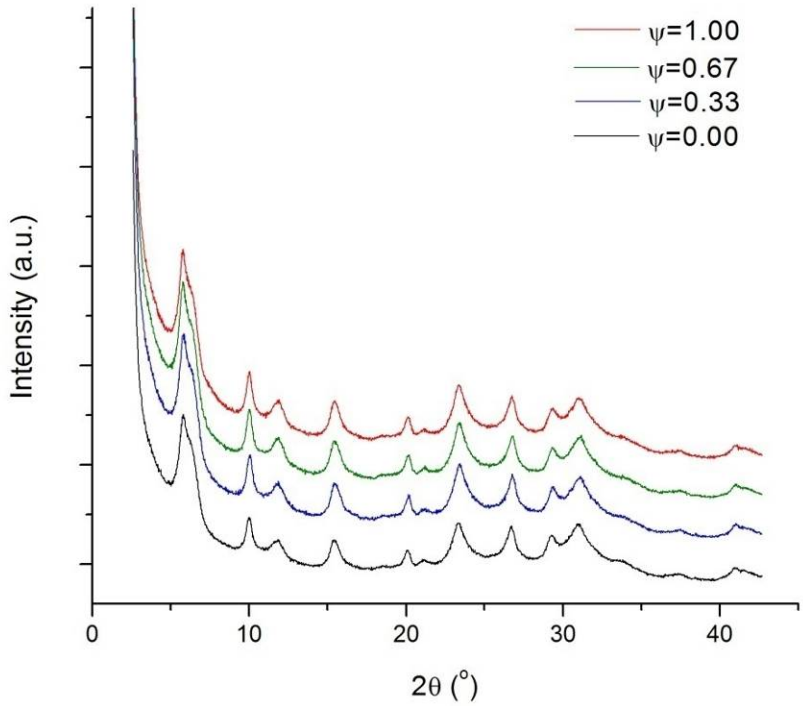

Figure 7-12 XRD patterns of the particles made with two silicon sources: sodium silicate solution and LUDOX HS-40, where the fraction of SiO_2 in sodium silicate solution is ψ.

Synthesis using a mixture of sodium silicate solution and LUDOX HS-40 was also studied. In this series of experiments, the total SiO_2 to be added is divided to two parts: a fraction of ψ of total SiO_2 was added as sodium silicate solution, and 1-ψ was added as

LUDOX HS-40. However, the products made with 4 different ψ (0, 0.33, 0.66, and 1) did not show obvious difference in XRD patterns (as shown in Fig. 7-12). Sodium silicate solution alone was chosen as the method for future studies, since sodium silicate solution can be more easily obtained and used in industrial preparation of zeolites..

As an attempt to prepare pure FAU nanoparticles, besides the study of synthesis parameters, the system was also heated for different lengths of time at 70°C (1 h, 2 h, 6 h, and 24 h) to see if there is phase conversion from EMT to FAU. However, no phase conversion to FAU was observed, as shown in Fig. 7-12. Instead, dense phases (such as SOD) were formed after prolonged heating.

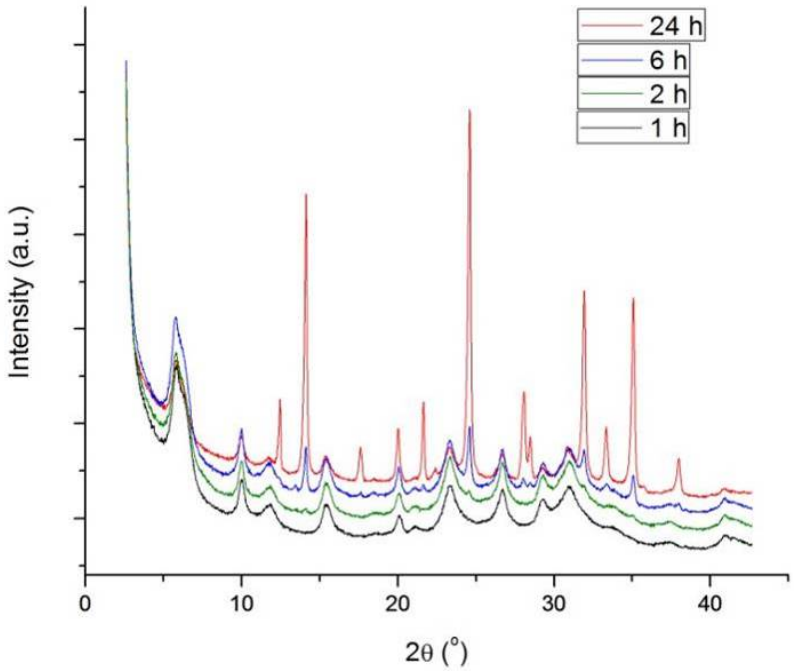

Figure 7-13 XRD patterns of the particles heated for different amount of time at 70°C.

Room temperature synthesis

Room temperature synthesis is usually desired for studying formation mechanisms of zeolites, since prolonged crystal growth process renders sampling more reproducible and

more convenient. With composition (M) 54 Na_2O : 4 Al_2O_3 : 42 SiO_2 : 1236 H_2O, (L) 54 Na_2O : 4 Al_2O_3 : 42 SiO_2 : 977 H_2O, and (N) 56 Na_2O : 4 Al_2O_3 : 40 SiO_2 : 977 H_2O that remain clear after mixing silicon and aluminum sources, room temperature synthesis was also attempted. For these compositions, the systems were aged at room temperature without stirring for 16 hours, and stirred at 30°C for 7 days. The product from these experiments showed the same XRD patterns as the heated systems. (Fig. 7-13)

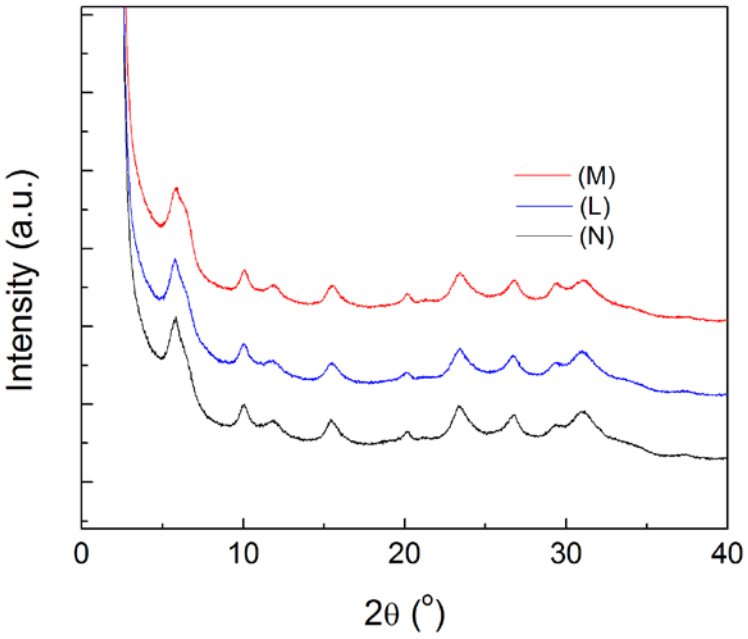

Figure 7-14 Powder X-ray diffraction patterns of the samples after heating at 30°C for 7 days: (M) 54 Na_2O : 4 Al_2O_3 : 42 SiO_2 : 1236 H_2O, (L) 54 Na_2O : 4 Al_2O_3 : 42 SiO_2 : 977 H_2O, and (N) 56 Na_2O : 4 Al_2O_3 : 40 SiO_2 : 977 H_2O.

Furthermore, composition (K) 54 Na_2O : 4Al_2O_3 : 42SiO_2 : 750H_2O was able to yield crystalline faujasite after prolonged room temperature aging (20°C) without stirring. In this system, after the silicon and aluminum sources were mixed in the ice bath and stirred for 1 hour, the system was left at room temperature for 56 days and 105 days. Both systems turned crystalline after the room temperature aging, as shown in the XRD patterns in Fig. 7-15. The patterns are comparable with the pattern of (K) in Fig. 7-10,

where crystallization happened with heating. From this observation, composition (K) could be a good system to follow with small angle X-ray scattering and cryo-TEM to study the formation mechanisms of the nanocrystalline faujasite. In addition, it could also be a good system for confined synthesis (such as synthesis inside 3DOm carbon[44] or other hard templates), since the crystallization does not require stirring or heating.

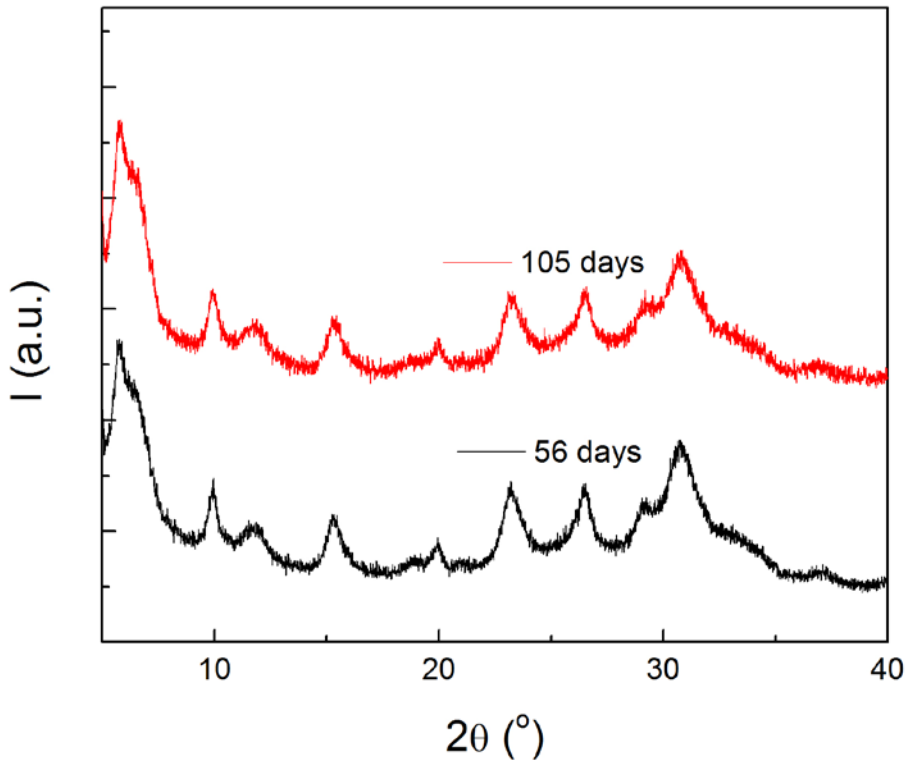

Figure 7-15 XRD patterns of the system (K) after room temperature aging for 56 days and 105 days.

Other parameters

Other parameters involved in the synthesis process were also studied, such as silica source (methods introduced in section 7.2), stirring in the hydrothermal growth, and additives, although they turn out to be minor in the product morphology and phase.

7.4 Characterization

The early stages of crystal formation

Small-angle X-ray scattering (SAXS) and cryogenic transmission electron microscopy (cryo-TEM) are in situ methods complimentary to each other in studying the evolution of particulate systems. Collective information of particle shape and size can be obtained from SAXS patterns, while local structural features can be visualized from cryo-TEM. Although the early stage growth of MFI, one of the most popular and important zeolites in industry, has been studied extensively with SAXS and cryo-TEM,[52, 56] very little has been done to studying the early stages of FAU (an equally popular and important zeolite as MFI) formation. In this section, SAXS and cryo-TEM were attempted to study the early stages of the faujasite nanoparticle formation.

In the previous section, clear systems (K) 54 Na_2O : 4 Al_2O_3 : 42 SiO_2 : 750 H_2O, (L) 54 Na_2O : 4 Al_2O_3 : 42 SiO_2 : 977 H_2O, and (M) 54 Na_2O : 4 Al_2O_3 : 42 SiO_2 : 1236 H_2O were obtained by optimizing the synthesis parameters. These systems were aged for up to 16 hours, and underwent heating at various temperatures. The same systems were studied using SAXS, and the methods to study the systems using cryo-TEM were also proposed. The photos in Fig. 7-16 are the systems (L) and (M) during room-temperature aging. As shown, the systems turn cloudy and forms a thick and translucent gel upon 16 h room-temperature aging.

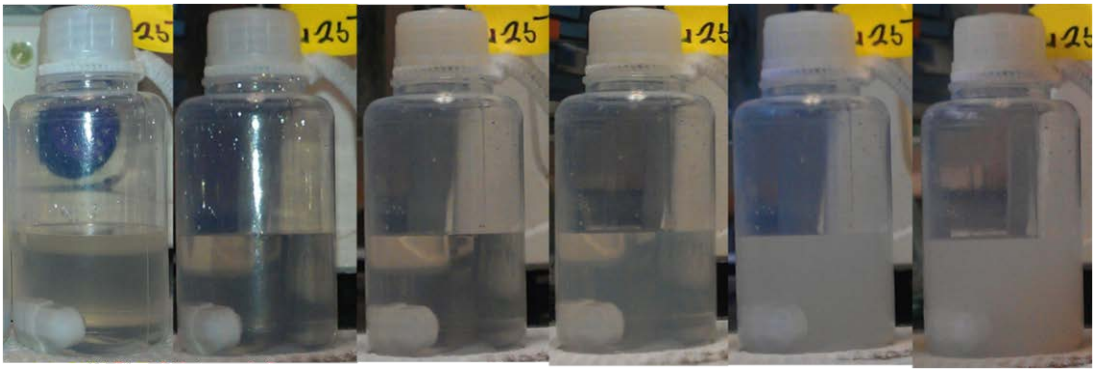

(L)

(M)

Figure 7-16 Photos of the system (L) and (M) taking after different amount of time during room-temperature aging (0 min, 20 min, 50 min, 2.5 h, 3 h, 6.5 h from left to right in both (L) and (M)).

Small-angle X-ray scattering

The system described above was followed by small-angle X-ray scattering to study the structure of the early stage of the synthesis mixture.

As soon as the 1-hour mixing was done in the ice bath, a small amount of mixture was transferred to the quartz holder for a scattering pattern. The synthesis mixture was then taken out and divided to many parts for room-temperature aging. After 1, 2, 3, 4, 8, and 16 hours of room-temperature aging, as well as 0.75, 1.50, 3, 6, and 9 hours heating at 50^{o}C after the room-temperature aging, a scattering pattern was taken. The scattering

patterns are shown in Fig. 7-17 and Fig. 7-18, where the patterns in Fig. 7-18 are those with background (water and holder) subtracted.

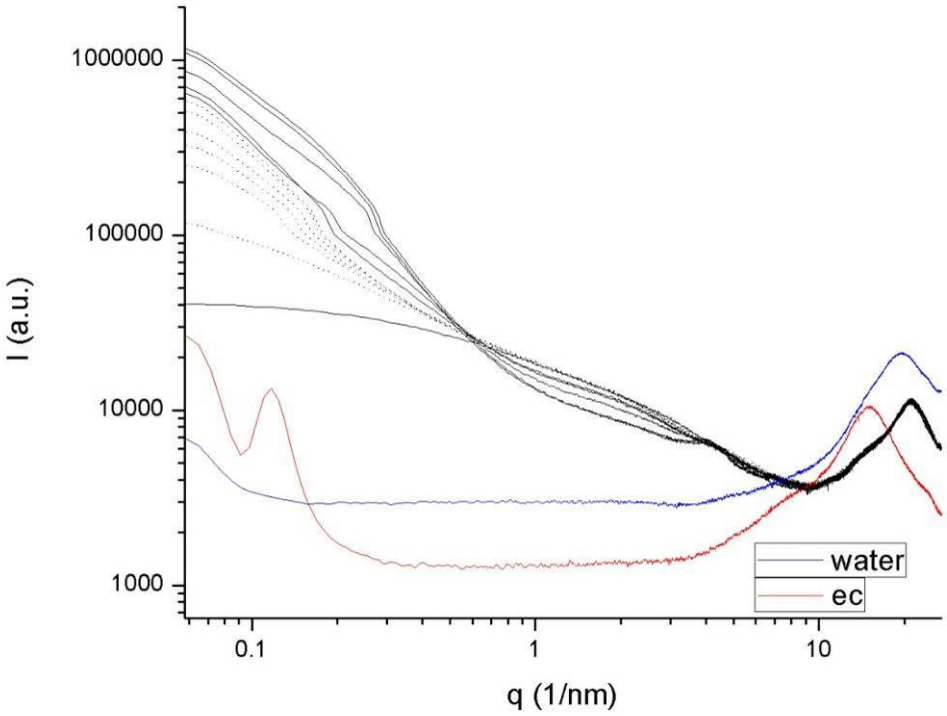

Figure 7-17 SAXS patterns of the system (L) after different amount of room-temperature aging time and heating time. (At q=0.1 nm^{-1}, from low to high intensity: water (blue), empty cell (red), 0 h (solid line), 1 h, 2 h, 3 h, 4 h, 8 h, and 16 h of R.T. aging (dashed lines), 45 min, 90 min, 3 h, 6 h, and 9 h of heating at 50°C (solid lines))

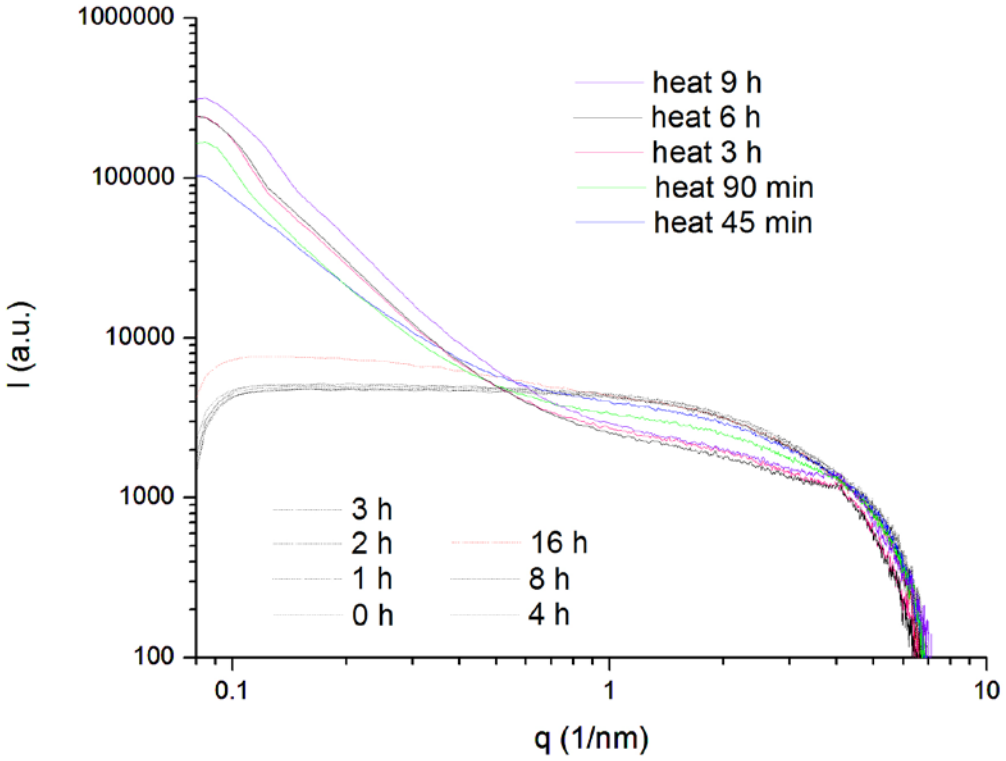
1000000
100000
10000
1000
100
I (a.u.)
0.1
1
10
q (1/nm)
heat 9 h
heat 6 h
heat 3 h
heat 90 min
heat 45 min
3 h
2 h
1 h
0 h
16 h
8 h
4 h

(K)

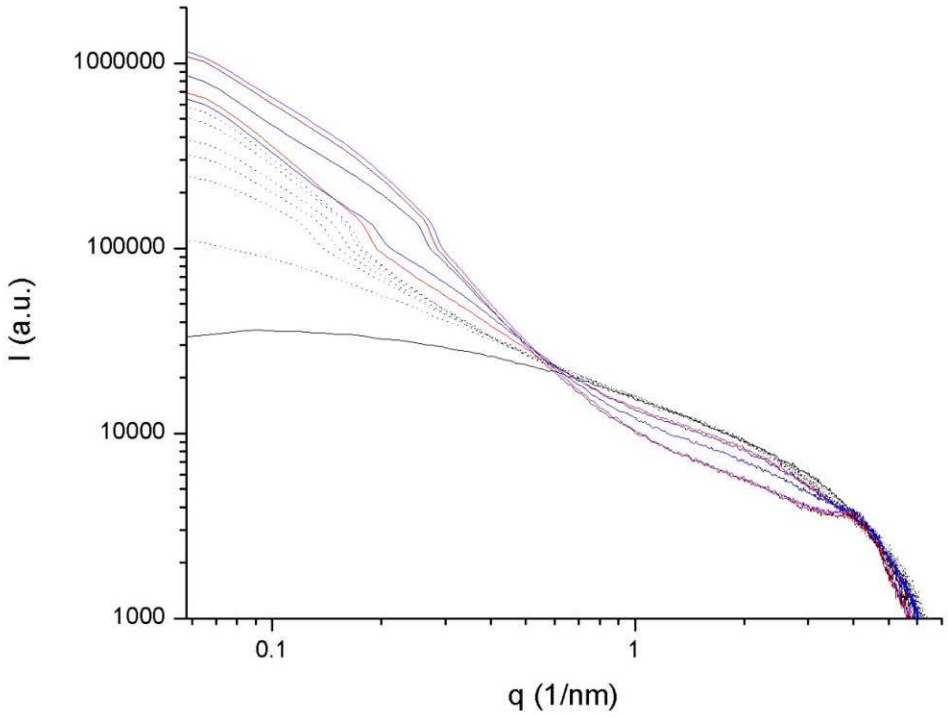
1000000
100000
10000
1000
I (a.u.)
0.1
1
q (1/nm)

(L)

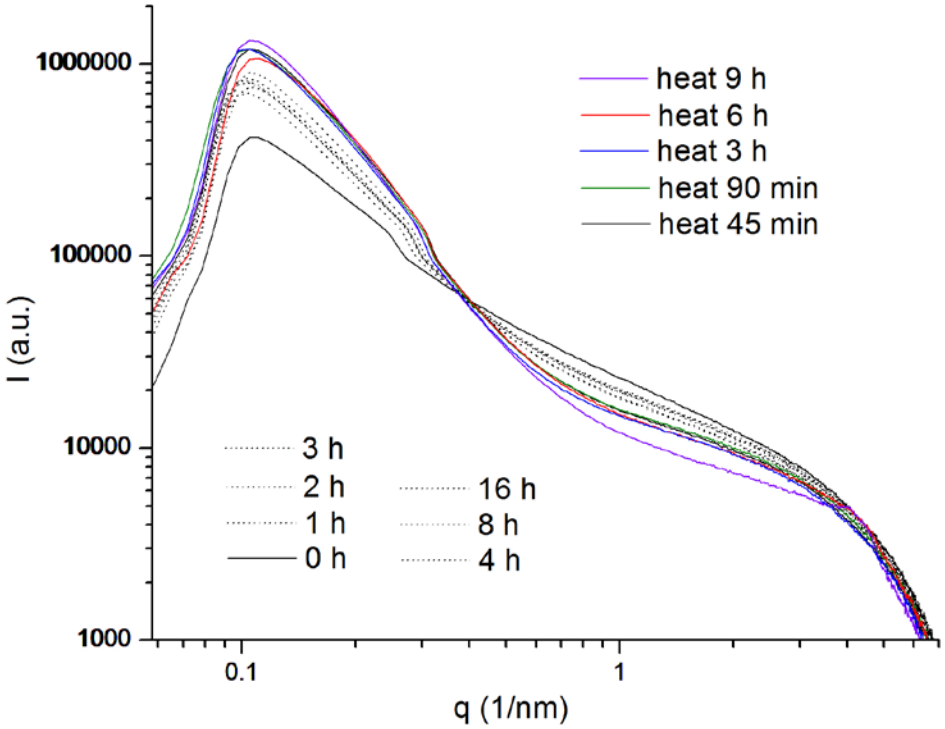

(M)

Figure 7-18 SAXS patterns with background subtracted (For (L), at q=0.1 nm-1, from low to high intensity: 0 h (solid line), 1 h, 2 h, 3 h, 4 h, 8 h, and 16 h of R.T. aging (dashed lines), 45 min, 90 min, 3 h, 6 h, and 9 h of heating at 50oC (solid lines). Legends of (K) and (M) are drawn on the graphs.)

From the patterns (Fig. 7-18), it can be concluded that nanoparticles start to form during the room temperature aging. Comparing to (L), system (K) has less water, and the majority of nanoparticles started to emerge at a later stage (after 16 h aging); while in (M), with more water, nanoparticles emerge right after mixing silicon and aluminum sources, although the system is still optically transparent at that stage. Therefore, the systems at early stages are good candidates to be examined with cryo-TEM for evidences of nucleation. For all 3 systems, the scattering intensity kept increasing during aging and heating. The main observation from these scattering patterns is a feature moving to larger scattering vector q with time, which could possibly relate to a feature with decreasing size. Using $d=\pi/q$ as an estimation, for the specific feature in (L) that appears from 0.2

nm^{-1}, the corresponding size evolved from 24 nm to 17 nm during R.T. aging, and from 17 nm to 11 nm during heating. This is probably due to the crystallization procedure. The size of this feature also depends on the amount of water in the system: in (M), the features appear within a very narrow range around 0.3 nm^{-1}, which corresponds to a smaller feature size; in (K), the features appear at 0.1 nm^{-1} (some larger features are beyond the resolution of the instrument), which corresponds to a larger feature size. However, small angle X-ray scattering alone cannot provide direct evidence of this feature or the types of particles in the system. Cryo-TEM studies should be performed to this system to reveal the evolution of the system.

For systems (L) and (M), TEM images were taken after 16 hours room temperature aging as well as after heating the system, as shown in Fig. 7-19 and Fig. 7-20, respectively. From these images, it turned out that right after aging, the size and morphology of the particles already resemble those of the crystals (such as the hexagons in Fig. 7-19 (a) that are not crystalline). Also considering that room temperature aging for prolonged time can also lead to crystallization, we can infer that the crystallization probably happens within each nanoparticle formed during the aging stage. This could also be related with the shrinking feature observed from the gradual evolution of the SAXS patterns. However, more direct characterization methods, such as microscopy, are needed to unveil this.

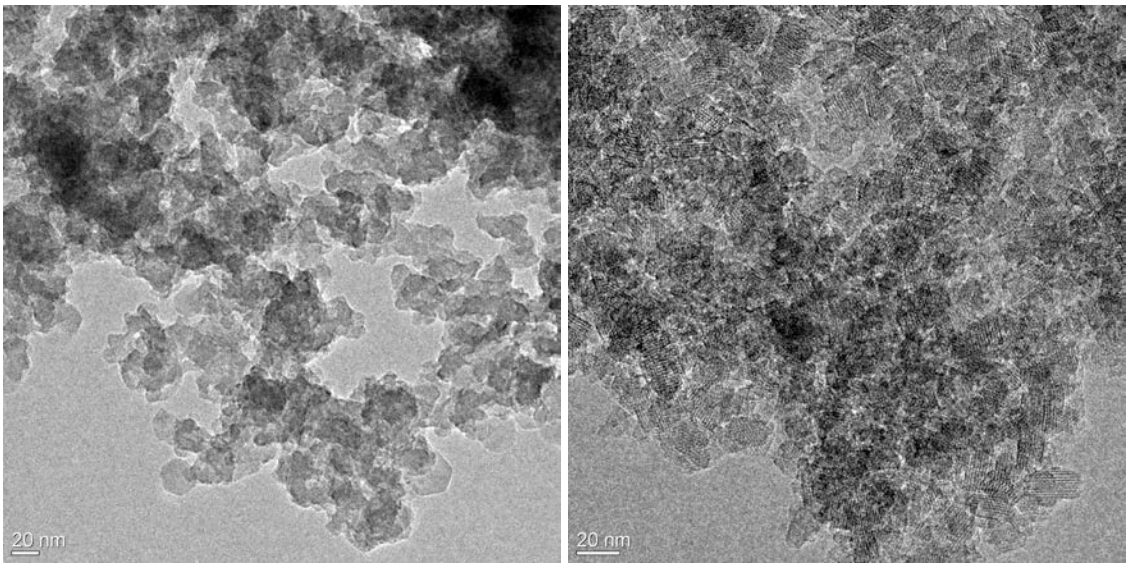

(a) (b)

Figure 7-19 System (L) after room temperature aging (a) and after heating at 50°C for 9 hours (b).

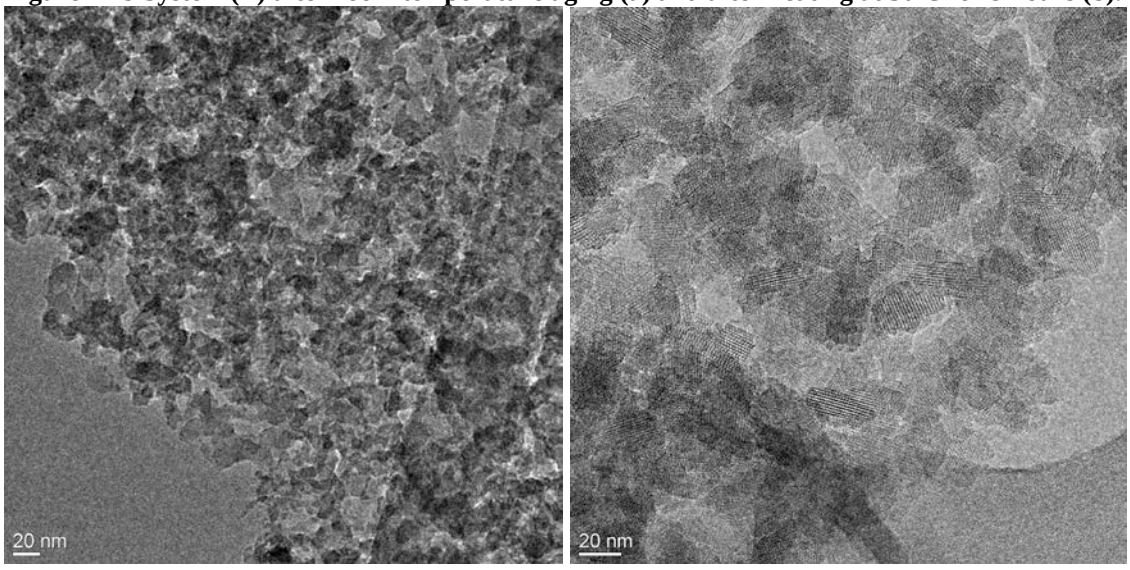

(a) (b)

Figure 7-20 System (M) after room temperature aging (a) and after heating at 50°C for 9 hours (b).

Cryo-TEM

Cryogenic transmission electron microscopy (cryo-TEM) was attempted to the synthesis mixture. In sample preparation of cryo-TEM, samples are vitrified at a fast cooling rate, with which solvent in the system will not form crystalline phase. This prevents the solvent from being an artifact in the imaging of particles of interest. This method will hopefully be helpful for revealing the morphology and structure change of the particles in the early stages of the nanoparticle formation.

There are mainly two available methods for the sample preparation of cryo-TEM. One method is plunge freezing[57], the other is high-pressure freezing followed by cryo-microtomy[136]. In the former method, 3 μL sample was taken out and deposited onto a copper grid in a controlled environment vitrification system (FEI Vitrobot III), where the temperature of the chamber of the Vitrobot was maintained at 25^{o}C, and the humidity was maintained at 100%. The grid was quickly plunged into liquid ethane, and a vitrified thin layer of the system is obtained. This method was applied to the system being studied. However, comparing to the TEOS-TPAOH-water system for studying MFI formation, the synthesis mixture in this work is more concentrated, the sample prepared using plunge-freezing was too thick for TEM. Two images are shown in Fig. 7-21.

Cryo-TEM sample preparation by plunge freezing will be attempted more. In addition, cryo-microtomy is another method to prepare samples for cryo-TEM. In this method, the synthesis system will be vitrified at a very fast rate using high-pressure freezing, and sectioned to thin slices at liquid-nitrogen temperature (cryo-microtomy) for

TEM studies. These two methods will both be applied to the system of interest, and more studies will be performed in the future.

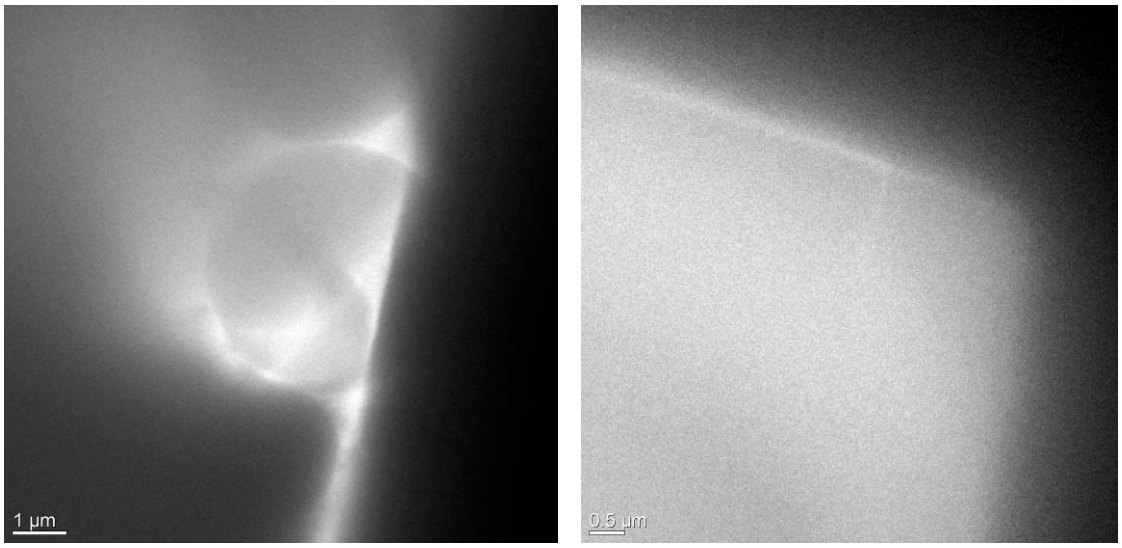

(a) (b)

Figure 7-21 Cryo-TEM images of the sample prepared by plunge-freezing

Intergrowth and phase determination using simulation methods

Intergrowth of FAU and EMT is common in faujasite, where FAU sheets and EMT sheets stack sequentially in a certain pattern in one crystal.[115] Each pattern of intergrowth can be classified into one material. Intergrowth is also seen in the particles prepared in this project. For example, in systems (E) and (G), FAU/EMT intergrowth was observed from TEM (Fig. 7-22), where the stacking faults are circled out.

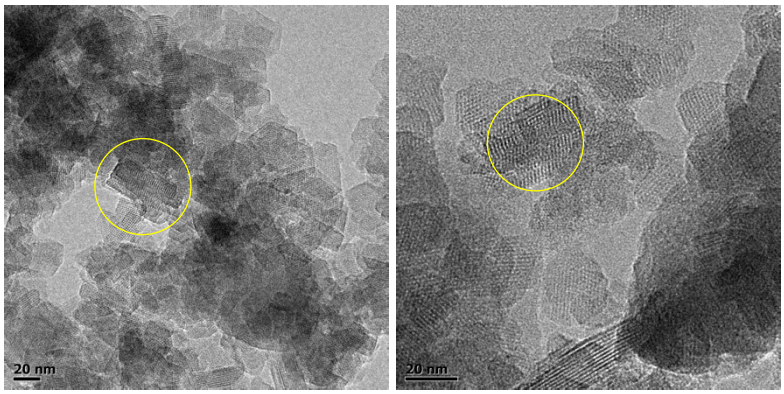

(a) (b)

Figure 7-22 FAU/EMT intergrowth observed in systems (E) and (G). The stacking faults are circled out.

The degree and pattern of intergrowth can be observed from TEM images. However, in order to get collective information, powder XRD should be a better method. DIFFaX is a software package for simulating powder XRD patterns of particles with intergrowth.[137] In order to study and control the phases of the particles, simulation using DIFFaX was performed. The experimental results are compared with the simulation.

Following Treacy et al.[115], a series of simulation was done to FAU/EMT intergrowth system. The following is a set of XRD patterns of bulk phases (infinite layer size, infinite layer number) simulated using DIFFAX (Fig. 7-23). They agree well with those in Treacy et al.

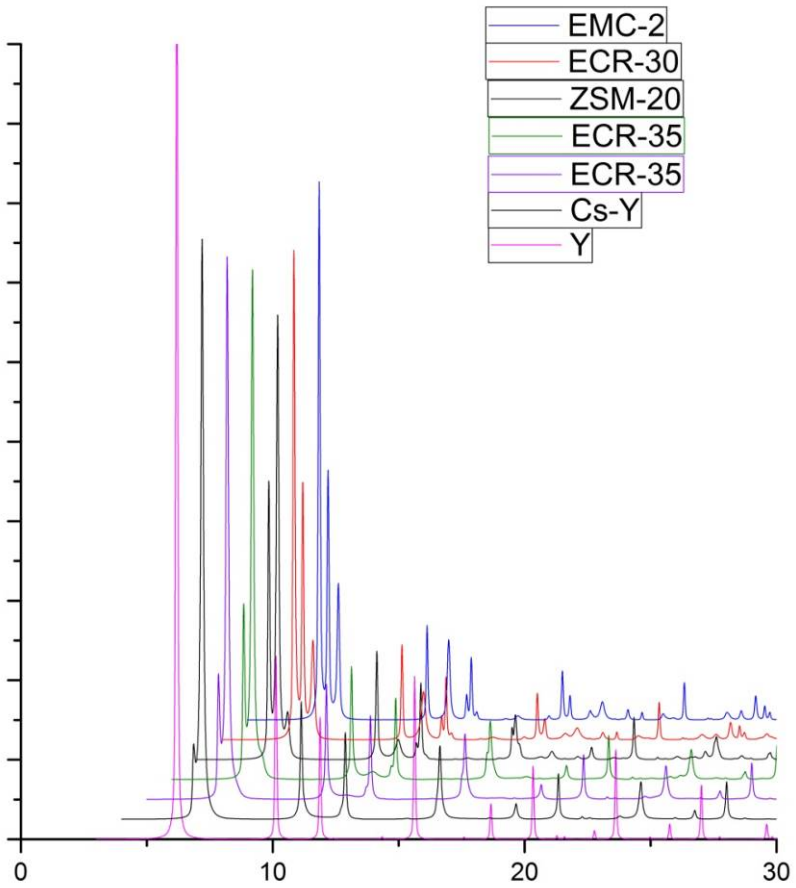

Figure 7-23 Simulated powder XRD patterns of bulk phases (infinite layer sizes, infinite number of layers) using DIFFaX, where the phases are those studied in Treacy et al. The patterns agree well with those in Treacy et al.[115]

The simulated particle size was then decreased from bulk phase to the actual size observed from TEM, i.e., 25 nm wide, 15 nm thick plates (25 nm wide layers, 15 layers for each particle). The simulated patterns are shown in Fig. 7-24. With the same particle size, a map of XRD patterns from α_{FF}=0-1, α_{EE}=0-1 was also generated for reference (Fig. 7-25).

In these maps, α_{FF} and α_{EE} are overall transition probabilities of the whole sample: α_{FF} is the probability of the next layer being FAU given that the current layer is FAU, α_{EE} is the probability of the next layer being EMT given that the current layer is

EMT. Each type of faujasite has its own pair of α_{FF} and α_{EE} to define its pattern of stacking fault.

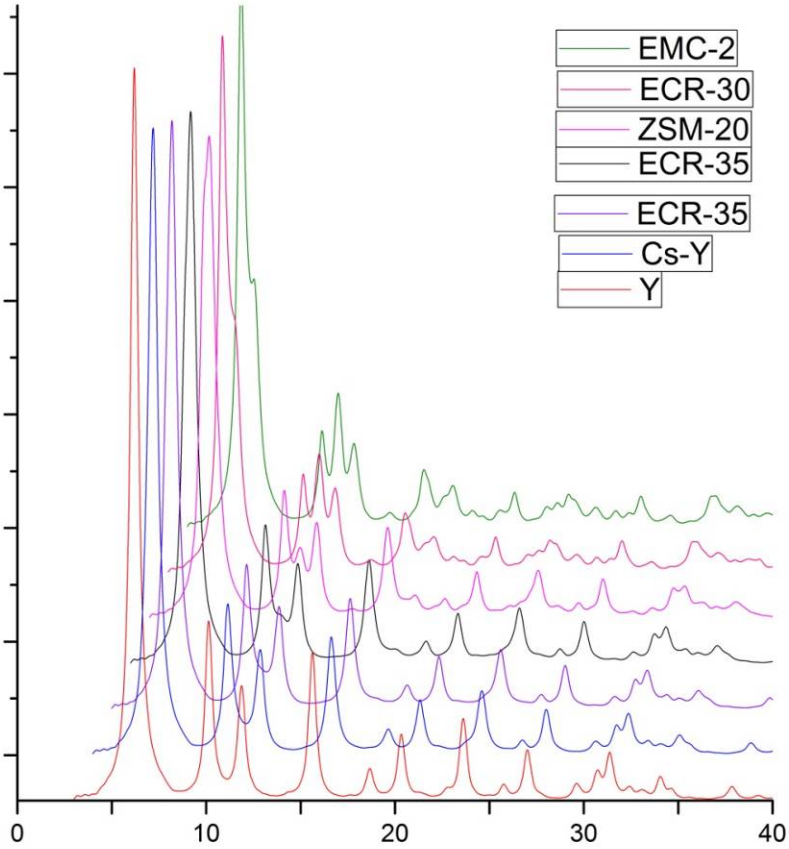

Figure 7-24 Simulated powder XRD patterns of nanoparticles using DIFFaX, where the phases are those studied in Treacy et al.[115] The nanoparticle dimensions are: 25 nm wide layers, 15 layers for each particle.

Figure 7-25 Simulated powder XRD patterns of nanoparticles using DIFFaX. The nanoparticle dimensions are: 25 nm wide layers, 15 layers for each particle. The horizontal axis is α_{EE} from 0 to 1 (0.0, 0.2, 0.4, 0.6, 0.8, and 1.0), the vertical axis is α_{FF} from 0 to 1 (0.0, 0.2, 0.4, 0.6, 0.8, and 1.0).

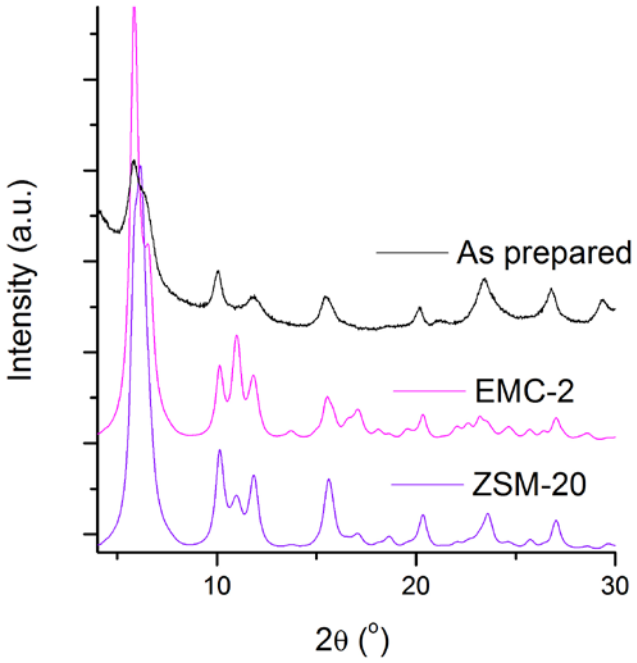

Figure 7-26 Comparison of the experimental XRD pattern with simulated XRD pattern of EMC-2 and ZSM-20 (simulated particle dimension: 25 nm wide layers, 15 layers for each particle).

The peaks are broadened after decreasing the size. Although the agreement is not excellent, the pattern from ZSM-20 (α_{FF}=0.90, α_{EE}=0.90) is very similar to the experimental pattern (Fig. 7-26). Therefore, structures around the ZSM-20 range were taken for further studies (Fig. 7-27). The particle size was also decreased to 10 layers to simulate similar broadening as the experimental patterns (Fig. 7-28).

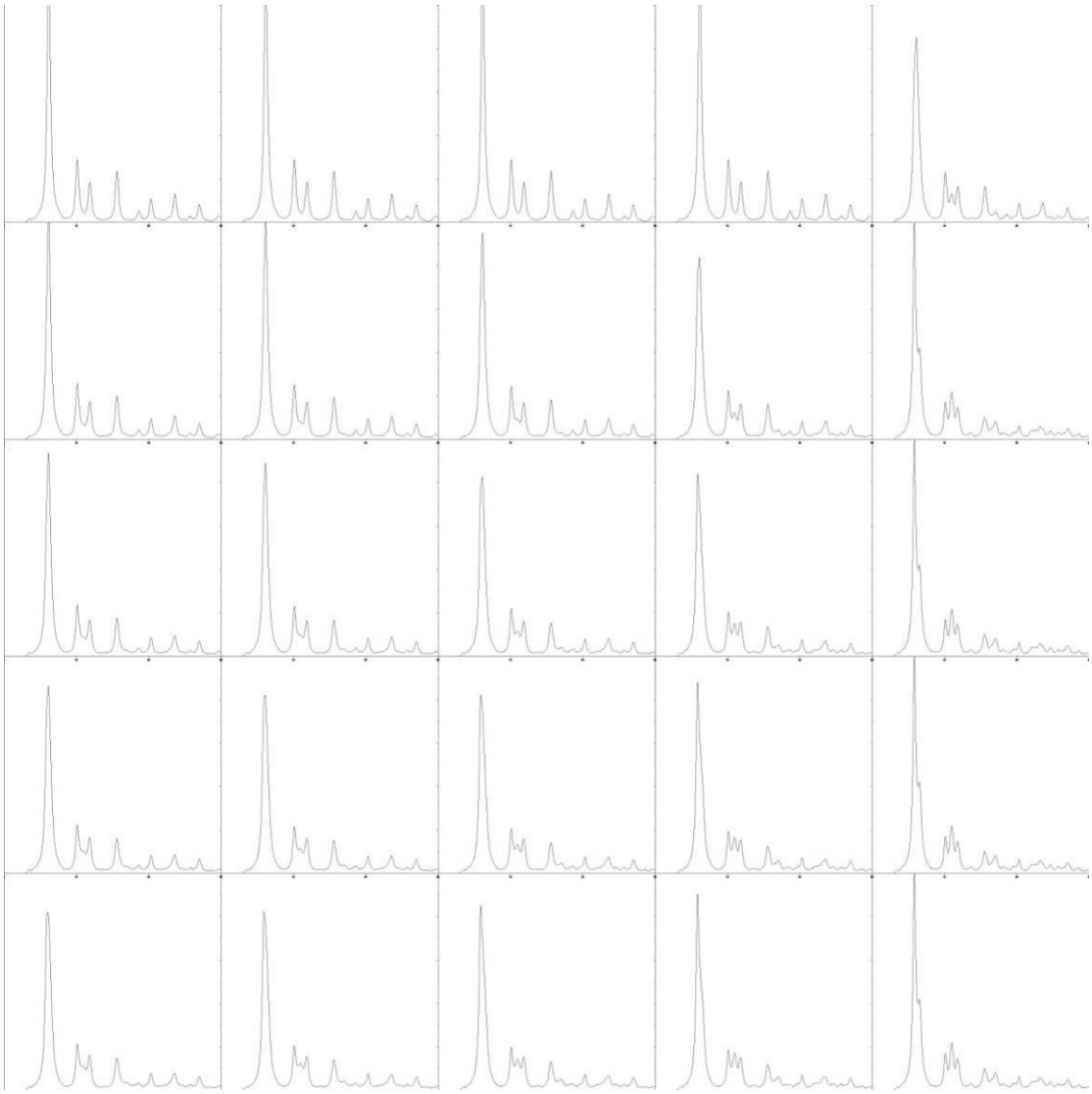

Figure 7-27 Simulated powder XRD patterns of nanoparticles using DIFFaX. The nanoparticle dimensions are: 25 nm wide layers, 15 layers for each particle. The horizontal axis is α_{EE} from 0.80 to 1 (0.80, 0.85, 0.90, 0.95, and 1.0), the vertical axis is α_{FF} from 0.80 to 1 (0.80, 0.85, 0.90, 0.95, and 1.0).

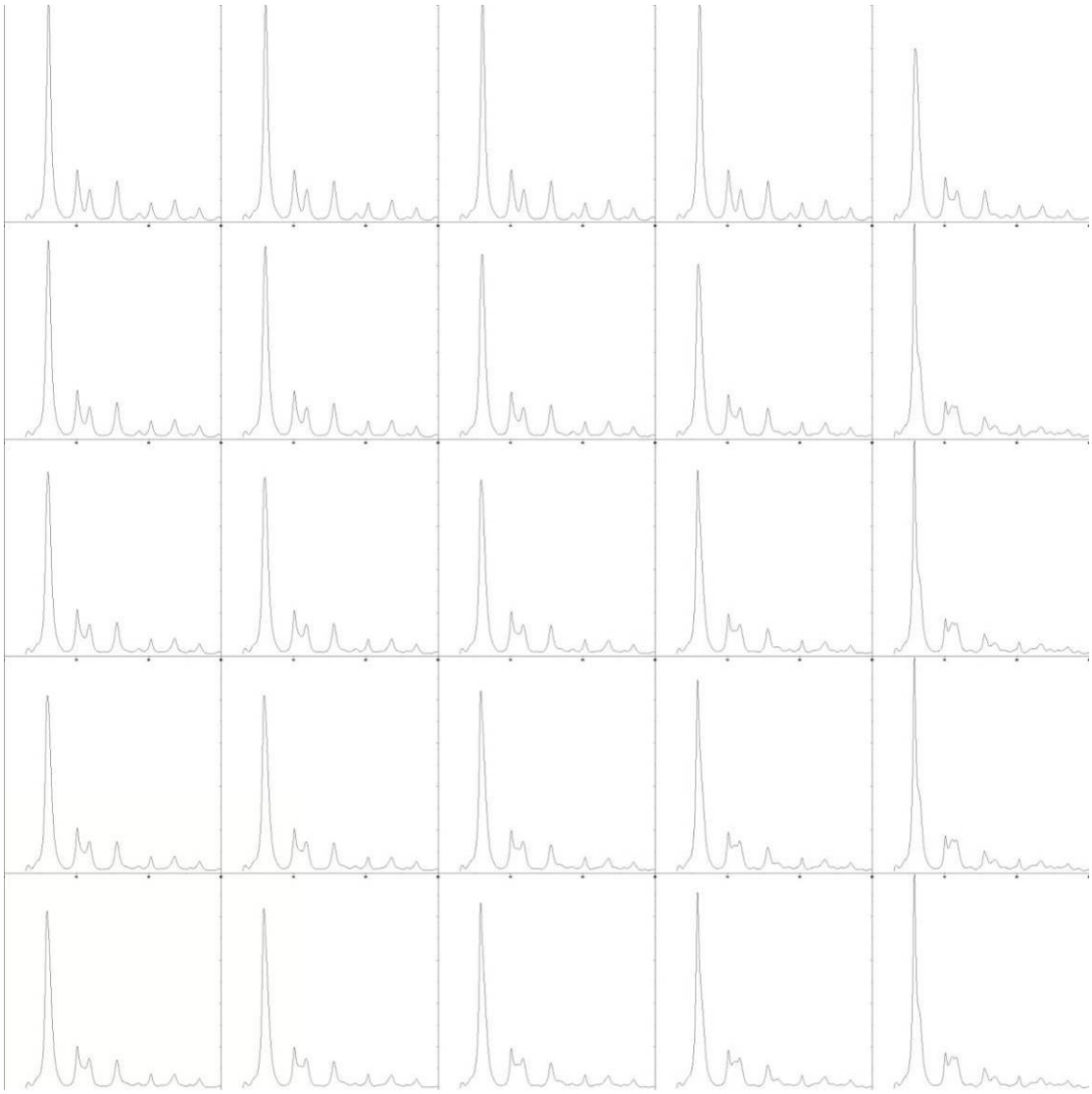

Figure 7-28 Simulated powder XRD patterns of nanoparticles using DIFFaX. The nanoparticle dimensions are: 25 nm wide layers, 10 layers for each particle. The horizontal axis is α_{EE} from 0.80 to 1 (0.80, 0.85, 0.90, 0.95, and 1.0), the vertical axis is α_{FF} from 0.80 to 1 (0.80, 0.85, 0.90, 0.95, and 1.0).

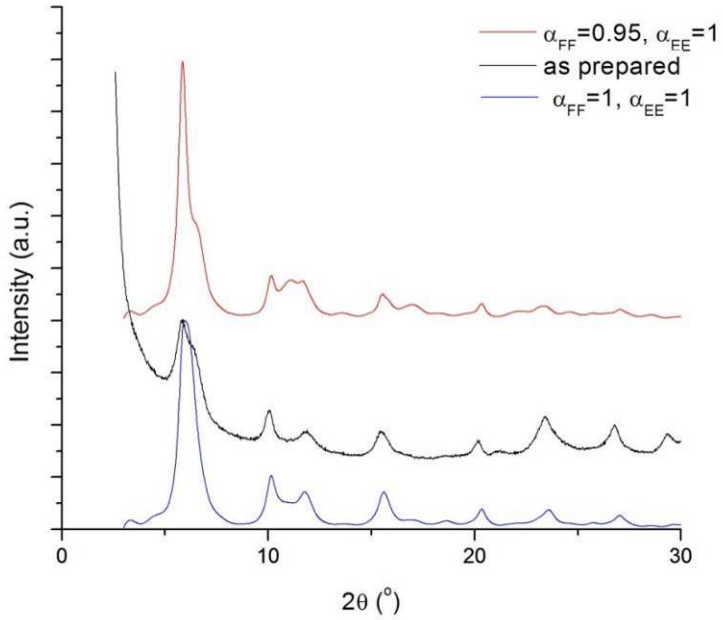

Figure 7-29 Comparison between experimental XRD pattern and simulated patterns (α_{FF}=0.95, α_{EE}=1, and α_{FF}=α_{EE}=1).

However, by comparing the experimental pattern with the simulated pattern (Fig. 7-29), no distinct conclusion can be drawn. In Fig. 7-29, the experimental pattern agrees well with α_{FF}=α_{EE}=1 at high angles (2θ>10°), but agrees with α_{FF}=0.95, α_{EE}=1 at lower angles. It is possible that the as-synthesized product is a mechanical mixture of two phases: when the particles are large (with infinite layers), it is easier to calculate the transition probabilities accurately due to the large number of layers involved; however, when the particles have limited stacking layers, it is very probable that each particle exhibit its own stacking pattern, thus its own transition probabilities, i.e., each nanoparticle is a different material. Simulation from nanoparticles using powder power theorem should be applied to this system and compare with the experimental pattern.[30] The degree of intergrowth should also be calculated from TEM images to provide more information of the phase of the material.

7.5 Conclusions and proposed future work

In this chapter, several clear systems to form faujasites nanoparticles were found. The particle size formed with those methods is below 30 nm. The particles are intergrowth of FAU and EMT. Systems that can crystallize faujasites at room temperature were also found. Characterization methods were developed to study the structure and formation process of the nanoparticles.

In the future, more synthesis parameters will be studied, as an effort to prepare pure FAU nanoparticles, instead of FAU/EMT intergrown particles. The parameters include: (1) the content of dissolved CO_2 in the water for the synthesis; (2) cations and anions contaminations in the synthesis system; (3) other possible contaminations in the system; and (4) more compositions.

For the study of formation mechanisms of the nanoparticles, high-pressure freezing followed by cryo-microtomy and cryo-TEM will be attempted, in order to visualize the formation of the zeolite nanoparticles.

Apart from X-ray diffraction and scattering (experiments and simulation), gas adsorption will also be used as an attempt to determine the phase of the materials (FAU and EMT). Argon adsorption of pure FAU and EMT will be performed, and compared, which could possibly reveal the difference in their micropore structures. If argon adsorption is able to distinguish FAU and EMT, it will be applied to the nanoparticles made in this chapter.

Chapter 8 Concluding remarks

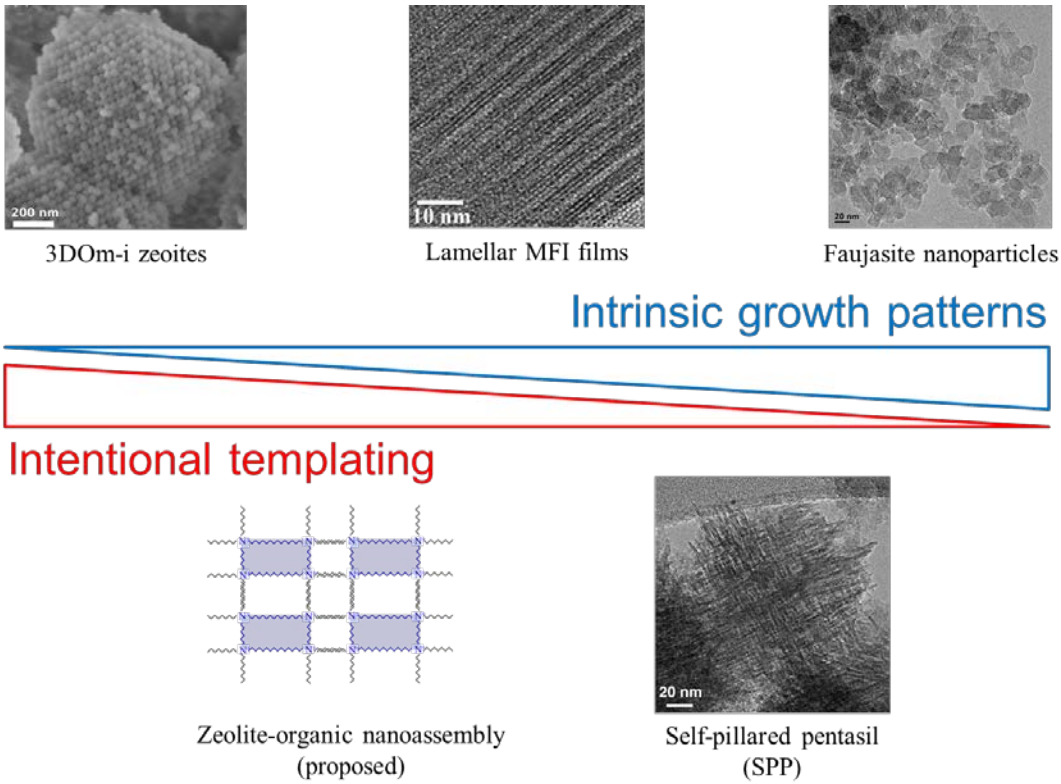

Figure 8-1 The driving force of zeolite nanoparticle formation: from the utilization of more intentional templating to more intrinsic growth patterns.

Throughout the dissertation, various methods to prepare zeolite nanoparticles are introduced in detail. (Fig. 8-1) The methods vary from imprinting from hard templates, where the particle size and morphology is completely defined by the hard template, to template-free synthesis, where the driving force is the intrinsic growth pattern of the particles in the specific environment without any template. For successful templating, the templates need to occupy the micropores or the mesopores; however, before the zeolites particles can be used, the templates need to be removed to open the pore systems. Thus, preparation and sacrificing of the templates could lead to high cost. Although intentional

templating usually provides direct paths toward nanostructure design, the ultimate goal for nanostructure preparation should be utilizing the intrinsic growth patterns of the crystals with simple templates or no template.

Zeolite is one material that has large specific surface area, most of which can be attributed to the internal surface area from the micropore walls. As seen in Chapter 6, with the preparation of SPP, apart from the internal surface area from the micropores, branching of microporous zeolite nanosheets creates additional surface area from the lamellae. In the specific case of SPP, the crystal planes exposed ((010) planes) also helps shorten the diffusion path, since the straight channel of MFI is perpendicular to (010) planes. This strategy utilized repeated epitaxial growth of ultra-small features (2 nm-thick nanosheets) to form high surface area morphologies, where the intrinsic crystal growth pattern, rather than intentional templating, is the main driving force.

Taking another look at Chapter 7, the preparation of the ultra-small zeolite nanoparticles is achieved by a template-free method, where the conditions are precisely controlled. It is not uncommon to have FAU and EMT intergrown in one particle. Considering the fact that particles with intersecting FAU lamellae was recently made by using an alkoxy silane with long chain[138], it is plausible to have FAU and EMT intergrow to form a self-pillared lamellar faujasite, possibly without organic template. The cocrystallization of ZSM-5 (MFI) and ZSM-11 (MEL) was also prepared without organic template recently[139], which provided hope for template-free synthesis of SPP. If this could be done, two most important zeolites in catalytic reactions, ZSM-5 and FAU (X and Y), can both be easily prepared with ultra-small diffusion path with large

mesopores by the template-free repetitive branching approach.

"There is plenty of room at the bottom." [140] Being not exclusive to zeolites, the repetitive branching growth pattern also exists in other materials, such as CdSe and CdTe tetrapods [112, 141], and TiO_2 (rutile) with "elbow branching" [142]. Inspired by this, microporous materials (such as zeolites and metal-organic frameworks) or non-porous materials (such as metal oxides) could also be made with ultra-high surface area by repetitive epitaxial growth. One potential use of these materials is natural gas processing. Unlike petroleum, natural gas is one energy source the United States does not depend on foreign producers for its own needs: in 2010 and 2011, US is a net exporter of natural gas. [143] In addition, gas hydrate, a solid form of methane hydrate, was very recently found to be quite abundant in the US. [144][145] Besides its abundance, natural gas also outperforms other energy sources in many aspects. As the demand of natural gas increases in recent years, one emerging problem started to draw more of scientists' attention: the removal of acidic gases from natural gas, or, "sweetening", in order to improve the quality of natural gas use, reduce the negative environmental impact of the use of fossil fuels, and safety for natural gas exploitation. [146] CO_2 and H_2S are the major acid gases existing in crude natural gas and gas hydrates, which takes up 5% - 8% (volume)[147], an enormous amount after considering that almost 70 billion cubic feet natural gas is produced per day [143]. Currently, affordable natural gas processing methods involve adsorption in liquid amines [146], and adsorption onto metal oxides and their mixtures. [146, 148-150] Solid adsorbents are usually preferred because they can be recycled and reused. Although the manipulation of morphology of particles is very well

developed, including that for higher specific surface area and selectively exposed facets, not so much was actually applied to natural gas processing. By applying the repetitive branching strategy, solid adsorbents with (1) high specific surface areas, (2) fast and selective adsorption properties, and (3) easy and reversible desorption are desirable for future research. Metal oxides and MOFs are the materials to be studied first.

Hopefully, with the development of new high surface area materials by repetitive branching, an economical and general synthesis approach for porous nanoparticles with repetitive branching features will be explored. Furthermore, they could also be used for applications such as adsorption and catalysis. Hopefully, with the successful achievement of these proposed research, the preparation of industrial particles will enter a new era, where the potential of intrinsic crystal growth pattern is further unleashed. As a result, particles with useful morphologies and architectures will not come with high cost, and they will be one great step closer to actual industrial applications.

Bibliography

[1] M. E. Davis, *Nature* **2002**, *417*, 813-821.
[2] E. L. First, C. E. Gounaris, J. Wei, C. A. Floudas, *Phys Chem Chem Phys* **2011**, *13*, 17339-17358.
[3] M. A. Snyder, M. Tsapatsis, *Angewandte Chemie* **2007**, *46*, 7560-7573.
[4] M. Tsapatsis, *Science* **2011**, *334*, 767-768.
[5] A. Corma, *J. Catal.* **2003**, *216*, 298-312.
[6] J. Perez-Ramirez, C. H. Christensen, K. Egeblad, C. H. Christensen, J. C. Groen, *Chem. Soc. Rev.* **2008**, *37*, 2530-2542.
[7] K. Varoon, X. Zhang, B. Elyassi, D. D. Brewer, M. Gettel, S. Kumar, J. A. Lee, S. Maheshwari, A. Mittal, C.-Y. Sung, M. Cococcioni, L. F. Francis, A. V. McCormick, K. A. Mkhoyan, M. Tsapatsis, *Science* **2011**, *333*, 72-75.
[8] X. Zhang, D. Liu, D. Xu, S. Asahina, K. A. Cychosz, K. V. Agrawal, Y. Al Wahedi, A. Bhan, S. Al Hashimi, O. Terasaki, M. Thommes, M. Tsapatsis, *Science* **2012**, *336*, 1684-1687.
[9] S. Z. Chen, K. Huddersman, D. Keir, L. V. C. Rees, *Zeolites* **1988**, *8*, 106-109.
[10] M. E. Leonowicz, J. A. Lawton, S. L. Lawton, M. K. Rubin, *Science* **1994**, *264*, 1910-1913.
[11] A. Corma, V. Fornes, S. B. Pergher, T. L. M. Maesen, J. G. Buglass, *Nature* **1998**, *396*, 353-356.
[12] M. Choi, K. Na, J. Kim, Y. Sakamoto, O. Terasaki, R. Ryoo, *Nature* **2009**, *461*, 246-U120.
[13] M. A. Snyder, M. Tsapatsis, *Angew. Chem.-Int. Edit.* **2007**, *46*, 7560-7573.
[14] K. Varoon, X. Zhang, B. Elyassi, D. D. Brewer, M. Gettel, S. Kumar, J. A. Lee, S. Maheshwari, A. Mittal, C. Y. Sung, M. Cococcioni, L. F. Francis, A. V. McCormick, K. A. Mkhoyan, M. Tsapatsis, *Science* **2011**, *333*, 72-75.
[15] A. P. Alivisatos, *J Phys Chem-Us* **1996**, *100*, 13226-13239.
[16] V. E. Henrich, *Rep Prog Phys* **1985**, *48*, 1481-1541.
[17] G. M. Rignanese, A. De Vita, J. C. Charlier, X. Gonze, R. Car, *Phys Rev B* **2000**, *61*, 13250-13255.
[18] B. J. Alder, T. E. J. Wainwright, *J. Chem. Phys.* **1957**, *27*, 1208-1209.
[19] P. Hohenberg, W. Kohn, *Phys. Rev. B* **1964**, *136*, 864-871.
[20] M. Levy, *Proc Natl Acad Sci U S A* **1979**, *76*, 6062-6065.
[21] R. Car, M. Parrinello, *Phys Rev Lett* **1985**, *55*, 2471-2474.
[22] M. A. Camblor, A. Corma, M. J. Diaz-Cabanas, C. Baerlocher, *J. Phys. Chem. B* **1998**, *102*, 44-51.
[23] A. Corma, V. Fornes, J. M. Guil, S. Pergher, T. L. M. Maesen, J. G. Buglass, *Microporous Mesoporous Mat.* **2000**, *38*, 301-309.
[24] H. van Koningsveld, J. C. Jansen, H. van Bekkum, *Zeolites* **1990**, *10*, 235-242.
[25] P. Giannozzi, S. Baroni, N. Bonini, M. Calandra, R. Car, C. Cavazzoni, D. Ceresoli, G. L. Chiarotti, M. Cococcioni, I. Dabo, A. Dal Corso, S. de Gironcoli, S. Fabris, G. Fratesi, R. Gebauer, U. Gerstmann, C. Gougoussis, A. Kokalj, M.

Lazzeri, L. Martin-Samos, N. Marzari, F. Mauri, R. Mazzarello, S. Paolini, A. Pasquarello, L. Paulatto, C. Sbraccia, S. Scandolo, G. Sclauzero, A. P. Seitsonen, A. Smogunov, P. Umari, R. M. Wentzcovitch, *J. Phys.-Condes. Matter* **2009**, *21*.
[26] J. P. Perdew, K. Burke, M. Ernzerhof, *Phys. Rev. Lett.* **1996**, *77*, 3865-3868.
[27] B. E. Warren, *X-ray diffraction*, Addison-Wesley Pub. Co., Reading, Mass.,, **1969**.
[28] A. Guinier, *X-ray diffraction in crystals, imperfect crystals, and amorphous bodies*, Dover, New York, **1994**.
[29] P. Scherrer, *Gött. Nachr.* **1918**, *2*, 98.
[30] J. L. Schlenker, B. K. Peterson, *J. Appl. Cryst.* **1996**, *29*, 178-185.
[31] D. D. Kragten, J. M. Fedeyko, K. R. Sawant, J. D. Rimer, D. G. Vlachos, R. F. Lobo, M. Tsapatsis, *J. Phys. Chem. B* **2003**, *107*, 10006-10016.
[32] J. M. Cowley, A. F. Moodie, *Acta Crystallogr.* **1957**, *10*, 609.
[33] E. J. Kirkland, R. F. Loane, J. Silcox, *Ultramicroscopy* **1987**, *23*, 77-96.
[34] R. F. Loane, P. R. Xu, J. Silcox, *Acta Crystallogr. Sect. A* **1991**, *47*, 267-278.
[35] E. J. Kirkland, *Advanced Computing in Electron Microscopy*, 2nd ed., Springer, New York, **2010**.
[36] N. M. Butt, J. Bashir, B. T. M. Willis, G. Heger, *Acta Cryst.* **1988**, *A44*, 396.
[37] J. C. Meyer, A. K. Geim, M. I. Katsnelson, K. S. Novoselov, T. J. Booth, S. Roth, *Nature* **2007**, *446*, 60-63.
[38] Z. P. Lai, G. Bonilla, I. Diaz, J. G. Nery, K. Sujaoti, M. A. Amat, E. Kokkoli, O. Terasaki, R. W. Thompson, M. Tsapatsis, D. G. Vlachos, *Science* **2003**, *300*, 456-460.
[39] J. Choi, H. K. Jeong, M. A. Snyder, J. A. Stoeger, R. I. Masel, M. Tsapatsis, *Science* **2009**, *325*, 590-593.
[40] M. Woo, J. Choi, M. Tsapatsis, *Micropor Mesopor Mat* **2008**, *110*, 330-338.
[41] G. Xomeritakis, A. Gouzinis, S. Nair, T. Okubo, M. Y. He, R. M. Overney, M. Tsapatsis, *Chem Eng Sci* **1999**, *54*, 3521-3531.
[42] T. Bein, *Chem Mater* **1996**, *8*, 1636-1653.
[43] M. C. Lovallo, M. Tsapatsis, *Aiche J* **1996**, *42*, 3020-3029.
[44] W. Fan, M. A. Snyder, S. Kumar, P.-S. Lee, W. C. Yoo, A. V. McCormick, R. L. Penn, A. Stein, M. Tsapatsis, *Nat Mater* **2008**, *7*, 984-991.
[45] J. C. Groen, L. A. A. Peffer, J. A. Moulijn, J. Perez-Ramirez, *Micropor Mesopor Mat* **2004**, *69*, 29-34.
[46] M. Ogura, S. Y. Shinomiya, J. Tateno, Y. Nara, M. Nomura, E. Kikuchi, M. Matsukata, *Appl Catal a-Gen* **2001**, *219*, 33-43.
[47] T. Suzuki, T. Okuhara, *Micropor Mesopor Mat* **2001**, *43*, 83-89.
[48] G. N. Karanikolos, J. W. Wydra, J. A. Stoeger, H. Garcia, A. Corma, M. Tsapatsis, *Chem Mater* **2007**, *19*, 792-797.
[49] A. Gouzinis, M. Tsapatsis, *Chem Mater* **1998**, *10*, 2497-2504.
[50] G. Bonilla, M. Tsapatsis, D. G. Vlachos, G. Xomeritakis, *J. Membr. Sci.* **2001**, *182*, 103-109.
[51] V. Nikolakis, E. Kokkoli, M. Tirrell, M. Tsapatsis, D. G. Vlachos, *Chem Mater* **2000**, *12*, 845-853.

[52] S. Kumar, Z. Wang, R. L. Penn, M. Tsapatsis, *J. Am. Chem. Soc.* **2008**, *130*, 17284-17288.
[53] M. A. Snyder, J. A. Lee, T. M. Davis, L. E. Scriven, M. Tsapatsis, *Langmuir* **2007**, *23*, 9924-9928.
[54] T. Yokoi, Y. Sakamoto, O. Terasaki, Y. Kubota, T. Okubo, T. Tatsumi, *J Am Chem Soc* **2006**, *128*, 13664-13665.
[55] I. Schmidt, C. Madsen, C. J. H. Jacobsen, *Inorg Chem* **2000**, *39*, 2279-2283.
[56] T. M. Davis, T. O. Drews, H. Ramanan, C. He, J. S. Dong, H. Schnablegger, M. A. Katsoulakis, E. Kokkoli, A. V. McCormick, R. L. Penn, M. Tsapatsis, *Nat. Mater.* **2006**, *5*, 400-408.
[57] C. V. Iancu, W. F. Tivol, J. B. Schooler, D. P. Dias, G. P. Henderson, G. E. Murphy, E. R. Wright, Z. Li, Z. H. Yu, A. Briegel, L. Gan, Y. N. He, G. J. Jensen, *Nat Protoc* **2006**, *1*, 2813-2819.
[58] M. A. Camblor, A. Corma, S. Valencia, *Micropor Mesopor Mat* **1998**, *25*, 59-74.
[59] A. Zukal, V. Patzelova, U. Lohse, *Zeolites* **1986**, *6*, 133-136.
[60] C. F. Blanford, C. B. Carter, A. Stein, *J Microsc-Oxford* **2004**, *216*, 263-287.
[61] A. Iwasaki, T. Sano, *Zeolites* **1997**, *19*, 41-46.
[62] M. E. Davis, R. F. Lobo, *Chem. Mater.* **1992**, *4*, 756-768.
[63] C. S. Cundy, P. A. Cox, *Chem Rev* **2003**, *103*, 663-701.
[64] A. Stein, F. Li, Z. Wang, *J Mater Chem* **2009**, *19*, 2094-2098.
[65] B. J. Schoeman, J. Sterte, J. E. Otterstedt, *Zeolites* **1994**, *14*, 208-216.
[66] S. Mintova, N. H. Olson, T. Bein, *Angew Chem Int Edit* **1999**, *38*, 3201-3204.
[67] B. A. Holmberg, H. T. Wang, J. M. Norbeck, Y. S. Yan, *Micropor Mesopor Mat* **2003**, *59*, 13-28.
[68] Z. J. Li, C. M. Lew, S. Li, D. I. Medina, Y. S. Yan, *J. Phys. Chem. B* **2005**, *109*, 8652-8658.
[69] J. Motuzas, A. Julbe, R. D. Noble, C. Guizard, Z. J. Beresnevicius, D. Cot, *Micropor Mesopor Mat* **2005**, *80*, 73-83.
[70] V. P. Valtchev, A. C. Faust, J. Lezervant, *Micropor Mesopor Mat* **2004**, *68*, 91-95.
[71] R. Van Grieken, J. L. Sotelo, J. M. Menendez, J. A. Melero, *Micropor Mesopor Mat* **2000**, *39*, 135-147.
[72] W. Song, R. E. Justice, C. A. Jones, V. H. Grassian, S. C. Larsen, *Langmuir* **2004**, *20*, 8301-8306.
[73] J. Aguado, D. P. Serrano, J. M. Escola, J. M. Rodriguez, *Micropor. Mesopor. Mater.* **2004**, *75*, 41-49.
[74] G. S. Zhu, S. L. Qiu, J. H. Yu, Y. Sakamoto, F. S. Xiao, R. R. Xu, O. Terasaki, *Chem Mater* **1998**, *10*, 1483-1486.
[75] M. Tsapatsis, M. Lovallo, T. Okubo, M. E. Davis, M. Sadakata, *Chem Mater* **1995**, *7*, 1734-1741.
[76] M. Choi, K. Na, J. Kim, Y. Sakamoto, O. Terasaki, R. Ryoo, *Nature* **2009**, *461*, 246-249.
[77] M. Choi, H. S. Cho, R. Srivastava, C. Venkatesan, D.-H. Choi, R. Ryoo, *Nat. Mater.* **2006**, *5*, 718-723.

[78] P. K. Dutta, M. Jakupca, K. S. N. Reddy, L. Salvati, *Nature* **1995**, *374*, 44-46.
[79] G. Bonilla, I. Diaz, M. Tsapatsis, H. K. Jeong, Y. Lee, D. G. Vlachos, *Chem Mater* **2004**, *16*, 5697-5705.
[80] S. Masse, G. Laurent, T. Coradin, *Phys Chem Chem Phys* **2009**, *11*, 10204-10210.
[81] R. F. Lobo, S. I. Zones, M. E. Davis, *J Inclus Phenom Mol* **1995**, *21*, 47-78.
[82] D. W. Lewis, D. J. Willock, C. R. A. Catlow, J. M. Thomas, G. J. Hutchings, *Nature* **1996**, *382*, 604-606.
[83] P. A. Wright, M. J. Maple, A. M. Z. Slawin, V. Patinec, R. A. Aitken, S. Welsh, P. A. Cox, *J Chem Soc Dalton* **2000**, 1243-1248.
[84] A. Merrouche, J. Patarin, H. Kessler, M. Soulard, L. Delmotte, J. L. Guth, J. F. Joly, *Zeolites* **1992**, *12*, 226-232.
[85] R. M. Barrer, P. J. Denny, *J. Chem. Soc.* **1961**, 971.
[86] T. Tomohiro, K. Uoto, H. Y. Okuno, *J Heterocyclic Chem* **1990**, *27*, 1233-1239.
[87] H. Zahn, H. Spoor, *Chemische Berichte* **1959**, *92*, 1375.
[88] Y. Okuno, K. Horita, O. Yonemitsu, K. Shibata, T. Amemiya, R. H. Holm, *J Chem Soc Perk T 1* **1984**, 1115-1118.
[89] M. Rothe, M. Lohmuller, U. Breuksch, G. Schmidtberg, *Angewandte Chemie-International Edition in English* **1994**, *33*, 1960-1961.
[90] A. Jackowski, S. I. Zones, S. J. Hwang, A. W. Burton, *J Am Chem Soc* **2009**, *131*, 1092-1100.
[91] *U.S. Patent 7,341,872.*
[92] J. M. Newsam, T. Bein, J. Klein, W. F. Maier, W. Stichert, *Micropor Mesopor Mat* **2001**, *48*, 355-365.
[93] D. E. Akporiaye, I. M. Dahl, A. Karlsson, R. Wendelbo, *Angew Chem Int Edit* **1998**, *37*, 609-611.
[94] J. D. Rimer, R. F. Lobo, D. G. Vlachos, *Langmuir* **2005**, *21*, 8960-8971.
[95] S. I. Zones, S. J. Hwang, S. Elomari, I. Ogino, M. E. Davis, A. W. Burton, *Cr Chim* **2005**, *8*, 267-282.
[96] M. A. Camblor, L. A. Villaescusa, M. J. Diaz-Cabanas, *Top Catal* **1999**, *9*, 59-76.
[97] K. Na, M. Choi, W. Park, Y. Sakamoto, O. Terasaki, R. Ryoo, *J Am Chem Soc* **2010**, *132*, 4169-4177.
[98] S. Choi, J. Coronas, E. Jordan, W. Oh, S. Nair, F. Onorato, D. F. Shantz, M. Tsapatsis, *Angew Chem Int Edit* **2008**, *47*, 552-555.
[99] S. Maheshwari, E. Jordan, S. Kumar, F. S. Bates, R. L. Penn, D. F. Shantz, M. Tsapatsis, *J. Am. Chem. Soc.* **2008**, *130*, 1507-1516.
[100] V. Valtchev, B. Schoeman, J. Hedlund, S. Mintova, J. Sterte, *Zeolites* **1996**, *17*, 408-415.
[101] M. Matsukata, M. Ogura, T. Osaki, P. R. H. P. Rao, M. Nomura, E. Kikuchi, *Top Catal* **1999**, *9*, 77-92.
[102] C. Madsen, C. J. H. Jacobsen, *Chem Commun* **1999**, 673-674.
[103] B. T. Holland, L. Abrams, A. Stein, *J Am Chem Soc* **1999**, *121*, 4308-4309.
[104] K. Na, M. Choi, W. Park, Y. Sakamoto, O. Terasaki, R. Ryoo, *J. Am. Chem. Soc.* **2010**, *132*, 4169-4177.
[105] K. Lund, N. Muroyama, O. Terasaki, *Micropor Mesopor Mat* **2010**, *128*, 71-77.

[106] Y. X. Wang, H. Gies, B. Marler, U. Muller, *Chem. Mater.* **2005**, *17*, 43-49.
[107] W. J. Roth, D. L. Dorset, *Micropor. Mesopor. Mater.* **2011**, *142*, 32-36.
[108] D. Liu, A. Bhan, M. Tsapatsis, S. Al Hashimi, *ACS Catal.* **2011**, *1*, 7-17.
[109] J. Wang, W. Yue, W. Zhou, M.-O. Coppens, *Micropor. Mesopor. Mater.* **2009**, *120*, 19-28.
[110] D. P. Serrano, J. Aguado, J. M. Escola, A. Peral, G. Morales, E. Abella, *Catal. Today* **2011**, *168*, 86-95.
[111] K. Na, C. Jo, J. Kim, K. Cho, J. Jung, Y. Seo, R. J. Messinger, B. F. Chmelka, R. Ryoo, *Science* **2011**, *333*, 328-332.
[112] L. Manna, D. J. Milliron, A. Meisel, E. C. Scher, A. P. Alivisatos, *Nat. Mater.* **2003**, *2*, 382-385.
[113] Y.-w. Jun, H.-W. Chung, J.-t. Jang, J. Cheon, *J. Mater. Chem.* **2011**, *21*, 10283-10286.
[114] T. Ohsuna, O. Terasaki, Y. Nakagawa, S. I. Zones, K. Hiraga, *J. Phys. Chem. B* **1997**, *101*, 9881-9885.
[115] M. M. J. Treacy, D. E. W. Vaughan, K. G. Strohmaier, J. M. Newsam, *Proc. R. Soc. A* **1996**, *452*, 813-840.
[116] H. K. Jeong, J. Krohn, K. Sujaoti, M. Tsapatsis, *J. Am. Chem. Soc.* **2002**, *124*, 12966-12968.
[117] T. Okubo, T. Wakihara, J. Plevert, S. Nair, M. Tsapatsis, Y. Ogawa, H. Komiyama, M. Yoshimura, M. Davis, *Angewandte Chemie* **2001**, *40*, 1069-1071.
[118] L. Karwacki, M. H. F. Kox, D. A. M. de Winter, M. R. Drury, J. D. Meeldijk, E. Stavitski, W. Schmidt, M. Mertens, P. Cubillas, N. John, A. Chan, N. Kahn, S. R. Bare, M. Anderson, J. Kornatowski, B. M. Weckhuysen, *Nat. Mater.* **2009**, *8*, 959-965.
[119] G. R. Millward, S. Ramdas, J. M. Thomas, *Proc. R. Soc. A* **1985**, *399*, 57-71.
[120] K. Moeller, T. Bein, *Science* **2011**, *333*, 297-298.
[121] W. Fan, M. A. Snyder, S. Kumar, P.-S. Lee, W. C. Yoo, A. V. McCormick, R. L. Penn, A. Stein, M. Tsapatsis, *Nat. Mater.* **2008**, *7*, 984-991.
[122] S. D. Kim, S. H. Noh, J. W. Park, W. J. Kim, *Micropor. Mesopor. Mater.* **2006**, *92*, 181-188.
[123] P. I. Ravikovitch, A. V. Neimark, *Colloids Surf., A* **2001**, *187*, 11-21.
[124] N. S. John, S. M. Stevens, O. Terasaki, M. W. Anderson, *Chem. Eur. J.* **2010**, *16*, 2220-2230.
[125] C. A. Fyfe, H. Gies, G. T. Kokotailo, C. Pasztor, H. Strobl, D. E. Cox, *J. Am. Chem. Soc.* **1989**, *111*, 2470-2474.
[126] H. van Koningsveld, J. C. Jansen, H. van Bekkum, *Zeolites* **1990**, *10*, 8.
[127] P. Cheung, A. Bhan, G. J. Sunley, E. Iglesia, *Angewandte Chemie* **2006**, *45*, 1617-1620.
[128] L. Y. Hou, L. B. Sand, in *Proceeding of the Sixth International Zeolite Conference* (Eds.: D. Olson, A. Bisio), Guildford, Surrey, UK : Butterworths, Reno, USA, **1983**, pp. 887-893.
[129] T. C. T. Pham, H. S. Kim, K. B. Yoon, *Science* **2011**, *334*, 1533-1538.
[130] A. Tuel, Y. B. Taarit, *Micropor. Mater.* **1994**, *2*, 13.

[131] R. Aris, in *Elementary Chemical Reactor Analysis*, Dover, **1989**.
[132] O. Casanova, S. Iborra, A. Corma, *J. Catal.* **2010**, *275*, 236-242.
[133] R. M. Barrer, *J. Chem. Soc.* **1948**, 2158.
[134] H. Heinemann, *Catal Rev* **1981**, *23*, 315-328.
[135] *U.S. Patent 3,808,326.*
[136] M. S. Ladinsky, *Method Enzymol* **2010**, *481*, 165-194.
[137] M. M. J. Treacy, J. M. Newsam, M. W. Deem, *P Roy Soc Lond a Mat* **1991**, *433*, 499-520.
[138] A. Inayat, I. Knoke, E. Spiecker, W. Schwieger, *Angewandte Chemie* **2012**, *51*, 3.
[139] L. Zhang, S. L. Liu, S. J. Xie, L. Y. Xu, *Micropor Mesopor Mat* **2012**, *147*, 117-126.
[140] R. Feynman, in *There's Plenty of Room at the Bottom (lecture)*, Pasadena, CA, **1959**.
[141] L. Manna, E. C. Scher, A. P. Alivisatos, *J Am Chem Soc* **2000**, *122*, 12700-12706.
[142] E. R. Force, R. P. Richards, K. M. Scott, P. C. Valentine, N. S. Fishman, *Canadian Minerologist* **1996**, *34*, 605.
[143] *Short-Term Energy Outlook, October 2012. US Energy Information Administration.*
[144] E. D. Sloan, *Nature* **2003**, *426*, 353-359.
[145] *US Geological Survey: http://marine.usgs.gov/fact-sheets/gas-hydrates/title.html (accessed: Oct. 26, 2012).*
[146] A. B. Rao, E. S. Rubin, *Environ. Sci. Technol.* **2002**, *36*, 4467-4475.
[147] *National Gas Supply Association: http://www.naturalgas.org/environment/naturalgas.asp (accessed: Oct. 26, 2012).*
[148] M. Flytzani-Stephanopoulos, M. Sakbodin, Z. Wang, *Science* **2006**, *312*, 1508-1510.
[149] S. S. Tamhankar, M. Bagajewicz, G. R. Gavalas, P. K. Sharma, M. Flytzani-Stephanopoulos, *Ind. Eng. Chem. Proc. Des. Dev.* **1986**, *25*, 429-437.
[150] Z. Wang, M. Flytzani-Stephanopoulos, *Energy & Fuels* **2005**, *19*, 2089-2097.